Imperial College London
Department of Electrical and Electronic Engineering

Circuits and Systems for DNA Detection by Ion-Sensitive Field Effect Transistor

Mohammadreza Sohbati

September 2014

Supervised by Regius Professor Christofer Toumazou

Submitted for the degree of
Doctor of Philosophy in Electrical and Electronic Engineering of Imperial College London
and the Diploma of Imperial College London

Declaration

I hereby declare that this thesis and the work described is my own and that everything else is appropriately referenced and attributed.

Mohammadreza Sohbati

Copyright Declaration

Abstract

This thesis, after a review on the state-of-the-art sequencing and genotyping technologies, focuses on the semiconductor-based systems using pH change for DNA (Deoxyribonucleic acid) detection by ion-sensitive field effect transistors (ISFETs). Accuracy and throughput, besides cost, are the key concerns in these systems, which are reflected on their signal-to-noise ratio and ability to process enormous measurement data at low levels for base-calling. Simulations are provided on the signal behaviour, supported by the literature review.

The ISFETs have been investigated for their dimension and shape (single-plate vs mesh, and square vs octagonal). More complete formula and a design methodology (to suppress the process variations and signal drift) have been provided for the ISFET operation by including the coupling effect. The experiment results, on 8 dies each containing 15 devices, showed the decoupling parasitics dependency on the sensing area perimeter. A buffer-shield structure has been proposed to improve the ISFET coupling. In addition, based on the ISFET drift analysis, measuring the biasing reference electrode current is recommended for the drift direction monitoring/prediction.

Considering the two main applications of sequencing and genotyping, new readout configurations have been proposed to enhance the on-chip signal processing. Piecewise linear approximating (PLA), and temperature-insensitive continuous-time ΔpH to digital converter (TICTC), tackle the ISFET and temperature dependency. The TICTC has been designed for a resolution of $0.015pH$, easily scalable and only dependent on the relative aspect ratio of its current mirrors. Its dynamic range is not limited despite operating in weak inversion. For very large-scale sequencing arrays, common-mode noise elimination using the back-gate has been proposed. It allows on-chip suppression of the background noise in the sequencing microchips, reducing the low-level processing load. Moreover, a pseudo-inverter-based readout has been designed that may allow improving the conversion resolution by current-mode comparison and indirect feedback to the ISFET gate.

To my parents and my sisters

Acknowledgements

First and foremost, I would like to express my sincere appreciation to Professor Toumazou for his kindness, inspiration, patience, understanding and encouragements. I am so grateful to him for giving me the opportunity to be part of his wonderful research and industry families. His inspiration, vision, approach to innovation and remarkable ability in translating imaginations to words and products, have always motivated me on drawing bigger pictures without boundaries and sharing ideas without lines. I am so honoured to work under his supervision and experience research, academia and industry collaborations. Definitely things I have learned from him are much beyond the words in this thesis and I will always have him as a role model.

I would like to thank Dr. Pantelis Georgiou for his kindness, care and valuable advices. His knowledge, experience, hard work and patience are admirable. I am also thankful to Dr. Timothy Constandinou for encouragements and leading feedbacks especially on my early stage assessment, and giving me the opportunity to be one of his teacher assistants.

I have been fortunate to have support and insight from DNA Electronics. In particular, I would like to thank Mr. Samuel Reed for his inspiring and inventive discussions. I would also like to thank Dr. Leila Shepherd, Dr. David Garner, Mr Alpesh Patel, Ms Pearl Stevens, Dr. Chung-pei Ou, Mr Hua Bai, and Dr. Maurizio Lamura.

Especially, I would like to thank Ms. Wiesia Hsissen for her extraordinary kindness and care. Also especial thanks to Dr. Christos Papavassiliou for his encouragements during my MSc and for pursuing my PhD.

I would like to thank Ms Gifty Kugblenu for her wonderful care, and Ms Izabela Wojcicka-Grzesiak for her continuous kind support. I would also like to thank Ms Sandra Lock who looked after us very carefully during summer 2013. Experiments of this thesis would have not been possible without the kind help of Ms Maria Khaleeq.

I am so blessed to be living and working with many great people, with especial mention to my caring and encouraging friend Melina, and my kind supportive friend Amir. In particular, I would like to thank my remarkable friend Song from whom I learned a lot. I would like to thank my wonderful friends Yuanqi, Ermis, Yan, Lieuwe, Radu, Pete, Pau, Mohamed, Onur, Deren, Dora, Tatiana, Syvilla, Irina, Reza, Satoshi, Abdul, Olive, Ali...and all the noble people at Winston Wong Centre for Bio-inspired Technology. Especially I would like to thank Professor Tor Svere Lande (Bassen) for his stunning discussions, Dr. Konstantin Nickolic, Prof. David Skellern, Dr. Andrea Gonzalez, and Dr. Belinda Nedjai.

On my journey, I have had the company of my dear friends Arta, Parisa, and Mani. And definitely the start of this particular quest goes way before. I would like to thank my bright friends Ramtin, Keivan, Sohail, Babak, Afshin, Khashayar, Mohammad, Mostafa, Hossein,...

A big thank to my lovely aunt Rezieh and my dear cousin Amir. They have been a blessing for me and a caring family since I moved to London. Their company is always full of joy.

My deepest gratitude to my wonderful noble sisters, Samira and Mandana. Their encouragements, support, patience and love is so remarkable that I can't put it in a statement. No word can express how grateful I am to my family. I am the luckiest child in the world to have the most passionate, dedicated, generous, extremely wonderful, truly supportive and kind parents. A tremendous thank to my parents Forough and Alireza, for their unique greatness and sacrifices they have made to get me where I am today. I dont know how to say and how to write it. You are the greatest. Nothing could be possible without you. This thesis is dedicated to you! Thank you xx

Contents

List of Tables

List of Figures

Directory of Companies

Company	Website	Location	Telephone
23andMe	www.23andme.com	1390 Shorebird Way, Mountain View CA 94043, USA	+1-650-938-6300
Affymetrix	www.affymetrix.com	3420 Central Expressway Santa Clara, CA 95051, USA	+1-888-362-2447
Agielnt	www.agilent.com	5301 Stevens Creek Blvd Santa Clara, CA 95051, USA	+1-877-424-4536
Applied Biosystems		A Life Technologies Brand	
Beckman Coulter Inc	www.beckmancoulter.com	250 S. Kraemer Blvd Brea, CA 94043, USA	+1-714-993-8750
CombiMatrix	www.combimatrix.com	300 Goddard, Suite 100 Irvine, CA 92618, USA	+1-800-710-0624
Complete Genomics	www.completegenomics.com	2071 Siterlin Court, Mountain View CA 94043, USA	+1-650-943-2800
Custom Array Inc	www.customarrayinc.com	18916 North Creek Parkway Suite 115, Bothell WA 98011, USA	+1-425-609-0923
DNA Electronics	www.dnae.co.uk	56 Wood Lane, London W12 7SB, UK	+44-207-036-2144
Electron Optica	www.electronoptica.com	1000 Elwell Court #110 Palo Alto California, USA	+1-415-706-1557
Electronic Biosciences	www.electronicbio.com	5754 Pacific Center Blvd. Ste. 204, San Diego CA 92121, USA	+1-858-412-1704
Filmarray	www.filmarray.com	390 Wakara Way Salt Lake City Utah 84108, USA	+1-800-735-6544
Geneapsys	www.geneapsys.com	200 Cardinal Way, 3rd floor Redwood City CA 94063, USA	+1-650-330-1096
Genelink Inc	www.genelink.com	190 Saw Mill River Rd. Hawthorne, NY 10532, USA	+1-800-436-3546
GeneU	www.geneu.com	65 New Bond Street, London W1S 1RN, UK	+44-207-499-7161
GenMarkDx	www.genmarkdx.com	5964 La Place Court Carlsbad, CA 92008, USA	+1-800-373-6767
Genia	www.geniachip.com	325 E. Middlefield Rd. Mountain View CA 94043, USA	+1-650-300-5970
GnBio	www.gnubio.com	1 Kendall Square, Building 1400 Suite B14201, Cambridge MA 02139, USA	+1-617-446-6744
IBM	www.ibm.com	1 New Orchard Rd, Armonk NY 10504, USA	+1-914-499-1900
Illumina	www.illumina.com	5200 Illumina Way, San Diego CA 92122, USA	+1-858-202-4500

Company	Website	Location	Telephone
Intel	www.intel.com	2200 Mission College Blvd Santa Clara CA 95054-1549, USA	+1-408-765-8080
Ion-Torrent		A Life Technologies Brand	
LaserGen	www.lasergen.com	8052 El Rio Street, Houston Texas 77054, USA	+1-713-747-3380
Life Technologies	www.lifetechnologies.com	3175 Staley Road, Grand Island NY 14072, USA	+1-800-955-6288
Lightspeed Genomics	www.lsgen.com	2255 Martin Avenue, Suite F Santa Clara, CA 95050, USA	+1-408-988-2700
Nabsys	www.nabsys.com	60 Clifford St., Providence RI 02903, USA	+1-401-276-9100
NHGRI	www.genome.gov	31 Center Drive, Bathesda, MD 20892-2152, USA	+1-301-402-0911
NobleGen Biosciences	www.noblegenbio.com	58 Elsinore St. Concord MA 01742, USA	+1-978-405-2533
Oxford Nanopore	www.nanoporetech.com	Edmund Cartwright House 4 Robert Robinson Avenue Oxford Science Park Oxford OX4 4GA, UK	+44-845-034-7900
Pacific Biosciences	www.pacificbiosciences.com	1380 Willow Rd. Menlo Park CA 94025, USA	+1-650-521-8000
Qiagen	www.qiagen.com	Spoorstraat 50, 5911 KJ Venlo, Netherlands	+31-77-320-8409
QuantuMDx	www.quantumdx.com	Market Keepers House International Centre for Life Times Square, Newcastle NE1 4EP, UK	+44-870-803-1234
Reveo	www.reveo.com	6 Skyline Drive, Hawthorne NY 10532, USA	+1-646-539-3300
Roche	www.roche.com	Konzern Hauptsitz Grenzacherstrasse 124, CH-4070 Basel Switzerland	+41-61-688-1111
SkinDNA	www.skindna.com.au	Suite 602, Level 6 2 O'Connell Street Sydney 2000, Australia	+61-2-9043-1300
Stratos Genomics	www.stratosgenomics.com	World Trade Center East 2211 Elliott Ave. Suite 210 Seattle, WA 98121, USA	+1-206-448-7961
Thermofisher	www.thermofisher.com	81 Wyman Street, Waltham MA 02451, USA	+1-781-622-1000
Two Pore Guys	www.twoporeguys.com	103 Lisa Ct, Santa Cruz CA 95060, USA	+1-831-515-8515
ZS Genetics	www.zsgenetics.com	9 Audubon Road, Wakefield MA 01880, USA	NA

Glossary

$1,000 genome It is a catchphrase used to discuss the future of biomedical sciences and personalised care when genome sequencing would cost less than $1,000. It became a goal for sequencing industries to reduce the cost of sequencing to this point. 46

α-hemolysin A bacterial peptide creating pores in eukaryotic cell membranes. 41

αHL α-hemolysin. 41

μ-BAR Microfluidic Biomolecular Amplification Reader. 5

μ-TAS Micro Total Analysis Set-up. 5, 14, 21, 162, 168

2's complement A binary signed number representation. xvii, 151, 155, 156, 158

AC Alternate Current. 29

acrylamide A colourless crystalline solid which readily forms water-soluble polymers. 55

adapter In sequencing and genotyping it is a chemically synthesized DNA linked to the end(s) of the target DNA in order to be immobilized on a surface or attached to another strand of DNA. 15, 22–24

ADC Analogue to Digital Converter. 52, 116, 143, 148

Adenine A nitrogenous base type. 10

Ag/AgCl Silver/Silver-Chloride. 75, 89, 103, 148

aliphatic Relating to or denoting organic compounds in which carbon atoms form open chains (as in the alkanes), not aromatic rings. 19

amino acid A simple organic compound containing both a carboxyl (COOH) and an amino (NH2) group. Amino acids form the basic constituents of proteins. 9, 12

antibiotic A medicine (such as penicillin or its derivatives) that inhibits the growth of or destroys microorganisms. 6

APS Adenosine 5' Phosphosulfate. 22

apyrase Adenosine diphosphatase, an enzyme that can degrade un-incorporated nucleotides and ATP. 22, 54

ATP Adenosine Triphosphate. xxii

ATP sulfurylase An enzyme that catalyses the activation of sulphate ions by ATP to form adenosine-5'-phosphosulfate and pyrophosphate. 22

back-gate Also known as bulk and body, a terminal of MOSFET used for biasing the transistor. iv, xvii, 8, 40, 59, 125, 126, 128, 133, 134, 165

band gap The energy difference (in electron volts) between the top of the valence band and the bottom of the conduction band in insulators and semiconductors. 74

base-call The process of assigning signal changes during sequencing to certain type of nucleotide(s). iv, 3, 16, 41, 52, 56, 58–61, 64, 68, 69, 126, 163, 167

base-pair A pair of nucleo-bases that complementary-match each other. 5, 10

biomarker A certain bio-molecule that may hybridize with a target molecule based on their structure and form bonds. 2, 5, 8, 21, 165

biosensor Sensor for biological reaction monitoring. 2, 7, 9, 28, 29, 42, 43

biotin In molecular biology it is a non-radioactive label for DNA molecules. 20

body effect Body effect occurs when body/substrate/back-gate of transistor is not biased at same level as that of source, which results in change of threshold voltage by change in the body-source potential. 125

Cadence Spectre A computer aid software for designing integrated circuits. 83, 122, 145, 157

CBCM Charge-based Capacitive Measurement. xiv, 31–33

CCD Charge Coupled Device. 19, 22–24, 46, 52, 61

cDNA complementary DNA. 19, 20

CDS Correlated Double Sampling. xiv, 37

CE Capillary Electrophoresis. 17

chelator A chemical compound in the form of a heterocyclic ring, containing a metal ion attached by coordinate bonds to at least two nonmetal ions. xv, 40

ChemFET An ISFET with modified membrane to sense other chemicals. 42

chronic disease A long-lasting condition that can be controlled but not cured. 6

cloud In computing, a network of remote servers hosted on the Internet and used to store, manage, and process data in place of local servers or personal computers. 7

CMOS Complementary Metal-Oxide-Semiconductor. xv, 3, 4, 6, 36, 39, 42–47, 57, 68, 70, 71, 74–77, 79–81, 88, 89, 103, 105, 109, 116, 125, 161–163, 165, 167

CTAT Complementary to Absolute Temperature. 48

Cytosine A nitrogenous base type. 10

DAC Digital to Analogue Converter. 116, 140, 143–145

dATP deoxyadenosine Triphosphate. 17

DC Direct Current. 29, 42

DC offset A mean amplitude displacement from zero. iv, 8, 75, 103, 106, 108–111, 113–115, 118, 124, 125, 134, 135, 137, 143, 161, 162, 164–166

dCTP deoxycytidine Triphosphate. 17

ddATP dideoxyadenosine Triphosphate. 17

ddCTP dideoxycytidine Triphosphate. 17

ddGTP dideoxyguanosine Triphosphate. 17

ddNTP dideoxyribonucleotide Triphosphate. 14, 17, 18

ddTTP dideoxythymidine Triphosphate. 17

de-novo Anew, starting from the beginning. 16

DFF D-Flip Flop. A digital logic device that stores the status of its "D" input whenever its clock input makes a certain transition (low to high or high to low). 145, 146, 154, 156

dGTP deoxyrguanosine Triphosphate. 17

dipole A pair of equal and oppositely charged or magnetized poles separated by a distance. 71, 75

DNA Deoxyribonucleic Acid. iv, 1–3, 5, 7–17, 19–24, 26, 28, 29, 31, 32, 36–41, 45–47, 50–53, 55, 60, 61, 104, 105, 135, 136, 143, 161–163

DNA amplification The process of synthesising more copies of DNA molecule(s). xiv, 2, 10, 13, 14, 16, 46, 48, 68, 162

DNA elongation Extending a DNA strand by incorporation of a nucleotide or oligonucleotide. 38, 52, 55, 143

DNA extension Extending a DNA strand by incorporation of a nucleotide or oligonucleotide. xv, 40, 42

DNA methylation DNA methylation is a biochemical process where a methyl group is added to the cytosine or adenine DNA nucleotides. 112, 113

dNTP deoxyribonucleotide Triphosphate. 11, 14, 17, 21–23, 38–40, 42

dTTP deoxythymidine Triphosphate. 17

EIS Electrochemical Impedance Spectroscopy. 31, 33–35, 42

electrophoresis The movement of charged particles in a fluid or gel under the influence of an electric field. 17

emulsion PCR In emulsion PCR, individual DNA molecules are isolated along with primer-coated beads in aqueous droplets within an oil phase. A PCR then coats each bead with clonal copies of the DNA molecule. 24, 53, 60

ENOB Effective Number of Bits. 143

epigenetic Relating to or arising from non-genetic influences on gene expression. 3, 7

epigenetics The study of changes in organisms caused by modification of gene expression rather than alteration of the genetic code itself. 168

epoxy An adhesive, plastic, or other material made from a class of synthetic thermosetting polymers containing epoxide groups. It is used as an insulating material. 51, 148

exothermic Acompanied by release of heat. 15

Faradaic sensor A sensor operating based on electrical induction and exchange of charge carriers. 76

FDA Food and Drug Association. 5

FET Field Effect Transistor. xiv–xvi, xviii, 33, 34, 36, 38, 40, 70, 74, 75, 81, 83–91, 94–100, 102, 103, 108, 109, 124, 125, 163, 164, 166, 167, 198, 200, 202

Finite State Machine A model of a computational system, consisting of a set of states. 116

fixed pattern noise A temporally constant lateral non-uniformity forming a constant pattern, used mainly for digital imaging. 36, 37

flicker noise A type of electronic noise with a $1/f$ or pink power density spectrum. 38, 41, 67

floating-gate A transistor gate having no resistive path to the ground. The gate is electrically isolated forming a floating node in DC. xvi, 104–106, 109, 116, 118, 119, 121, 122, 128

fluorescence The property of absorbing light of short wavelength and emitting light of longer wavelength. 17, 20, 24

fluorescent Having or showing fluorescence. xxiv, 19, 20, 24

fluorophore A fluorescent chemical compound that can re-emit light upon light excitation. 15, 19, 28

FPN Fixed Pattern Noise. 36

FSM Finite State Machine. 116

gene A segment of DNA that encodes for a specific cellular function and trait. 3, 10, 12, 19

gene expression The process that a gene is translated to functional products. xiv, 12, 19–21, 26, 28, 42, 43, 45, 135, 162

genetic Relating to genes or heredity. 1–3, 7, 9, 10, 20, 168

genetics The study of heredity and the variation of inherited characteristics. 9

genome The genetic material of an organism. 2, 3, 5, 9, 10, 12, 17, 21, 22, 24, 26, 162

genotyping Analysis for certain gene(s) and differences in genetic make-up. iv, 2, 5–9, 12, 17, 19–21, 29, 39, 40, 42, 43, 45–48, 52, 54, 68, 69, 103–105, 114–116, 119, 134, 135, 140, 143, 159–162, 165–168

geotagging Assigning geographical location to data like photographs, videos, post on social media, etc. 7

gigabyte 10^9 bytes or strictly 2^30 bytes. 4

Guanine A nitrogenous base type. 10

HapMap A multi-country effort to identify and catalogue genetic similarities and differences in human beings. 11

HDA Helicase-dependent Amplification. 15

helicase An enzyme for separating DNA strands. 10, 12

HIV Human Immunodeficiency Virus. 6

homo-polymer A polymer that is constructed of identical monomers. 23

human genome project The project to sequence whole human genome DNA. 9

inkjet A technology for printing in minute jets of ink from nozzles. 19

inosine A nucleoside. 24

Internet of Things A proposed development of the internet in which everyday objects have network connectivity, allowing them to send and receive data. 1

ISFET Ion-Sensitive Field Effect Transistor. iv, xv–xviii, 2–8, 36, 38, 39, 42, 43, 46–48, 50–52, 54–58, 61, 64, 67–72, 74–94, 96–106, 108, 109, 111–119, 121, 122, 124–128, 132–140, 142, 144, 145, 147–168, 196, 198, 200, 202, 204, 206

ISFET-based DNA logic A concept introduced by Christofer Toumazou et al to use DNA detection reactions switch logic gates using ISFETs. xvii, 8, 135–137, 140, 160, 165

Johnson-Nyquist formula It defines the electrical noise by thermal agitation of charge carriers. $V_n^2 = 4kTR$ where k is the Boltzmann constant, T the absolute temperature in Kelvin, and R the resistance of the medium. 77

lab-on-chip Miniaturising lab functions on a milli-meter dimension chip. A semiconductor chip used to analyze the composition of a person's body fluids (blood, saliva, urine) for medical purposes. It combines microfluidics and semiconductor processing on the same structure. 5, 14, 21, 28, 39, 46, 47, 68, 105, 162, 167, 168

LAMP Loop-mediated Amplification. xxviii, 15, 16

library In sequencing and genotyping genomic library is a collection of the total genomic DNA from a single organism. 15, 16, 22, 24

ligase An enzyme facilitating the joining of two DNA strands. 24, 166

lithography The process of printing from a flat surface treated so as to repel the ink except where it is required for printing. In semiconductor industry is a method analogous to lithography, used in making printed circuits. 4, 26

LoD Limit of Detection. 44

LSB Least Significant Bit. 142–145, 147, 151, 154, 155, 158

luciferase A generic term for a type of oxydative enzyme used in bioluminescence. 22

luciferin A generic term for a type of light emitting compound generating bio-luminescence by undergoing an enzyme-catalyzed oxidation. xxviii, 22

MATLAB Matrix Laboratory, is a multi-paradigm numerical computing environment. 7, 61

metagenomic Relating to or arising from the genetic material recovered directly from environmental samples. 7

metagenomics The study of genetic material recovered directly from environmental samples. 3

Mg Magnesium. 57, 61, 64

microarray An array of micro-dimensional DNA spots attached on a slid surface. xiv, 5, 17, 19–21, 30, 31, 34, 51, 162

microchip A tiny wafer of semiconducting material used to make an integrated circuit. iv, xv, 1, 3, 4, 6–8, 46–49, 51–54, 58, 60, 61, 64, 67, 68, 103, 124, 126, 134, 159–162, 164–168

microfluidic Relating to or arising from microfluidics. 21, 48, 51, 52, 68, 114, 162, 167, 168

microfluidics A multidisciplinary field intersecting engineering, physics, chemistry, biochemistry, nanotechnology, and biotechnology, with practical applications to the design of systems in which small volumes of fluids will be handled. xxvii

microsecond 10^{-6} second. 26

Miller effect The increase in equivalent impedance between two nodes when there is a gain between them. 109

millisecond 10^{-3} second. 26

mixed-signal An integrated circuit/system containing both analogue and digital circuits. 115, 134, 165, 166

mobility The ability of charged particles (such as electrons or protons) to move through a medium in response to an electric field. 74

molecular biology The branch of science that deals with microorganisms. 9, 161

Moore's law It is originally for the computing hardware where Gordon Moore, co-founder of Intel Corporation predicted doubling of transistor's density every two years. Later this was quotes as every 18 months. The law basically is applied to show an exponential improvement trend. 5

MOSFET Metal-Oxide-Semiconductor Field Effect Transistor. xvi–xviii, xxvii, xxix, 70, 74, 77, 79, 82, 85, 87, 88, 93, 96, 106, 108, 109, 111, 117–119, 124–130, 160, 165, 166, 198, 200

MPS Massive Parallel Sequencing. 2, 21, 52, 68

MSB Most Significant Bit. 143, 144

mutant Resulting from or showing the effect of mutation. 49, 50

mutation The changing in the structure of a gene. xxvii, 50

NAND A Boolean operator which gives the value zero if and only if all the operands have a value of one, and otherwise has a value of one (equivalent to NOT AND). 136

nanopore A very small pore in nano-meter dimensions. 3, 28, 40, 41, 43

NASBA Nucleic Acid Sequence-based Amplification. 15

NAT Nucleic Acid Test. 5, 6, 12, 15, 21, 47

Nernstian sensitivity The ideal maximum theoretical sensitivity defined by Nernst equation, about $59mV/pH$ for pH-sensitivity at room temperature. 105, 149

NGS Next Generation Sequencing. 2, 21, 52

NHGRI National Human Genome Research Institute. 2, 3, 5, 21

NMOS N-channel MOSFET. 136, 139–142, 144, 145, 147, 148

non-Faradaic sensor A sensor working based on capacitive coupling with no exchange of charge carriers. 67, 76, 77

NOR A Boolean operator which gives the value one if and only if all operands have a value of zero and otherwise has a value of zero (equivalent to NOT OR). 136

nosocomial Originating in a hospital. 6

nucleic acid A complex organic substance present in living cells, especially DNA or RNA, whose molecules consist of many nucleotides linked in a long chain. 5, 9, 15, 28, 47

nucleo-base Nitrogenous compounds in nucleotides. 2, 10, 12

nucleotide Organic compound as the building block of DNA. 10–17, 19–26, 38, 39, 41, 162, 163, 166

oligonucleotide A poly-nucleotide (a chain of nucleotides) whose molecules contain a relatively small number of nucleotides. 14, 17, 19, 24, 166

oxyluciferin Oxidised luciferin. 22

p-n junction A boundary between p-type and n-type material in a semiconductor device, functioning as a rectifier. 111

pathogen A bacterium, virus, or other microorganism that can cause disease. 3, 6, 7, 168

PCB Printed Circuit Board. 48, 148

PCR Polymerase Chain Reaction, a process to replicate DNA strands using thermal cycles. xxviii, 5, 14, 22, 24, 106, 143, 162

perinatal Relating to the time, usually a number of weeks, immediately before and after birth. 6

PG-ISFET Programmable-gate Ion-Sensitive Field Effect Transistor. xvii, 106, 110, 116, 138

pH A figure expressing the acidity or alkalinity of a solution on a logarithmic scale. pH is equal to $-log_{10}[H^+]$ where $[H^+]$ is the hydrogen ion concentration. iv, xvi, 2, 8, 36, 38, 44, 46, 47, 49, 50, 54, 57, 58, 63–65, 68, 70–76, 81, 82, 102–106, 108, 110, 112, 113, 116–119, 122–125, 135, 137, 139, 140, 143, 148, 149, 151, 153–155, 157, 158, 160, 161, 165, 166

pH-LAMP An isothermal DNA amplification method based on LAMP but measuring pH change instead of optical sensing. 48

pH-PCR A DNA amplification method based on PCR but measuring pH change instead of optical sensing. 48

PLA Piecewise Linear Approximating. iv, 115–117, 122, 124, 125, 165, 166

PMOS P-channel MOSFET. 112, 119, 131, 136, 139, 140, 142, 144, 145, 147, 154

POC Point of Care. 5, 15, 21

point-of-care Clinical point of care is when clinicians deliver healthcare products and services to patients at the time of care. 1, 5, 6, 8, 9, 12, 15, 21, 43, 46, 68, 105, 124, 161, 165, 166, 168

Poisson-Boltzmann equations The PoissonBoltzmann equation is a differential equation that describes electrostatic interactions between molecules in ionic solutions. It is the mathematical base for the GouyChapman double layer theory. 72

polymer A substance which has a molecular structure built up chiefly or completely from a large number of similar units bonded together. 9, 10

polymerase An enzyme facilitating the polymerization of nucleotides to make a DNA strand. 10, 12, 14, 15, 22, 24, 26, 38, 166

potentiometric A method of measuring analyte concentration by measuring the potential difference between two electrodes. 42

PPi Pyrophosphate. xv, 22, 39, 40

primase An enzyme for making primer. 12

primer A molecule that serves as a starting material for a polymerization process. 10, 12–17, 19–21, 24, 26, 38, 39, 43, 50, 51, 54, 55, 60

probe A small DNA synthesized to detect a certain sequence in a sample DNA by its hybridization if complementary-matches the sample DNA. 50, 51

PTAT Proportional to Absolute Temperature. 48

pyrosequencing A method of sequencing by synthesis based on detection of pyrophosphate. 21, 39

quantitative amplification A method for estimation of the amount of a given sequence in a sample from amplification of that sequence. 19

quaternary Fourth in order. 9

RCA Rolling Circle Amplification. 15

read length In sequencing it is the number of bases detected from a single spot of analysis like a micro-well. 3, 44

readout In electronics readout is an interface circuit to transfer a sensor's signal for next stages of processing. iv, xvi, xvii, 8, 44, 45, 47, 48, 50, 52, 58, 59, 61, 66, 69, 70, 76, 77, 79, 82, 100, 102, 104–108, 110–119, 121–123, 125, 129, 131, 133, 134, 151, 160, 162, 163, 165, 166, 168

RedOx Reduction Oxidation. xiv, 28–30, 43, 162

reference electrode An electrode having an accurately maintained potential, used as a reference for measurement by other electrodes. 70, 71, 74, 75, 78, 82, 89, 92–94, 96–99, 103, 136, 137, 139, 140, 148, 153, 157, 164, 165

REFET Reference Field Effect Transistor. xvi, xvii, 106, 108, 109, 113, 114, 116, 125, 126, 128–130, 133, 134, 151, 153, 156, 165

reversible chain termination A sequencing by synthesis method using terminated nucleotides for limiting the incorporation to one nucleotide at a time. The terminating part can be removed to allow further incorporation and synthesis. 23, 26, 166

RNA Ribonucleic Acid. 12, 13, 19, 20, 26, 45, 135

rNTP ribonucleotide Triphosphate. 12, 13

ROM Read-only Memory. 139

SAR ADC Successive Approximation Register Analogue to Digital Converter. 143

SDA Strand Displacement Amplification. 15

SEM Scanning Electron Microscope. 40

sequencing DNA sequencing, the process of determining the order of nucleotides in a DNA molecule. iv, xiv, xv, xvii, 2–10, 12, 15–19, 21, 23, 24, 26, 28–30, 39–43, 45, 46, 52–56, 60, 61, 64, 67–69, 103–105, 114–116, 125, 126, 133–135, 140, 143, 149, 161–163, 165–168

sequencing by ligation A sequencing by synthesis method using oligonucleotides and ligase enzyme. 26

sequencing by synthesis A method of sequencing which synthesizes a complementary second strand on template DNA by extending the hybridized primer. xiv, 23, 25, 26, 38, 52, 166

silane Any hydride of silicon. 19

single-strand sequencing Sequencing using only a single strand of the sample DNA instead of requiring prior amplification/replication. 26

SMRT Single Molecule Real Time. xiv, 26, 28

SNP Single Nucleotide Polymorphism. xv, xvii, 10, 19, 20, 28, 38, 39, 47, 50, 135–137, 143, 165

SNR Signal to Noise Ratio. 13, 48, 55, 61, 136, 160

SoC System on Chip. xv, 48, 50, 68, 168

SOI Silicon on Insulator. xv, 40

SOLiD Sequencing by Oligo Ligation Detection or Support Oligonucleotide Ligation Detection. xiv, 24, 26, 69

solid-state The state of matter in which materials are not fluid but retain their boundaries without support, the atoms or molecules occupying fixed positions with respect to each other and unable to move freely. 41

system-on-chip An integrated circuit (IC) that integrates all components of a computer or other electronic system into a single chip. 48

targeted sequencing Sequencing for a specific subset of the genomez. 3

Thymine A nitrogenous base type. 10, 12, 13

TICTC Temperature-insensitive Continuous-time Converter. iv, xvii, xviii, 151, 156, 157, 159, 160

transfer function A mathematical function relating the output or response of a system to an input. xiv, 33–35

tuberculosis An infectious bacterial disease characterized by the growth of nodules (tubercles) in the tissues, especially the lungs. 6

Uracil A nitrogenous base type. 12, 13

USB Universal Serial Bus. 41, 48

Verilog-A A hardware description language used to model electronic systems. 85, 122, 157

Warburg impedance It is created by diffusion in a cell and represents a semi-infinite linear diffusion within the solution. $Z_w = (1-j)\sigma/\sqrt{\omega}$ where σ is the Warburg coefficient, $\omega = 2\pi \times frequency$. 33

wild-type A strain, gene, or characteristic which prevails among individuals in natural conditions, as distinct from an atypical mutant type. 49, 50

zeptolitre 10^{-21} litre. 26

ZMW Zero Mode Waveguide. 26, 28

1. Introduction

Tomorrow, it may look primitive what we can do today. But still is fascinating to experience the change we make. There wasn't a big gap between the invention of semiconductor transistor and the discovery of DNA back in late 1940s, though it took us a couple of decades to put them in a common phrase. And the journey continues.

1.1. Motivation

The semiconductor industry has been a key player in defining the modern world for the human being. It has formed the basis for information and communication technology. Its scaling and mass production helps increasing processing power while reducing the cost which allows developing powerful miniaturised microchips at the heart of our personal gadgets. Inclusion of sensors for imaging and measurement of physical and chemical signals further broadened its applications; and so has its advent to the biomedical sciences as a game-changing technology. Replacing the bulky instrumentations with portable point-of-care and remote monitoring devices, as well as development of prosthetics and bio-inspired system-on-chips for neural recording and stimulation, molecular analysis, wireless implants, etc, are where semiconductors have contributed to make considerable changes in healthcare.

At the same time, the birth of molecular biology enabled learning the biological functions at a molecular level reshaping the medical diagnostics[1]. Infectious diseases, genetic disorders and cancer are a few examples of its application fields where humankind is severely challenged with. On the other hand, a new wave of personalised healthcare is forming prognostics and therapy applications; not only in the pharmaceutical and healthcare services, but also in the daily lifestyle of the human being. And perhaps be the merit of modernity at its coming time to the consumer market, if the *Internet of Things* does not appear as exceptional and exciting for the people of its era. Companies like *23&Me*[2], *Genelink Biosciences Inc*[3], *SkinDNA*[4] and *GeneU*[5]...have started offering customised diet and cosmetic recommendations based on individual's genetic construction. People's genetically inherited strengths, weaknesses and susceptibilities are evaluated for any risk in for example organ failure, drug metabolism, cancer development, skin

[1] *M&M* (A market research company and consulting firm http://www.marketsandmarkets.com) has estimated molecular diagnostics a cumulative annual growth rate of 9.7% during 2013 − 2018 to $7.9 billion worth in 2018.
[2] www.23andme.com
[3] http://genelinkbio.com/
[4] www.skindna.com.au
[5] www.geneu.com

ageing, etc. However, its success is dependent on a technological shift bridging the gaps of nature-laboratory, and laboratory-highstreet/online shops.

Engineering has contributed remarkably in the development of instruments for biological and molecular studies. Many inventions since the introduction of Sanger's sequencing method [1] in decoding DNA, the famous code of life, has helped in facilitating the experiments and reduction of costs. On this journey, semiconductor industry has been a key player, not only in computation, but also in imaging and development of integrated assays. In spite of all the valuable achievements, there is still a step to pace.

Looking at the platforms developed for assaying DNA, despite the overlaps, they can be divided into two general categories of sequencing and genotyping. The fundamental fact behind the operation of both is that nucleo-bases on the two strands of DNA are complementary. The genetic information is encoded in the sequence of the bases (four types) on the two strands. Therefore, a known DNA strand as a biomarker can find and hybridise to its complementary fragment on the target DNA. In sequencing, the instrument reads the order of the bases in a DNA strand. In genotyping, the sample DNA is compared with predefined biomarkers to find the matching one. With different degrees of complexity, all follow three steps of preparation, detection and computation. In preparation, sample DNA is extracted (for instance from saliva or blood), purified, and readied for the assay. In majority of the methods, it is replicated (known as DNA amplification) to generate more copies of the molecule for better signal power in detection. In detection, the prepared samples are applied to the assay for analysis. In computation, signals from the assay are processed to extract the genetic make-up information.

Method of detection identifies the workload for the preparation and the computation steps, and consequently affects the overall accuracy and throughput of the system. Primary technologies all relied on optics. Due to their cost and complexity alternative methods have been sought. The advent of biosensors promised cost-efficient fully-electronic systems eliminating the optical requirements. Among them, ISFET[6] has been a transformative element from the semiconductor family in pH-based DNA detection, for both sequencing and genotyping.

1.1.1. Sequencing

The start of sequencing dates back to the works of Sanger on detection of the order of nucleo-bases in nucleic acids. Sanger's method of sequencing in 1977 was further improved in all aspects of sample preparation, detection, and analysis. Ten years later, Applied Biosystems developed automated Sanger machines that helped in the completion of sequencing a human genome in 2001 [2]. The initial human genome sequencing took more than a decade with an estimated cost of $70 million [3]. In 2004 National Human genomes Research Institute (NHGRI) founded an initiative which aimed for reducing the cost of genome sequencing to $1000 in ten years. New technologies with different approaches have been developed to run sequencing of large amounts of DNA in parallel at lower costs. These technologies are referred to as *next-generation sequencing* (NGS) and *massive-parallel sequencing* (MPS) [4]. A summary of the

[6] Ion-Sensitive Field Effect Transistor

commercially available platforms in the sequencing industry is provided in Table 1.1.

Applications for such technologies are many; whole genome sequencing, targeted sequencing, discovery of gene variants, genome-wide profiling of epigenetic marks, species classification and/or metagenomics gene discovery, inherited disorders, etc [2–6]. Sequencing of the human genome and pathogens has a major impact on the emerging field of genomic medicine where all diseases have a genetic basis, either inherited or induced by the environment or from a pathogen [6, 7]. Comprehensive understanding of genetic diversity requires high-throughput systems enabling the study of organisms biology at a molecular level.

Until 2011 all the machines introduced to the market were based on optical detection, which required labeling of molecules with dyes and use of sophisticated imaging. The advent of ion-sensitive transistors in detection of the change in ionic concentration during the synthesis of DNA strands in 2001 led to the development of pH-based sequencing on CMOS[7] microchips later in the decade. Another non-optical platform introduced in the same period, measures the change of current during trans-location of a DNA strand through a nanopore for single-strand sequencing.

Accuracy and throughput, besides cost, are the key figures to merit each upon another. DNA is chopped into smaller fragments which are sequenced in parallel on the assay. The sequenced fragments are then reassembled to build the whole DNA or mapped to a reference one. The accuracy tells what fraction of the read bases (the base-calls) were correct when comparing with a reference sequence. A key challenge on accurate base-calling is the correct detection of repetitive bases in a DNA sequence. Limit of detection and the chemistry of operation may set a trade-off on the read length and accuracy. The longer the reads from each fragment are, the easier is the mapping and reassembly. The number of bases that can be detected at a run of sequencing is defined as throughput. According to Table 1.1, the relatively young ISFET-based products by Ion-Torrent seem comparable with a majority of the platforms in the table, although a compromise seems to have been made for the read length. The higher values of throughput are in fact from microchips with more sensors (ISFETs)[8]. One of the focal points of this thesis is on the performance criteria and scaling.

The sequencing market has so far been dominated by the optical systems. In January 2014 Illumina[9], holding the largest share, claimed to have reached the $\$1,000$ target, but it is questioned to be only the cost of reagents and not the system depreciation, maintenance and utilisation. The machine itself costs $\$1M$, sold in packages of ten. NHGRI, in the latest release of the sequencing cost figures, reports $\$4,920$ in April 2014[10]. In addition to the products listed in Table 1.1, there are several other companies founded to push the limitations for cost-effective reliable systems. Figure 1.2 shows some of the currently active companies[11].

[7] Complementary metal-oxide-semiconductor.

[8] $1.2M$ for $PGM314$, $6.1M$ for $PGM316$, $11M$ for $PGM318$, $165M$ for $ProtonI$, and $660M$ for $ProtonII$.

[9] www.illumina.com

[10] www.genome.gov/sequencingcosts

[11] Among the platforms introduced, PacBio and Oxford Nanopore in the recent (2014) Advances in genomes Biology and Technology meeting, gained the most attention for their single molecule sequencing with considerably long reads. However, the accuracy of base-calls (detection of bases correctly) has remained unresolved, while Illumina and Ion-Torrent have shown progresses.

Table 1.1.: Commercialised sequencing systems. The underlined numbers are calculated by the author based on the information obtained in other columns.

Company Platform	Price $	Cost $/run	Cost $/Mb	Run Time	Output per run	Read length	Accuracy %	Ref
ABI 3130xL	95k	4/800bp	2,400	20min 3hrs	1.9 84k	400-900b	99.999	[2]
Roche 454 GS FLX	500k	7,000	10	24hrs	0.7G	700b	99.9	[2]
Roche 454 GS FLX+	500k	6k	8.57	23hrs	700Mb	upto 1kb		allseq.com
ABI SOLiDv4	495k	15,000/Gb	0.13	7 days	120G	2x50b	99.94	[2]
ABI SOLiD 5500Wxl	665k	5k	0.021	10 days	240Gb	2x50b		allseq.com
ABI SOLiD 5500xl	595k	10k	0.105	6 days	95Gb	2x60b		allseq.com
PacBio RS	695k	-	2	2hrs	100Mb	Avg. 1,500b	<90	[8]
PacBio RSII P4C2	700k	400	1.45	180min	275Mb	5.5kb	86 (50x>99.999)	allseq.com
Illumina MiSeq	128k	-	0.502	27hrs	1.5 2G	upto 150b	>99.9	[8]
Illumina MiSeq	125k	1400	0.093	65hrs	15Gb	2x300b		allseq.com
Illumina NextSeq 500High	250k	4k	0.033	29hrs	129Gb	2x150b		allseq.com
Illumina HiSeq 2000	690k	6,000	0.07	3 10 days	600G	50b	98	[2]
Illumina HiSeq 2500HTv4	740k	29k	0.029	6 days	1Tb	2x125b	>80% of bases at 99.9	allseq.com
Illumina HiSeq HiSeq X	1M	12k	0.007	3 days	1.8Tb	2x150b	>75% of bases at 99.9	allseq.com
Ion-Torrent PGM 318	80k	-	1	2hrs	1Gb	200b	99	[8]
Ion-Torrent PGM 318	50k	250Reagent 499 Chip	0.375	4-7 hrs	upto 2Gb	200b		allseq.com
Ion-Torrent PGM 316	50k	250Reagent 299 Chip	0.549	3-5 hrs	upto 1Gb	400b		allseq.com
Ion-Torrent PGM 314	50k	250Reagent 99 Chip	3.49	2-4 hrs	upto 100Mb	400b		allseq.com
Ion-Torrent Proton I	149k	300Reagent 699 Chip	0.999	2-4hrs	10Gb	200b		allseq.com
Ion-Torrent Proton II	149k	300Reagent 699 Chip	0.031	2-4hrs	32Gb	100b		allseq.com

Nevertheless, what makes the ISFET-based sequencing unique and more promising is its compatibility with CMOS technology to leverage all the scaling and cost advantages of semiconductor industry. The signal is a function of ionic concentration rather than absolute amount of sample, and the sensor is of the same type as the transistor in computing electronic microchips. The system is integrated on a single semiconductor die using the same lithography fabrication as for other electronic microchips. However, it does have challenges and places for optimisation. For instance, the read data from the assay is several gigabytes per second, consuming almost 80% of the computation for processing the signals at a low level [9]. Scaling further adds to the noise level and the evanescence of signal due to quicker diffusion of ions

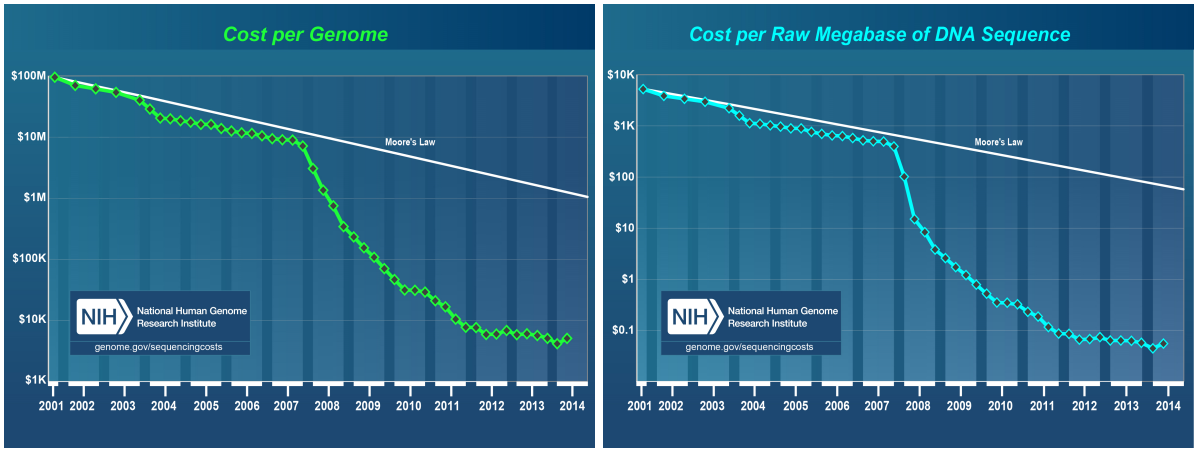

(a) Genome sequencing cost. (b) Sequencing cost per million base-pairs.

Figure 1.1.: Sequencing cost from NHGRI website (www.nhgri.gov). Since the introduction of the next generation sequencing technologies, there is a significant drop in cost, overtaking the Moore's law prediction.

to the background analyte. Smaller window of detection means a need for a higher rate of sampling, a larger bandwidth and an accumulated low-level processing. On the other hand, the sensor inherently operates based on capacitive coupling which makes its efficiency dependent on its geometry. Chapter 3 describes the performance figures and chapters 5, 6 and 4 introduce potential solutions for optimisation, from the ISFET and interface design point of view.

1.1.2. Genotyping

Traditionally genotyping has been mainly dependent on microarrays and PCR[12] with optical detection. On the microarrays, biomarkers are immobilised and matching DNA strands are optically detected. In amplification and detection, the sample DNA is amplified for the sequence of biomarker in case of matching, which is also labeled for luminescence detection. These set-ups like Affymetrix[13], Agilent[14], Flimarray[15],...are desktop systems of tens of thousands of dollars with a cost of hundreds of dollars per test.

Recent developments in lab-on-chip instrumentation, particularly micro-total analysis set-ups (μ-TAS), introduced several designs automating and miniaturising the assays for point-of-care nucleic acid test (POC NAT). In these systems, the detection of matching biomarkers is based on the amplification of sample DNA. Isothermal methods, operating at certain fixed temperatures, were introduced and preferred over PCR in these set-ups for reducing the time and power consumption. Hand-held sample-in result-out systems were proposed like μ-BAR[16], but taking one hour only for loading the inlets [10]. However, no device has yet been FDA[17]-

[12] Polymerase Chain Reaction. It is a method of replicating DNA strands using cyclic temperature change, explained more in Chapter 2.
[13] www.affymetrix.com
[14] www.agilent.com
[15] filmarray.com
[16] Microfluidic Biomolecular Amplification Reader.
[17] Food and Drug Administration.

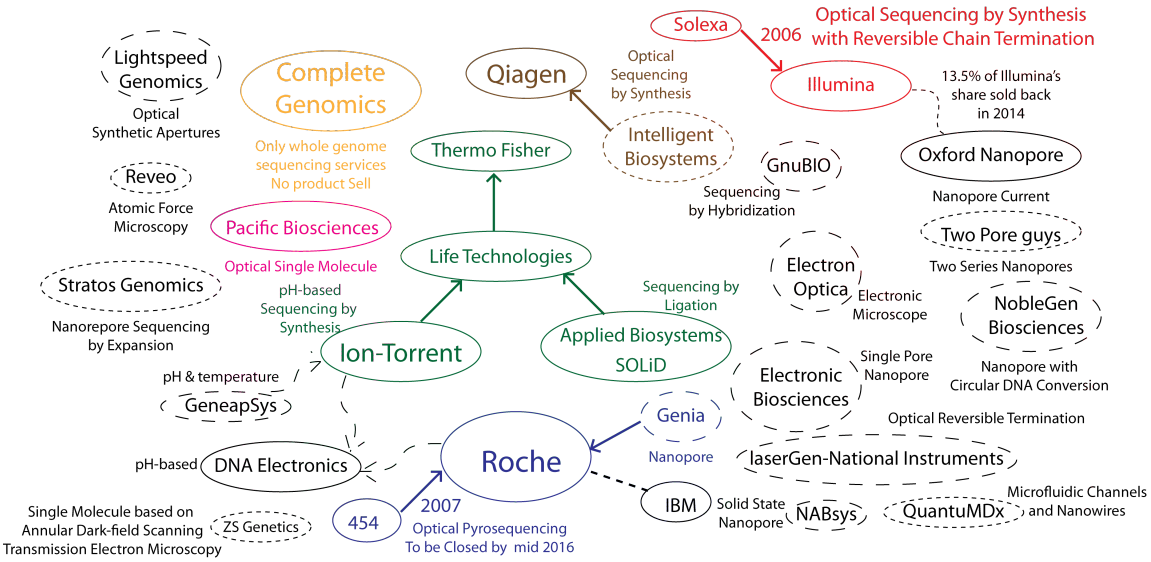

Figure 1.2.: Sequencing companies active in next generation development. The dashed circles means the product is under development and not released to the market yet. Solid arrows tell the acquisitions and dashed ones licensing. Dashed lines also tell collaboration/investment.

cleared. Non-optical devices with electrochemical detection have been developed but mainly stayed in desktop configurations for laboratory use like CustomArrays[18] ElectraSense® and GenMarkDx[19] e-SENSOR™. These systems rely on measuring the impedance change in functionalised electrode arrays which limits their scalability. In contrast, the ion-sensitive transistors allowed implementation of a miniaturised set-up on a microchip commercialised by DNA Electronics[20]. Integration of sensor arrays of ion-sensitive transistors along with resistive heating elements with processing circuitry, is a unique breakthrough for the point-of-care molecular diagnostics. The CMOS-based fabrication of this NAT processor makes it scale in capacity and cost for higher throughput and lower price.

Such a cost-effective easy-to-use point-of-care molecular analysis set-up can frame the application of molecular biology with direct impact on personal life and socio-economical policies. Diagnosis management of tuberculosis, HIV, perinatal and nosocomial infections, drug susceptibility, pathogen identification, antibiotic resistance, and chronic disease monitoring [11, 12], are examples of the applications in health care. Miniaturised and integrated devices may reduce the assay cost, interaction of sample with external factors, and contamination [13]. The technology is also applicable for food and agriculture, controlling plant pathogens destructions [14]. Moreover, portability allows running tests where having a centralised laboratory is not feasible.

Nonetheless, implementation of ISFET-based genotyping microchips using standard CMOS process, though cost-efficient, has non-idealities in the performance, particularly from the ISFET side. Sensitivity, random offset, signal drift, and temperature influence are some of the accuracy

[18] customarrayinc.com
[19] www.genmarkdx.com
[20] www.dnae.co.uk

confronts. The aim in this thesis is to propose ideas that may help rectifying such obstacles.

1.1.3. Future Vision

In analogy with the scope of communication technologies growing in the company of semiconductors, one may envisage having genetic analysis for *anything, anytime, anywhere*. It will not only accelerate the genetic experiments, but also authenticate epigenetic and metagenomic studies by an inclusion of the already established geotagging and cloud-based data management technologies. Therefore, promoting the emergence of sciences on an ISFET-based microchip, will direct the next step of understanding and managing living organisms with a reform in applying molecular biology to identify pathogens, know our inherited disorders, improve agricultural crops, etc. Yet, the picture needs some fine brushes.

1.2. Thesis Overview

With the potential advantages of semiconductor-based sequencing and genotyping, this thesis investigates some of the challenges and proposes some solutions from an ISFET design perspective. Throughout the chapters, the two mentioned aspects of genetic analysis are considered. For sequencing, high level of integration of sensors and the strains of miniaturisation, and for genotyping, on-chip integrated processing, are the focus of the work.

1.2.1. Sequencing and Genotyping: Industry and Research

Chapter 2 gives a summary on the prior art in sequencing and genotyping. It starts with a brief description of DNA and the principal genetic analysis. Some of the optical methods that enhanced the sequencing industry are reviewed. Although the detection method is different, a variety of approaches discussed may be applied for the improvement of pH-based detection. Then, a literature review on some of the fully-electronic methods relying on the biosensors is presented, concluding with remarks on the use of ion-sensitive transistors.

1.2.2. pH-based DNA Genotyping and Sequencing

Chapter 3 gives a detailed look into the pioneering pH-based technologies developed. It introduces performance-limiting factors, and scaling challenges in particular. A simulation on synthesis (in fact elongation of a hybridised marker strand) of a DNA strand, showing the signal generation and the ionic concentration change, in MATLAB environment, is provided. It highlights the drawbacks of scaling in decrease of signal coupling efficiency, higher level of noise, and necessity for higher sampling rate, and hence larger processing burden at low-level computation.

1.2.3. ISFET Geometry

Chapter 4 investigates the geometrical effects of ISFET as the building block of the pH-based DNA detection on semiconductor microchip. Following a review of its operation, a design methodology is proposed with the introduction of a coupling efficiency term into the current-voltage characteristics of the ISFET. Experiments on the influence of parasitic decoupling capacitors, which reduce the coupling efficiency of the signals, show their dependency on the perimeter of the sensing layer of this transistor. Common and well-known issues of ISFETs like signal drift and DC offset, as well as shape and meshing of the sensing membrane, are analysed. In conclusion, design trade-offs and possible configurations for enhancing the efficiency of the ISFET coupling are described.

1.2.4. Analogue Readout Circuits

Chapter 5 starts with a review on the ISFET interface circuits with analogue outputs. The majority of the readouts in the literature convey the pH-change signal as a voltage output, and a few of them process the signal tackling the temperature effect, drift, and/or DC offset. Two approaches are proposed, one focusing on the potential of utilising the back-gate terminal of the ISFET, and the other providing a temperature-insensitive linear approximation with a current output. The back-gate can be used for calibrating the transistor to eliminate its DC offset. It is shown how it may suppress the common-mode background noise in the arrays, which eventually reduces the computation load for large-scale sequencing systems. The other readout may be suitable for point-of-care devices where on-chip processing is more advantageous.

1.2.5. Digital Readout Circuits

Chapter 6 first reviews the ISFET-based DNA logic and chemical switch concepts based on the fact that the information from these assays, particularly the genotyping, is of one bit value, telling whether a biomarker matched the sample DNA or not. Accordingly, a pseudo-inverter-based readout is proposed. The advantage of it would be increasing the resolution of readout, though at a cost of dynamic range reduction. From Chapter 3 it is learned that the signal dynamic range is a maximum of a few tens of millivolts. With an asymmetric ISFET-based pseudo-inverter it is shown that for a sufficient range of operation, the digital conversion resolution can be improved without any extra amplification unit trading-off the area. Sequencing is the application it is proposed for. In addition, a continuous-time temperature-insensitive ΔpH-to-digital converter for genotyping assays is proposed that its operation range is not limited by the power supply and may be scaled easily by adding further digital registers.

1.2.6. Conclusions and Future Work

Chapter 7 summarises the highlights of the thesis with suggestions for future work.

2. Sequencing and Genotyping: Industry and Research

The contributions of Fredrick Sanger in determination of the sequence of bases in nucleic acids, leading to his second Nobel prize in 1980 shared with Walter Gilbert and Paul Berg [1], opened a new door in molecular biology and genetics. Sanger's method introduced in 1977 [1] for sequencing DNA, the well known genetic code, using chain termination and radio-active detection, is the basis of many machines and instruments in sequencing and genotyping industry. However, the laborious process, high cost, long time of test, and low throughput always limited the utilisation and application of such devices. In 1987 Applied Biosystems[2] introduced an automated Sanger machine making it faster and more accurate. Further improvements in Sanger's technology helped in completion of the human genome project in 2001 which encouraged development of new powerful and cost-efficient systems [2]. The initial human genome sequencing took more than a decade with an estimated cost of $70 million [3].

Over the past decade, several new systems has been introduced to the market, reducing the cost and improving the process. These efforts may be generalised in three aspects of preparation, detection and analysis. In this chapter, after a brief description of DNA and its predominant genres of analysis, we will review some of the recent commercialised technologies with different approaches mainly relying on optical detection. Then we will look at fully-electronic methods proposed for eliminating the need for molecular labelling and optical instruments; which would make them potentially cost-efficient. Using biosensors, these methods are compared over scalability and limit of detection, whether beneficial for high-throughput sequencing or preferred in point-of-care nucleic acid tests.

2.1. The Principal Life Codes

Body functions at the cellular level are encrypted in quaternary codes made by nucleic acid polymers. These codes are transcribed from a main recipe into messages that instruct the development of amino acids. Amino acids then form proteins that perform the functions. Genetics has been studying these codes to learn their relation with our traits, which also allows predicting any malfunction creating diseases. This section describes the structure of these codes, followed by their detection methods.

[1] www.nobelprize.org

[2] Part of LifeTechnologies (www.lifetechnologies.com), a Thermofisher Scientific (www.thermofisher.com) brand.

2.1.1. DNA

DNA (deoxyribonucleic acid) is the code of life, containing the genetic information and instruction for cellular activities. Figure 2.1 gives an overview of its structure. It is a large helical double-stranded molecule, chain-like polymer of nucleotides, located in the nucleus of every cell [15–17]. The nucleotides are made of a sugar, a phosphate group and a nitrogenous base. The sugar is a $2'$-deoxyribose (a pentose having lost an OH bond on its carbon number 2). The phosphate group is attached on carbon number 5 of the sugar, and the nitrogenous base on number 1. To chain the nucleotides and make a DNA strand, the phosphate group loses two of the phosphates and the sugar loses the hydrogen of the OH group on carbon 3. The remaining phosphate group replaces the hydrogen. This gives the polymer $3'$ and $5'$ ends and so a direction in the order of the nucleotides on each strand.

In DNA, nucleotides are of four types, different in their bases: Adenine (A), Cytosine (C), Guanine (G) and Thymine (T). They sit on the sugar-phosphate backbone in a complementary manner on the two strands. Adenine pairs with Thymine with two hydrogen bonds, and Cytosine pairs with Guanine with three. This pairing puts the strands in an optimum distance. The genetic information are encoded in the order of these nucleotide bases. Besides the direction, by knowing the order of the nucleotides on one strand, one can tell the sequence of the nucleotides on the other. This fact allows a single strand of DNA to act as a template for development of the other. It is the fundamental behind the cellular transcriptions and the methods introduced for reading the sequence of DNA nucleo-bases; sequencing.

During cell division, DNA is copied for new cells. DNA replication occurs based on the mentioned complementary rule. Enzymes regulate creation of more copies of the DNA molecule by denaturing it (using enzyme helicase) into single strands and creating new ones by complementary copying of second strand, using a *primer* sequence and DNA polymerase enzyme; Figure 2.2. A similar process happens when DNA is transcribed for a particular function. In analogy, for a sample DNA to analyse, multiple copies of it are created using a primer sequence defining the segment to be replicated. Section 2.2 explains DNA amplification (replication) which is used in preparation of samples and helps improving the signal detection.

2.1.2. Gene

From the entire 3 billion-base-pair DNA molecule, only 2% of it are coding for proteins and the rest is considered non-coding. These segments forming the units of heredity are called genes. In the human genome, there are $20,000$ genes with average lengths of 10 to $15,000$ bases, separated with varying distances. The non-coding parts have recently been reported to control switching on the coding parts [18]. Differences in the genetic configuration may lead to different behaviour or characteristic of a corresponding organ or organs among individuals. It is valuable to look into specific genes and their polymorphisms for particular traits. In this respect, the humankind are 99.9% similar and 0.1% different.

Single nucleotide polymorphism (SNP) is a single base mutation of a gene that is observed in at least 1% of the population. Many SNPs are associated with diseases and/or deficiencies.

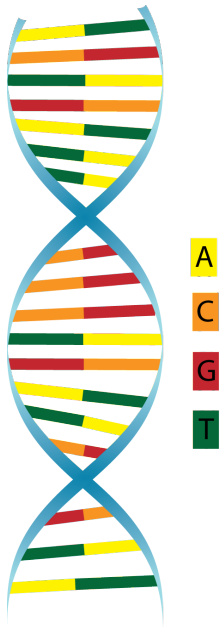

(a) Double-helical DNA.

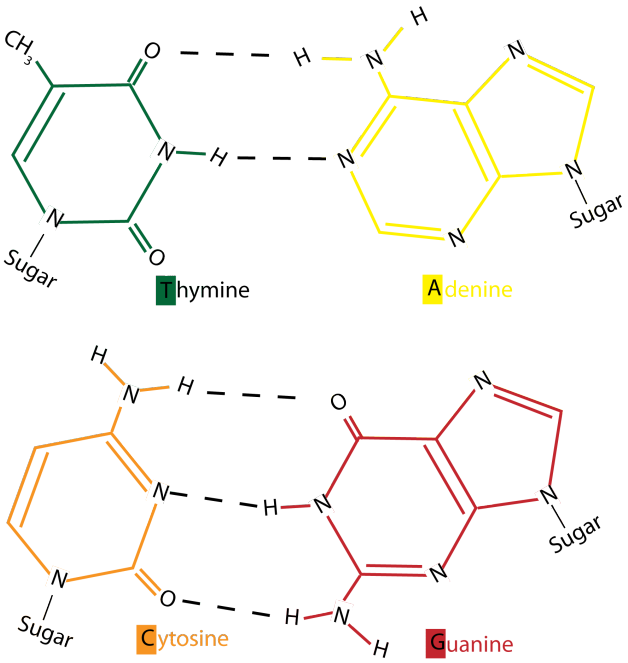

(b) Nucleotide base pairing.

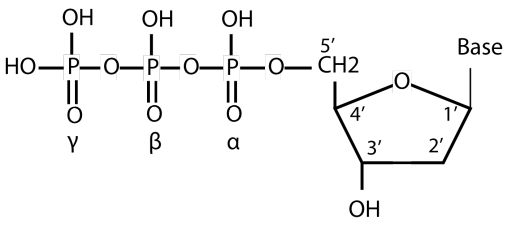

(c) Deoxyribonucleotide triphosphate (dNTP).

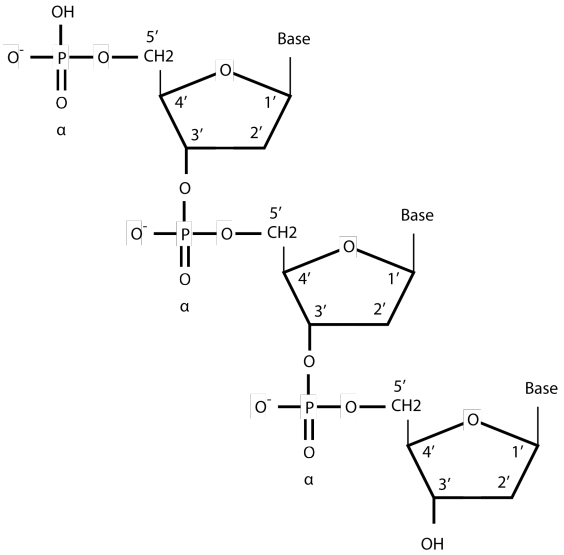

(d) Poly-nucleotide.

Figure 2.1.: Deoxyribonucleic acid molecular structure. Figures redrawn according to [16, 17].

Detection of such polymorphisms provides valuable information, for example on organ failure, allergies, metabolism of specific drugs like Warfarin, or suitability of a certain antibiotic in infectious diseases treatment. HapMap project[3] formed internationally to collect such information and make it accessible for the researchers and the public[4].

[3] www.hapmap.com

[4] Another example is SNPedia (www.snpedia.com). Companies like 23 and Me (www.23andme.com), Genelink (www.genelink.com), Skin DNA (www.skindna.com) and GeneU (www.geneu.com) are the commercialised examples trying to improve the individuals life style by customised diets, nutritions and cosmetics[19, 20].

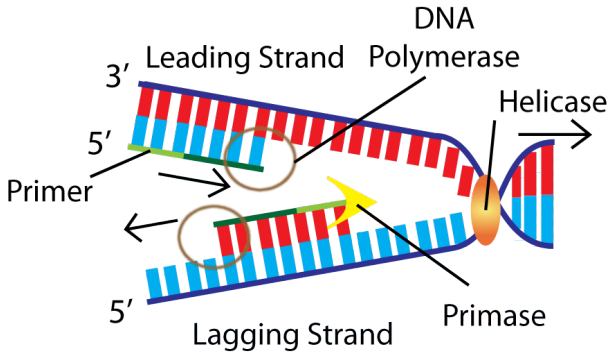

Figure 2.2.: DNA replication. Helicase unwinds the strands, primase catlyzes the synthesis of primer, and DNA polymerase assembles the nucleotides. Figure redrawn according to [16, 17].

Although sequencing can provide whole-genome information, it is expensive and time consuming. Genotyping examines specific genes and allows targeting comparison of mutations.

2.1.3. RNA

DNA sends its messages through a similar molecule, RNA (ribonucleic acid), which is a special copy of DNA; Figure 2.3. The process is called transcription. Unlike DNA, RNA is single-stranded and unstable. The deoxyribose sugar is replaced with ribose, and Thymine base with Uracil, which has a methyl group less. The gene expression process (turning on and off the creation of RNA) is alike DNA replication. A promoter and a terminator tell from where and up to where this special copy of DNA has to be made from rNTPs (ribonucleic tri-phosphate). RNA polymerase is the enzyme in control of the process building the RNA in $5'$ to $3'$ direction.

Though DNA is the same in all cells, the expression of genes can be affected by the environmental and cellular conditions. Moreover, for a specific trait, several genes might involve but with different effects. Therefore, comparison of their expression would be valuable. Generally, by moving from the micro parts to macro ones, for example from DNA to RNA and then amino acids and proteins, narrower correlations can be found.

2.1.4. Code Detection

Among the Nucleic Acid Test (NAT) instruments, perhaps we can categorise the DNA assays into three main groups of sequencing, genotyping, and gene expression analysis. Sequencing looks into the order of nucleo-bases in the whole genome's DNA . Genotyping targets specific segments of DNA for particular gene(s). And gene expression analysis compares the projection of certain genes or mutations. In theory maybe each can be used for the other, but in practice, application, time, and cost enforce the distinction. For example, sequencing might give the ultimate result of the whole code, but the amount of data generated, the time it takes, and the reagents it consumes, may not make it suitable and cost-effective when looking for a specific mutation, or applying in point-of-care pathogen detection. Following sections give a description

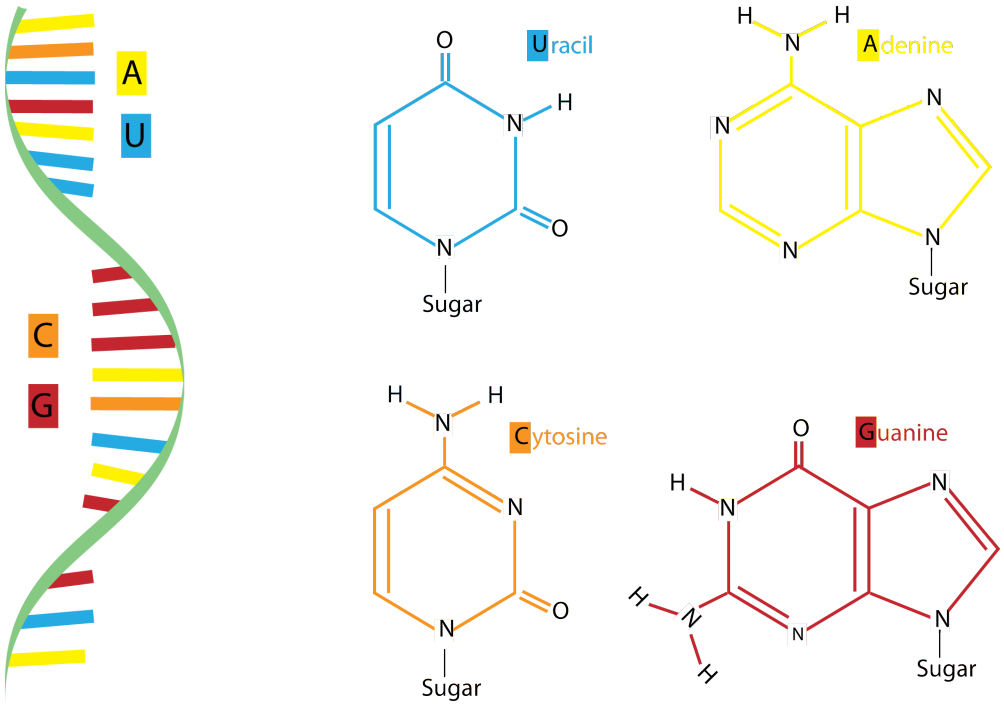

(a) RNA structure.

(b) RNA nucleotides.

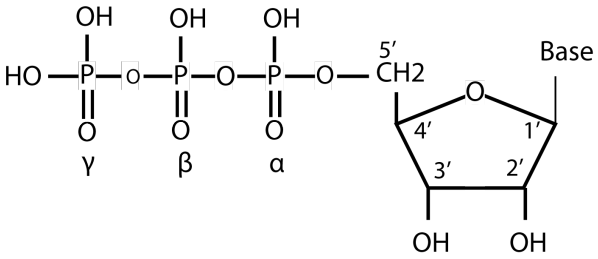

(c) Ribonucleotide triphosphate; rNTP.

Figure 2.3.: RNA structure is similar to DNA but single stranded. In RNA, Thymine is replaced with Uracil. Figures redrawn according to [16, 17].

of each after briefly reviewing DNA amplification which is a common procedure in almost all the platforms for preparation and/or detection.

2.2. DNA Amplification (Replication)

Majority of the detection methods need to have enough of the target DNA molecule whereas the extracted amount of DNA from a sample (normally blood or saliva) may not contain the required copies for a proper signal-to-noise ratio (SNR). In order to have the necessary number of molecules, DNA has to be replicated, as it is done naturally in vivo during cell division. In vitro, it may be done through enzymes at a fixed temperature activating the reactions, or it may be through thermal cycles.

To amplify a certain segment of DNA, as in cells, a primer strand, normally tens of nucleotides long and complementary to part of the target segment, is considered. After untwisting the DNA,

the primer hybridises with the complementary single strand of sample DNA. In the presence of nucleotides and enzymes, a second copy is made by extension of the primer on the sample strand.

2.2.1. PCR

In the Polymerase Chain Reaction (PCR), DNA is first heated up to $95°C$ at which the twisted structure is unwound, and the DNA exists in a single-strand form; denatured. Cooling it down to $55°C$, the primer strand hybridises with the DNA's single strand. Then by increasing the temperature to $72°C$, the polymerase enzyme synthesises and incorporates dNTPs[5]. The length of synthesis can be determined by using terminating nucleotides (ddNTP[6]) or oligonucleotides[7]. The temperatures can also be optimised as the melting point is dependent on the length and number of Guanine-Cytosine pairs on the double-stranded DNA.

The procedure is repeated for multiple cycles to make more copies out of the new ones. Theoretically at every cycle run, the number of DNA molecules should double and after n cycles, 2^n copies are produced; Figure 2.4. However, in practice less copies are generated and it depends on the ratio of dNTPs and ddNTPs as well as activity of the enzymes [21].

This technique has also been implemented in miniaturised analysis systems to provide lab-on-chip solutions [22]. In such Micro Total-Analysis Systems (μ-TAS), thermocycling either takes place by heating and cooling cycles, or through the motion of fluid over different temperature zones [23, 24]. An advantage of PCR is control over the progress of amplification. A disadvantage is usually the slow speed.

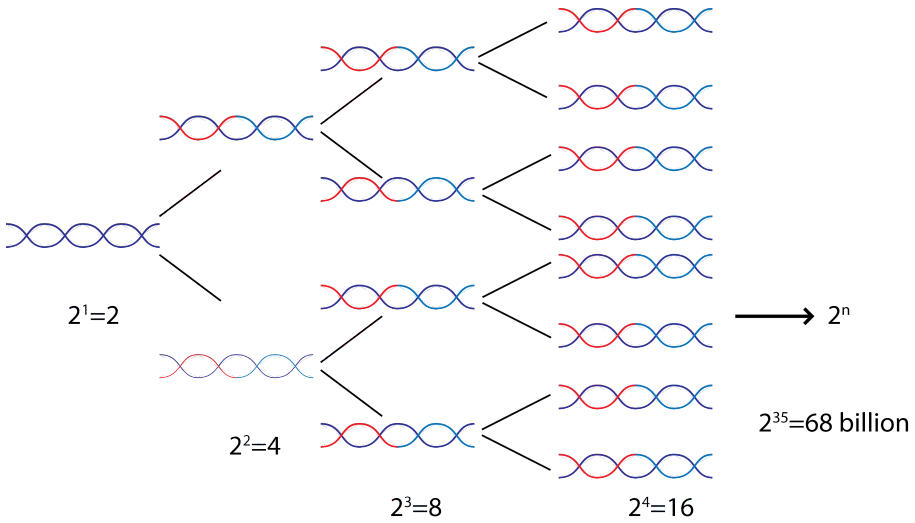

Figure 2.4.: DNA amplification; PCR. Figure redrawn according to [16]

[5]deoxyribonucleic tri-phosphate. Please see Figure 2.1c

[6]dideoxyribonucleotide tri-phosphates. ddNTP has a similar structure to dNTP with its 3′ hydroxyl group replaced by a hydrogen. Therefore, its hybridisation instead of a dNTP, terminates the chain elongation of the second strand DNA.

[7]Oligonucleotide is a chain of nucleotides like DNA. A terminating one like ddNTPs cannot be extended.

2.2.2. Isothermal Amplification

Isothermal amplification follows a similar concept: denature a double-stranded molecule, add a primer and extend it on the single strand to make a copy, repeat the synthesis. NASBA[8], LAMP[9], HDA[10], SDA[11], and RCA[12] are some of the isothermal amplification methods. Isothermal nucleic acid amplifications operate at a constant temperature and their limitation depends on the enzyme activity. Therefore, they do not depend on thermal cycles and can provide billions of copies over about an hour. They are less complex and less expensive, and power consumption is low, making them suitable for low-resource settings. Depending on the enzymes, amplification runs at different fixed temperatures; normally $30°C$ to $65°C$. They can have simple resistive heaters or exothermic chemical heating [11]. A review of these methods can be found in [11, 25, 26]. Among them, LAMP is advantageous for working with blood and relatively impure samples [11]. A disadvantage may be less control over the progress of amplification, or possible lack of synchronicity in parallel amplification.

In LAMP, two sets of primers as well as DNA polymerase are used. Each set of primers start the amplification from an end of the DNA fragment. Several primers on each set and side makes DNA displacement which results in formation of loops and amplification of the specific primed region. For instance in Figure 2.5, primer $F2$ hybridises to region $F2c$ and extends. The outer primer $F3$ hybridises to $F3c$ and displaces the strand by its extension. Then, hybridisation of $F1c$ to $F1$ forms a loop at the end. Similar process happens at the other end of the DNA. Then, the resulted structure enters cyclic amplification by elongation and displacement.

Nevertheless, amplification may be used for sample preparation or for real-time detection. In point-of-care nucleic acid test devises (POC NAT), it is advantageous to have it built in the detection set-up.

2.3. Sequencing

Several sequencing platforms have been developed to detect the sequence of nucleotides on a fragment of sample DNA. In general, they work in three main steps: sample preparation, detection, and computation.

In preparation, the sample DNA is extracted and sheared into smaller segments which form the library of DNA for detection. Similar to cellular functions, primers/adapters may be used to hybridise with a section of the library DNA fragments and enable sequencing of that segment using enzymes and nucleotides. Depending on the method, library DNA, adaptors, nucleotides or enzymes may be modified. For example, in optical methods they may be attached to a fluorophore molecule. For enhancement of signal, the library DNA might undergo an amplification (replication) to generate more copies of its DNA.

[8]Nucleic acid sequence-based amplification
[9]Loop-mediated amplification
[10]Helicase-dependent amplification
[11]Strand displacement amplification
[12]Rolling circle amplification

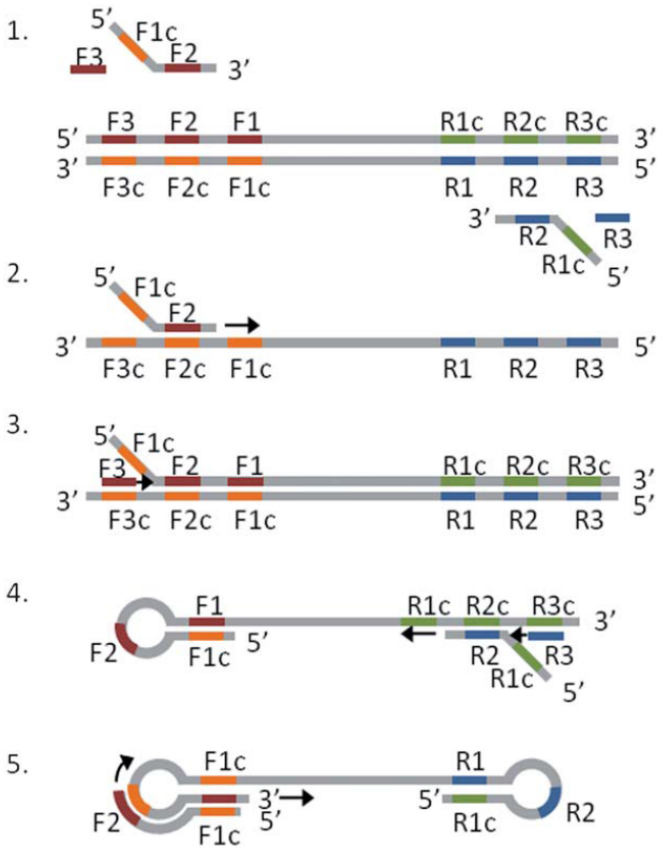

Figure 2.5.: LAMP isothermal DNA amplification process using two sets of enzymes [26].

Figure 2.6.: Sequencing major steps.

In detection, the complementary rule in sitting of nucleotides on a double-stranded DNA is followed. The order of the matching nucleotides that allowed formation of a second strand on the library DNA fragments, with the help of the primers and enzymes, is detected. In the next section, Sanger sequencing method is described and the commercialised next generations in section 2.7.

In computation, the signals from the assay are processed for detection of the sequences. The processing in detection of individual bases is called base-calling. The detected sequences from the library fragments are aligned to rebuild the whole DNA (de-novo), mapped against an existing sequence, or studied for the mutations that may correlate with a particular trait. The longer the reads are in the detection, the easier is the assembly.

Advantages of a system upon another depends on each of the above steps to help in time, cost, throughput and accuracy. Throughput is the instrument output per run or the number of bases it detects at each time running a test. Accuracy measures the percentage of the bases detected correctly in a specific read length. For example a 99% in 100 bases means that one base among the read 100 bases may be incorrectly detected. The importance of read length

is mainly reflected on the processing effort in reassembling the whole genome from the read fragments. Therefore, it is desirable to have a system on which sequencing price and time are as low as possible and the accuracy, throughput and read length as high as possible.

2.4. Sanger Sequencing

The work of Sanger's group in the 1970s resulted in the development of the first method for sequencing DNA [1]. In Sanger's method a primer is designed to match with part of the target DNA. Then it is extended by providing the necessary dNTPs (dATP, dCTP, dGTP and dTTP) and enzymes, forming the second strand from the part the template has hybridised. The process is run in four different tubes. In each tube, in addition to the dNTPs, one type of terminating ddNTPs is used (ddATP, ddCTP, ddGTP or ddTTP).

Each tube analyte is applied to electrophoresis gel. With electrophoresis, all the new DNA molecules are in a similar electric field while they are different in length (because of the mass-to-charge ratio), as in each reaction the extension has stopped for a different ddNTP. Consequently, with either dNTP or ddNTP labelled with ^{32}P (a radioactive isotope of phosphorous), the emitting point from each fragment on the gel, when exposed to an X-ray film, is different. The illuminating point of each can tell which nucleotide has incorporated before the others; Figure 2.7[13]. This process based the succeeding technologies. However, in principle it is time-consuming and can take a whole day for manual reading and analysis of a fraction of the sample DNA. To cover a wide range, numerous primers and assays are necessary.

Later, automated Sanger methods were developed to reduce the manual work and run multiple assays in parallel. Nucleotides were labelled with fluorescences of different wavelengths and colours, each corresponding to a base type, so that the reactions could take place in one chamber. Other improvements were made on synthesising oligonucleotide primers, thinner and longer gels, automated pipetting,...This method has been further developed by automated capillary electrophoresis (CE) systems. Applied Biosystems Inc (now part of Life Technologies[14]) and Beckman Coulter Inc. market this platform. Scanning laser beam crossing the gel plates surface replaced the laborious works on gel drying, X-ray film developing, autoradiograph reading, and hand entry of the results. Nevertheless, the cost remained high and the yield low, necessitated new technologies leading to next generations of sequencing [28, 29]. The recent developments in detection methods are discussed in the following sections after a review on two other assays of DNA.

2.5. Genotyping and SNP Detection

Genotyping verifies DNA for specific gene(s) instead of sequencing the whole genome. It may be done by targeted sequencing, real-time detection during amplification, or using DNA microarray.

[13] Picture from tle.westone.wa.gov.au.

[14] Life Technologies was acquired by Thermo Fisher in February 2014 and is now considered as a brand of Thermo Fisher on its biotechnology sub-brands.

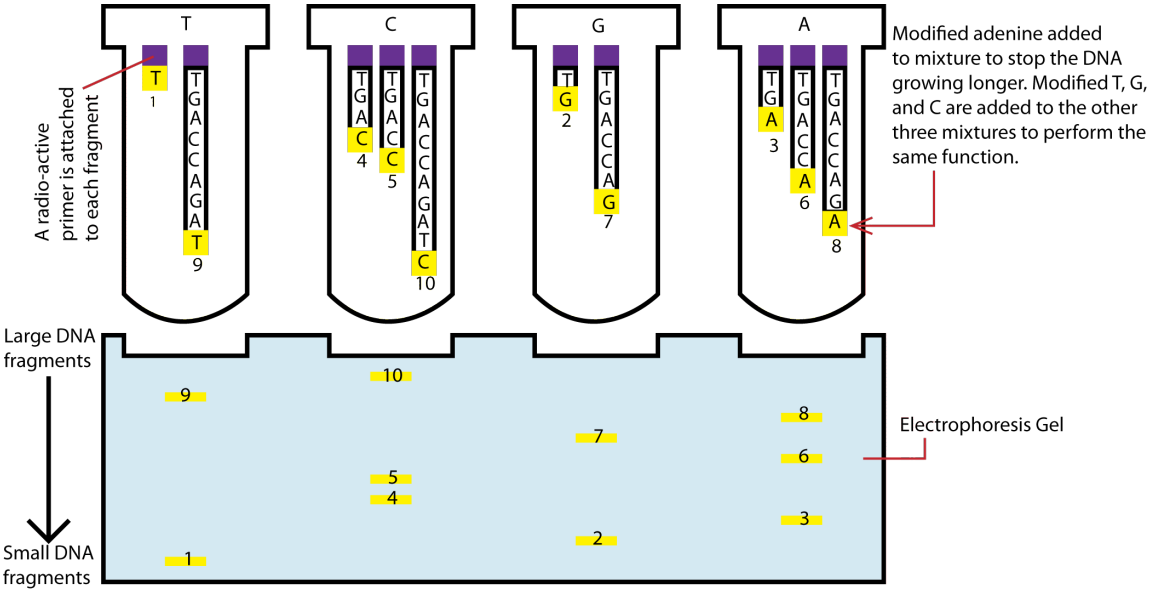

(a) Detection of labelled ddNTPs.

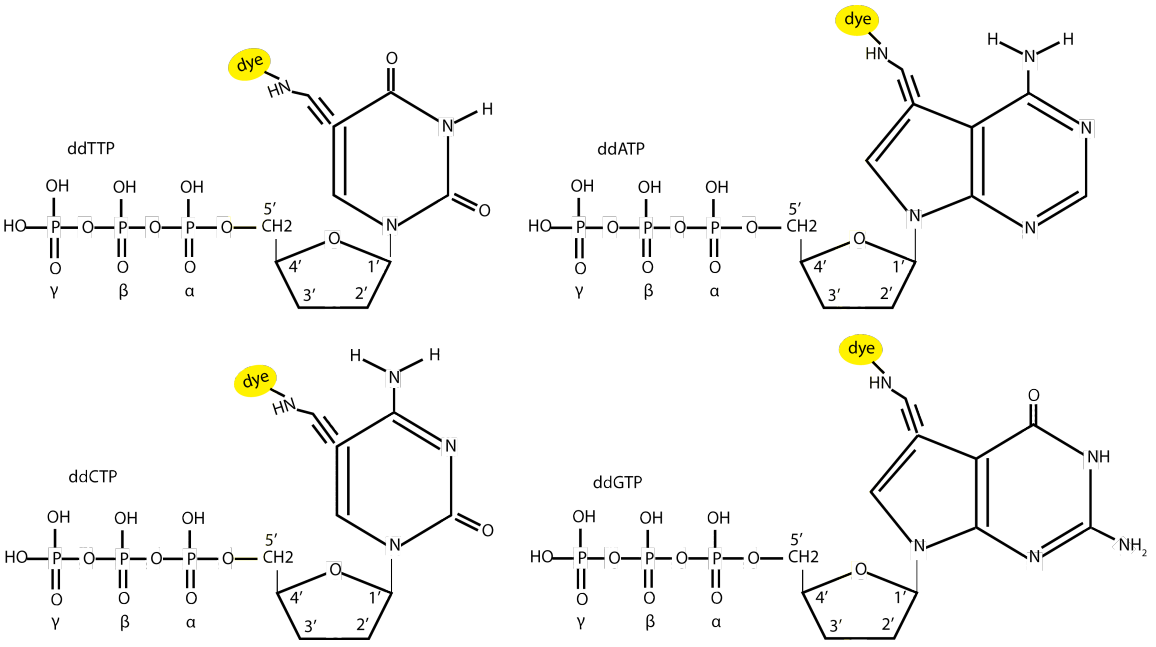

(b) Labeled ddNTPs.

Figure 2.7.: Sanger's sequencing by chain termination. Figures redrawn based on [27].

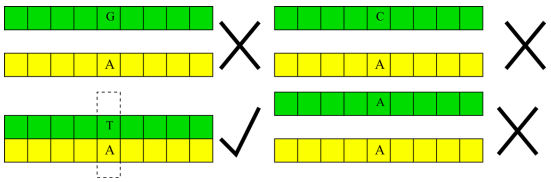

Figure 2.8.: SNP detection by detecting the hybridising probe.

In targeted sequencing , primers are designed for a specific segment of DNA. The sequencing result shows the mutations in the order of the bases, and so the SNPs. In real-time amplification and detection, only a matching primer can proceed the amplification while several primers different at the target nucleotide location are used for comparison. The amplified strands are optically identified which requires labelling of the molecules. DNA microarrays also rely on labelling and optical detection, but in comparison with amplification, they provide a massive parallel assay.

DNA microarrays have thousands of probes (a short sequence of single strand DNA like primer to be hybridised to its complementary part) immobilised on a solid surface. The probes may be pre-synthesised complementary DNA (cDNA) strands, or may be synthesised in situ. In the former case, probes of 500-5000 bases long covalently or electrostatically are attached to a glass or plastic plate. In the latter case, the microarray plate is functionalised with chemical linkers covalently bonding with short DNA oligonucleotides via silane or aliphatic amine (NH_2) group. Primers are added and the array is washed with a solution of one type nucleotide. Light is used to remove the blocking group on the end of last base to allow the synthesis. It may be selective by using masks or microarray mirrors. Another recent way is the use of inkjet technology [30].

The analyte is introduced onto the array and the matching probes hybridise. Then a washing removes the unhybridised analyte. A fluorescently labelled probe may be applied to hybridise to the immobilised analyte, or the analyte itself may carry the fluorophore. The array is then scanned by a laser and imaged with a CCD (Charge Coupled Device) camera. The location of the illuminating spots tells which probes have hybridised with the sample. In addition to genotyping and SNP detection, this platform can be used for re-sequencing.

Sequencing and genotyping make the fundamental platforms in studying DNA and genes. Another assay using similar technology looks into the expression of genes and the RNA.

2.6. Gene Expression

Although the difference among humankind DNA genes is only 0.1%, the expression of genes can be very different, either because of a mutation, or the environment effects on its transcription. A similar gene might be expressed more in some people than the others. Even though DNA is the same in all cells of an organism, not all the genes are expressed by every cell. Gene expression is measured by the amount of RNA copies it generates. Quantitative amplification or microarrays, similar to genotyping with complementary probes, may be used to evaluate the expression level.

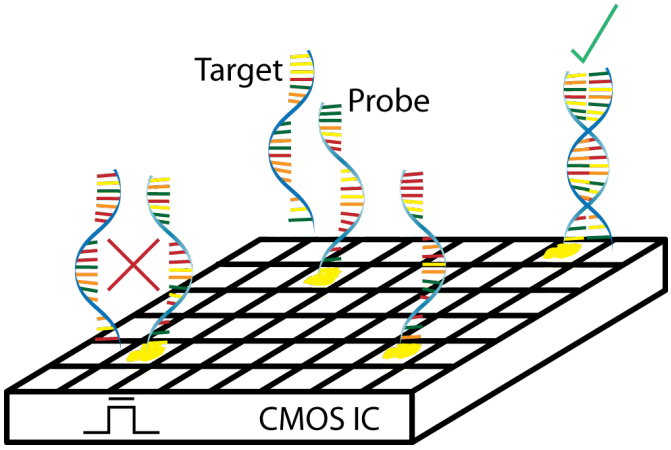

Figure 2.9.: DNA microarray overview.

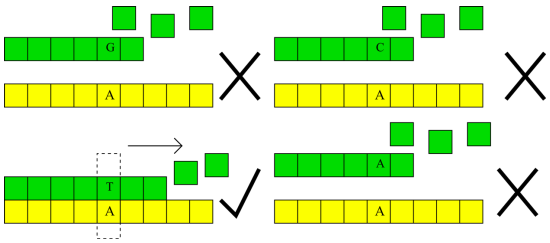

Figure 2.10.: SNP detection by extension of a primer that has the complementary nucleotide in its sequence.

In amplification with the optical detection, the intensity of light would show the progress of amplification, and later from the trace and the number of cycles, the primary amount of RNA molecules creating cDNA would be estimated [31]. However, several parameters affect this measurements and it is reported relative to a control amplification. The primary cycles of amplification might not show strong signals and it needs to pass a threshold. On the other hand, in optical methods fluorescence is a non-linear phenomenon. The fluorescence labels have a greater binding affinity to one type of nucleotide. Therefore, the strands that have more of it, will appear brighter. The quality of DNA and cDNA samples depend on the purity [32]. Cross-hybridisation and partial hybridisations of probes are other sources of errors in amplification and integrated microarrays [33].

In microarrays, complementary probes are immobilised and amplified RNA strands, tagged with biotin, are introduced for hours to allow hybridisation of matched strands. Then the array is rinsed to wash away the unhybridised RNAs. Applying fluorescent stain over the array, it attaches to the biotin of the hybridised strands. Scanning the array with a laser stimulates the stain and the hybridised spots glow. The intensity can tell if there was a high or low expression of the corresponding gene. An example of microarrays image from Affymetrix is shown in Figure 2.11b. On the array are 1.3 million probes testing for nearly $50,000$ RNAs [34].

The primary assays and processes described, has certainly had a considerable impact on the genetic studies. However, the complexity and cost in such implementations, has limited the application of genotyping and gene expression analysis to desktop systems in laboratories.

(a) Affymetrix GeneChip. (b) Gene expression microarray.

Figure 2.11.: Affymetrix GeneChip and an example of gene expression microarrays image [34].

Alike sequencing, considerable effort has been made in research to develop miniaturised systems that can allow point-of-care detection particularly for infectious diseases (known as POC NAT and μ-TAS). Improving sample preparation and designing microfluidic systems to facilitate the analysis by making lab-on-chip devices, are examples of such endeavours [10]. However, change in the method of detection may further reduce the complexities, also in preparation and readout. Non-optical methods can have the advantage of removing the labelling and optics. Some of the fully electronic approaches are discussed in section 2.8. Before that, next section describes some of the commercialised innovations on optical sequencing technologies. Such methods may potentially be applied to some of the non-optical technologies for enhancement of operation. In genotyping and gene expression, detection of a matching biomarker is the question, whereas in sequencing, the detection of the order of nucleotides, and so the approaches are more variant.

2.7. Trends in Optical Sequencing

Sanger method and its automation was successful in the primary sequencing of the human genome. However, the limitations, particularly on cost and time, created demands for high-throughput technologies to generate large data quickly and at a low cost. An initiative by National Human Genome Research Institute (NHGRI) in 2004 aimed for reducing the cost of genome sequencing to $1000 in ten years time. New technologies with different approaches have been developed to run sequencing of large amounts of DNA in parallel in lower costs. These technologies are referred to as *next-generation sequencing* (NGS) and *massive-parallel sequencing* (MPS) [4]. A summary of different technologies is provided in Table 1.1. This section gives a brief review on the commercially available methods that use optical detection.

2.7.1. 454 Life Sciences

454 Life sciences, in 2005 introduced its sequencing system operating based on pyrosequencing [35]. In pyrosequencing the release of pyrophosphate, a side product of dNTP incorporation in extending a hybridised primer, is detected. When a dNTP matches and complements the

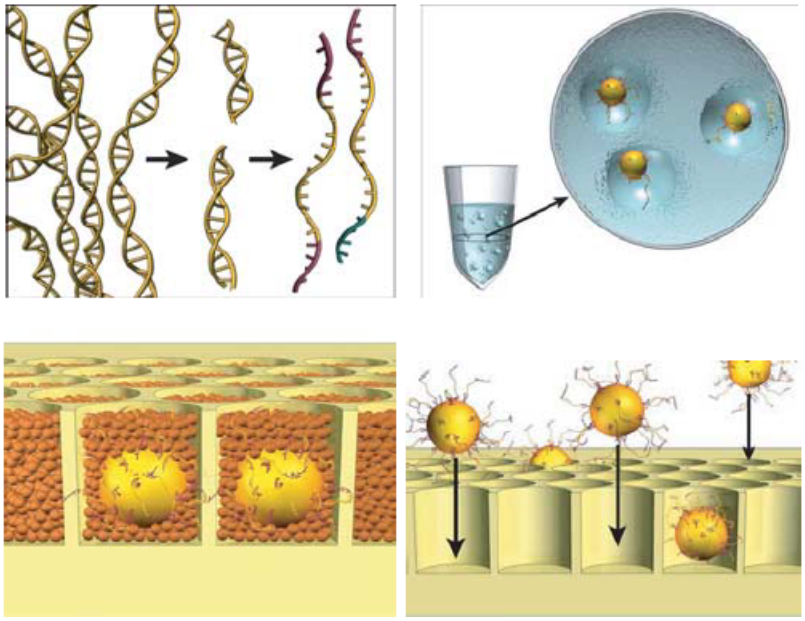

Figure 2.12.: 454 sample preparation and bead loading, from ligation of DNA fragments to adapters in the top left picture, clockwise to the clonal amplification and bead deposition onto the micro-well array [36].

DNA (in presence of polymerase), pyrophosphate (PPi) is generated equivalent to the amount of nucleotide incorporated. With the help of ATP sulfurylase, luciferase, APS (adenosine 5' phosphosulfate) and the generated PPi, luciferin is turned into oxyluciferin and generates visible light.

454 shears the entire genome to generate random libraries of DNA fragments and isolates single DNA molecules by limiting dilution [36]. Common adapters are added to the fragments and then captured by their own beads. The individual fragments on the template-carrying beads are then clonally amplified within droplets of an emulsion by PCR. The beads are distributed over an array of open wells made by etching cores of fibres on a fibre-optic slide; Figure 2.12. The fibre-optic slide is made by slicing a fibre-optic block formed by repeated drawing and fusion of optic fibres.

The slide, loaded with beads, is located in a flow chamber-above the wells opening. The other unetched side of it is connected to an imaging fibre-optic bundle and a CCD sensor. Photons generated during the synthesis are received from the bottom of each well.

In addition to the template-carrying beads, two types of smaller beads are used to carry enzymes and polymerase. In the flow chamber, the reagents are delivered cyclically and flown to the wells perpendicularly. After each step/flow apyrase is used to degrade the unmatched dNTPs and a washing step is applied in the interval of the nucleotides insertion to remove any leftover chemicals. The reagents and by-products are added and removed by convective and diffusive transport. The depth of the wells should be accordingly set. It needs to be deep enough to maintain DNA-carrying beads in spite of the flow, and prevent diffusion of by-products to neighbour wells. On the other hand, wells have to be shallow enough to let the diffusion of

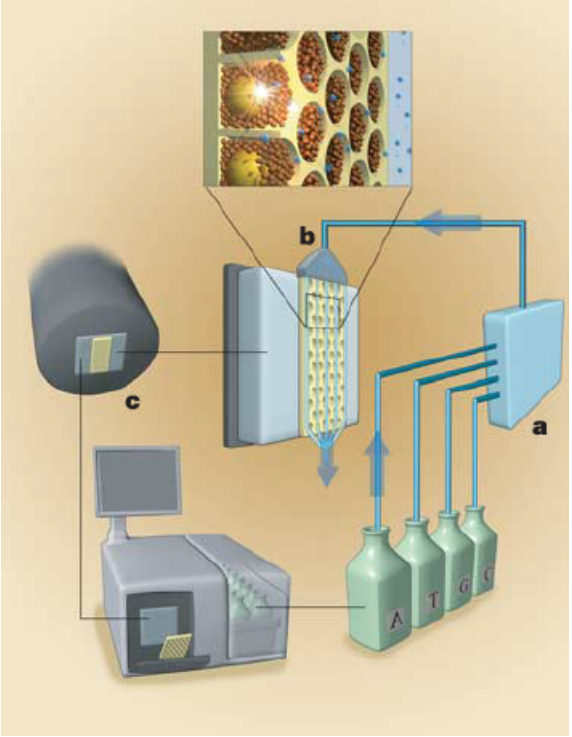

Figure 2.13.: 454 sequencing instrument with major parts to be (a) fluidic assembly, (b) flow chamber containing the fibre-optic slide, (c) CCD camera imaging. [36].

nucleotides into, and the by-products out of the wells rapidly. The signal generation is in a time-scale of $0.02 - 1.5s$ dominated by mass transport effects.

The yield of the array is not 100%. In order to identify the wells loaded with template DNA beads, a known key sequence of the four nucleotides at the beginning of reading is considered on the adapter. The signals are subtracted from the background and normalised. The normalised signal intensity at each flow tells the number of nucleotides incorporated and if the extension of the DNA was for a single base or a homo-polymer. Some of the template strands on the beads might lose their synchronisation by getting ahead or falling behind the rest. This is believed to be mainly due to the leftover nucleotides in the well or incomplete extensions. Such errors may lead to cumulative errors. For a high quality read, oversampling and averaging may increase the reliability.

The read length of 454 was initially $100 - 150bp$ in 2005 and could output $20Mb$ per run. Later by introducing GS FLX Titanium it improved the read lengths up to 600 with $450Mb$ throughput with 10 hour run time. The latest version increased the read length to 1000 with $700Mb$ throughput but in 23 hour run.

2.7.2. Solexa/Illumina Genome Analyzer

Genome Analyzer (GA) was introduced by Solexa in 2006. Later in 2007 the company was sold to Illumina. GA adopts the sequencing by synthesis with reversible chain termination. Basically instead of dNTPs it uses terminating nucleotides so that only one nucleotide can extend the

primer.

Figure 2.14 shows the operation cycles in the Solexa/Illumina Genome Analyser. In preparation, the library is generated by fragmentation and shearing of the DNA. DNA fragments are ligated to a pair of adaptors and denatured to single strands. The single strands are annealed at one end to complementary oligonucleotides (for both of the adapters) immobilised on a solid surface. The other free end of the strand is also hybridised with its complementary immobilised adapter, forming a bridge. The adapters act as the primers in presence of the polymerase enzymes and PCR reagents, helping amplification of the single-stranded DNA fragments. After a couple of cycles and creation of about 1000 copies of each fragment, clusters of DNA with about $1\mu m$ diameter are formed.

The necessary reagents and polymerase enzymes along with the four terminating nucleotides are supplied on the solid surface/flow cell. Each of the nucleotides is labelled with a different fluorescence dye. After incorporation of the complementary one, it is detected by CCD. Then its terminator group at the $3'$-end of the base as well as the dye are removed. The synthesis cycles repeat for read lengths of about 35 nucleotides while tens of millions are being sequenced in parallel [38–40]. The primary GA throughput was $1G$ per run [2] and in the recent model HiSeq X has improved to $900Gb$ per flow channel with a run time of less than three days for the whole genome.

2.7.3. Applied Biosystems SOLiD

SOLiD (Sequencing by Oligo Ligation Detection [2] or Support Oligonucleotide Ligation Detection [3]), was developed by J. Shendure and colleagues and McKernan and colleagues at Agencourt personal Genomics, later acquired by Applied Biosystems in 2006. Applied Biosystems, now part of Life Technologies, released the first SOLiD system in 2007. It uses DNA ligase and detects ligation of di-base fluorescent labelled probes in a cyclic manner.

In sample preparation, the DNA fragments sheared in specific sizes are ligated to adapters from both ends. They may be single DNA fragments, or mate-paired with two pieces of the target DNA in a known distance from each other. Each molecule, unique from the library of millions of molecules representing the whole target DNA, is amplified clonally onto beads in an emulsion PCR reaction. The beads are then attached to a glass substrate with covalent bonds. Templates on the beads are combined with universal primers. The probes which are made of two bases (and so Di-base), inosine bases and fluorescent label, are ligated to the primer if the immediate next two bases of the template are complementary to the ligation site, the two bases of the probe. None-ligated probes are washed away and the imaging system records the fluorescent signal. The dyes are then removed by cleavage of the last three bases of the probe so that the primer may be further extended for the next cycles of probe ligation, imaging and probe cleavage.

4 dyes are used for the 16 possible combinations of the two ligation bases of the probes. After the synthesis of the complementary DNA strand, it is removed for the next round of sequencing but with a primer placement of one base offset. The cyclic synthesis of DNA with moving

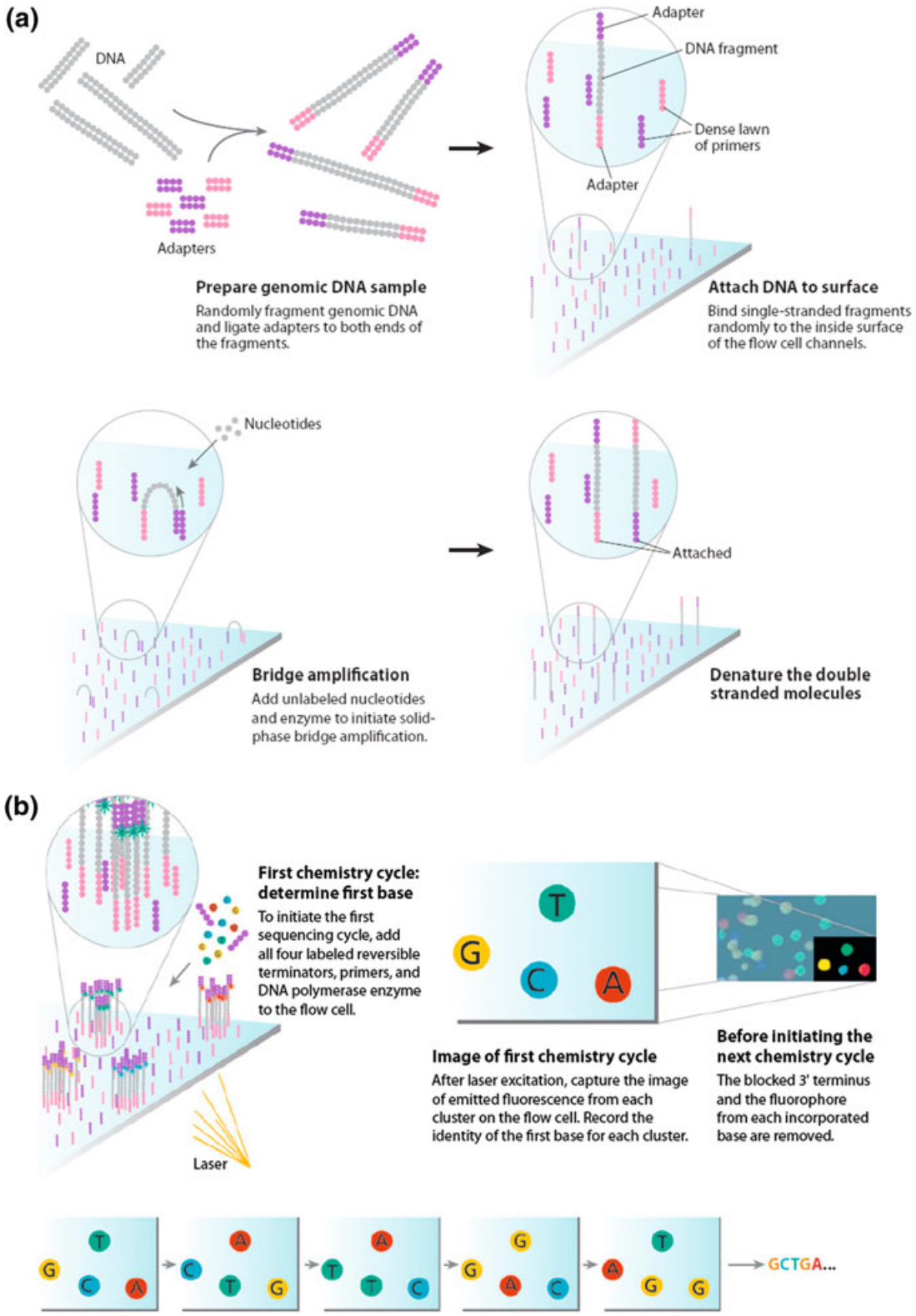

Figure 2.14.: Illumina (Solexa) sequencing by synthesis operation cycle. (a) Fragmentation and bridge amplification. (b) Base Detection by labelled reversible terminated nucleotides [37].

the primer placement allows measuring each of the bases twice and decode the 4 colours into individual nucleotides.

The initial read length of SOLiD was 35 bases with $3G$ data throughput per run and accuracy of 99.85% after filtering. In later series of this product the read length and throughput have been improved. In 5500W model, the sample preparation utilised walking template amplification instead of beads reducing the preparation time from 8 hours to 2 hours. The SOLiD platform may be used for whole-genome sequencing and targeted sequencing, gene expression and small RNA analysis.

2.7.4. Pacific Biosciences SMRT

In 2009 Pacific Biosciences introduced its Single Molecule Real Time (SMRT) DNA sequencing platform. The key differences of the new system were two. One was the attachment of the label to the phosphate group of the nucleotide rather than the base, which would release the label by cleavage of the phosphate by incorporation. Consequently the background noise would be less and there would be no bulk of dye molecules limiting the enzyme activity. The other is the use of metallic cylindrical zero mode wave guide (ZMW), implemented with electron beam lithography and ultraviolet photo-lithography [41], in depths of $70nm$ and volumes of $20 zeptolitre$ ($10^{-21} Litre$) where only a single molecule of polymerase is immobilised to synthesise the DNA strand. Tens of thousands of ZMWs are located in a SMRT cell and nucleotides may diffuse in and out within microseconds, incorporating in milliseconds, and extending the DNA strand with more than 10 bases per second.

Each ZMW is illuminated from bellow its fused silica bottom layer, while the wavelength of the light is too large to pass through. As the base is held in detection volume, a light pulse is produced. A highly parallel confocal imaging system that permits high sensitivity and resolution [42] records a movie of the sequencing process in real time. A heavy concrete foundation maintains the optical confocality while internal robotic arms place the SMRT cell packs. The movies are then processed to create a trace file for each ZMW in real time. Traces are analysed to extract pulses and then call the bases. The SMRT may provide long reads in the order of 1000 bases but the throughput in immobilising the DNA polymerase has been reported to be one third of the ZMW array. Sample preparation time has also been reduced since no amplification would be required.

2.7.5. Summary

The mentioned technologies may be categorised into: sequencing by synthesis, reversible chain termination, sequencing by ligation, and single-strand sequencing[15]. Among them, Illumina announced achieving to the $1000 goal in 2014, but the machines are in hundreds of thousand dollars[16]. Nevertheless, the optical nature of detection asks for labelling as well as sophisticated

[15] Besides the above is Complete Genomics, acquired by Beijing Genome Institute, but only providing sequencing services and not selling products.

[16] Please see Table 1.1.

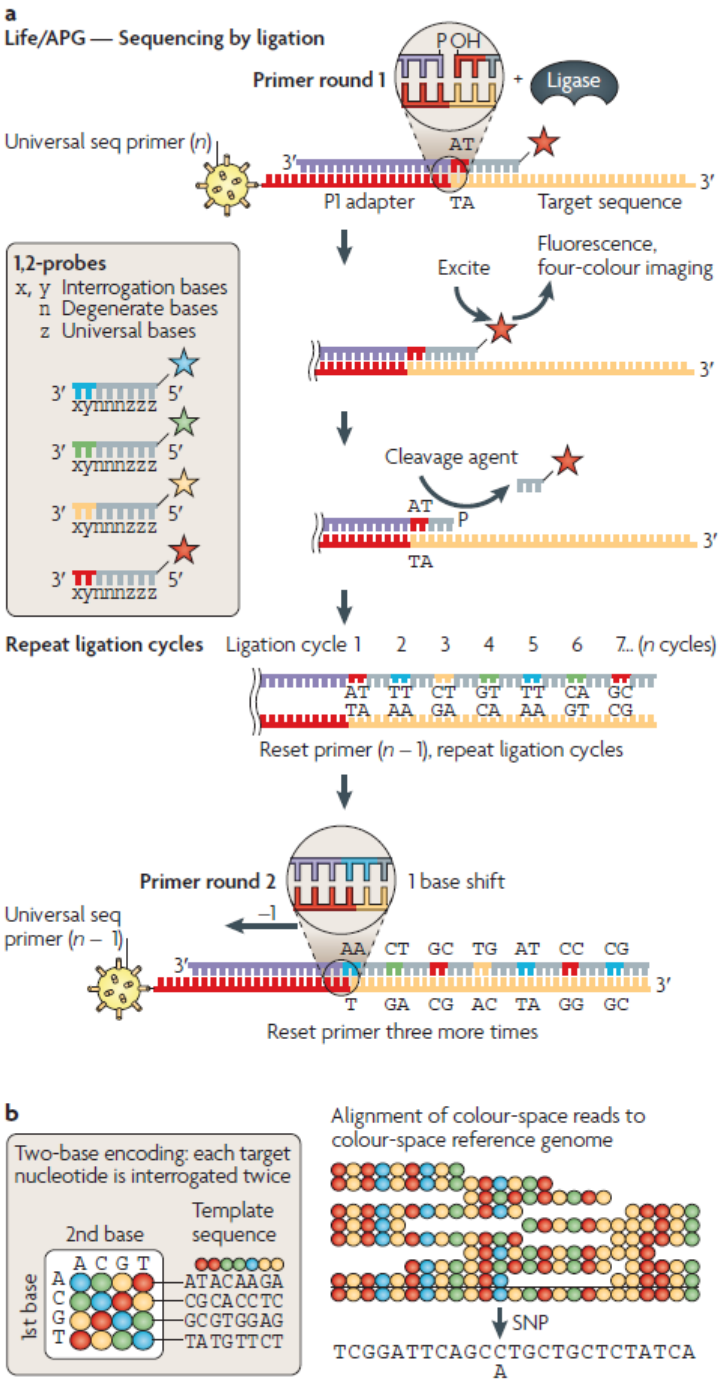

Figure 2.15.: (***a***) Di-base probes ligation and their cleavage by silver ions after imaging. The process is repeated by shifting the primer location, (***b***) Di-base encoding scheme [3].

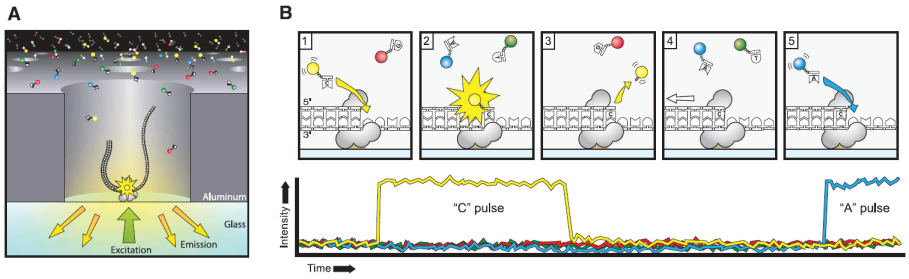

Figure 2.16.: (A) SMRT ZMW chamber, (B) Schematic of the incorporation and signal generation in SMRT [43].

multi-stage design and stack of components (basically the reaction chambers/wells), the light medium and the imaging device. Unless further improvements and scales of production help, a fully-integrated non-optical platform may be more promising for cheap sequencing.

2.8. Fully Electronic Methods

In previous sections, a brief explanation of different nucleic acid analyses (basically for sequencing, SNP detection, and gene expression) was provided with their conventional methods relying on optical instrumentation. Recent achievements in the optical detection methods managed to reduce the cost and increase throughput. However, still in complicated systems limited to laboratory desktops. In this section, fully-electronic methods proposed over the past two decades are introduced. The advantages of such approaches would be elimination of labelling and optics, implementation of miniaturised lab-on-chip assays, reducing the manual and expertise work, less necessary chemical reagents, lower cost, faster response, and application at the point of care.

The methods discussed here, relying on electrical biosensors[17], are categorised into four groups. Some base on RedOx cycling and need electrochemical labelling, and some try to measure changes in physical parameters of equivalent circuit model, like in impedance spectroscopy and capacitive measurements. The third group looks at the change in the charge, either negative intrinsic charge of the DNA, or the ion concentration. And the fourth group, gaining more attention recently, translocates a single molecule through a nanopore and measures the change in the current passing through the pore. Certainly, they are correlated. When setting a model for the electrolyte-electrode impedance, the change in equivalent resistances and capacitances can be in result of ionic concentration change. From another point of view, these methods can be categorised to Faradaic and non-Faradaic; the ones in which the sensor passes a current through the analyte, and the ones that work based on coupling of charges, respectively.

Daniels and Pourmand have done a thorough review on biosensors [44], and defined biosensor as a device designed to detect or quantify a biochemical molecule such as a particular DNA

[17] Most biosensors, particularly non-electrical, require labelling like fluorophores, magnetic beads, ... Labelling a biomolecule can change its binding properties and yield [44].

sequence or protein. Many of them are affinity-based, using a probe to bind with the target molecule selectively. Among the sensors in this category, electrical biosensors rely only on the current/voltage measurements to detect the binding reactions, and thus not on light, mechanical motion, magnetic particles, etc. The electrical biosensors can further be grouped as voltametric, amperometric and impedance sensors. In the first two, DC or pseudo-DC changes are measured while in the last, the AC. They may be evaluated based on [45]:

Selectivity (Specificity) the sensor only responds to the target and not other molecules.

Limit of Detection smallest amount of target that can be reliably detected.

Sensitivity slope of the response curve.

Dynamic Range the range between the limit of detection and the largest measurable target concentration.

Resolution the smallest detectable change.

Stability ability to fabricate, store and transport the biosensor to the end user without significant changes in performance. It is mainly defined by the chemistry on the surface of the sensor.

On the other hand, having sequencing and genotyping application in mind, scalability to provide parallel analysis on a miniaturised set-up is a key in discrimination. In this aspect, methods that need a significant compromise over size for accuracy may be less favourable.

2.8.1. RedOx Cycling

In this method, the probe DNA strands are immobilised on electrodes (chemically bounded on an inert electrode like gold) and the target DNA molecules, which are labelled with enzymes, are exposed to the sites of the electrodes. When the analyte containing the target molecules is applied, hybridisation occurs for matching DNA probes. Later, the chip is washed and a chemical substrate[18] is applied, resulting in creation of electrochemically RedOx-active compounds by the enzyme labels. Then, applying a reduction/oxidation potential at the electrodes causes formation of a current in the electrodes. The current increases in electrodes when hybridisation has occurred.

Figure 2.17 shows an example [46–50] array with pixels made of a pair of inter-digitated gold electrodes with a spacing and width of $1\mu m$, in a disc shape of diameter $250\mu m$. The implementation of electrodes required a post fabrication processing of the chip to etch away the passivation, deposit tungsten, titanium and then gold; Figure 2.18a. Circular compartments were used to prevent contamination of neighbouring sensors during immobilisation of different probes. Figure 2.18b depicts the readout circuit implemented beneath the electrode. A band gap reference circuit sets a constant current which is mirrored to pass through a series of resistors that enter the circuit by collector/generator select signals, to set the reduction/oxidation

[18] Aminophenylphosphate

potentials, through the use of buffers. The current is then converted to a digital signal for further processing and measurements or calibration. The potentiostat sets the analyte counter electrode potential.

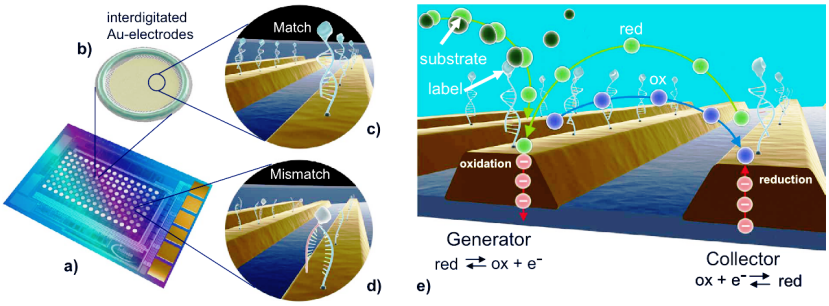

Figure 2.17.: RedOx cycling. a) Array. b) Pixel. c) Hybridisation in case of matching. d) Single strands in mismatch (no hybridisation). e) Creation of RedOx-active enzyme label molecules [49].

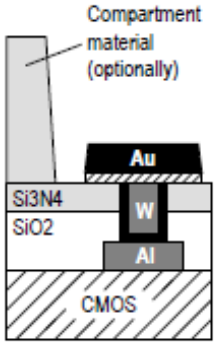

(a) Redox cycling pixel electrode fabrication cross-section.

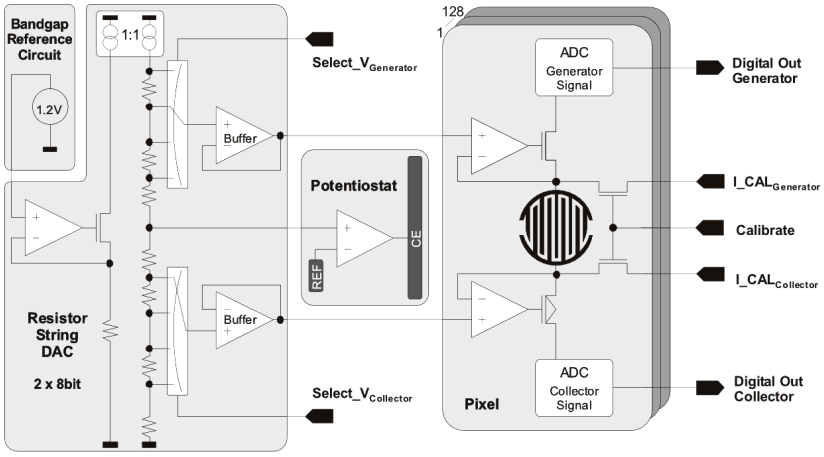

(b) RedOx cycling pixel readout configuration.

Figure 2.18.: RedOx cycling pixel electrode and readout [49].

While the reported results claim the possibility of detection, there are several drawbacks with such structure besides power consumption. First and foremost is size and scalability. The application will be limited to hybridisation detection and not sequencing. The immobilisation and electrochemical labelling are the other factors not much welcomed.

Commercial examples of RedOx are Combimatrix array and Motorola e-SENSOR^{TM}. Combimatirx in 2007 published its 12,533 platinum electrode array (ElectraSense®) performing parallel immunoassay for virus and bacteria detection [51]. The ElectraSense® platform is now used by CustomArrays. However, it is only used for detection of hybridisation while all the preparation and amplification is run separately. Motorola published its e-SENSOR^{TM}made of plastic and printed circuit board with 4×4 gold microarrays in 2001 [13]. Not in a micro-scale, but advantageous for full integration of sample preparation and detection in a disposable

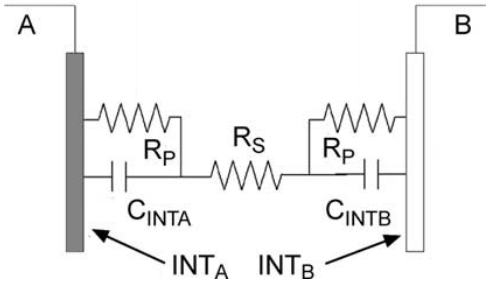

Figure 2.19.: Electrolyte-electrode interface circuit model [54]. INT is the interface of electrode.

cartridge, it is now commercialised by GenMarkDx[19] within a desktop setup.

2.8.2. Capacitance Measurement and Impedance Spectroscopy

Capacitance measurement and Electrochemical Impedance Spectroscopy (EIS) gained interest for their label-free nature. In these methods, the intrinsic changes in result of hybridisation are measured between electrodes on which the probes are immobilised. The idea is based on the difference in dielectric constant and ionic strength of the analyte between a match case (where hybridisation occurs) and a mismatch case (where the probe and the target do not hybridise). The impedance change between the electrodes due to hybridisation is measured. Guiducci [52] has referenced a change of the relative dielectric constant of the electrolyte from 1.9 to 2.5 after hybridisation and a change of the thickness[20] from $2nm$ to $5.5nm$ for the immobilised molecules on the electrodes, expecting an approximately a 50% reduction in capacitance, theoretically. Stagni et al reported a 25% change [53].

On the other hand, these methods depend on the equivalent circuit model considered for the electrolyte-electrode interface. Figure 2.19 shows a simple circuit model for electrode-electrolyte-electrode impedance, a series of capacitances formed at the surface of the electrodes and a bulk capacitance by the electrolyte (which is negligible), in parallel with resistances that represent the ionic nature of the electrolyte [54] .

The capacitance at the surface of the active electrodes is made of the biochemical layer (when the electrode is functioned with probe DNA) and the double-layer capacitance as a result of balancing the ion charges at the surface of the electrode. The functioned electrode layer changes if hybridisation occurs, thus changes the layer capacitance and the total electrode capacitance.

Direct measurement of the capacitance is not possible and several methods have been proposed to observe the expected change [55]. Some of them rely on charge-based capacitive measurement (CBCM). This can be achieved by applying a periodic pulse and measuring either the average current and voltage difference on the electrodes [52, 54, 56] (Figure 2.20), or the time-constant of the discharging voltage [57, 58]. In the former case, the relation between the average current

[19] www.genmarkdx.com

[20] The thickness change is questionable as it would mean that the DNA strands are immobilised from their sugar-phosphate backbone whereas in other methods as for microarrays strands are linked to the surface from their ends.

(I_{avg}), frequency of the pulse (f), the pulse step voltage (V_{step}), and the total capacitance in between the electrodes (C_{tot}) is

$$I_{avg} = I_{offset} + C_{tot} V_{step} f \tag{2.1}$$

The offset current (I_{offset}) is the resulted dc current from switching between the charge and discharge phases. The dependency of the readout on the actual capacitance value means the high importance of dimensions in the resolution of measurement, and the challenge in scaling to smaller pixel sizes for high-density arrays.

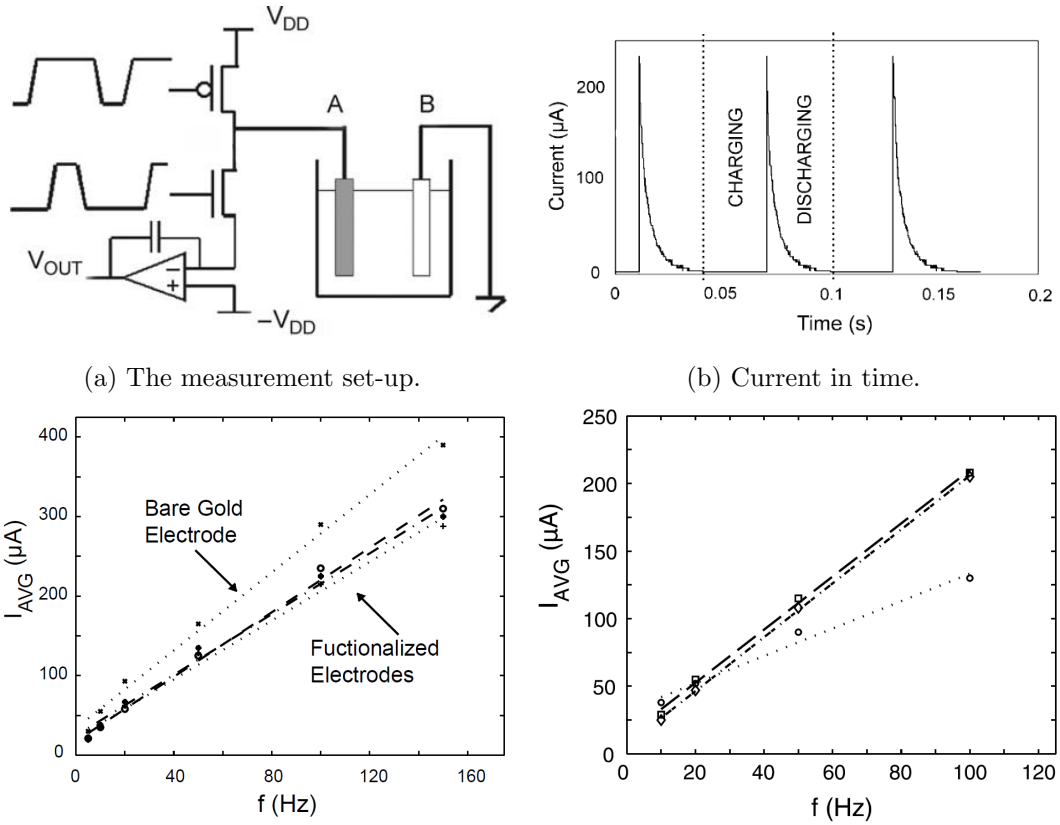

(a) The measurement set-up.

(b) Current in time.

(c) Current versus frequency with $0.5V$ step.

(d) Current versus frequency, before exposure (dashed-dotted line), after exposure to matching DNA (dotted line), and after exposure to non-complementary DNA (dashed line).

Figure 2.20.: CBCM based on average current measurement in [52].

In the other case, measuring time constant change, reference electrodes are formed by non-hybridising single strands of DNA immobilised on them. The current difference (differential measurement) between such references and the sensing electrodes is integrated over time t. Similar to model displayed in Figure 2.19, the interface parallel capacitors and resistors are replaced with C_{ref} and C_{sens}, and R_{ref} and R_{sens} respectively for the mentioned reference electrode and the sensing one (Figure 2.21). In this model the series resistance was ignored as it

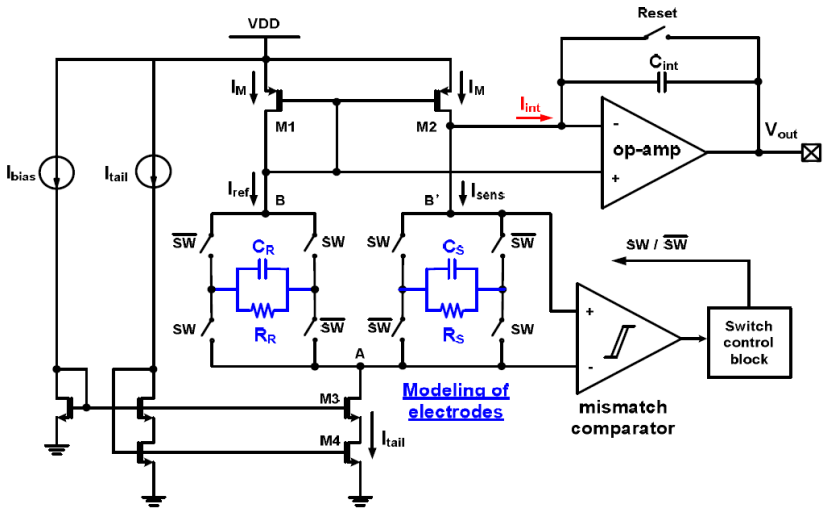

Figure 2.21.: CBCM based on integrated current measurement in [56].

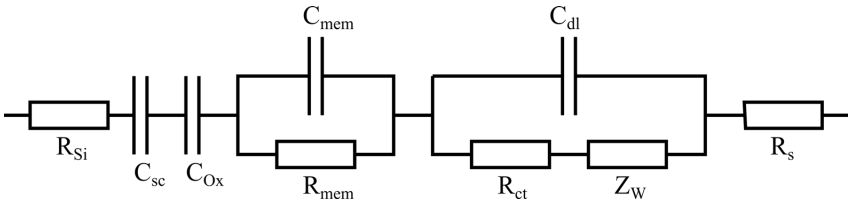

Figure 2.22.: Equivalent circuit of a FET with a modified membrane [59].

depends on the ionic strength of the buffer, usually estimated as several Ohms. The calculated relation between the output voltage change and the interface capacitance was reported as

$$\Delta V_{out} = -\int_{-}^{t} I_{int}/C_{int}dt = t.I_{tail} \times \frac{C_R - C_S}{C_{int}(C_R + C_S)} \tag{2.2}$$

EIS on the other hand, uses small-signal analysis and looks for a change in the transfer function of the readout circuit, or the equivalent impedance between the electrodes. In some cases electrodes are replaced with field effect devices and the probe is immobilised on an electrode directly connected to the gate of a FET [60, 61]. Figure 2.22 [59] provides a fairly more complete model taking into account the FET capacitance and resistance. In this model C_{mem} is the bulk capacitance of the membrane, R_{mem} the bulk membrane resistance, C_{dl} double-layer capacitance at the membrane interface, R_{ct} charge transfer resistance at the membrane, and Z_w the Warburg impedance representing the diffusion of ions to the membrane interface. In a simplified model, the last three as well as the silicon electrode resistance R_{si} and space charge C_{sc} are ignored. Therefore, only the membrane parameters and the oxide capacitance C_{ox} are taken into account. They could be important in very low frequencies ($f < 5Hz$) but not considerable in frequencies above [59]. Accordingly, the transfer function for the FET was calculated to be

$$H(j\omega) = \frac{1 + j\omega R_{mem} C_{mem}}{1 + j\omega R_{mem}(C_{mem} + C_{ox})} \tag{2.3}$$

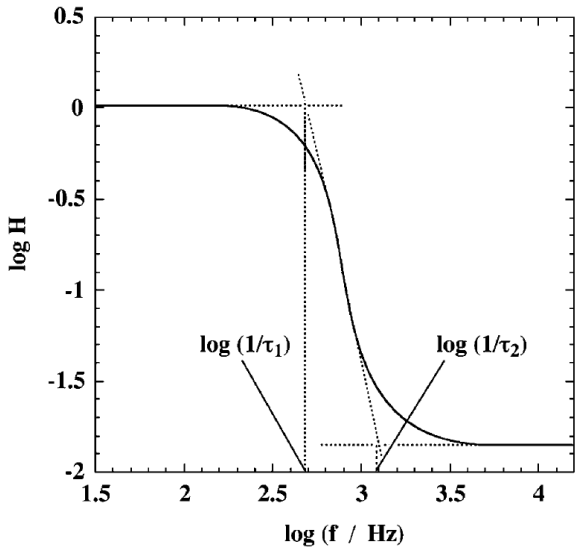

Figure 2.23.: Theoretical transfer function of FET with modified membrane [59].

which results in one pole and one zero that can be calculated as

$$\tau_1 = R_{mem}(C_{mem} + C_{ox}) \approx R_{mem}C_{ox} \tag{2.4}$$

$$\tau_2 = R_{mem}C_{mem} \tag{2.5}$$

However, although presented with supporting results in the work of Offenhausser et al [60], Figure 2.24, and similar publications [61], this method suffers from some sever non-ideal issues, such as the place of the reference electrode, the ionic concentration of the buffer (the volume of molecules should be high to be able to detect hybridisation), sensor drift, and temperature drift. Moreover, it takes long time to provide the result and needs complex processing.

Hassibi takes advantage of the low frequency of the operation in such arrays to switch bias the noisy parts and reduce the $1/f$ noise[21] [62, 63]. In his programmable microarrays for EIS, he utilises three sets of electrodes: counter electrode (C), reference electrode (R), and working electrode (w), while only the working electrodes have capturing probes; Figure 2.25. Reference electrode is identical to the working electrode except it doesn't have any probes. Therefore, taking a pseudo-differential signal from the two with a common input at the counter electrode, can tell the change in the impedance between the working electrode and the other two, in result of hybridisation of the probe.

2.8.3. Charge Coupling

In previous sections, electrodes and field effect devices were used to show change in the impedance of either bulk buffer solution or the sensor membrane and the bulk interface. In this section, methods that look at a shift in the characteristic of a FET, in result of DNA hybridisation at

[21] flicker noise. f:frequency.

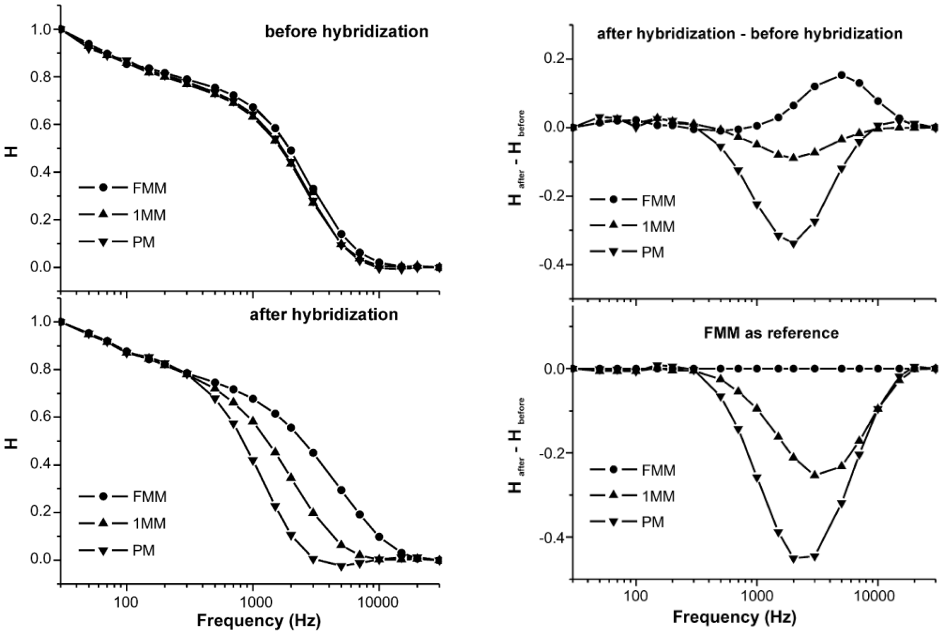

(a) Transfer Function. (b) Differential transfer Function.

Figure 2.24.: Change of transfer function and difference between the cases the probe and target are fully mismatch (FMM), mismatch (MM), and perfect match (PM). The magnitudes were normalised for $30Hz$ [60].

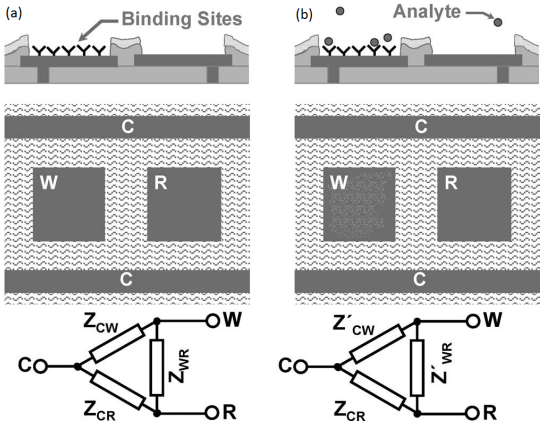

(a) EIS pixel configuration. (a) Capturing Probe on working electrode, (b) Molecular binding resulting in change of impedance.

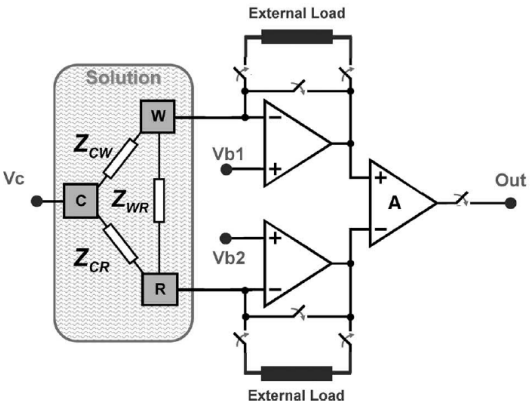

(b) EIS interface circuit.

Figure 2.25.: Change of Impedance after hybridisation [62]

.

its extended membrane are discussed. Perhaps, the difference among the works discussed here is the different viewpoint on what parameter or signal to look at, while the principals are quite similar if not the same. For sure, change in the impedance on the membrane causes the shift in the current/voltage of the FET beneath, which is indeed influenced by the change in the charge coupled on its corresponding floating gate. In the charge based methods, some measure the change in the intrinsic negative charge on the DNA (the phosphate backbone), and some look at the side products of DNA strands elongation.

DNA Negative Charge

Sakata [64], Barbaro [65], and Kim [66, 67] considered the intrinsic negative charge in DNA molecules with different approaches. In case of hybridisation or extension of DNA strands, this negative charge increases and shifts the FET signal/characteristic when it is applied at the gate of a FET.

Sakata used the passivation layer of Si_3N_4/SiO_2 as the sensing membrane coupling the negative charges in the analyte, biased with a reference electrode to the floating gate of the FET. This is quite similar to the use of Ion-Sensitive Field Effect Transistor (ISFET) in measuring the pH.

Barbaro extended the gate of the FET, added one control capacitor to couple a control voltage as an input to the gate as well as the intrinsic charge of the DNA which makes the other input of the gate; Figure 2.26. He used the control input to play the role of reference electrode. He opened a pad and deposited an interface on the aluminium metal on which single strands of DNA are immobilised. In result, the input to the gate of the FET is a combination of the control voltage and the negative charge of the DNA molecules. The charge can increase when the single strands hybridise. The effective shifted threshold voltage was then defined by the control capacitor C_C, parasitic capacitor C_F, the FET intrinsic threshold voltage V_{TH0}, the charge initially trapped in the floating gate Q_0 (also a function of control voltage), and the charge of DNA molecules Q_{DNA}:

$$V_{THF} = V_{TH0} - \frac{Q_{DNA} + Q_0}{C_C + C_F} \tag{2.6}$$

Implemented as an array, in order to overcome the common noise, for each device there was a counterpart on which non-matching probe was immobilised, so that the difference in the output would show the selectivity of the work. To overcome the fixed pattern noise (FPN), caused because of the floating gate nature of the device and possible random accumulation of charge on the gate during fabrication, at each stage of the work the outputs were subtracted from their previous stage value.

Kim et al [66, 67] utilised the top metal of CMOS process directly exposed rather than depositing a membrane and immobilising the probes. The top metal aluminium naturally oxides quickly and forms a layer of Al_2O_3 less than $10nm$. Unlike the discussed works, the sensing plate was not directly connected to the gate of a FET. A switch transistor would select which of the plates in the array should be connected to the gate of a voltage-follower input

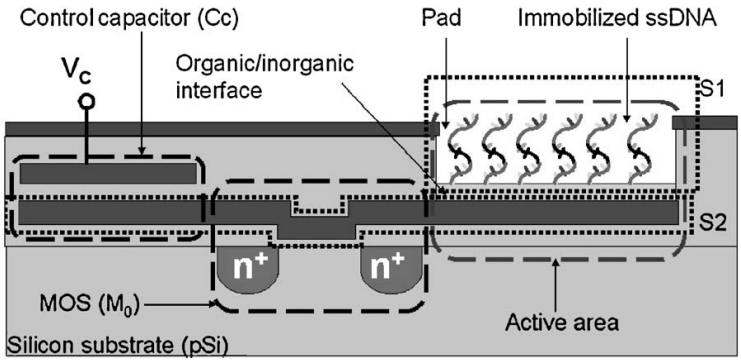

Figure 2.26.: Negative Charge Coupling with a Control input [65].

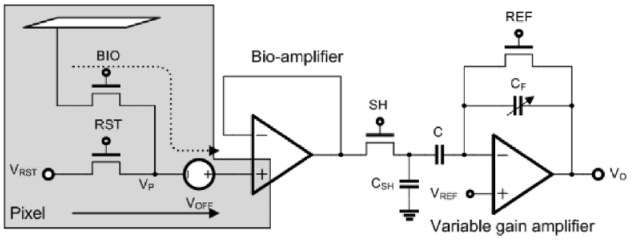

Figure 2.27.: Simplified schematic of CDS used in the Al/Al_2O_3 electrode array of [67] to sense negative charge of DNA.

transistor. A simplified circuit schematic for a single pixel, and the circuit model of the sensing operation, are depicted in Figure 2.27 and Figure 2.28.

Correlated double sampling (CDS) was used to reduce the fixed pattern noise. At first the reset was high and the capacitor was charged with the reset voltage input (V_{RST}) and noise (V_n). At the next phase that the voltage on the sensor was switched into the amplifier, the input to the capacitor C would be $V_{DNA}+V_n$, the voltage induced from the DNA charge (biased with the reference electrode) and the common noise. The output voltage was calculated to be

$$V_{OUT} = V_{REF} - (C/C_F).(V_{DNA} - V_{RST}) \tag{2.7}$$

Change in the negative charge of the DNA molecules in result of hybridisation would make V_{DNA} and consequently output voltage change. Though, the other concern might be the leakage through the switches which was justified to be negligible as it would be less than $0.1fA$, and the electrode capacitance would be larger than $65pF$ with parasitic of $C_P \approx 136fF$, taking more than 650 seconds to induce potential change of $1mV$.

While there was a more than 10 times improvement in the noise of the readout using CDS, from $5.13mV_{rms}$ to $0.41mV_{rms}$, the reported drift of $3mV/s$ at the beginning of experiment, $10\mu V/s$ afterwards, and $2mV$ during the $20s$ considered transition time, would limit its detection resolution.

Similarly, Hassibi's group [68] reported a work for monitoring the charge using the top-metal aluminium as the electrode with its natural Al_2O_3. The dynamic range for the 90×90 array

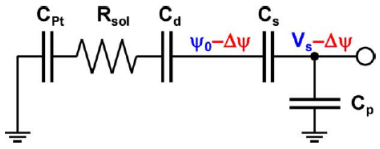

Figure 2.28.: Equivalent circuit model for the Al/Al_2O_3 electrode [67]. C_{Pt} represents the platinum-deposited reference-electrode capacitive interface with the solution, and R_{sol} the solution resistance, C_d the double-layer, C_s the sensing membrane, and C_p the parasitic capacitances.

was $+90dB$ consuming $4mW$ power in $0.18\mu m$ process. Correlated double sampling was used for reducing the flicker noise. Sawada et al [69] by immobilisation and use of active pixel sensor (APS) concept as for imagers made a DNA sensor array to sense the charge change after hybridisation.

Nevertheless, in Chapter 4 we will see that Al_2O_3 is considered as a pH sensitive material. A side product of DNA elongation is the release of hydrogen ions , increasing H^+ concentration, which may influence the negative charge measurement.

pH-based methods

Direct detection of DNA hybridisation with a field effect device seemed to be first introduced by Souteyrand et al in 1997 [70]. A former application of FET as an ISFET for real-time monitoring of DNA polymerase was proposed in 1992 [71], which claimed that for low buffer capacity, the pH increases in result of elongation and could be detected by the pH sensor. Whereas Toumazou and Pourushotaman [72] were the first to use the ISFET to actually detect the drop of pH in sequencing by synthesis.

Figure 2.29.: Release of H^+ ions by nucleotide incorporation and synthesis of DNA.

Toumazou et al used ISFET to detect the pH drop in result of the extension of primer DNA on target DNA. When the primer hybridises, in presence of dNTPs and enzymes, it is extended to synthesis a complementary strand [73]. This extension generates pyrophosphate and releases H^+ ions (equation 2.8, Figure 2.29 and section 2.1.1) dropping the pH [74].

$$DNA_{(n)} + dNTP \rightarrow DNA_{(n+1)} + PPi + H^+ \tag{2.8}$$

In the first application for SNP detection [75], they used a differential configuration (Figure 2.31) in order to cancel out the common noises. A reference was designed to intentionally not undergo any synthesis, while for a working sample, the required dNTP was provided with a matching primer. The difference between them was the pH change from the elongation of

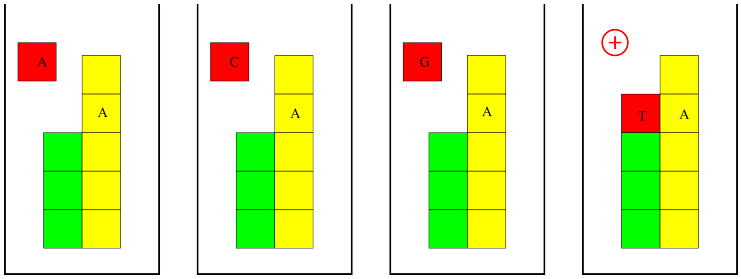

Figure 2.30.: Release of H^+ ions by extension of DNA strand in SNP detection.

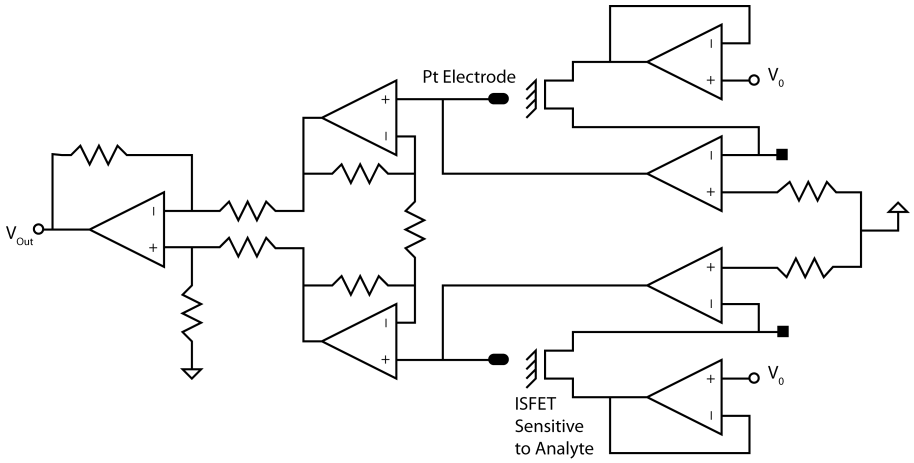

Figure 2.31.: Differential configuration used for ISFET-based SNP detection [75].

matching primer, detected by the differential circuit. The successful results made this the platform for a system-on-chip [76] capable of amplification and detection of matching DNA templates simultaneously.

The principle in the primary works is similar to early Sanger method. For each SNP, four chambers with only one type of dNTPs are used (Figure 2.30), in addition to the reference. Only the one (in case of homozygous) or two (when heterozygous) in which the primer could be extended, were considered as the detected mutations in the target DNA.

The advantages of this technology, in addition to being label-free and fully electronic, is the totally CMOS-compatible fabrication of the assay without any immobilisation. The advent of ISFET into this industry promises a low-cost robust platform for implementing new lab-on-chip structures. The application of this technique into both genotyping and sequencing is specifically studied in Chapter 3.

Pyrophosphate Capturing

In section 2.1.1 it was shown that a side product of the extension of the DNA strands is pyrophosphate (PPi). This pyrophosphate is from the nucleotide incorporation releasing two of its triphosphate's phosphate groups. In pyrosequencing, PPi was used to cause illumination of luciferin for detection. Intel in 2012 [77] published its work on taking advantage of this fact on implementing a platform similar to the pH-based method described, but with modifying the

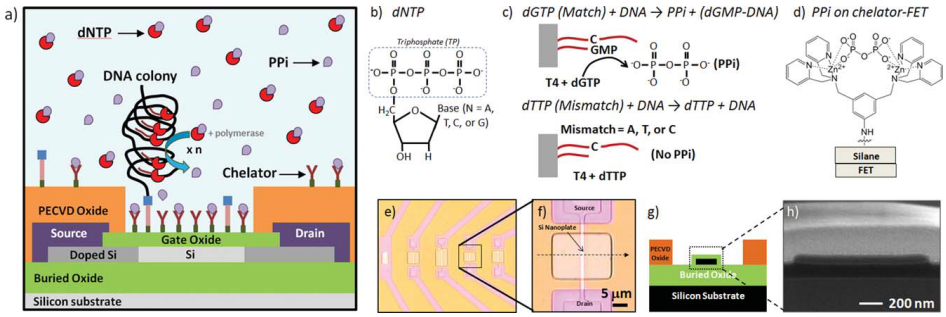

Figure 2.32.: DNA extension detection by chelator modified SOI-FET capturing the releasing PPi. (a) functioned surface, (b)(dNTP) base, (c) matching base incorporation generates pyrophosphate, (d) PPi attached to chelator on modified FET surface, (e) optical microscopy images of low density SOI nanoplate FET array, (f) image of one of the devices used in the experiments, (g) cross-section schematic of Si nanoplate FET device, and h) high resolution SEM image of 25 nm Si nano-plate cross-section of same device shown in (f)[77].

surface of the sensor with chelator[22] to capture PPi molecules (PPi contains negative charge) on a silicon-on-insulator field effect transistor (SOI-FET).

Figure 2.32 depicts the scenario on the surface of the FET. The device was functionalised with both the amplified DNA on the surface in the form of DNA colonies, and chelator groups to capture pyrophosphates produced from the enzymatic incorporation reaction of a matching DNA base. At a fixed drain-source bias, the back-gate bias was swept while only the capture of the released pyrophosphate could increase the carriers of a p-type accumulation mode SOI-FET, shifting its current/voltage characteristic. To increase the number of parallel reactions, rolling circle amplification was used.

The advantage of this method over the other ones with immobilisation described is perhaps the dependency on pyrophosphate release rather than detection of hybridisation of DNA strands based on impedance changes, especially when there is a chance of cross-hybridisation or partial hybridisations on such arrays. It is applicable for sequencing and not limited to genotyping. Besides the supporting results provided, it was also mentioned that the shift in the characteristic was not exactly as expected. Perhaps existence of different positive ions caused this effect. The other issue is the capacity of the pixels formed with this structure. There is an inevitable trade-off between the length of the sequencing at each pixel and the density of sensors on the fabricated silicon wafer. Certainly, scaling and chelator saturation is the other compromise to be made.

2.8.4. Nanopore Current Measurement

A different approach from the discussed optical and fully electronic methods is using nanopore structure to detect single bases of DNA. Nanopore is an aperture of nano-meter size in a membrane that separates two analytes. Since the inner diameter of nanopore is in the same order as a single molecule, it is used to monitor molecules through the restriction they create at

[22] A chemical that binds to certain ions and deactivates them.

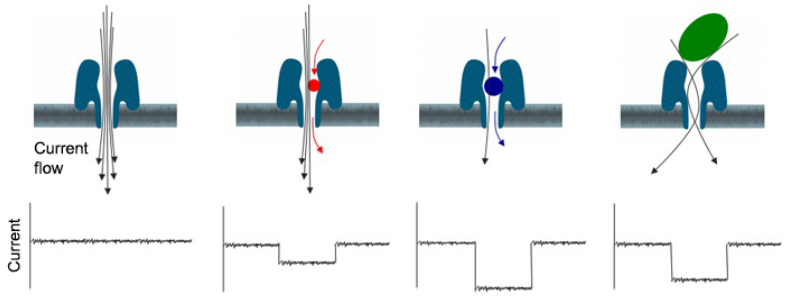

Figure 2.33.: Translocation of a molecule via a nanopore changes the current passing through it [78].

the pore. For a long chain molecule like DNA (and about $4nm$ wide), it is electrophoretically driven through the nanopore. Electrodes at the two sides of the membrane apply a potential difference which translocates the DNA. The current through the aperture changes as a base passes, which is different for each of the four nucleotides [28].

However, the thickness of the membrane is several nano-meters, causing an accommodation of several bases at a time at the nanopore, hence adding error in the detection of the current change. Also, the speed of translocation is about 1 nucleotide/μs, or equivalently a signal in the order of $1MHz$. To overcome these challenges, several solutions like use of progressive enzymes cleaving the DNA nucleotides and slowing the translocation speed, and chemically modifying the pore and probe complementary nucleotides [28], were introduced.

The first membrane used (and still in use) is α-hemolysin(αHL) protein. Solid-state materials like silicon nitride, silicon or metal oxides, and graphene have also been investigated to replace the organic supports for their limited thermal and chemical stability, and difficulty in integrating with micro devices [13, 79]. Nevertheless, this sophisticated approach is quite attractive for allowing possible longer reads (about $5.4kb$ single-stranded DNA with solid-state and $25kb$ with protein membrane) and reducing the number of samples required for sequencing. Oxford Nanopore is pioneering in the commercialisation of miniature nano-pore sequencing machines at a USB stick sise. However, the systems despite all the improvements in readout, suffers from errors in base-calling [80]. Another commercial example is Genia acquired by Roche[23] in June 2014.

2.8.5. Noise

The uncertainty in the electrochemical sensors is from one side related to the electronic part that the electrons are the carrying charges, and from the other side the chemical part that the ions carry charge. The unwanted fluctuations on each side degrades the resolution of the system as well as the minimum detection level.

The main electrical noises in the interface circuitry and the system are flicker noise and thermal noise. They are very well studied in major relevant references like [81]. But flicker noise is much more dominant due to the relatively slower pace of reactions and low-frequency

[23]Before that Roche 454 Life Sciences had collaboration with IBM to develop nanopore sequencing machines.

nature of the signal(dNTP incorporation in every $3ms$ during DNA extension [74]), which makes the DC measurements vulnerable in such frequency range. From this point of view, EIS techniques might seem preferable, though as discussed, their complexity and impracticality in higher levels of integration, do not make them promising.

The challenge in low frequencies and DC measurements become more complicated as the chemical noise at the electrode-electrolyte interface in such systems is believed to have a $1/f$ characteristic at thermal equilibrium too [82]. In biosensors, the hybridisation of probe and target are not 100% selective and non-specific bindings are always probable to occur as well as partial hybridisations where not necessarily the whole probe is bound (cross hybridisation). For immobilised assays, where the analyte is exposed to an array of probes on top of the sensors, the spread of molecules was assumed to be diffusive. Accordingly, with a Markov stochastic process, a biological shot noise was derived for the affinity-based sensors [33, 83]. Such noise particularly affects the estimations for gene expression levels [84]. Diffusive and convective flow of reagents also add fluctuation to the measurements, where a common fluidic link is used to supply the assay.

2.8.6. Miniaturisation

Miniaturisation or scaling down the sensor dimensions, offers benefits like lower volume of sample analyte (and therefore less amount of reagents), higher integration of sensors, increased number of tests that can be run in parallel, increased reliability/redundancy by considering multiple sensors/pixels for the same probe, and possibly lower cost. However, there are some drawbacks with scaling too.

In impedance spectroscopy, capacitive measurements, and ampero-metric methods, the reduction in the dimension of electrodes, reduces the impedance changes and the resolution for an individual sensor, whereas using multiple pixels per spot improves the resolution and the limit of detection [85, 86]. On the other hand, it was assumed that scaling would not affect the potentiometric sensors, ChemFETs and ISFETs. While theoretically it might be correct, due to parasitic decoupling capacitors, the coupling efficiency is degraded. For the ISFETs, the geometrical effects are studied in Chapter 4.

Other drawbacks of miniaturisation in fabrication are higher mismatch among the sensors, complexity of layout design [85], liquid evaporation with higher surface to volume ratio, and sensor storage and diffusive mixing [87]. The smaller the distances, the quicker the diffusion, and consequently the higher the necessary sampling and scanning rate in arrays.

2.8.7. Summary of Label-free Fully-electronic Methods

This section provided a review on the recent fully-electronic methods proposed for genotyping and sequencing. They can be credited based on their simplicity (in other words their complexity and scalability) which influences their cost and robustness. Compatibility with CMOS technology, which allows leveraging from its mass production and inexpensive fabrication, is more advantageous. It provides on-chip processing of the signals, but for a higher density of parallel

analysis, the more complicated the detection method is, the more area would be consumed by the processing circuitry rather than sensor devices. Power consumption is the other factor discriminating the designs especially by the interfaces and signal conditioning blocks. With the goal of portable genotyping devices, low-power instrumentation will significantly play a key role. Noise, sensitivity and reliability are the other factors to be taken into account for the limit of detection and resolution. Linearity and quantification of changes, like in gene expression assays and sequencing, severely matters. Dependency on the dimension of biosensor, alongside its change measurement method, is a key on these performance parameters and a bottleneck for massively parallel operation. Table 2.1 gives a comparison of the discussed methods.

Among the described methods, charge-based methods and in particular pH-based/ISFET-based detections gained considerable attention for CMOS compatibility. In comparison to RedOx and impedance spectroscopy techniques, ISFET-based detection can satisfy almost all the requirements mentioned. In the first two groups, the precision is dependent on the size of the electrodes which already requires a modified fabrication process to develop the electrodes. The signal is not directly generated and a sweep of voltage/current or frequency is required, as well as recording the signal for processing and extracting the parameters with a computation burden. Such implications in small-scale genotyping may not seem competitive but in sequencing it further complicates the analysis. Moreover, immobilisation needs a high precision instrumentation to deposit probes/primers and function the surface adding to the preparation steps and cost. It may limit the lifetime for pre-made cartridges for degradation over time, and challenge storage and miniaturisation for possibility of evaporation and loss of incubated reagents [87]. Additional study on biosensor systems in CMOS processes can be found in [13, 88]. Overall, the ISFET-based technology has proved to be promising and has been commercialised both for sequencing and point-of-care genotyping. Chapter 3 describes their operations in detail and the following chapters study further on ISFET performance and propose new readout configurations for potential enhancement. Nonetheless, described in the last section, nanopore sequencing, may be a competitor technology, but besides customised fabrication and complexity of developing the nanopore structure, accuracy has remained an unresolved challenge.

Table 2.1.: Summary of fully-electronic methods.

Method	Pros/Cons	Ref
RedOx	- Complex readout - Electrochemical label required - LoD and resolution depend on the electrode size - Not scalable for very large-scale integration - Requires immobilization - Only detects hybridization of matching strands - Expensive complex customized fabrication	[46, 49, 89] [47, 48]
Capacitive Measurement and Impedance Spectroscopy	- LoD and resolution depend on o electrode/pixel size o clock o supply voltage - not scalable for high integration level - Reference electrode place matters - Requires Immobilization - Only detects hybridization of matching strands - May be less susceptible to low-frequency noise	[52, 54, 56] [59, 60, 62] [53, 57, 58] [55, 61, 63]
DNA Intrinsic Negative Charge	- Some require immobilization -Only hybridization detection - Not scalable to large-scale integration -Signal depends on dimension - pH change may degrade the measurement - A reference counterpart is a must - Performance may degrade by going to lower supply and deeper submicron process	[64, 65, 67] [66, 68]
Pyrophosphate Charge	-Requires immobilization - May saturate - Limited sequence read length - Signal may be degraded by pH change	[77]
pH-based	- CMOS-compatible -Cost-effective -Scalable to large-scale integration -No immobilization is needed	[72, 75, 76] [73, 90, 91]
Nanopore	Single molecule detection -Scalable -Prone to errors -Modified fabrication	[28, 79]

2.9. Summary

This chapter started with a brief review on DNA and RNA as the principal codes instructing the cellular functions. Three main sets of test were described; sequencing, genotyping and gene expression analysis. They were primarily relying on optical detection which would make expensive instrumentation and running cost. Next generations optimising the performance for higher throughput were discussed, but still highly priced. Fully-electronic approaches that would eliminate the labelling and optical imaging have gained interest. There are several criteria for their practicality. Cost, robustness, accuracy, scalability, and simplicity are the high-level expectations. Breaking them down to the design constraints precision, processing time, memory and power are the main issues. The methods were compared especially for scalability and simplicity of readout, highlighted the potentials of using ion-sensitive transistors.

For a sequencing device, accuracy, throughput, speed and cost are the main concerns. The method of detection defines the complexity in development and preparation effort for enhancing the signal. In genotyping, ability to run amplification and detection simultaneously is key for a miniaturised set-up. Scaling in both cases allows parallel analysis and adding redundancy for accuracy. However, noise and diffusion may constrain the design.

pH-based detection for its compatibility with CMOS technology have been developed both for miniaturised portable genotyping, and for massively parallel sequencing. The next chapter will focus on the operation of these systems.

3. pH-based Genotyping and Sequencing

The detection of the release of hydrogen ions during DNA synthesis, using ion-sensitive transistors by Toumazou et al in 2001 [92] based the introduction of a new generation of sequencing and genotyping set-ups with semiconductor microchips at their heart.

CMOS[1] compatible ISFETs[2] replaced the CCD[3] cameras and eliminated the molecular labelling. The technology was scalable as for its semiconductor platform. Two sets of products, one focusing on genotyping at the point-of-care and one on sequencing massively parallel, have been introduced to the market. Chapter 2 reviewed the alternative approaches in this industry. At the point-of-care and for targeted gene analysis, having a low-cost user-friendly fast miniaturised lab-on-chip capable of running DNA amplification and detection was described as the desire. In sequencing, price and speed were the challenges for the $\$1,000$ genome. Here, the operation of the two products are explained.

The key to these systems is the increase of H^+ concentration and pH drop from the incorporation of matching nucleotides in the elongation of a hybridised marker strand on a template DNA strand. Using ion-sensitive transistor allows monitoring the synthesis process on a microchip.

$$DNA_{(n)} + dNTP \rightarrow DNA_{(n+1)} + PPi + H^+ \tag{3.1}$$

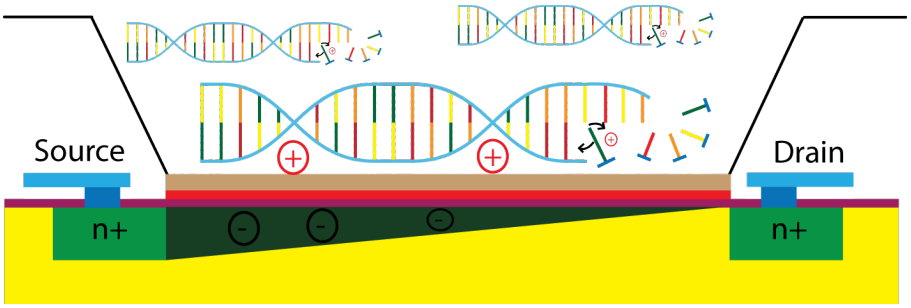

Figure 3.1.: Incorporation of a nucleotide to elongate a DNA strand causes release of a hydrogen ion. The ionic concentration change can be sensed by an ion-sensitive transistor in which the channel is accordingly modulated.

Figure 3.1 and Figure 3.2 give an overview of the concept. The ionic concentration change modulates the potential on the ISFET sensing membrane $V_{G'}$. This potential is a function of the biasing reference electrode V_{Ref}, and the electrode-electrolyte-insulator junctions V_{Chem}.

[1] Complementary Metal-Oxide-Semiconductor
[2] Ion-sensitive Field Effect Transistors
[3] Charge Coupled Device

V_{Chem} may also be divided into two terms of pH-sensitive (with a sensitivity of S_{pH}) and pH-independent (γ) parameters.

$$V_{G'} = V_{Ref} - V_{Chem} \tag{3.2a}$$

$$V_{Chem} = \gamma + S_{pH}.pH \tag{3.2b}$$

The pH-modulated signal is coupled onto the intrinsic floating gate (V_{FG}) of the transistor by a coupling factor $1/(1+\zeta)$. ζ is defined as the ratio of the total decoupling capacitance to the coupling capacitance, and it is a function of the ISFET geometry. Chapter 4 provides detailed explanation on the ISFET performance. The signal on the gate is conveyed by readout circuits to the next stages for processing, digital conversion, and transmission.

$$V_{FG} = \frac{V_{G'}}{1+\zeta} \tag{3.3}$$

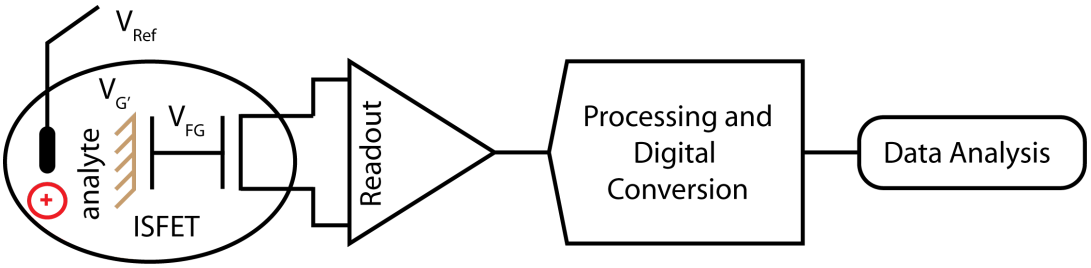

Figure 3.2.: An overview of the processing stages for pH-change detection.

3.1. ISFET-based Genotyping Lab-on-chip

DNA Electronics introduced the first CMOS lab-on-chip for electrochemical SNP detection [76]. The operation of this system is based on the detection of hydrogen ions released during the elongation of DNA strands using ion-sensitive transistors, as mentioned in section 2.8.3. The novelty of this work is in utilisation of CMOS microchips with no post-fabrication modifications. The ion-sensitive transistor uses the passivation layer of the microchip, which was intended for the protection of the chip, as its ion-sensitive membrane. Applying the scalable, mass-producible CMOS technology in such a set-up for nucleic acid test (NAT) applications, particularly genotyping, significantly reduces the costs of development, while allowing integration of processing systems along with the sensors on a single microchip. For sample preparation, a kit with a mechanical configuration extracts the DNA from saliva, and mixes the necessary enzymes and reagents, delivering a droplet on the microchip. Figure 3.3 shows Genalysis from DNA Electronics.

This section is predominantly developed based on [23, 75, 76, 90, 92, 93].

(a) Preparation kit and USB interface. (b) Microchip and cartridge.

Figure 3.3.: DNA Electronics' Genalysis preparation kit and disposable microchip cartridge. Pictures are the courtesy of DNA Electronics.

3.1.1. System Architecture

Figure 3.4 shows an overview of the DNA Electronics chip and its operation, and Figure 3.5 the system-on-chip (SoC) architecture. The $4.8mm \times 5.5mm$ chip contains 40 ISFETs and 10 temperature sensors each with a readout circuit, a low-pass filter ($G_m - C$ with f_{3dB} of 8), and a 2^{nd} order sigma-delta data converter with SNR[4] of $80dB$. The microchip is planted and wire-bonded onto a printed circuit board (PCB). An array of microfluidic chambers sits on top of the chip. Underneath each chamber is an ISFET allowing measurement of the electrochemical signals [76].

An on-chip control unit manages the operation of the system and transmission of data via serial peripheral interface bus. Resistive heaters with the temperature sensors (10 distributed differential PTAT-CTAT[5]) in a closed-loop configuration set the temperature with $0.5°C$ accuracy and in chamber precision of $0.1°C$. Controlling the temperature enables running DNA amplification (replication) on the microchip while monitoring the progress using the ISFETs [76].

3.1.2. Amplification

The system can run thermo-cycling for PCR[6], or fix the temperature for isothermal DNA amplification. To distinguish it from the conventional optical methods, the former is called pH-PCR, and an example of the latter is called pH-LAMP (loop-mediated isothermal amplification) [90][7]. For a standard two-temperature ($95°C$ and $66°C$) PCR, the system can be programmed to have active heating with resistive elements and passive cooling with $3°C/s$ rate, making 40 cycles in 35 minutes. The isothermal method runs faster giving a total genotyping time of 30 minutes from saliva sample to result. The amplification in a chamber is done in the presence

[4]Signal to noise ratio
[5]Proportional to absolute temperature-complementary to absolute temperature
[6]Polymerase Chain Reaction
[7]The amplification methods are reviewed in Chapter 2 section 2.2.

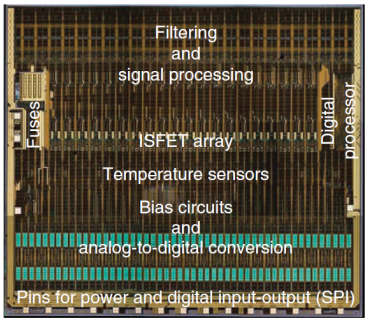

(a) DNA Electronics microchip.

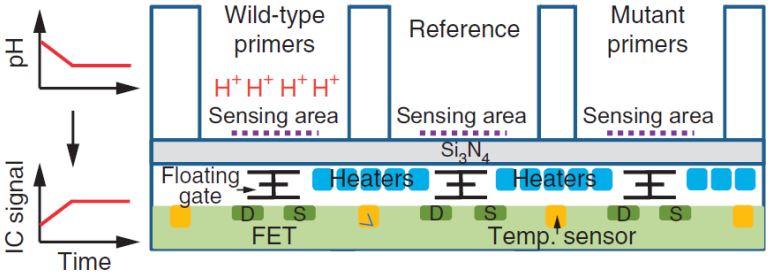

(b) Amplification takes place in micro-chambers on the chip. In addition to chambers testing for wild-type and mutant, a reference with no reaction is considered.

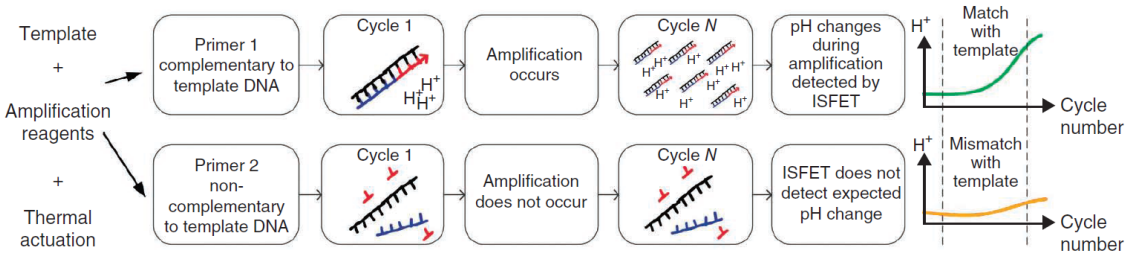

(c) Operation overview.

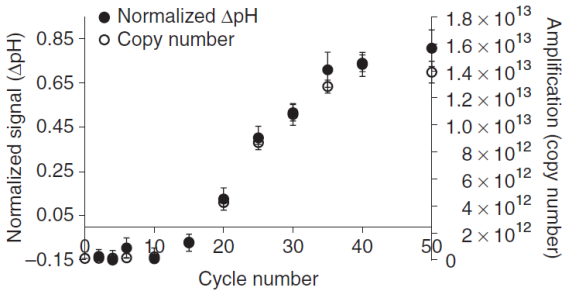

(d) Amplification cycle number and pH change example.

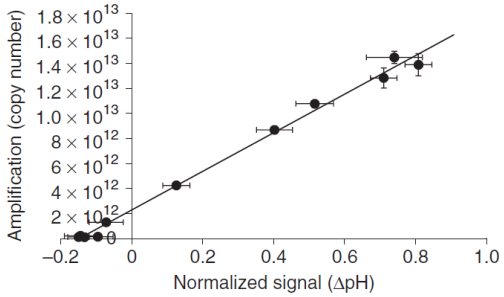

(e) Amplification copy number and pH change example.

Figure 3.4.: DNA Electronics microchip operation overview for simultaneous amplification and detection [90].

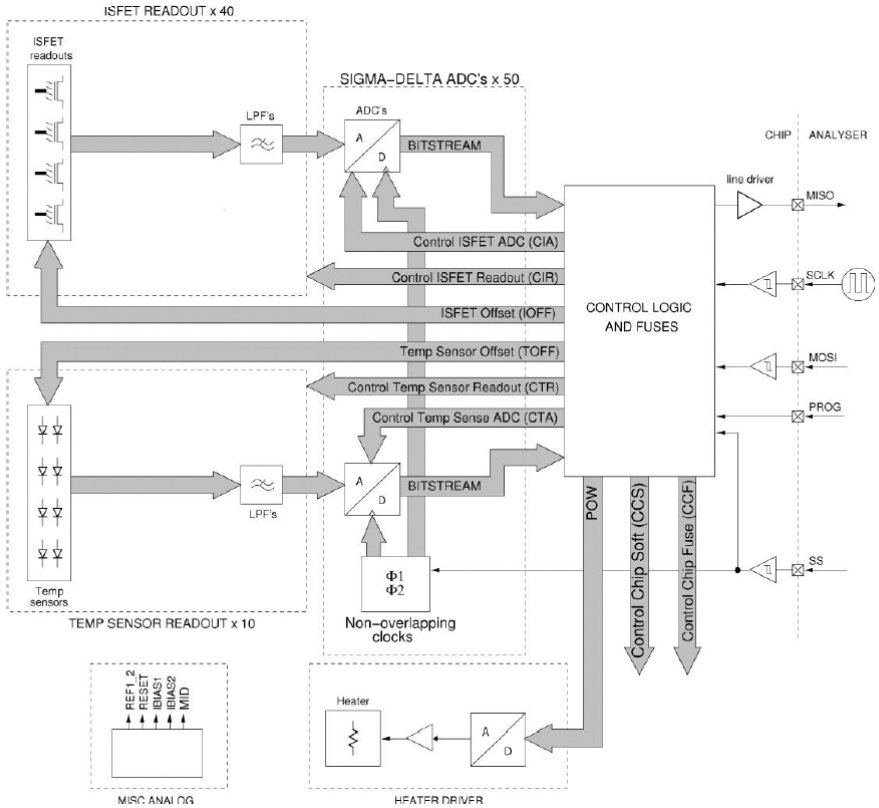

Figure 3.5.: DNA Electronics SoC overview for ISFET-based SNP detection [76].

of $dNTP$s and enzymes like polymerase, only if the primer/probe DNA matches the extracted template DNA.

3.1.3. Differential Measurement

Instead of fluorescence signals, the ISFET's readout voltage change, representing the pH change, is evaluated for the progress of amplification and quantification of the copies. To overcome non-idealities in the signals, like electrochemical disturbances, fabrication variabilities, temperature dependencies, and sensor drifts, a reference chamber is considered. The reference chamber undergoes the same procedure as others, but intentionally there is no matching primer to cause synthesis and amplification. Differentiating out its signal from the other chambers improves the measurement accuracy by removing common noise. Figure 3.4b shows one reference chamber where no reaction can take place in order to eliminate the common noise, and two chambers one testing for a wild-type mutation and the other for a mutant.

3.1.4. Integration Limits

The advantages of this platform are numerous particularly in bringing this technology into the hands of consumers as well as scientists[8]. However, there is place for optimisation in the

[8]More details on its advantages are discussed in Chapter 1.

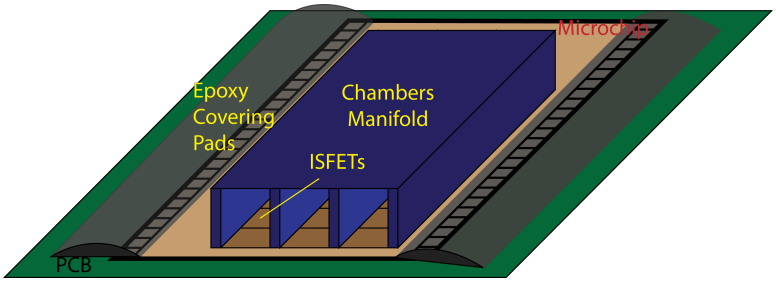

Figure 3.6.: Microfluidic chambers manifold sitting on top of a microchip. This is only an overview, not a particular design and not in scale.

recent primary works and there are non-negligible issues that require further investigations, improvements and compromises. Some of the aspects to consider are:

Non-linearity On the chemistry and molecular side, the buffering characteristic of the analyte and reversibility of the reactions can limit the dynamic range for the detection of all of the generated H^+ ions. Chapter 4 explains that the voltage signal on the ISFET, as well as the sensitivity, are a linear function of $pH = -log[H^+]$ which makes a non-linear relation between the released ions and the equivalent voltage change, particularly in a wide range.

Temperature Raising the temperature not only increases the molecular kinetics in the analyte and may affect the reactions, but also directly influences the sensitivity of the ISFETs. Change of temperature may add error in measuring the signal, also by increasing the thermal noise both in the analyte and the circuits.

Cross-hybridisation Specificity of the primer/probe DNA, especially influenced by its length, is quite important to ensure that only the target segments are amplified. However, alike microarrays and conventional PCR, there is a chance of hybridisation or partial hybridisation of the primer/probe to a wrong fragment [33, 83]. Amplification of cross-hybridised targets adds noise and reduces the signal.

Density of Chambers On the microfluidic aspect, the size of the chambers asks for a compromise. Not only for the number of chambers in a certain area, but also in the amount of reagents required. On the other hand, ISFETs need to be located away from the microchip pads/terminals to avoid the possible effect of the spread of the insulator (for example epoxy) that covers the pads and wire-bonds on the microchip. Otherwise, the insulator may cover the sensing membrane. Moreover, there should be proper spacing for the microfluidic chambers positioning on top. Figure 3.6 gives an overview of the configuration.

ISFET ISFET's signal coupling efficiency and susceptibility to process variations in the sensing membrane/passivation, is defined by its geometry. Increase in parasitics can degrade the signal amplitude received on the circuits. Detailed analysis is provided in Chapter 4. Moreover, ISFET's bias is dependent on the reference electrode, implementation of which is also a concern.

In addition to the geometrical effects, scalability for increasing the capacity of the microchip is another figure of merit to consider. Multiplexing for the processing unit components, like sharing the ADCs and filters, might be the first thing to note for optimisation from the system overview in Figure 3.5. However, it depends on the application and space limitations imposed by the microfluidic chambers dimensions.

Large chambers may allow integration of the ISFET interface, processing, and converters within their corresponding sensors pitches/gaps. But, smaller chambers for higher density may demand separation of ISFETs and processing, or development of new space-efficient circuits. Noise of the interface circuits, limit of detection, resolution of conversion and dynamic range of the data are the other parameters affecting memory and power. Relatively small dynamic range (about $1pH$ with sensitivity of about $60mV/pH$ ideally at room temperature) means the signal may change in a few of the less significant bits, not requiring large words. On the other hand, the uncertainty on the ISFETs offset might necessitate the maximum possible range and result in such long digital words, demanding large memory. Readout circuits with analogue and digital outputs trying to tackle the resolution, dynamic range, and temperature influence are proposed in chapters 5 and 6.

3.2. ISFET-based Sequencing Machine

The advent of ISFET in genotyping for monitoring the release of hydrogen ions as a side product of DNA elongation, also opened the door for the implementation of a next generation sequencing (NGS) machine with fully-electronic detection.

Ion-Torrent[9] applies the same concept and technology as DNA Electronics but for developing massively parallel sequencing (MPS) systems. The microchip is likewise the key player and advantage, but not in a portable fashion, rather in a $30kg$ desktop machine[10]. In comparison with the previous optical methods, it takes a similar approach to 454, sequencing by synthesis. However, the detection of incorporation is direct and electrochemical since the assay is integrated on the microchip. Whereas in 454, scientific high-resolution CCD cameras were used to detect the optical signals from the fiber-optic micro-wells.

The procedure is similar to the other sequencing systems starting with DNA sample extraction and preparation, running the operation and detection, and then processing the recorded signals for base-calling and alignment/assembly[11]. A control unit manages the system functions.

This section is predominantly developed based on [9, 91, 94–97].

3.2.1. Preparation

The first step is fragmentation of sample DNA. The fragments are ligated to adapters and amplified to provide enough copies. The amplified strands are bound onto template carrying

[9]Part of Life Technologies branding the ISFET-based sequencing machines. Life Technologies was acquired by Thermo Fisher in February 2014.
[10]Weight from the product specifications on the company's official website
[11]The main procedure is explained in Chapter 2 section 2.3

Figure 3.7.: Ion-Torrent Personal Genome sequencing machine. Picture from www.lifetechnologies.com.

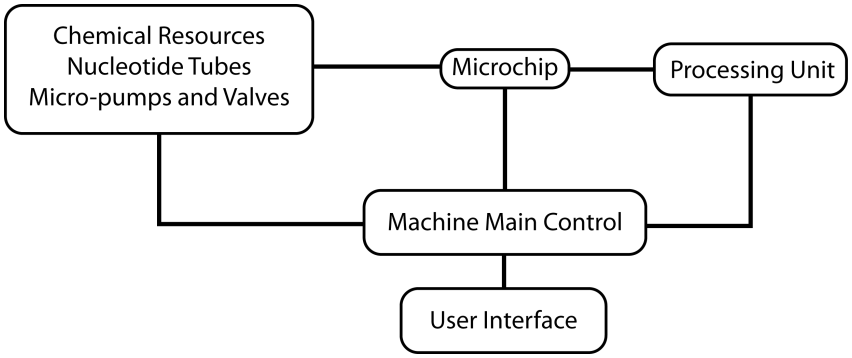

Figure 3.8.: Ion-sequencing system overview.

microbeads. On each bead, the bound template is clonally amplified using emulsion PCR so that enough copies generate a proper signal during synthesis and nucleotide incorporation. The strands on the beads are primed for synthesis. The beads are then loaded on the microchip.

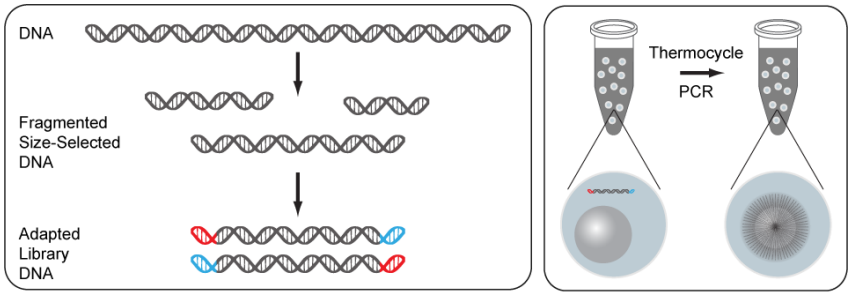

Figure 3.9.: In preparation, sample DNA is fragmented. Each fragment is attached to adapters to bind onto a bead. The template on the bead is clonally amplified [91].

3.2.2. The Microchip

Figure 3.10 shows the sequencing microchip published in [91]. The microchip consists of a large-scale array of ISFETs and interface circuits transferring the digitally converted signals to the computation and processing units. On top of the chip, an array of micro-wells ($3.5\mu m$ diameter in [91]) is implemented with assigning each well with an ISFET. The passivation on the microchip is etched away and replaced by an ion-sensitive membrane (Ta_2O_5 for better performance in pH sensitivity) for the ISFETs. The micro-wells are created by an insulator with a depth ($3\mu m$ in [91]) that can contain only one bead. Similar to the ISFET-based genotyping microchip, the sensing array is implemented at the central part of the microchip.

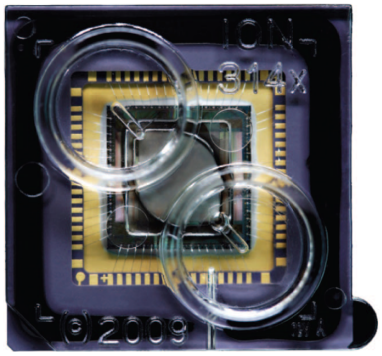

(a) Microchip packaged with fluid inlet and outlet [91].

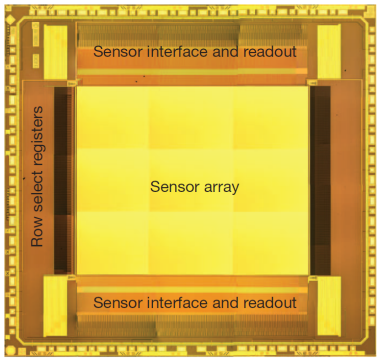

(b) Microchip sections [91].

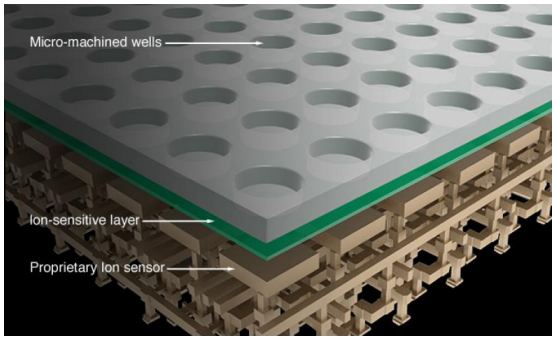

(c) A 3D cross-section overview of the microchip from www.lifetechnologies.com.

Figure 3.10.: Ion-sequencing microchip and its cross-sectional schematic.

3.2.3. Operation

The enriched template-carrying microbeads are loaded onto wells using a centrifuge unit. Nucleotides are flown onto the chip one at a time, with wash steps (by apyrase) in between to remove any leftover nucleotides from the previous step. The reagents get into the wells by diffusion and convection. If the nucleotide matches the template base immediate after the end of the primer, it incorporates and extends the second strand on the template. The incorporation results in H^+ release that may be detected by the ISFET. The amplitude of the signal is

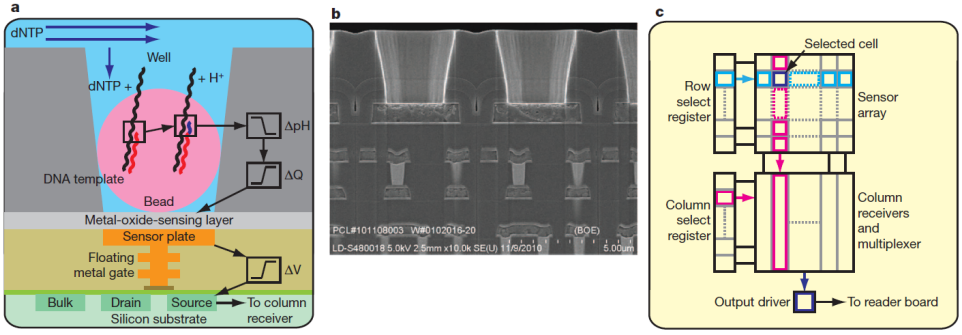

(a) Ion-Torrent system overview for ISFET-based DNA sequencing [91]. (a) is the schematic of well and bead on top of the ISFET. (b) shows an electron micrograph of the well and the ISFET beneath it. (c) displays the array overview.

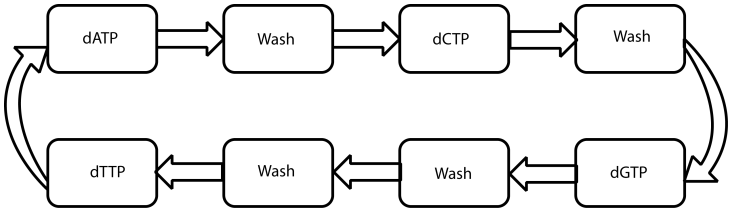

(b) One nucleotide at a time is flown onto the chip for synthesis and elongation of the primer strand. A wash step in between each nucleotide flow removes any leftover from previous step.

Figure 3.11.: Ion-sequencing operation overview.

a function of the concentration change (ideally proportional to $pH = -log[H^+]$). Therefore, according to the amplitude of the change in the signal, one can tell if the DNA elongation was only for one base or multiple (repetitive) bases. In case of multiple base incorporation, homo-polymerisation, a greater change in the signal is seen. The washing step reduces the chance of wrong homo-polymerisation detection by removing the previously flown-in nucleotide and ensuring that only the recent nucleotide can incorporate in the well.

3.2.4. H^+ Signal

Figure 3.12a shows the series of reactions involved in the elongation of a primer on a template DNA. Nucleotide incorporation time is in milliseconds ($3ms$ [74]), and the rate and amplitude of the change is defined by the reaction constants.

The signal on the ISFET is influenced by several parameters like

Microbead Size The microbead carries the template. The larger it is the more templates it contains and so more hydrogen ions are produced from the incorporations. The number of templates it can carry is proportional to the surface area of the microbead. For the first generation of the sequencing machine, the $2\mu m$ diameter acrylamide microbead would carry $800,000$ templates resulting in SNR[12] of $10dB$.

[12]Signal-to-noise Ratio. The SNR 10 according to the supplementary information of [91] is after primary processing of the signal

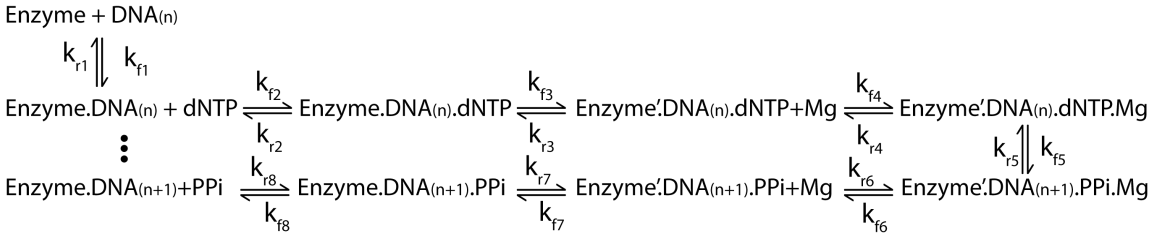

(a) A series of reactions takes place for the synthesis and elongation of the strand for one nucleotide. The enzymes catalyse the reactions [98].

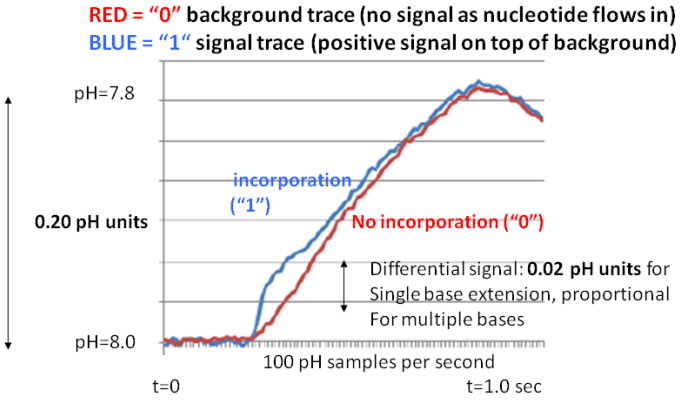

(b) An example of signals sensed by the ISFET, one in case of incorporation and one with no incorporation. The difference is used for base-calling [9].

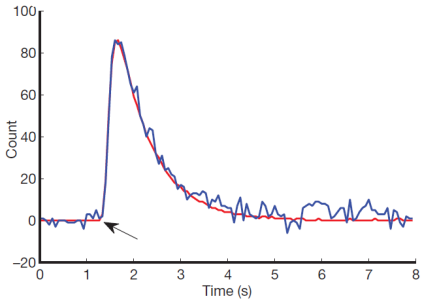

(c) An example of the incorporation signal after differentiation and normalisation, having a signal model fit to it [9].

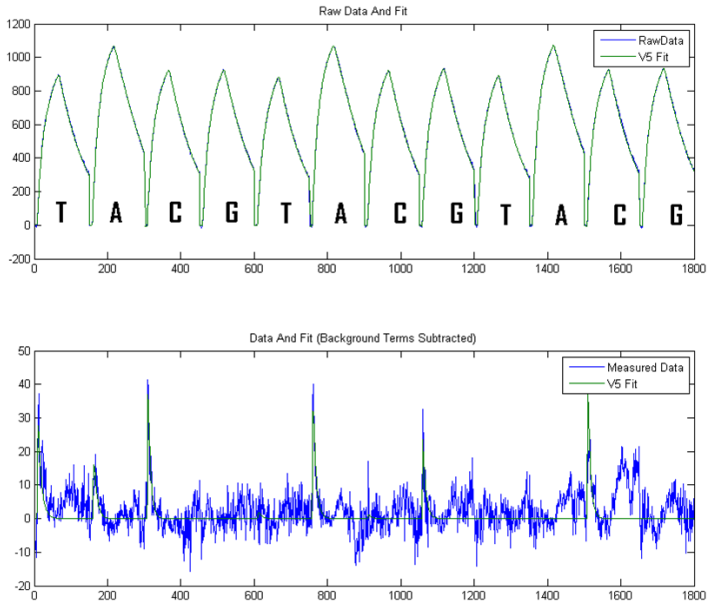

(d) An example of the incorporation signal detection in series, when in 12 consequent nucleotide flows only 5 cause incorporation. The upper figure is the signal dominated by the background change, and the bottom figure is the differentiated and model-fitted signal [9].

Figure 3.12.: Ion-sequencing ISFET signal and base-calling.

Micro-well Geometry The volume of the well needs to be large enough to contain a microbead, and provide enough space for the diffusion of the reagents and modulation of the concentration signal on the ISFET. But it has to be small enough to not allow any more beads in, and to let the generated ions, that are proportional to the number of templates involved in the incorporation, make a detectable change in the concentration. The slope of the walls also need to be optimum to ease the flow of reagents and beads, but not too gradual to replace the microbeads by the flow.

Diffusion The ions' diffusion out of the wells limits the window of detection of incorporation. Its diffusion into and from neighbouring wells creates a chemical crosstalk, and adds to the background noise signal. The rate of diffusion is dependent on the electrolyte but the time depends on the size of the well and the pitch of the pixels. The smaller they are, the quicker the ions are missed.

ISFET and Array Geometry ISFET is a non-Faradaic sensor operating based on the coupling of charge/potential of its sensing membrane. This coupling causes an attenuation of signal by decoupling and parasitics. Chapter 4 investigates how the ISFET structure from the sensing membrane to its inherent FET can be optimised. Moreover, a cross-coupling among the ISFETs can cause an electrical cross-talk in the measurements. Certainly a key factor in this on-chip chemistry-electronic interface is the sensing membrane sensitivity. The factors defining the sensitivity and a list of pH sensitive insulators[13] compatible with CMOS technology are provided in Chapter 4.

Noise Any disturbances, either mechanically, chemically, thermally, or electrically can imply an error in the measurement of the H^+ concentration. It may be from the motion of the fluid, diffusion of H^+ ions, or the activity of other ionic ingredients like the pyrophosphate negative charge, or the Mg^{2+} catalyst. The noise in the interface circuits needs to be minimum, and the reference electrode biasing the bulk analyte and the ISFETs needs to be stable.

On the other hand, the signal sensed by the ISFET, from voltage point-of-view, is proportional to the change in pH, which is a logarithmic function of the concentration. Therefore, the released H^+ ions may have a higher equivalent potential change when the initial value is more basic than acidic[14]. Ahn et al recommend a pH of 9 [99].

3.2.5. Pixel Configuration

The number of transistors and the shape of the pixel may affect the pitch and the integration level/density of the sensors. Three-transistor square-shape pixels and two-transistor hexagonal pixels have been published, with the latter reported to give a smaller pitch. One-transistor configuration has also been patented [100]. In the one-transistor design, rather than putting

[13]The insulator has to provide binding sites for the ions and so amorphous structures are advantageous.
[14]Chapter 4 explains that signal drift is more in higher pH values.

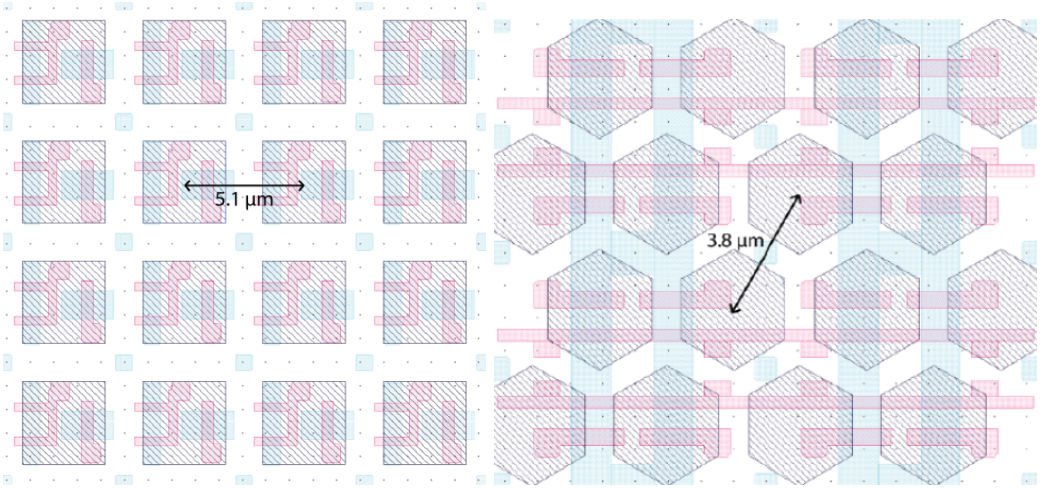

(a) Three-transistor square pixels. (b) Two-transistor hexagonal pixels.

Figure 3.13.: Ion-Torrent pixel shape and transistor in a $0.35\mu m$ process [91].

the select switch next to the ISFET in the pixel, the ISFETs share their drain and/or sources, and a single switch is used to address/select the ISFETs. The higher integration level might be at a cost of leakage currents from the terminal-sharing non-selected ISFETs. Moreover, since the H^+ signal is coupled onto the gate of the ISFET, there is attenuation in the signal which is dependent on the geometry of the pixel (ISFET).

3.2.6. Interface

The H^+ signal is coupled onto the floating gate of the ISFET. An interface circuit conveys this signal to the next stages of processing and digital conversion. For a large-scale array of micro-size ISFETs, the interface is shared with a subset of ISFETs, for example between the ISFETs of every column, while one row at a time is read. The complexity of the readout may define the area of the chip occupied by the interface circuit. In the first generation published work, it seems about 1/3 of the microchip; Figure 3.10b. In the next generations the yield on the chip further improved by minimising the interface circuit area and increasing the number of sensors/micro-wells.

3.2.7. Base-calling

The evanescence of the signal with the ions diffusion and drift, besides the background noise, gives a short window of detection, and entails complexity in processing and base-calling. Figure 3.12 shows an example of signals sensed by the ISFETs in such arrays. In this figure, signals are drawn for their equivalent pH change. The transient $0.02pH$ peak is almost $1mV$ on the ISFET, which indicates the need for high-resolution converters. The extraction of this signal requires differentiating out the pixel ISFET signal from a reference one. The reference pixel should be one that does not experience any incorporation. It may be a well with no microbead, or a well with a microbead that has not been enriched with templates. The process starts

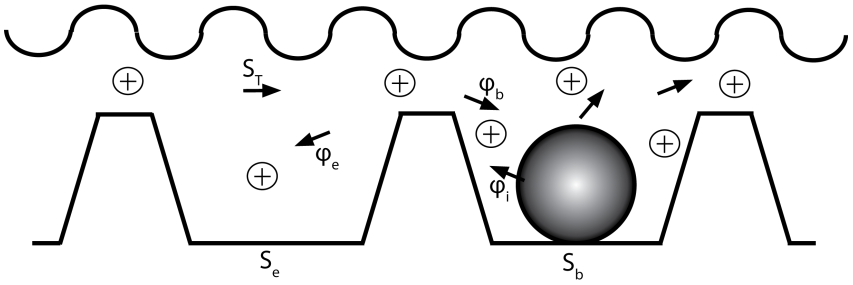

Figure 3.14.: Ions diffuse out of and into the wells. Picture redrawn according to [91, 97].

with short known key sequences from the adapters. Their detection helps in adjusting the fit parameters for the rest of the sequences. However, unless physically defined, it adds further computation burden to detect pixels that their signal power has been less in comparison with others and consider them as the reference in base-calling. For removing the common background noise/signal and developing reference pixels for the readouts, a configuration using the back-gate is suggested in Chapter 5.

Ion-Torrent models the H^+ generation and diffusion, and fits this model to the differentiated signal [91, 97]. Based on it, the incorporations and homo-polymerisations are extracted. In Figure 3.14 and equations 3.4, S_T is the background measured signal, S_b the measured signal from a bead-carrying well, and S_e the measured signal from an empty well. ϕ_b, ϕ_e and ϕ_i are the net flux of hydrogen ions respectively, between the bead-carrying well and background, between the empty well and background, and the ions generated from nucleotide incorporation. α_b and α_e are diffusion constants, and β_b and β_e are buffering capacities, similarly for the loaded and empty wells [15].

$$\phi_b = \frac{S_T - S_b}{\alpha_b} \tag{3.4a}$$

$$\frac{\delta S_b}{\delta t}\beta_b = \phi_b + \phi_i \tag{3.4b}$$

$$\frac{\delta S_b}{\delta t} = \frac{S_T - S_b}{\alpha_b \beta_b} + \frac{\phi_i}{\beta_b} \tag{3.4c}$$

$$\phi_e = \frac{S_T - S_e}{\alpha_e} = \frac{\delta S_e}{\delta t}\beta_e \tag{3.4d}$$

3.2.8. Alignments

After reading the sequences from each pixel/fragment, the sequences are aligned to build the whole genome, or may be processed for detection of mutations. The read length of base-calling is a key parameter in the accuracy of the analysis as well as the complexity of data processing. The longer the reads from the wells are, the easier is to find correlations and align short sequences.

[15] In the later patents more complete relations between the wells are derived to specifically calculate the actual signal based on individual neighbouring pixels [101].

3.2.9. Performance

The main goal is to have a sequencing machine generating the DNA sequence with a high accuracy, in a short time, and at a low cost[16]. The performance of the ion-sequencing machine is dependent on several factors requiring optimisation and compromise. One aspect is related to the yield and throughput in the generation of the incorporation signals, and another is the processing and computation for the extraction of information.

A high yield and throughput is achieved by optimisation on several aspects like

Bead Loading Maximising the number of templates and increasing the length of fragments, as well as selective collection of templated beads from the emulsion PCR can help in optimum enrichment of the beads on the chip.

Chip Loading Proper sizing and fitting of the beads and wells, helps increasing the number of loaded wells. On the other hand, empty wells across the chip are required to play as reference pixels in signal processing and base-calling, for removal of the background noise.

Sensor Count Increasing the number of sensors allows increasing the number of parallel sequencing fragments. However, it comes with a trade-off over area (which also defines the price of the microchip) and density, which consequently affects the loading, signal, noise, and diffusion.

Read Length In addition to making longer template fragments on the beads, enzyme activities from the chemistry side and base-calling algorithms from the signal processing side may determine the maximum number of bases can be called from a sample fragment.

Read Accuracy The quality of sequencing and base-calling is measured by comparing the read bases with a reference genome sequence. It is reported as the percentage of correct reads in a certain length of sequence from a well[17]. It is dependent on the base-calling performance in discriminating the measured signal from noise. A major issue is the detection of homo-polymerisations that are perceived to be proportional to the signal amplitude. Accuracy may be improved by increasing the signal-to-noise ratio from the sequencing chemistry and preparation step, upgrading and developing robust base-calling methods, and adding redundancy in sequencing to reduce the errors. Redundancy may be in the flow of nucleotides (by having XYX nucleotide orders instead of ACGT to reduce the effect of leftover nucleotide incorporations, aka dephasing), by re-sequencing with a different primer and flow order, or by sequencing in both directions of the template DNA by re-priming the templates from the other end.

Computation Data generated from the microchip is orders of magnitude more than the information acquired. The bottleneck of this computation burden (80% of the total computation

[16]Table 1.1 shows the latest pH-based sequencing machine in 2014 may have an average read length of 100 and generate 32G bases in about 2-4 hours.

[17]It is reported with a log scale of error. For example, $100AQ20$ means in the first 100 bases read, the error possibility is $10^{-20/10}\%$, or the aligned quality is 99%.

effort) is at the lowest level and at a high rate. Data is generated at about $30GB/s$ almost 1000 times the CCD imaging systems for the optical methods. A consequence is inability in storing the acquired raw data and need for immediate fast processing, using high-bandwidth pipelined computing units, to shrink the data load and then discarding it in seconds.

Nevertheless, compromises are inevitable and optimisations necessary. In preparation, although double amplification (one for library and one for bead templates) allows extraction from as low DNA amount as possible, it takes few hours (4 to 8 [8]). Enzymatic methods of fragmentation and amplification instead of physical techniques [8], as well as automation from sample preparation to chip loading [9], can improve the time to result. On the other hand, it is the SNR that has direct impact on the accuracy and computation burden. On the chemistry side it is the reagents concentration and supply, and on the measurement side is the sensor coupling efficiency with high-precision readouts and converters. Chapters 5 and 6 suggest potential circuit-level ideas as interface circuits improving resolution and/or processing. Chapter 4 explains the sensitivity and coupling efficiency of the ISFET as the building block of the measurement. Next section shows an abstract modelling of the nucleotide incorporation signal.

3.3. Nucleotide Incorporation Simulation

Figure 3.12a shows the reactions involved in the elongation of a DNA strand for one nucleotide [99, 102]. Dissociation constants (k) in both forward and reverse directions define the progress of the synthesis. Accordingly, production and consumption of each over time can be summarised in equations (3.5). DNA_n is the DNA strand of length n, to be extended for one nucleo-base with nucleotide $dNTP$, in the presence of polymerase enzyme Enz and Mg^{2+}, to make DNA_{n+1}. $Enza$ is the enzyme Enz activated in the incorporation, and PPi is the pyrophosphate released from the nucleotide incorporation. The H^+ generated is equivalent to the PPi [99]. Based on these equations and according to the Ion-Torrent base-calling method discussed in section 3.2.7, here an abstract simulation of the signal generation by the author is provided.

In the MATLAB environment, the equations of Figure 3.12a are solved as in equations 3.5 with iterative calculation of change in every minuscule time-step of $100\mu s$, with primary concentrations and dissociation constants summarised in Table 3.1. The code is provided in Appendix B. The change in every iteration is written as a function, which is used both to simulate single nucleotide incorporation, and to cascade for multiple incorporations (homo-polymerisation).

To emphasise the diffusion effect which mainly affects the sequencing microchips with micro-well arrays, the signal is emulated in two cases, one with no diffusion effect and loss of ions (as probably may be the scenario in genotyping microchips that use micro-chambers for isolation), and one with the diffusion of ions[18].

[18] A more accurate simulation would be accompanied by the diffusion and distribution of ions into the well/chamber along with Poisson-Boltzmann equations, taking into account the effect of all ions. Here a simplified version is implemented for time comparison over a burst change of the concentration in fraction of a second, and the gradual effect of diffusion dependent on the physics of the assay.

Table 3.1.: Incorporation reactions simulation parameters values.

$[DNA_n]$	1×10^{-6}	$[Enz]$	3×10^{-6}	$[dNTP]$	3×10^{-6}	$[Mg]$	3×10^{-6}
k_{f1}	1.2×10^{7}	k_{r1}	0.06	k_{f2}	1.25×10^{7}	k_{r2}	250
k_{f3}	50	k_{r3}	3	k_{f4}	9.5×10^{5}	k_{r4}	100
k_{f5}	150	k_{r5}	40	k_{f6}	100	k_{r6}	4
k_{f7}	4	k_{r7}	4	k_{f8}	60	k_{r8}	1.45×10^{4}

$$\frac{\delta[EnzDNA_n]}{\delta t} = k_{f1}[Enz][DNA_n] - k_{r1}[EnzDNA_n] \tag{3.5a}$$

$$\frac{\delta[DNA_n]}{\delta t} = k_{r1}[EnzDNA_n] - k_{f1}[Enz][DNA_n] \tag{3.5b}$$

$$\begin{aligned}\frac{\delta[Enz]}{\delta t} =& k_{r1}[EnzDNA_n] - k_{f1}[Enz][DNA_n] + \\ & k_{r2}[EnzDNA_n dNTP] - k_{f1}[EnzDNA_n][dNTP] + \\ & k_{r1}[EnzDNA_{n+1}] - k_{f1}[Enz][DNA_{n+1}]\end{aligned} \tag{3.5c}$$

$$\begin{aligned}\frac{\delta[EnzDNA_n dNTP]}{\delta t} =& k_{f2}[EnzDNA_n][dNTP] - k_{r2}[EnzDNA_n dNTP] + \\ & k_{r3}[EnzaDNA_n dNTP] - k_{f2}[EnzDNA_n dNTP]\end{aligned} \tag{3.5d}$$

$$\frac{\delta[dNTP]}{\delta t} = k_{r2}[EnzDNA_n dNTP] - k_{f2}[EnzDNA_n][dNTP] \tag{3.5e}$$

$$\begin{aligned}\frac{\delta[EnzaDNA_n dNTP]}{\delta t} =& k_{f3}[EnzDNA_n dNTP] - k_{r3}[EnzaDNA_n dNTP] + \\ & k_{r4}[EnzaDNA_n dNTPMg] - k_{f4}[EnzaDNA_n dNTP][Mg]\end{aligned} \tag{3.5f}$$

$$\begin{aligned}\frac{\delta[Mg]}{\delta t} =& k_{r4}[EnzaDNA_n dNTPMg] - k_{f4}[EnzaDNA_n dNTP][Mg] + \\ & k_{f6}[EnzaDNA_{n+1} PPiMg] - k_{r6}[Mg][EnzaDNA_{n+1} PPi]\end{aligned} \tag{3.5g}$$

$$\begin{aligned}\frac{\delta[EnzaDNA_n dNTPMg]}{\delta t} =& k_{f4}[EnzaDNA_n dNTP][Mg] - k_{r4}[EnzaDNA_n dNTPMg] + \\ & k_{r5}[EnzaDNA_{n+1} PPiMg] - k_{f5}[EnzaDNA_n dNTPMg]\end{aligned} \tag{3.5h}$$

$$\begin{aligned}\frac{\delta[EnzaDNA_{n+1} PPiMg]}{\delta t} =& k_{f5}[EnzaDNAndNTPMg] - k_{r5}[EnzaDNA_{n+1} PPiMg] + \\ & k_{r6}[EnzaDNA_{n+1} PPi][Mg] - k_{f6}[EnzaDNA_{n+1} PPiMg]\end{aligned} \tag{3.5i}$$

$$\begin{aligned}\frac{\delta[EnzaDNA_{n+1} PPi]}{\delta t} =& k_{f6}[EnzaDNA_{n+1} PPiMg] - k_{r6}[Mg][EnzaDNA_{n+1} PPi] + \\ & k_{r7}[EnzDNA_{n+1} PPi] - k_{f7}[EnzaDNA_{n+1} PPi]\end{aligned} \tag{3.5j}$$

$$\begin{aligned}\frac{\delta[EnzDNA_{n+1} PPi]}{\delta t} =& k_{f7}[EnzaDNA_{n+1} PPi] - k_{r7}[EnzDNA_{n+1} PPi] + \\ & k_{r8}[EnzDNA_{n+1}][PPi] - k_{f8}[EnzDNA_{n+1} PPi]\end{aligned} \tag{3.5k}$$

$$\frac{\delta[PPi]}{\delta t} = k_{f8}[EnzDNA_{n+1} PPi] - k_{r8}[EnzDNA_{n+1}][PPi] \tag{3.5l}$$

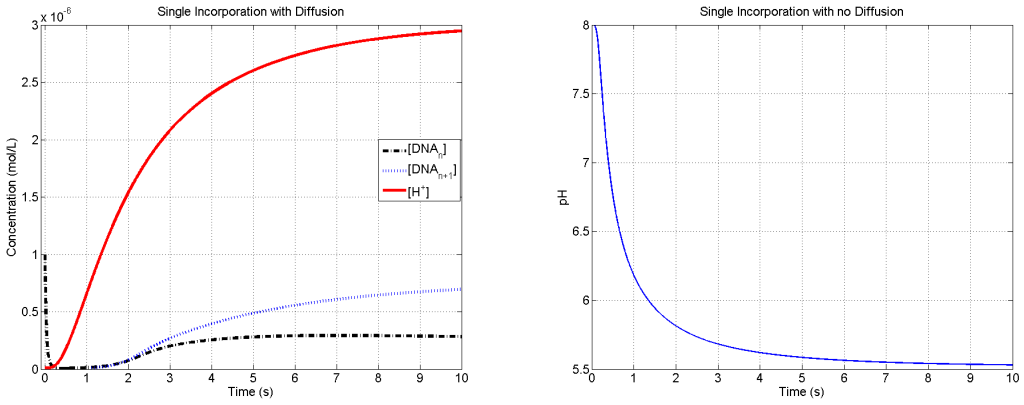

(a) Concentration change. (b) pH change.

Figure 3.15.: Single incorporation simulation with no diffusion.

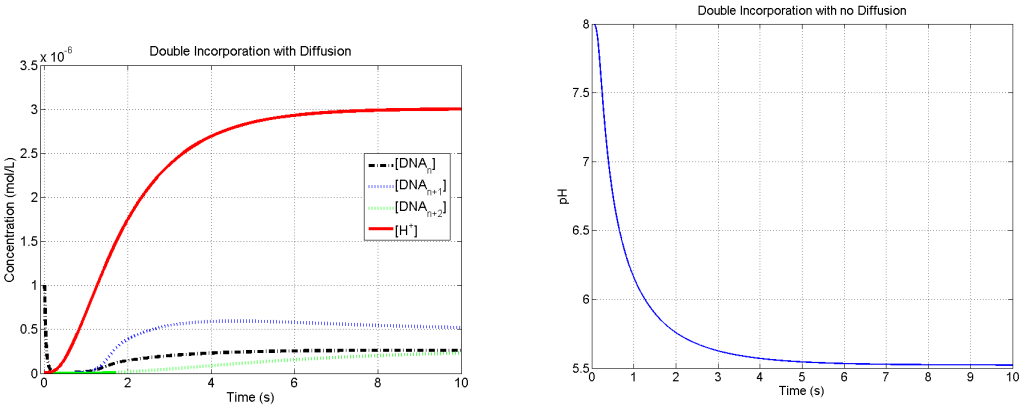

(a) Concentration change. (b) pH change.

Figure 3.16.: Double incorporation simulation with no diffusion.

$$\frac{\delta[EnzDNA_{n+1}]}{\delta t} = k_{f8}[EnzDNA_{n+1}PPi] - k_{r8}[EnzDNA_{n+1}][PPi] + k_{f1}[Enz][DNA_{n+1}] - k_{r1}[EnzDNA_{n+1}] \quad (3.5m)$$

$$\frac{\delta[DNA_{n+1}]}{\delta t} = k_{r1}[EnzDNA_{n+1}] - k_{f1}[Enz][DNA_{n+1}] \quad (3.5n)$$

3.3.1. Without Diffusion Loss

With no diffusion or loss of the ions, the signal is monotonic, with a faster change at the beginning, and makes the maximum concentration change eventually. Figure 3.15 shows the change for a single incorporation in the concentration and pH. In case of multiple incorporations, for example double-incorporation in Figure 3.16, the produced H^+ is slightly more and so the DNA_n consumed.

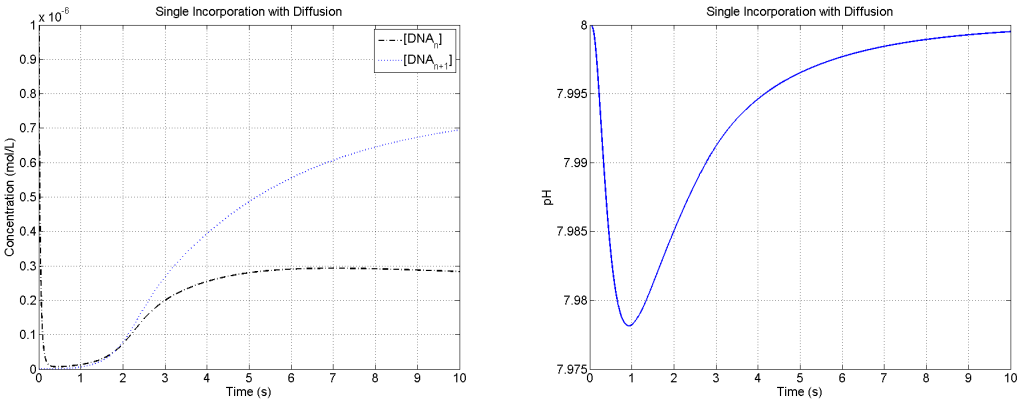

(a) Concentration change.

(b) pH change.

Figure 3.17.: Single incorporation simulation with diffusion.

3.3.2. With Diffusion Loss

Diffusion causes loss of the signal and so a non-monotonic change. Taking a similar approach to section 3.2.7 assuming that the background signal, the concentration of the bulk analyte on top of the micro-wells, remains constant at pH_0 ($pH_0 = -log[H_0^+]$), the ion concentration change can be calculated by

$$\frac{\delta[H^+]}{\delta t} = \frac{H_0^+ - H^+}{\alpha\beta} + \frac{1}{\beta}H_i^+ \tag{3.6}$$

α represents the diffusion effect and β the buffering capacity of the micro-well. $\alpha\beta$ appears like a time constant for the exchange of ions between the micro-well and the background analyte, dependent on the physics of the microchip design.

Two scenarios are considered all assuming that ideally all the H^+ generated remains and is not absorbed, $\beta = 1$, and $\alpha = 5$ making a 20% fraction of the concentration difference be exchanged[19]. In one scenario, instant flow of reagents is considered, and in the other, a $1s$ flow of nucleotide, enzyme, and Mg^{2+} as if their concentration remains constant at the first second of operation. In the former case the difference between the pH changes of single and double incorporation are less.

Change in the shape of the signal in result of scaling is simulated in Figure 3.21, with a larger α resulting in less diffusion effect and wider bells, and a smaller α with narrower ones.

3.4. Scaling

In sequencing, besides increasing the read length and loading yield, one way to improve the throughput is scaling to have more pixels (micro-wells/ISFETs) on the chip. A higher integration level can be achieved by extending the microchip area, reducing the interface circuits

[19]These numbers are selected only for illustration and emphasis of diffusion effect, resulting in the need for a model-fitting approach for base-calling.

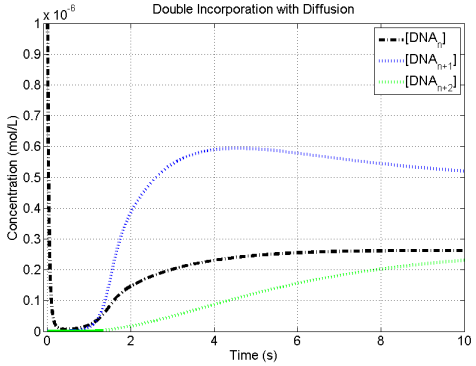

(a) Concentration change.

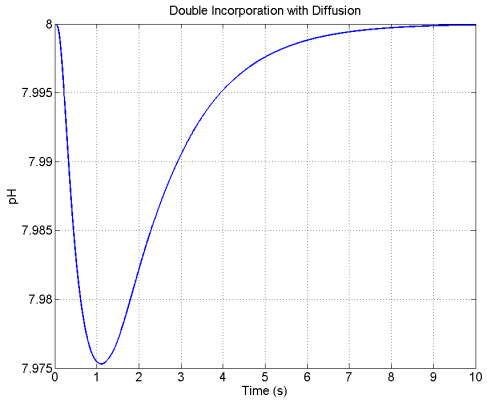

(b) pH change.

Figure 3.18.: Double incorporation simulation with diffusion.

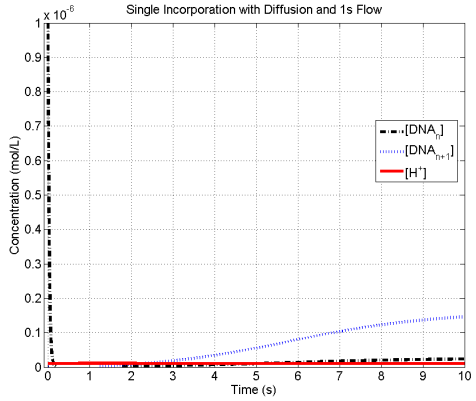

(a) Concentration change.

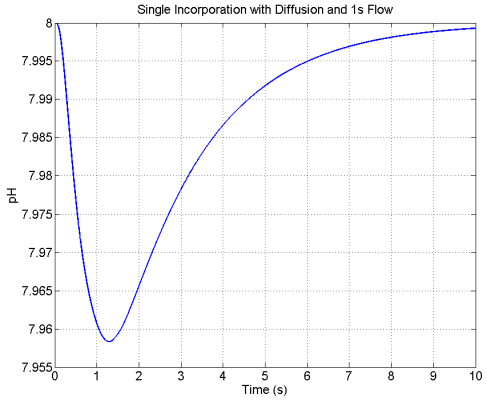

(b) pH change.

Figure 3.19.: Single incorporation simulation with diffusion and 1s flow.

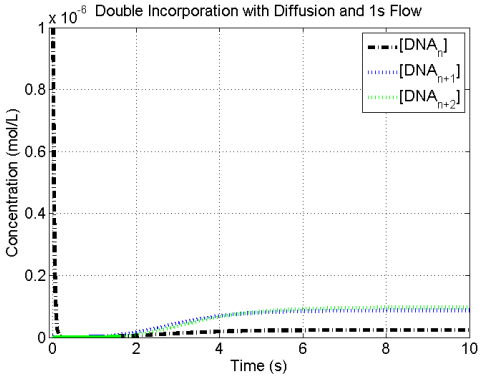

(a) Concentration change.

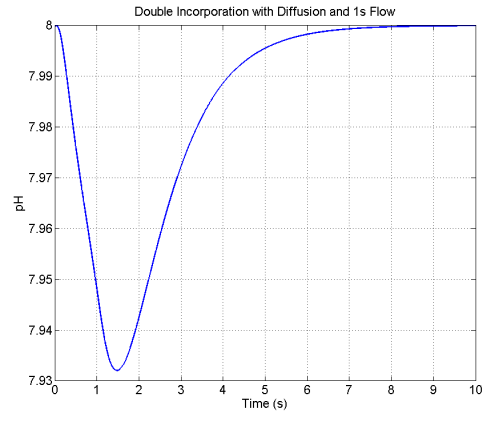

(b) pH change.

Figure 3.20.: Double incorporation simulation with diffusion and 1s flow.

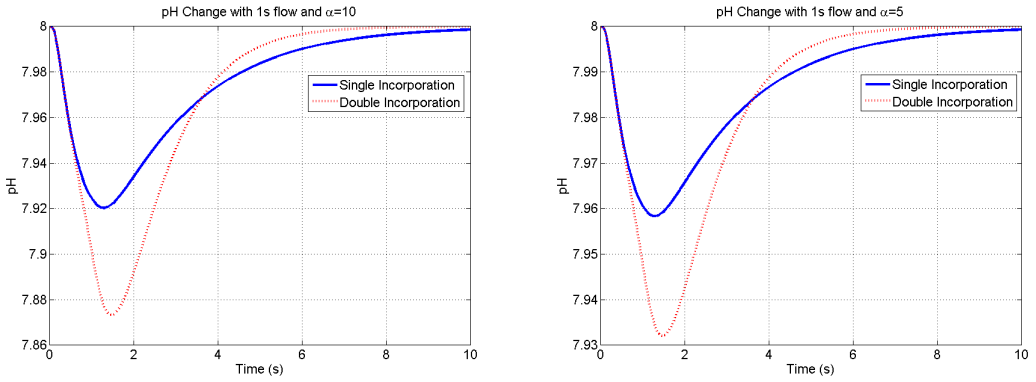

(a) $\alpha = 10$ equivalent to 10% of difference exchange.

(b) $\alpha = 5$ equivalent to 20% of difference exchange.

Figure 3.21.: Incorporation simulation with $1s$ flow for comparison of the diffusion loss factor effect.

and increasing the sensing area, designing with a smaller feature size, or a combination of them. However, the price of a chip is proportional to its area, and there is a limit of typically $25mm \times 35mm$ by the manufacturer. A bigger chip reduces the yield from a wafer for increased probability of defects ($Yield = e^{-AD}$, A is the chip area and D defect density [103]). Reducing the interface area requires more compact and optimised designs. The Readout circuits are discussed in chapters 5 and 6 with proposing new ideas. On the other hand, for smaller dimensions, the compromise is more complicated.

The signal generated is the change in ionic concentration which follows the chemical equations in Figure 3.12a. Go and Alam [104, 105] reported some simulations of the scaling effect on the incorporation signal. They considered that ions are generated in a burst and then distributed and diffused to reach equilibrium. They concluded that scaling would not affect the signal amplitude. However, with charge-based point of view, scaling down the microbead and the micro-well may result in a larger change. If the number of templates are proportional to the surface of the microbead, scaling with a factor κ reduces the number of incorporated ions down for $1/\kappa^2$ while the volume is reduced for $1/\kappa^3$, increasing the concentration change κ times. Moreover, it is the single-bead policy in micro-well that might question this comparison[20].

On the other hand, a higher density makes losing the signal to diffusion faster. With a diffusion constant D, the distance x traveled by a particle in time t is

$$x = \sqrt{2Dt} \tag{3.7}$$

For example [87], in a saline solution, the diffusion time over a $1pL$ cube of $10\mu m$ is $50ms$. Reducing the dimensions drops the diffusion time quadratically ($t = \frac{1}{2D}x^2$). Review on the next products of Ion-Torrent with smaller feature size shows that the signal gets narrower [9]; Figure 3.22. The latest products with hundreds of millions of micro-wells are specified with shorter

[20] In the presented simulations the scaling and dimension effects were summarised in parameter $\alpha\beta$. Scaling down for smaller dimensions resulting in quicker diffusion of ions makes the signal narrower.

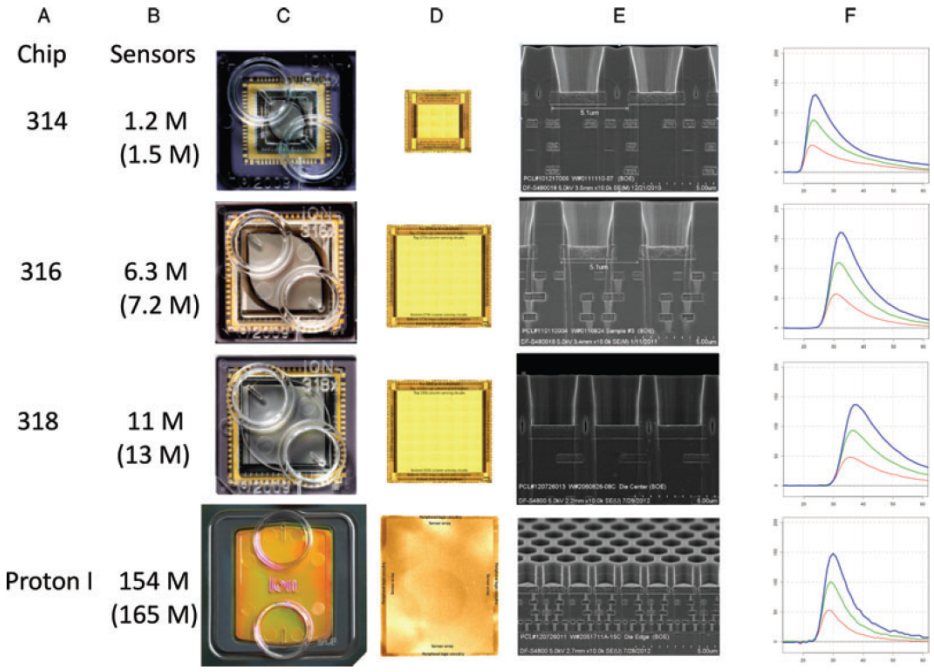

Figure 3.22.: Ion-Torrent scaling in sequencing microchips [9]. Column A is chip/product name, B number of sensors/wells on the chip, C image of the packaged chip, D relative size of the unpackaged cut die, E electron micro-graphs of sections through the sensor array, and F average incorporation signal from chip with $1-mer$, $2-mer$ and $3-mer$ incorporations.

read lengths (Table 1.1). Faster diffusion requires higher sampling rate. Higher sampling rate, while the number of pixels have also increased, means increase in data and required bandwidth, unless the data is reduced by compromising over the word lengths; for instance, reducing the analogue-to-digital converter dynamic range, or ignoring the transmission of the most significant bits as the signal change may not invert those bits.

While the perception might be that scaling does not affect the potentiometric sensors like ISFET (the signal dependent on the concentration and not dimension) [85], parasitic decoupling capacitances degrade the efficiency of coupling on these non-Faradaic sensors. Smaller sensing area increases the effect of decoupling capacitors and further attenuates the signal sensed on the gate of the intrinsic FET of the ISFETs. It is investigated in detail in Chapter 4.

In addition, the issue of scaling from the electronic side is the flicker noise. Reduction in the process feature size and thinner gate oxide, results in higher $1/f$ noise. The flicker noise power spectral density is calculated to be proportional to $1/L^3_{g(min)}$, where $L_{g(min)}$ is the minimum gate length or feature size [106–108]. Consequently, robust interfaces and signal processing techniques are required, especially as the supply shrinks when the feature size decreases.

3.5. Summary and Conclusion

Two state of the art ISFET-based systems, one for genotyping and one for sequencing were described. For point-of-care genotyping, implementing resistive[21] heating units enabling temperature control for DNA amplification, beside the ion-sensors in a commercial CMOS microchip, has been the unique advantage. For sequencing, the scalability of the system for MPS also allowed increasing the throughput and reduced the instrumentation cost to $\$80,000$ and lower in comparison with 6-digit-prices of the optical ones. However, the performance of both set-ups is limited by several physical and chemical factors.

In the genotyping SoC, temperature effect on the pH sensitivity requires further processing after reading and conversion of the signal. Its CMOS fabrication also brings the non-idealities of the passivation layer of the chip used as the sensing membrane[22]. The microfluidic structure on top of the chip may limit the scalability. On the other hand, the ISFETs geometry may also influence the efficiency of the signal coupling, increasing the limit of detection and reducing the accuracy.

Table 3.2.: pH-based DNA detection microchips comparison based on application.

	Genotyping	**Sequencing**
Number of parallel tests limited by	microfluidic chambers in dozens	pico-litre micro-wells scaling to hundreds of millions
Amplification	On chip	off-chip
Temperature control	On chip	off-chip
Window of detection	upto tens of minutes	evanecent, a fraction of a second
Sampling rate	relatively low	relatively high
Fabrication	unmodified CMOS	modified CMOS
Major noise	ISFET drift and temperature	diffusion and flux
Signal range	milli-volts	sub-milli-volts
Analyte loading	determined chambers	random bead deposition
Control reference	pre-defined => on-chip processing possible	unknown => massive off-chip processing
Operation set-up	hand held and portable	desktop-based

In sequencing the complexity increases in optimisation of the performance. Physics of the micro-well and chemistry of the operation were shown to influence the shape of the signal both in peak value and in width (detection window). Diffusion causes loss of the signal as well as interference, which complicates the processing for base-calling and requires higher sampling rates. Perhaps making the sampling flexible based on primary base-calling of the initial key sequences can help adjust the data rate. A simulation of the incorporation signal was provided. The signal from the reported works shows the significant impact of background noise requiring

[21] Perhaps an alternative would be microwave heating through dielectrics in the analyte as done for a lab-on-chip implementation [109].

[22] Perhaps once the economy of the production and market justify, modified process may be used for better measurement quality. This requires separate study that is not in the scope of this thesis.

differential measurement. One of the consequent fundamental concerns would be on the detection of homopolymers. In system level, the accuracy on the base-calling may be improved by taking approaches introduced in Chapter 2; for instance, using cyclic reversible termination to limit the incorporation to single bases as in the Illumina devices, or using oligonucleotides to reach longer reads besides adding redundancy as in the Applied Biosystems SOLiD. Hitachi Central labs proposed changing temperature for controlling the incorporation time [110]. A recent work by Geneapsys suggests measuring the temperature change in addition to the ionic concentration [111].

Nevertheless, the discussed microchips are the very first introduced and they need improvements at different levels for processing and scaling. Table3.2 summarises some of the requirements and specifications that each of the applications (genotyping or sequencing) may impose on the microchip design. Chapter 4 investigates on the ISFET limitations and methods of optimisation over its signal coupling. Chapters 5 and 6 propose new readouts.

4. ISFET Geometry

Piet Bergveld introduced the Ion-Sensitive Field Effect Transistor (ISFET) in 1970 [112] for neurophysiological measurements, combining a glass electrode and a MOSFET (Metal-Oxide-Semiconductor FET) to record ion activities based on two-electrode potential differences. Since then, there has been numerous works on improving the ISFETs performance as sensors, and introducing new materials sensitive to different ions, particularly H^+ to measure pH ($pH = -log[H^+]$)

Later on, their fabrication in commercial CMOS (complementary MOS) technology (Figure 4.1) opened the door for integrating these micro-electrochemical sensors with their readout circuitry and signal processing units. Using the passivation oxynitride (Figure 4.2) as the pH-sensitive material [113] allows manufacturing such intelligent set-ups in a scalable manner without any requirement for further post-fabrication alterations. ISFETs are attractive as they leverage the semiconductor technology for low cost, mass fabrication, and on-chip processing. However, there are some challenges on the way to their utilisation that ask for more robust designs. Here they are explained after briefly describing the principle behind the ISFETs operation. More complete formula is derived and a design methodology is described for suppressing the non-ideal behaviours. According to the experimental results highlighting the influence of decoupling parasitics, a new ISFET configuration is proposed.

4.1. ISFET Operation

The ISFET operation is usually explained with its MOSFET counterpart [114]. The difference is the way the signal is applied at the gate. For the ISFET, the gate of the intrinsic FET (the floating gate as there is no resistive path from it) gets its potential coupled from the surface of the sensitive membrane; which is modulated from the reference electrode (remote gate) through

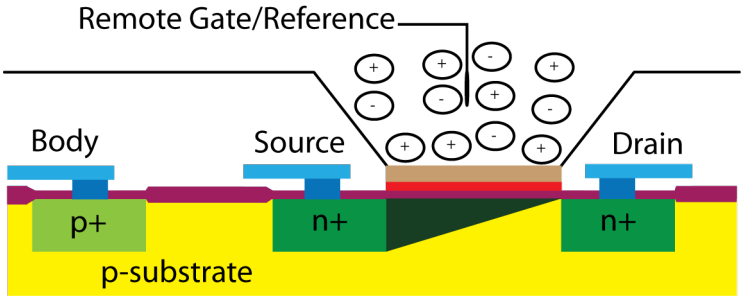

Figure 4.1.: ISFET is basically a MOSFET having its gate driven by charge coupling via an ion-sensitive insulator exposed to an electrolyte biased using a reference electrode.

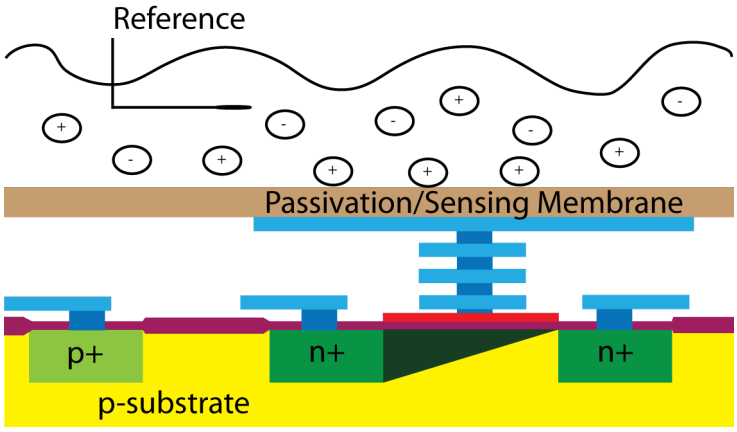

Figure 4.2.: ISFET in unmodified CMOS.

the electrolyte.

Many works have described the ionic interactions at the electrode-electrolyte-insulator junctions [115–121]. Here a summary of the operation of ISFET and its sensitivity is provided.

4.1.1. Electrolyte Potential Modulation

Figure 4.3 shows the potential distribution at an electrode-electrolyte-insulator interface. The voltage change from the reference electrode to the insulating sensing membrane is a function of the absolute electrode potential of the reference electrode E_{Ref}, liquid junction potential χ_{sol}, the electrolyte-insulator dipole potential χ_M, and the electrolyte-insulator potential ϕ_0. Among them, the latest is the only pH-dependent parameter and has been explained by site-binding and Gouy-Chapman-Stern double-layer theories [117]. Figure 4.3 illustrates the potential distribution.

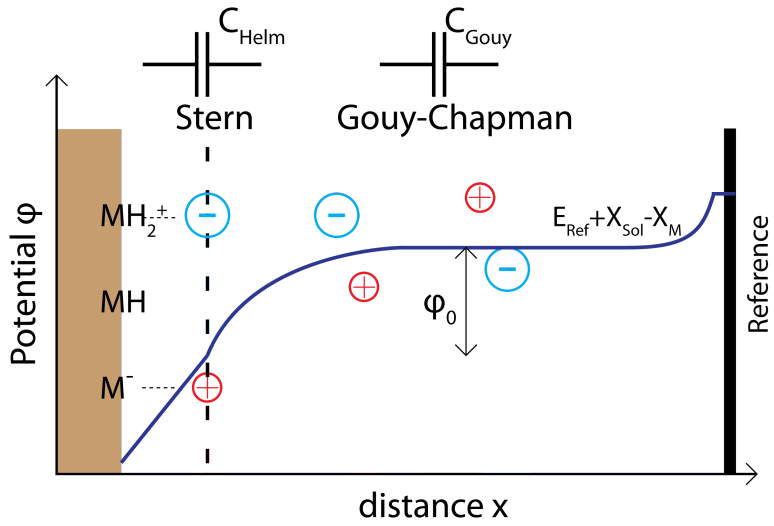

Figure 4.3.: Potential distribution across electrolyte-insulator modelled by Gouy-Chapman-Stern and site-binding theories.

Site-binding theory assumes discrete sites on the insulator at which the ions form a charge

layer. Representing the insulating membrane by M, the association and dissociation reactions may be written as

$$\mathrm{MH} \rightleftharpoons \mathrm{M^-} + \mathrm{H_B^+} \tag{4.1a}$$
$$\mathrm{MH_2^+} \rightleftharpoons \mathrm{MH} + \mathrm{H_B^+} \tag{4.1b}$$

B refers to the bulk of the analyte. In equilibrium,

$$k_a = \frac{\nu_M . a_{H_S^+}}{\nu_{MH}} \tag{4.2a}$$
$$k_b = \frac{\nu_{MH} . a_{H_S^+}}{\nu_{MH_2^+}} \tag{4.2b}$$

where k_i is the dissociation constant for each reaction[1], $a_{H_S^+}$ the H^+ activity at the surface, and ν_i the number of sites per unit area. Based on Poisson-Boltzmann equations describing the interactions in ionic solutions, the Gouy-Chapman model relates the surface charge concentration to the bulk by

$$a_{H_S^+} = a_{H_B^+} exp(-q\phi_0/kT) \tag{4.3}$$

k in this equation is the Boltzmann constant ($1.3806488 \times 10^{-23} m^2 kg s^{-2} K^{-1}$), T the absolute temperature in Kelvin ($K =^\circ C + 273.15$), q the electron charge ($1.60217657 \times 10^{-19} coulombs$) and ϕ_0 the potential change. With N_S sites per unit area, Θ^+ and Θ^- the fraction of sites with positive and negative charges respectively, and $[B]$ the difference in the number of negatively and positively charged sites per unit area, the surface charge density σ_0 is defined as

$$\sigma_0 = q(\nu_{MH_2^+} - \nu_{M^-}) = qN_S(\Theta^+ - \Theta^-) \tag{4.4a}$$
$$\sigma_0 = qN_S(\frac{a_{H_S^+}^2 - k_a k_b}{k_a k_b + k_a a_{H_S^+} + a_{H_S^+}^2}) = -q[B] \tag{4.4b}$$

Consequently, an intrinsic buffer capacity β_{int} is derived as the change in the number of charged groups for a small change in the surface pH (represented by pH_S),

$$\frac{\delta\sigma_0}{\delta pH_S} = -q\frac{\delta[B]}{\delta pH_S} = -q\beta_{int} \tag{4.5}$$

Based on the law of the conservation of charge, the charge in the electrolyte is opposite equal

[1]This makes ISFET to have a limited response time. Reported calculations claim from $1ms$ for low pH values to $600ms$ for high pH [122].

to the charge on the insulator. The Gouy-Chapman-Stern considers a diffuse layer between the insulator and the closest plane to it formed by the centres of the ions in the solution, Stern layer. It may be further divided into inner and outer Helmholtz planes for charges reaching the insulator surface and the charges being surrounded by water molecules. The charge density at this layer at distance d from the surface with a potential of ϕ_d is

$$\sigma_{DL} = -(8kT\epsilon n_0)^{1/2} Sinh(\frac{zq\phi_d}{2kT}) = -C_i\phi_0 = -\sigma_0 \tag{4.6}$$

n_0 is the bulk concentration of ions, z the magnitude of their charge, and ϵ the permittivity. C_i is the integral capacitance. A differential capacitance C_{dif} defining the ability of the electrolyte in storing charge in response to a change in the electrostatic potential, is

$$\frac{\delta\sigma_{DL}}{\delta\phi_0} = -\frac{\delta\sigma_0}{\delta\phi_0} = -C_{dif} \tag{4.7}$$

Having derived the intrinsic buffer capacity and the differential capacity, the potential change at the surface of the insulator per pH change in the bulk electrolyte is

$$\frac{\delta\phi_0}{\delta pH_s} = \frac{\delta\phi_0}{\delta\sigma_0}\frac{\delta\sigma_0}{\delta pH_S} = \frac{-q\beta_{int}}{C_{dif}} \tag{4.8}$$

which is a pH sensitivity of ideally ($\alpha = 1$) about $59.5mV/pH$ at $300K$ ($27°C$)

$$S_{pH} = \frac{\delta\phi_0}{\delta pH_B} = -ln(10)\frac{kT}{q}\alpha \tag{4.9a}$$

$$\alpha = \frac{1}{ln(10)kTC_{dif}/q^2\beta_{int} + 1} \tag{4.9b}$$

4.1.2. ISFET Primary Macro Model

Based on the models describing the sensitivity, a primary macro-model was introduced [115, 116] as in Figure 4.4.

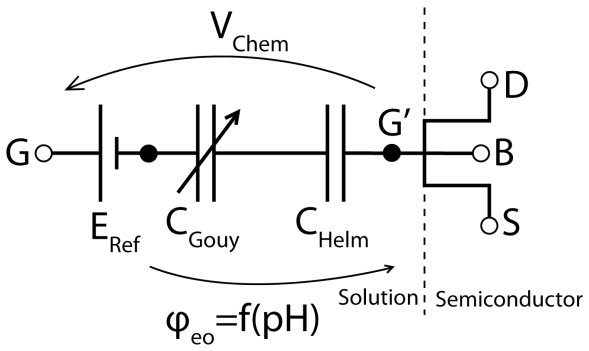

Figure 4.4.: ISFET behavioural macro-model redrawn from [115, 116].

The potential change from the reference electrode to the insulator may be written as

$$V_{Chem} = \gamma + S_{pH}.pH \tag{4.10}$$

where γ includes all the non-pH-dependent parameters related to the electrode-electrolyte and electrolyte-insulator junction potentials. V_{Chem} in the primary macro-modelling of the ISFET operation was used as a modulator of the FET threshold voltage[2]

$$V_{th-ISFET} = V_{th-MOSFET} + V_{Chem} \tag{4.11}$$

Later, a more complete model was used, to take into account the capacitive characteristic of the sensing membrane in the potential coupling [123]; as in Figure 4.5 where for the unmodified CMOS ISFET a capacitor representing the passivation layer is included.

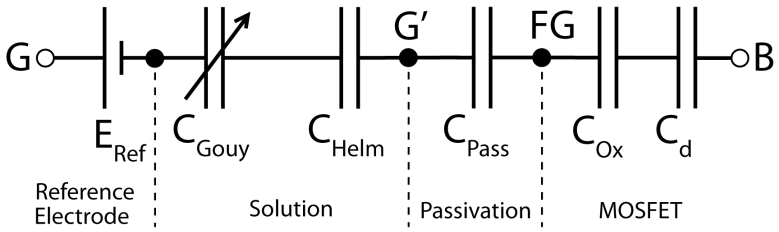

Figure 4.5.: ISFET capacitive model including the unmodified CMOS passivation and the gate capacitances redrawn from [123].

C_{Pass} along with the FET capacitances may define the coupling factor from the sensing membrane surface to the floating gate of the ISFET and so the attenuation of the chemical signal generated onto the gate. The coupling factor and its defining parameters are studied in more detail in section 4.3.

4.2. ISFET Issues and Limitations

Despite all the promising benefits of this micro-sensor, there are some non-ideal behaviours and short-comings that limits its performance and applications. Some of the issues may be mitigated by change in the development like the sensing membrane material and its deposition, and some may require proper design approaches for the commercial unmodified CMOS process.

4.2.1. Temperature Dependency

The effect of temperature on the operation of these sensors is partly due to the effects of temperature on the intrinsic FET threshold, and partly to the kinetics of the electrode-electrolyte-insulator interface. The FET dependency is inhibited in the charge carrier mobility μ, carrier concentration, and band gap energy. At the electrode-electrolyte side it is E_{Ref} and χ_{Sol} but

[2] A term ϕ_m/q is also considered in order to cancel out the metal work function in the MOSFET threshold voltage, when the ISFET implementation is not in the commercial process and does not have a metal layer in between the gate oxide and the insulator.

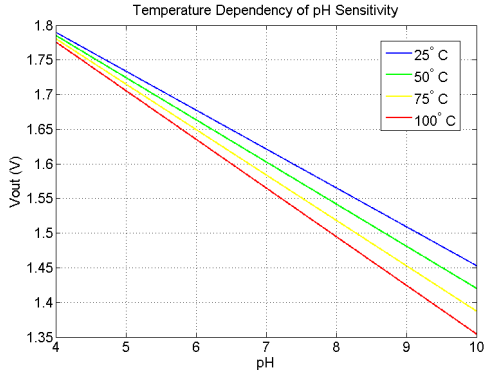

(a) pH sensitivity increases by increase in temperature.

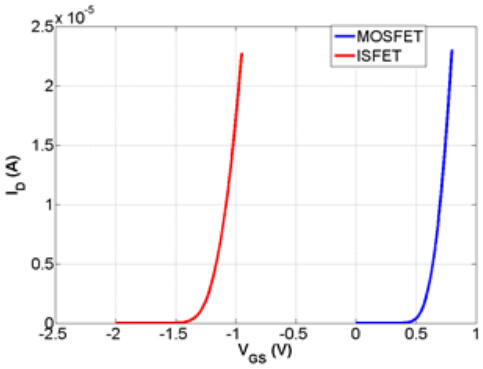

(b) DC offset from trapped charge shifts the current-voltage characteristic of ISFET.

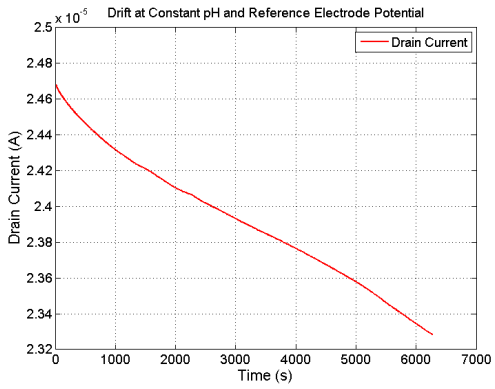

(c) Under a condition of constant pH, temperature and reference electrode potential, the ISFET signal may drift.

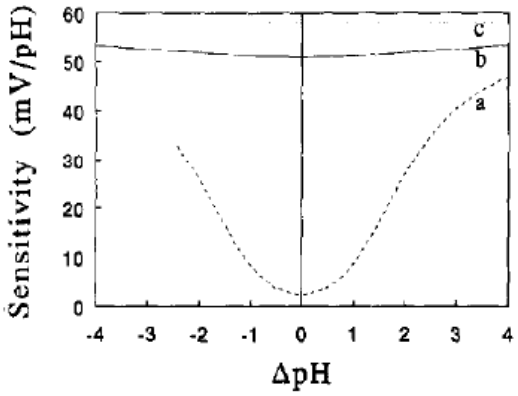

(d) Sensing membrane sensitivity dependency on pH for (a) SiO_2 (b) Al_2O_3 (c) Ta_2O_5 around point of zero charge [119].

Figure 4.6.: ISFETs operation is affected by different non-ideal behaviours.

they may be negligible by proper choice of reference electrode (e.g. for $Ag/AgCl$ the temperature sensitivity for E_{Ref} and χ_{Sol} are $140\mu V/K$ and $10\mu V/K$ [124]). At the electrolyte-insulator, we have the surface dipole potential χ_M and ϕ_0, the latter mainly because of the dissociation constants and the thermal voltage in the Poisson-Boltzmann distribution of charge/potential, which directly affects the sensitivity of the ISFET as in equation (4.9); [125–128]. Figure 4.6a shows an example change in sensitivity by temperature.

4.2.2. DC Offset

In commercial CMOS, as in Figure 4.2, in order to use the passivation nitride layer as the sensing membrane and couple the voltage, a sheet of top-metal is used to define the sensing area. It creates the coupling capacitance to convey the potential on the insulator to the floating gate of the FET, which accordingly has no resistive path to the ground. Therefore, possible existence of trapped charges induced during fabrication can leave an offset at the floating gate of the ISFET. The offset shifts the current-voltage characteristic of the transistor; Figure 4.6b. To study and overcome this parasitic, UV radiation and electron injection has been used [129,

130].

Besides the trapped charges, in this chapter the effect of dimensions on the threshold voltage of ISFETs is assessed according to the capacitive models used for explanation of this non-Faradaic sensor[3].

4.2.3. Drift and Hysteresis

Drift has been defined as the monotonic shift in the ISFET output (or technically the ISFET readout output) in a condition of constant pH and temperature; Figure 4.6c. Although it is slow, appearing in DC and low frequencies, and normally in the order of several milli-Volts per hour, it adds uncertainty to the measurements.

The ISFET drift has been explained by different reasons such as

- dispersive transport of species to buried surface sites raising the surface layer [131]
- degradation of the sensing membrane as a result of chemical modifications like creation of SiO_2 and oxynitirde when Si_3N_4 is the sensing membrane (as in commercial CMOS) [132]
- ion migration and diffusion of hydrogen ions into the sensing membrane changing its dielectric constant and thickness [133]

On the other hand, observing an increase in drift rate by increasing the pH, there is this hypothesis that in fact it is the OH^- groups diffusing onto the sensing membrane, due to their smaller size than hydrogen ions existing as hydronium ions H_3O^+ in an aqueous solution [133].

Hysteresis in addition, shows existence of memory or multiple time-constants for which the pH response of the ISFET may not return on the same curve [125, 134, 135]. The aforementioned issues may be dependent on the type of material selected as the sensitive insulator.

4.2.4. Sensing Membrane

The sensing membrane insulator certainly plays a key role in the performance of the ISFET. In terms of sensitivity, having described the operation in section 4.1, the buffering capacity (β_{int}) of the insulator-electrolyte (defined by the dissociation constants and dependent on the ionic concentration) along with the number/density of the binding sites (N_s), may limit the operating range of the ISFET; Figure 4.6d. The larger the number of sites, the higher the sensitivity and the wider the linear range of pH sensitivity [136]. Insulator thickness may also influence as the binding interactions take place between the sub-surface layer and electrolyte, with low sensitivity for about one nano-meter-thin membranes [137]. Amorphous membranes may give higher sensitivity [138]; their effect (summarised in the sub-Nernstian parameter α) adds non-linearity over the working range.

[3] At the interface of a non-Faradaic sensor there is no charge transfer reaction and the electrode is normally ideally-polarised like a capacitor. In a Faradaic sensor, there is a charge exchange at the electrode interface resulted from an oxidation/reduction process.

There are works in literature reporting super-Nernstian sensitivities [139–143]. However, it is contradictory to the maximum Nernstian limit of $ln(10)U_T$ approximately $59mV/pH$ at room temperature. But it was either due to an equivalent inherent amplification in the readout, double-gate structures for nano-scale devices, or there was no supporting drift/settling time justification.

In terms of signal stability, drift, and hysteresis, different materials and development/deposition structures have shown different behaviours and robustness to changes [137]. Table 4.1 provides a summary of a variety of publications on sensitive insulators. Among all, TiN may be an odd for it is a conductive material, though with better results reported than the others. To the author's best knowledge, only one recent (2013) work has been reported [144] since the referenced ones in 2001 and 1991.

Moreover, the thickness and its uniformity, effectively for arrays of ISFETs, may considerably affect the performance especially in unmodified CMOS where the passivation insulator is subject to 20% variation. This is more covered in section 4.3.

Table 4.1.: pH-sensitive materials in CMOS. Complete list in Table C.1.

Sensing Membrane	**Relative Permittivity**	**pH Sensitivity (min-Max) mV/pH**	**References Number**
Si_3N_4	7	40-58	[133, 145–150]
Ta_2O_5	22	50.2-59.7	[134, 138, 151, 152]
SiO_2	3.9	24-36	[146, 147]
Al_2O_3	9	48.8-53.23	[135, 152, 153]
SnO_2	9.6	58	[154, 155]
TiO_2	80	58	[156, 157]
Y_2O_3	15	56.09	[158]
TiN	Conductive	57-59	[159, 160]

4.2.5. Noise

Similar to temperature, noise can be studied in two parts, one related to its MOSFET and the other in the electrode-electrolyte-insulator. Jakobson reports that the dominant noise in low frequency is the MOSFET $1/f$ based on his experiments on ISFET with Al_2O_3 membrane [161, 162]. Hassibi [82] provides a more analytical calculation of the nature of noise in such electrochemical environments, claiming a chemical shot noise to be expected in such set-ups and proves with referring to some other reported measurements.

Accordingly, noise, in addition to the MOSFET part, depends on the nature of the sensor/electrode to be either Faradaic or non-Faradaic. This can also be of two sources, thermal equilibrium fluctuations as in non-Faradaic case, and non-equilibrium fluctuations in result of recombination and regeneration of charged particles as in Faradaic electrodes. Considering ISFETs as non-Faradaic sensors and representing the dissipative element in the electrolyte to be its bulk resistance (Rb), by applying the Johnson-Nyquist formula, Hassibi [82] suggested the

output current noise to be

$$\bar{i}_{no}^2(\omega) = \bar{i}_{nd}^2(\omega) + 4kTR_b \left[\frac{C_{gs}}{C_{gs} + C_{ref} + C_d}\right]^2 \left[\frac{\omega^2}{\omega^2 R_b^2 + 1}\right] \tag{4.12}$$

Where C_{ref} and C_d are the reference electrode and double-layer capacitances respectively, according to the model provided in Figure 4.7.

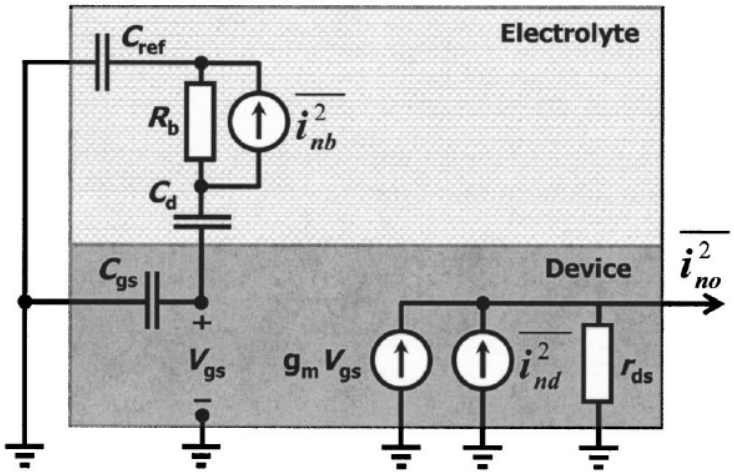

Figure 4.7.: Noise model for ISFETs operating in saturation [82].

4.2.6. Reference Electrode

Reference electrode creates one half of the analysis cell. The stability of the reference electrode standard potential, and its sensitivity to temperature, inertness to the analyte, life time, and impedance (to not disturb the measurement by a leakage current) , are the very first fundamental factors in defining the noise and drift [161, 163]. However, it becomes more challenging when a common reference electrode needs to be used for an array of ISFETs, each monitoring a particular reaction, like in SNP detection [76] where possibly micro-fabricated planar on-chip reference electrodes [164] may just add complexity.

4.2.7. Other Issues

More issues such as light sensitivity, packaging, and electrostatic discharge on the device arise when dealing with ISFETs [125, 165–168]. Although one might not completely eliminate all the problems and create an ideal ISFET device, can suppress their effects and improve the performance.

In the following sections, methods for having a controlled and well-behaved ISFET in commercial processes is investigated.

4.3. ζ-based Design

Having discussed the operation and issues of ISFET, in this section a new term, ζ, is introduced by the author in the formula of the ISFET which allows a better study of the geometrical factors influencing the ISFET performance.

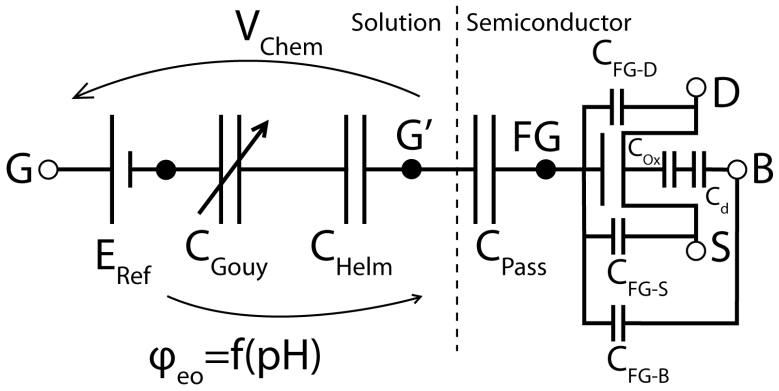

Figure 4.8.: ISFET capacitive model including the unmodified CMOS passivation and the floating gate capacitances based on [123].

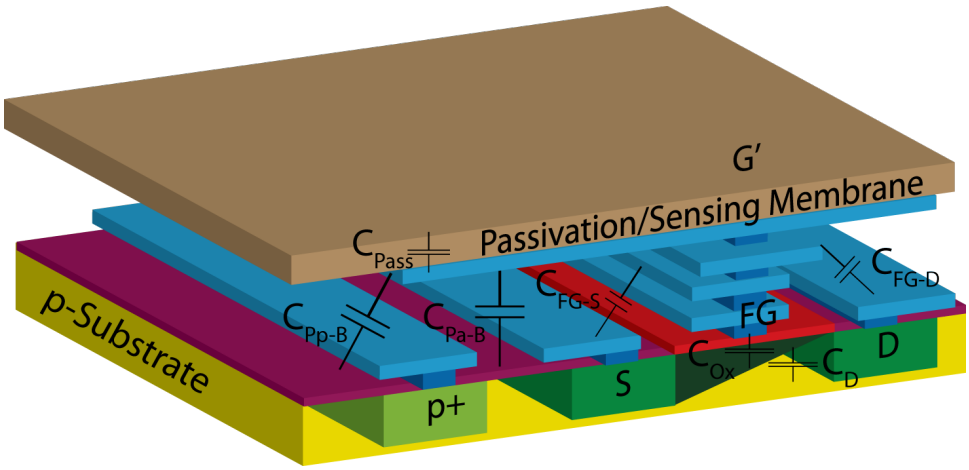

Figure 4.9.: ISFET 3D cross-section overview. Beside the coupling C_{Pass}, decoupling capacitors on the floating gate are depicted.

4.3.1. Introduction of ζ

The primary formula for the ISFET characteristics were presented in equations (4.9-4.11) which would replace the threshold voltage of the MOSFET in $I-V$ equations (4.13) [4]. Different readout circuits have been designed to track the changes in the threshold voltage by locking the

[4] All the subscripts represent the MOSFET conventional terminal names with initials. The equations are for NMOS but similarly apply to PMOS transistors, writing the absolute values relative to its body potential.

potential differences at other terminals (examples are provided in Chapter 5).

$$I_D = I_{D0} e^{V_G/nU_T}[e^{V_S/U_T} - e^{-V_D/U_T}] \qquad \textit{Weak Inversion} \qquad (4.13a)$$

$$I_D = \mu_n C_{Ox} \frac{W}{L}[(V_G - V_S - V_{th-ISFET})V_{DS} - \frac{V_{DS}^2}{2}] \qquad \textit{Strong Inversion Triode} \qquad (4.13b)$$

$$I_D = \frac{\mu_n C_{Ox}}{2} \frac{W}{L}(V_G - V_S - V_{th-ISFET})^2 \times [1 + \lambda(V_{DS} - V_{DS-Sat})] \qquad \textit{Velocity Saturation} \qquad (4.13c)$$

However, this formulation lacks the capacitive coupling effects. In addition to the coupling capacitance made by the insulating membrane, charges on the surface, and charges on the floating gate, there are decoupling capacitances sharing one terminal with the floating gate node. These capacitors are modelled in Figure 4.8 based on the previous capacitive models drawn in Figures 4.4 and 4.5. Figure 4.9 shows a 3D overview of the decoupling capacitors. C_{Pa-B} and C_{Pp-B} are the decoupling parasitic capacitors to the body made by the extended gate sensing metal plate, respectively by the surface (area) and the perimeter. Their influence is studied in sections 4.7 and 4.8.

Therefore, only a fraction of the potential change on the surface of the sensing membrane is sensed on the floating gate. This attenuation or coupling factor is mainly dependent on the dimensions of the ISFET.

Here the term ζ is defined as the ratio of the sum of the decoupling capacitors to the insulator coupling capacitor[5]. Accordingly, equations (4.13) may be reformulated by replacing the gate voltage V_G with the floating-gate potential of the ISFET V_{FG}, calculated by

$$V_{FG} = \frac{C_{Pass}}{C_{Pass} + C_{eOx}}(V_{Ref} - V_{Chem}) \qquad (4.14a)$$

$$\zeta = \frac{C_{eOx}}{C_{Pass}} \qquad (4.14b)$$

$$V_{FG} = \frac{1}{1 + \zeta}(V_{Ref} - V_{Chem}) \qquad (4.14c)$$

C_{eOx} is the equivalent gate oxide capacitance which contains the decoupling capacitances of the gate-oxide, depletion layer, gate-drain, and gate-source. C_{Pass} is the coupling capacitance of the sensing membrane; passivation as in unmodified CMOS which is the focus of this study.

Based on the model used, the value of these capacitors when considered as planar, is propor-

[5]The coupling capacitor is the one made by the sensing membrane insulator to couple the signal onto the intrinsic gate, and the decoupling capacitors are any that share the gate node and make a fraction of the coupling potential appear on the gate.

tional to their area. Representing their per-unit-area capacitances by a prime sign

$$\zeta = \frac{C_{eOx}}{C_{Pass}} = \frac{C'_{eOx}}{C'_{Pass}} \frac{A_e}{A_{Pass}} \tag{4.15a}$$

$$C' = \frac{\epsilon}{t} \tag{4.15b}$$

The per-unit-area capacitances are defined by the dielectric permittivity ϵ and its thickness t. A_e and A_{Pass} are the area of the FET oxide and the insulating passivation, respectively. When in unmodified CMOS, area is the only parameter that may be set by the designer to choose the proper ζ and the coupling factor. Particularly as the passivation layer thickness (in micro-meters) is significantly larger than the gate oxide (in nano-meters), but with a similar permittivity. This difference results in a consequential dominance of decoupling capacitors. Therefore, the area of the sensing membrane needs to be large enough to optimise the coupling factor.

4.3.2. Effects of ζ

The impact of ζ on the ISFET performance may be considered on its transconductance, threshold voltage, resolution of measurement, and susceptibility to process variations. The coupling factor versus ζ is depicted in Figure 4.10.

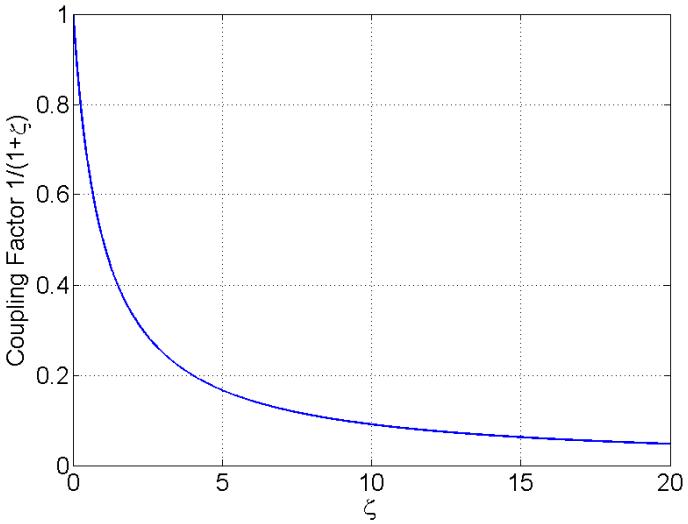

Figure 4.10.: Coupling factor $1/(1+\zeta)$ versus the decoupling to coupling capacitance ratio ζ.

Transconductance Showing the transconductance of the intrinsic FET by g_{m0}, the electrical and pH transconductances of ISFET may be derived as

$$g_{m0} = \frac{\delta I_D}{\delta V_{FG}} \tag{4.16a}$$

$$g_{m-ISFET} = \frac{\delta I_D}{\delta(V_{Ref} - V_{Chem})} = \frac{\delta I_D}{\delta V_{FG}} \times \frac{\delta V_{FG}}{\delta(V_{Ref} - V_{Chem})}$$

$$= \frac{1}{1+\zeta} g_{m0} \tag{4.16b}$$

$$g_{m-pH} = \frac{\delta I_D}{\delta pH} = g_{m-ISFET}.S_{pH} \tag{4.16c}$$

The bigger the ζ, the smaller the coupling factor $1/(1+\zeta)$, and the smaller the ISFET transconductance.

Threshold Voltage Considering the reference electrode as the remote gate, the threshold voltage of the ISFET (the difference between the reference electrode potential and the source terminal giving the same current as the MOSFET at the threshold bias) may now be redefined based on equation (4.14) as

$$V_{FG} - V_S = V_{th-MOSFET} \tag{4.17a}$$

$$V_{th-ISFET} = (1+\zeta)V_{th-MOSFET} + \zeta V_{SB} + V_{Chem} \tag{4.17b}$$

Perhaps a further detailed equation needs to include the effect of the trapped charges by adding an offset to the threshold voltage of the MOSFET. Nevertheless, a high value of ζ leads to a higher supply for the reference electrode to turn the ISFETs on, which may not be welcomed especially where power is limited.

Resolution The key terms in defining the resolution of an ISFET-based system are its sensitivity and noise. With the attenuation at the coupling, the equivalent electrical input-referred noise on the sensing membrane will be larger than its value on the floating gate. This may be a concern for very large-scale integrated arrays in deep sub-micron processes, or where the ISFET is acting as a processing component and not a sole sensor attached to a readout circuit.

$$V^2_{neq-ISFET} = (1+\zeta)^2 V^2_{neq-MOSFET} \tag{4.18}$$

On the other hand, the coupling factor effect, may influence the following circuits performance. For example, the pH-equivalent quantization step for a following converter may be larger for ISFETs with larger ζ, or it may need an amplification in between the ISFET and the converter to compensate for the coupling attenuation.

Process Variations The variations especially in the thickness and permittivity of the passivation, either from the fabrication process or from chemical modification of the surface by

Table 4.2.: The $0.35\mu m$ process insulator specification.

$\epsilon_{Si_3N_4}$	7.9
ϵ_{SiO_2}	3.9
Si_3N_4 Thickness (nm)	1000
SiO_2 Thickness (nm)	1030
Gate Oxide Thickness (nm)	7.1
$C'_{pass}(\mu F/m^2)$	22.65
C'_{ox} $(\mu F/m^2)$	4861

analyte (also a probable reason for the ISFET drift), may create a variance in the transconductance of ISFETs in an array as a result of changing the coupling factor. A smaller ζ which means an ISFET with a higher ratio of A_{Pass}/A_e (a relatively larger sensing area to FET area), may be subject to smaller deviation.

$$\zeta = \frac{C'_{eOx}}{C'_{Pass}} \frac{A_e}{A_{Pass}} \tag{4.19a}$$

$$S^{(1+\zeta)}_{C'_{Pass}} = \frac{C'_{Pass}}{(1+\zeta)} \frac{\delta(1+\zeta)}{\delta C'_{Pass}} \tag{4.19b}$$

$$= \frac{C'_{Pass}}{(1+\zeta)} \frac{-C'_{eOx}}{C'^2_{Pass}} \frac{A_e}{A_{Pass}} \tag{4.19c}$$

$$= \frac{-\zeta}{1+\zeta} \tag{4.19d}$$

4.4. ζ-based Design in a $0.35\mu m$ Process

In order to investigate the ζ-based design approach, and the shape and dimension effects on the ISFET operation, designs and simulations were done in Cadence Spectre environment using a $0.35\mu m$ 4-metal process. The passivation layer in this process consists of two insulating layers of SiO_2 and Si_3N_4 with gate and inter-metal dielectric of SiO_2. Table 4.2 provides the thickness and permittivities as well as the per-unit-area capacitance values.

The ISFET sensing area in unmodified processes is defined by a plate of top-metal (the top layer of metal) connected to the polysilicon gate through inter-metal via connections[6]. The charge on the passivation insulator is coupled to this metal plate modulating the potential of the floating gate and the FET channel.

The equivalent passivation coupling capacitance made of the two dielectric layers, and the

[6]In other words, the gate is extended to the top metal.

gate oxide decoupling capacitance are

$$\begin{aligned} C_{pass} &= \frac{\epsilon_{Si_3N_4} \times \epsilon_{SiO_2}}{\epsilon_{Si_3N_4} \times t_{SiO_2} + \epsilon_{SiO_2} \times t_{Si_3N_4}} \epsilon_0 A_{Pass} \\ &= C'_{Pass} A_{Pass} \end{aligned} \tag{4.20}$$

$$C_{Ox} = \frac{\epsilon_{SiO_2} \epsilon_0}{t_{Ox}} A_e = C'_{Ox} A_e \tag{4.21}$$

With an approximate calculation for the ζ value, it is known that for an ISFET operating in strong inversion, in order to have a coupling factor of about 0.8, the sensing membrane area should be ≈ 1000 times larger than the gate oxide area. Similarly in weak inversion where the depletion layer may reduce the equivalent gate capacitance, it has to be ≈ 220 times larger, considering a slope factor[7] of $n = 1.35$ [123]. Certainly in practice this ratio may be larger due to the gate-drain, gate-source and the parasitic capacitors.

$$\zeta = \frac{C'_{Ox}}{C'_{Pass}} \frac{A_e}{A_c} = 214.6 \frac{A_e}{A_C}; \ \textit{Strong Inversion} \tag{4.22}$$

$$C_D = (n-1) C_{Ox} \tag{4.23a}$$

$$\zeta = \frac{n-1}{n} \frac{C'_{Ox}}{C'_{Pass}} \frac{A_e}{A_c} = 55.6 \frac{A_e}{A_C} \quad ; \ \textit{Weak Inversion} \tag{4.23b}$$

Figure 4.11 estimates how much the sensing area should be bigger than the FET area to gain a certain ζ and coupling factor.

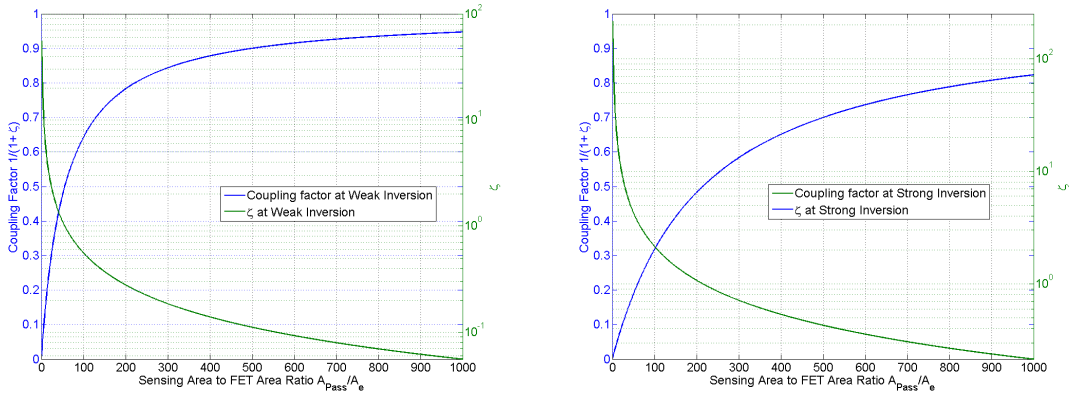

(a) Weak inversion.

(b) Strong inversion.

Figure 4.11.: Coupling factor $1/(1+\zeta)$ and decoupling to coupling capacitance ratio ζ versus the area ratio of the sensing area to the FET area.

[7] The slope factor is usually between 1 and 1.5 [169].

4.5. Test Set-up in $0.35\mu m$ Technology

The ISFETs considered for this study are summarised in Table 4.3 and Figure 4.13. Basically two sets of NMOS ISFETs are considered[8], one with $5\mu m/1\mu m$ FET[9] and one with $1\mu m/5\mu m$. Square-shape top-metal plates were used to minimise any potential perimeter effects (this is further discussed in section 4.7).

The sensing plates were $5\mu m \times 5\mu m$, $10\mu m \times 10\mu m$, $20\mu m \times 20\mu m$, $40\mu m \times 40\mu m$ and $80\mu m \times 80\mu m$. With the inverse relation derived in equation (4.15b), it is expected to see a linear pattern between $1/\zeta$ and the sensing area from this doubling of side size (quadrupling the area).

The test bias configuration is depicted in Figure 4.12. Body and source are grounded and the drain voltage is set to $0.7V$[10]. Reference MOSFETs with similar FET aspects were used to map the measured currents of the ISFETs to their equivalent floating gate voltages and to measure the FETs transconductances.

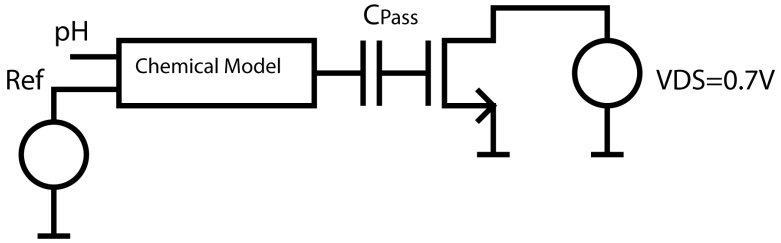

Figure 4.12.: Test configuration.

For simulations, a Verilog-A model based on the voltage modulation models discussed in section 4.1, equivalent to Martinoia's [115], was used. The passivation sensing membrane was modelled by a capacitor having its value set by equation (4.20) and Table 4.2.

For experiments, the layout of the ISFETs were drawn as in Figure 4.13. For the $40\mu m \times 40\mu m$ and $80\mu m \times 80\mu m$ plate ISFETs, it had to be split since the antenna rules would not allow a single-plate configuration due to potential break-down for electrostatic charge accumulation.

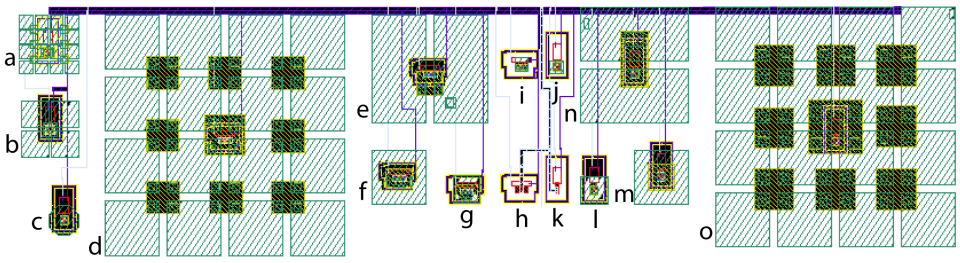

Figure 4.13.: Test ISFET devices layout.

[8]These dimensions were used, to be neither too big for a high area-ratio of sensing membrane to FET, nor too small to prevent from large ζ value analysis.

[9]In fact this is the FET channel aspect ratio. However, for ease of discrimination in this thesis only the short first term, FET, is mentioned.

[10]This is $\approx 200mV$ higher than the threshold voltage of the FETs, based on the simulation results, and so allows seeing all the three regions of operation by sweeping the gate/reference voltage.

Table 4.3.: Device names and their dimensions.

Device Name	Sensing Plate	Intrinsic MOSFET W/L	Figure Code
I_1_05	$5\mu m \times 5\mu m$	$5\mu m/1\mu m$	j
I_1_10	$10\mu m \times 10\mu m$	$5\mu m/1\mu m$	l
I_1_20	$20\mu m \times 20\mu m$	$5\mu m/1\mu m$	m
I_1_40	$40\mu m \times 40\mu m$	$5\mu m/1\mu m$	n
I_1_80	$80\mu m \times 80\mu m$	$5\mu m/1\mu m$	o
I_5_05	$5\mu m \times 5\mu m$	$1\mu m/5\mu m$	i
I_5_10	$10\mu m \times 10\mu m$	$1\mu m/5\mu m$	g
I_5_20	$20\mu m \times 20\mu m$	$1\mu m/5\mu m$	f
I_5_40	$40\mu m \times 40\mu m$	$1\mu m/5\mu m$	e
I_5_80	$80\mu m \times 80\mu m$	$1\mu m/5\mu m$	d
I_M05	$(4 \times 4)(5\mu m \times 5\mu m)$	$5\mu m/1\mu m$	a
I_M10	$(2 \times 2)(10\mu m \times 10\mu m)$	$5\mu m/1\mu m$	b
I_Oct	Octagonal $4.6\mu m$	$5\mu m/1\mu m$	c
M-1	Reference MOSFET	$5\mu m/1\mu m$	k
M-5	Reference MOSFET	$1\mu m/5\mu m$	h

Moreover, two ISFETs of equivalent area to I_1_20 ($20\mu m \times 20\mu m$ sensing and $5\mu m/1\mu m$ FET), one with a 4×4 mesh of $5\mu m \times 5\mu m$ plates (I_M05, **a** in Figure 4.13) and one with a 2×2 mesh of $10\mu m \times 10\mu m$ plates (I_M10, **b** in Figure 4.13), were designed in order to compare any advantage or disadvantage in meshing the sensing surface. It would help to benchmark any potential effect particularly from the fringing capacitances and perimeter capacitances that may prevent a confident comparison of the $80\mu m \times 80\mu m$ ISFETs with others.

An ISFET of octagonal shape[11] (**c** in Figure 4.13) was also developed with an area of about the same as I_1_10 ($10\mu m \times 10\mu m$ with $5\mu m/1\mu m$ FET). This was expected to show a comparison over the shape with more corners but higher area-to-perimeter ratio, since it was assumed that in practice parasitic capacitances may be related to the perimeter of the ISFET sensing membrane[12].

4.6. Primary Simulation Results

In the primary simulations at schematic level, model in Figure 4.5 was used to compare the transconductance, threshold voltage, ζ and passivation error suppression. Table 4.4 summarises the simulation results.

[11] An octagonal shape may give a higher area to perimeter ratio; Appendix D.

[12] An earlier experiment's results on the ISFET dimension effects encouraged further research on this topic to have a wider statistical population of data. The analysis of that chip, which matches the hypothesis developed in this chapter, are provided in Appendix E.

Table 4.4.: Summary of the primary simulations result.

	C_{pass} (fF)	V_{GI} at $10nA$	g_m at $10nA$	g_m/g_{m0} at $10nA$	ζ at $10nA$	V_{GI} at $1\mu A$	g_m at $1\mu A$	g_m/g_{m0} at $1\mu A$	ζ at $1\mu A$
I_1_05	0.566	5.208	2.10E-08	0.0779	11.839	NA	NA	NA	NA
I_1_10	2.265	1.575	6.76E-08	0.2509	2.985	2.4620	2.95E-06	0.1442	5.936
I_1_20	9.060	0.6678	1.57E-07	0.5818	0.719	1.0250	8.23E-06	0.4028	1.482
I_1_40	36.240	0.441	2.29E-07	0.8505	0.176	0.6660	1.50E-05	0.7319	0.366
I_1_80	144.96	0.3841	2.58E-07	0.9584	0.043	0.5763	1.87E-05	0.9144	0.094
I_5_05	0.566	5.124	1.70E-08	0.0738	12.556	NA	NA	NA	NA
I_5_10	2.265	1.623	5.64E-08	0.2440	3.099	4.0520	7.94E-07	0.1230	7.132
I_5_20	9.060	0.748	1.31E-07	0.5658	0.767	1.6010	2.32E-06	0.3593	1.783
I_5_40	36.240	0.5294	1.97E-07	0.8506	0.176	0.9889	4.47E-06	0.6920	0.445
I_5_80	144.960	0.4747	2.23E-07	0.9636	0.038	0.8358	5.82E-06	0.9002	0.111
I_M05	9.06	0.6678	1.57E-07	0.5818	0.719	1.0250	8.23E-06	0.4028	1.482
I_M10	9.06	0.6678	1.57E-07	0.5818	0.719	1.0250	8.23E-06	0.4028	1.482
I_Oct	2.314	1.55	7.03E-08	0.2608	2.835	2.4210	3.04E-06	0.1487	5.724
M_1	NA	0.3652	2.70E-07			0.5464	2.04E-05		
M_5	NA	0.4564	2.31E-07			0.7848	6.46E-06		

4.6.1. Transconductance

The transconductance was calculated at currents of $10nA$ and $1\mu A$ and relative to the value of the counterpart MOSFET at these points. The characteristic derived is in agreement with Figure 4.11. The higher the ratio of the areas and consequently the smaller the ζ, the higher the transconductance is; Figure 4.14.

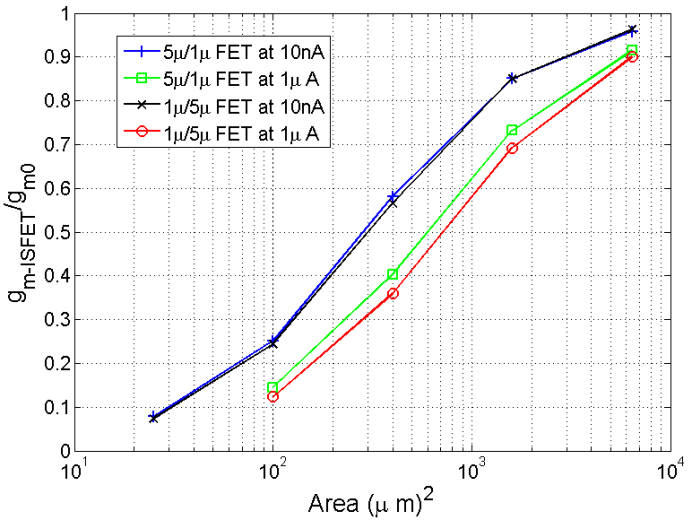

Figure 4.14.: ISFET transconductance relative to its MOSFET counterpart vs sensing area to FET area ratio.

4.6.2. ζ vs Dimensions

The value of ζ was extracted based on equation (4.16b) using the ISFET transconductance $g_{m-ISFET}$ and the reference counterpart MOSFET transconductance g_{m0}

$$\zeta = \frac{g_{m0}}{g_{m-ISFET}} - 1 \tag{4.24}$$

The extracted values were in complete agreement with equation (4.15b) showing a linear relation with the area ratio of the FET to sensing membrane; Figure 4.15.

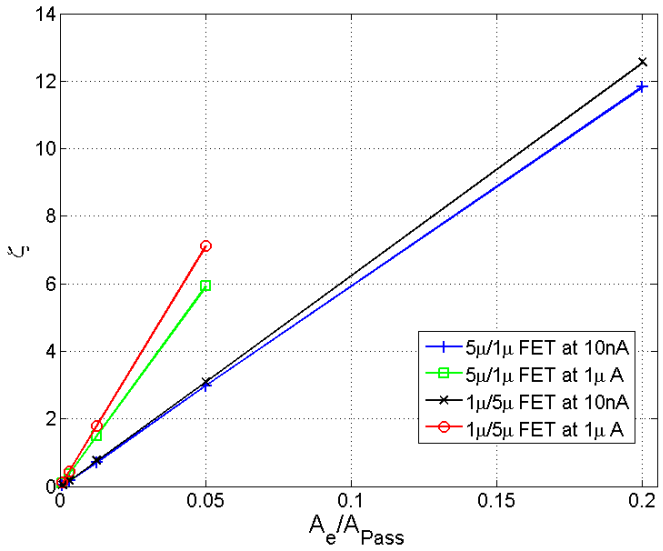

Figure 4.15.: ζ vs FET area to ISFET sensing area ratio.

4.6.3. Threshold Voltage

The threshold voltage change was compared by measuring the sensing membrane potential that would give a $10nA$ current; Figure 4.16. The value of ζ was extracted based on (4.24). The smaller the area ratio is, the higher the ζ is, and the higher the threshold voltage.

4.6.4. Passivation Error Suppression

As mentioned in sections 4.2.3, 4.2.4 and 4.3.2, two of the issues with ISFETs sensing membrane are the degradation due to chemical modification of surface, and variation in the passivation layer thickness and permittivity (particularly for unmodified commercial CMOS ISFETs). The effect was shown to be reflected on the ISFET characteristics through ζ.

In order to suppress such issues, one should reduce the value of ζ in a way that its changes are also negligible and the coupling factor sensitivity to it is small; equation (4.19). One way to do so is through the proper choice of the area ratio between the FET area and the chemical sensing membrane. Choosing this ratio high enough can suppress the ISFET non-ideal behaviours. Figure 4.17 and Figure 4.18 show the deviation of the coupling factor (as in relative

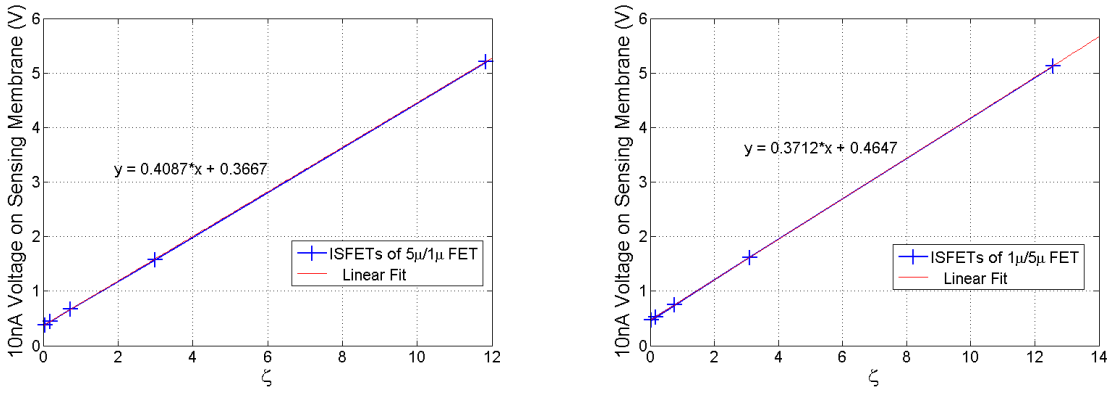

(a) ISFETs with $5\mu/1\mu$ FET.

(b) ISFETs with $1\mu/5\mu$ FET.

Figure 4.16.: Sensing membrane voltage giving a current of $10nA$, versus ζ at this operating point.

transconductance) and the threshold voltage (as in the remote-gate potential giving a $10nA$ bias), respectively, in result of a relative change in the coupling capacitance (the passivation in unmodified CMOS). In the simulations, the equivalent passivation capacitance based on Table 4.2 and the corresponding dimensions was selected. For the ISFETs with the same intrinsic FET aspect ratio, the ones with larger sensing area (larger coupling capacitance and smaller ζ) the error is less.

4.7. Experiment Results

The experiments were run in a Faraday cage at room temperature for 8 dies[13] in $pH04$, $pH07$ and $pH10$ solutions using $Ag/AgCl$ reference electrode and KEITHLEY 4200. An image of the test devices and set-up is provided in Appendix G.

KEITHLEY would accept four connections at a time, one was used for reference electrode and the other three for biasing the drain voltage of three ISFETs at each run. Every time testing a new chip or changing the buffer solution, a drift test of about $1hr20'$ was run both to analyse for the drift performance and to make sure the analyte is settled for the current-voltage characterisation tests. It was ensured all the time that the current through the reference electrode would not exceed $1nA$ so that the measurements would not be affected by any leakage or voltage drop at the reference electrode. Voltage sweeps were done from $-5V$ to $+5V$ with $1mV$ steps giving a $1s$ gap between the steps to ensure the voltage settling. A summary of the measurements at currents of $10nA$ and $1\mu A$ is provided in Table 4.5.

4.7.1. Transconductance

The transconductances show the similar intuitive expectation, increasing as the sensing membrane area increases; Figure 4.19. However, the values and the pattern seen is not the same as

[13]In addition to the primary 2 dies tested. Their results are provided in Appendix E.

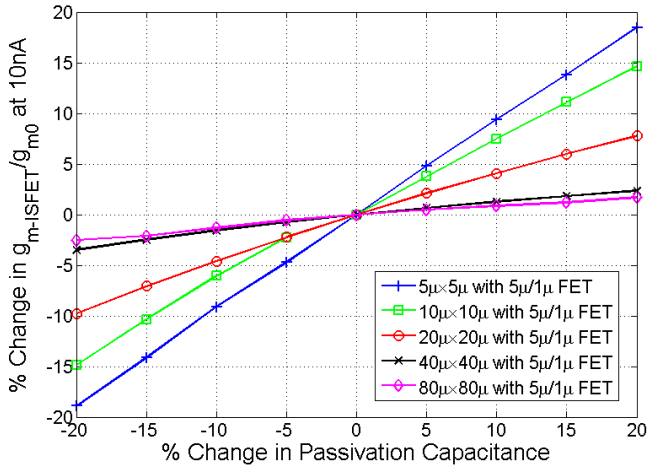

(a) ISFETs with $5\mu/1\mu$ FET.

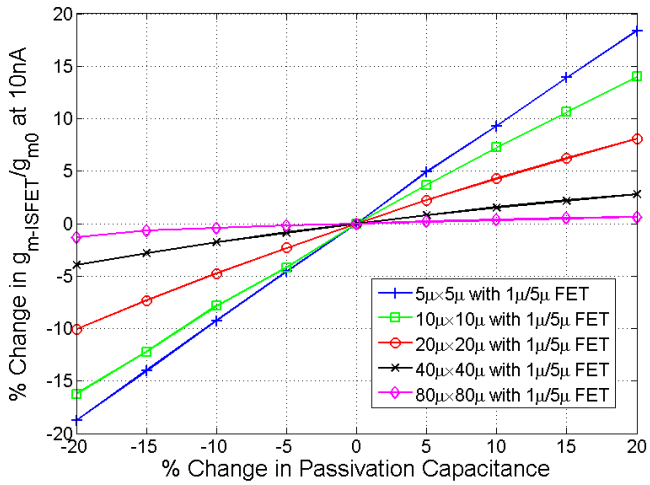

(b) ISFETs with $1\mu/5\mu$ FET.

Figure 4.17.: Suppression of the deviation of ISFET transconductance from passivation capacitance change.

the simulations. Table 4.6 shows the simulation and experiments results together for comparison. For smaller ISFETs of $5\mu m \times 5\mu m$ and $10\mu m \times 10\mu m$ the experimental transconductance measurements are larger than the simulations, and the changes in the values do not seem to be as significant as the changes in the simulations. The former might be due to the fringing capacitances [170] and the possible thinner passivation layer and not a planar type of capacitor. However, the difference in the pattern may be due to the existence of parasitic capacitors. This is further discussed in sections 4.7.2 and 4.8.

4.7.2. ζ

Similar to simulations, ζ was extracted based on equation (4.24) and the transconductances in Table 4.5. The value of ζ represents the ratio of the decoupling capacitors to the coupling capacitor. It was expected to see an inverse relation between ζ and the area of the sensing

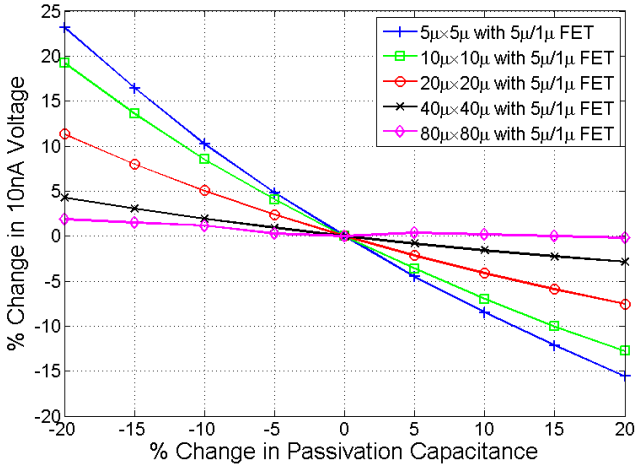

(a) ISFETs with $5\mu/1\mu$ FET.

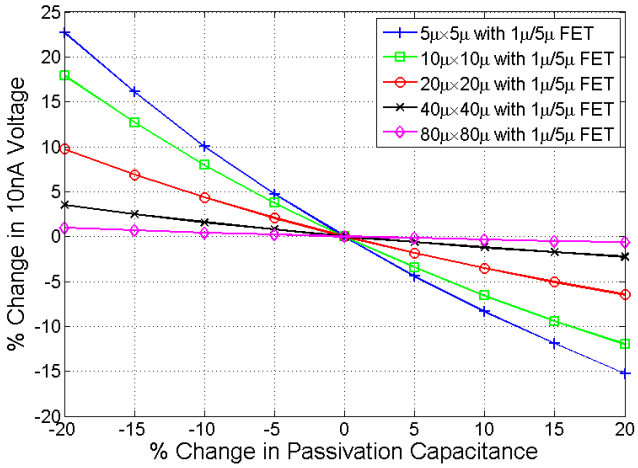

(b) ISFETs with $1\mu/5\mu$ FET.

Figure 4.18.: Suppression of the deviation of then ISFET threshold from passivation capacitance change.

membrane (which should be proportional to the coupling capacitance). However, this relation is not seen in the experiments as drawn in Figure 4.20. The fairly linear relation at single-plate smaller ISFETs builds this hypothesis that decoupling capacitances may be dominated by the perimeter of the sensing plates than the area.

Besides, Table 4.7 shows how ζ is multiplied by each time quadrupling the area. The change from $40\mu m \times 40\mu m$ to $80\mu m \times 80\mu m$ is less. One possible reason may be the use of wide and multiple lower metal layers to connect the separated plates. The excessive metal at lower levels might have created more decoupling capacitors with the substrate.

On the other hand, comparing the octagonal-shape ISFET *I_Oct* that has slightly more area and less perimeter (respectively about $102\mu m^2$ and $36.8\mu m$) with *I_1_10* ($100\mu m^2$ and $40\mu m$), the decoupling capacitance must have been slightly more (although expected less) for *I_Oct* with more corner edges making a larger ζ. The decoupling capacitance effect is further discussed in

Table 4.5.: Experiment results summary.

	g_m avg (A/V) at $10nA$	g_m std (A/V) at $10nA$	g_m/g_{m0} at $10nA$	ζ at $10nA$	g_m avg (A/V) at $1\mu A$	g_m std (A/V) at $1\mu A$	g_m/g_{m0} at $1\mu A$	ζ at $1\mu A$
I_1_05	4.23E-08	1.47E-09	0.151	5.6	2.31E-06	6.29E-08	0.113	7.85
I_1_10	8.57E-08	9.30E-10	0.307	2.26	4.88E-06	1.07E-07	0.239	3.19
I_1_20	1.42E-07	3.41E-09	0.511	0.96	8.83E-06	1.42E-07	0.432	1.31
I_1_40	1.83E-07	8.51E-09	0.655	0.53	1.25E-05	2.54E-07	0.611	0.64
I_1_80	2.10E-07	4.81E-09	0.754	0.33	1.46E-05	2.99E-07	0.714	0.4
I_5_05	3.63E-08	2.97E-09	0.143	5.98	NA	NA	NA	NA
I_5_10	7.11E-08	2.07E-09	0.28	2.57	1.33E-06	2.18E-08	0.205	3.86
I_5_20	1.20E-07	3.83E-09	0.474	1.11	2.51E-06	1.19E-07	0.386	1.59
I_5_40	1.59E-07	7.11E-09	0.625	0.6	3.93E-06	5.03E-08	0.606	0.65
I_5_80	1.86E-07	7.45E-09	0.732	0.36	4.80E-06	1.06E-07	0.739	0.35
I_M05	1.45E-07	5.33E-09	0.519	0.926	9.30E-06	8.22E-08	0.455	1.2
I_M10	1.48E-07	3.22E-09	0.530	0.886	9.23E-06	2.26E-07	0.451	1.21
I_Oct	8.37E-08	9.57E-10	0.300	2.33	4.76E-06	8.65E-08	0.233	3.29
M-1	2.79E-07	9.70E-09			2.04E-05	1.61E-07		
M-5	2.54E-07	8.41E-09			6.49E-06	7.20E-08		

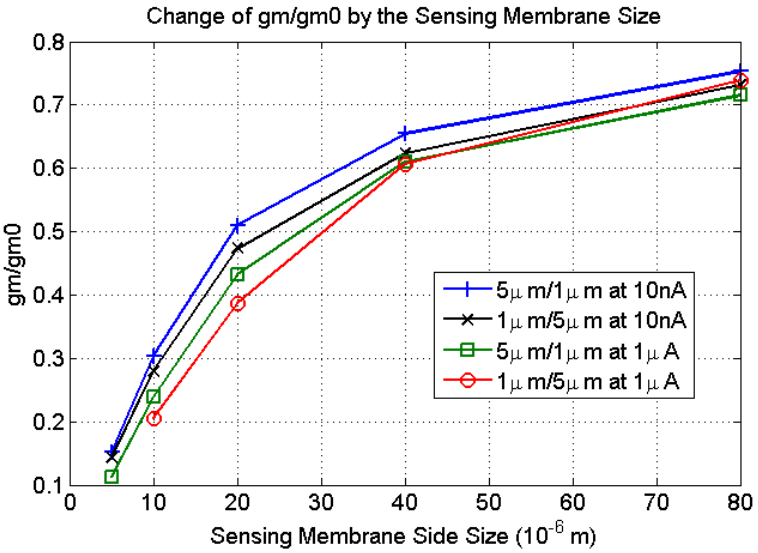

Figure 4.19.: Relative transconductance from experimental results derived using the average values in Table 4.5.

section 4.8.

4.7.3. Threshold and Offset

The ISFETs were tolerating different offsets possibly due to the unknown trapped charge effects. Therefore, it is quite difficult to make an assumption on the relation between the dimensions, and the threshold and offset. In the experiments, sometimes for some ISFETs the offset was so large that the $-5V$ to $+5V$ sweeping of the reference electrode potential could not cover the offset and turn on/off the ISFET. As an example of this difference, measurements at the first

Table 4.6.: Comparison of simulation and experiment results.

	gm at 10nA		*zeta* at 10nA		gm at 1uA		*zeta* at 1uA	
	Simulation	Experiment	Simulation	Experiment	Simulation	Experiment	Simulation	Experiement
I_1_05	2.10E-08	4.23E-08	11.839	5.599	NA	2.31E-06	NA	7.850
I_1_10	6.76E-08	8.57E-08	2.986	2.256	2.95E-06	4.88E-06	5.936	3.186
I_1_20	1.57E-07	1.42E-07	0.719	0.959	8.23E-06	8.83E-06	1.482	1.315
I_1_40	2.29E-07	1.83E-07	0.176	0.526	1.50E-05	1.25E-05	0.366	0.636
I_1_80	2.58E-07	2.10E-07	0.043	0.327	1.87E-05	1.46E-05	0.094	0.400
I_5_05	1.70E-08	3.64E-08	12.556	5.982	NA	NA	NA	#VALUE!
I_5_10	5.64E-08	7.11E-08	3.099	2.572	7.94E-07	1.33E-06	7.132	3.866
I_5_20	1.31E-07	1.20E-07	0.767	1.109	2.32E-06	2.51E-06	1.783	1.589
I_5_40	1.97E-07	1.59E-07	0.176	0.601	4.47E-06	3.94E-06	0.445	0.649
I_5_80	2.23E-07	1.86E-07	0.038	0.366	5.82E-06	4.80E-06	0.111	0.353
I_M05	1.57E-07	1.45E-07	0.719	0.926	8.23E-06	9.30E-06	1.482	1.196
I_M10	1.57E-07	1.48E-07	0.719	0.886	8.23E-06	9.23E-06	1.482	1.215
I_Oct	7.03E-08	8.37E-08	2.835	2.332	3.04E-06	4.76E-06	5.724	3.292
M-1	2.70E-07	2.79E-07			2.04E-05	2.04E-05		
M-5	2.31E-07	2.54E-07			6.46E-06	6.49E-06		

Table 4.7.: ζ ratio showing that area is not the dominant parameter in defining the coupling factor.

ζ Ratio of	at $10nA$	at $1\mu A$
I_1_05/I_1_10	2.441798	2.464379
I_1_10/I_1_20	2.388039	2.421946
I_1_20/I_1_40	1.822532	2.063537
I_1_40/I_1_80	1.60869	1.599072
I_5_05/I_5_10	2.324309	NA
I_5_10/I_5_20	2.315693	2.431763
I_5_20/I_5_40	1.845167	2.448404
I_5_40/I_5_80	1.641469	1.836736

exposure to the analyte at $pH10$, for 5 of the dies, at $10nA$ are provided in Table 4.8. On the other hand, the effect of ζ on threshold voltage is also inherent in these numbers as well as the electrode-electrolyte-insulator junction potentials.

Nonetheless, using the reference MOSFET gate voltages and the extracted ζ values, according to equation (4.14), for each chip and each ISFET, the offset referred to the reference electrode potential ($V_{RefEqOffset}$) was measured.

$$V_{RefEqOffset} = (1 + \zeta)V_{FG} - V_{Ref} \tag{4.25}$$

Among the single-plate ISFETs of $5\mu m \times 5\mu m$, $10\mu m \times 10\mu m$ and $20\mu m \times 20\mu m$ sensing area, the smaller ISFETs show less deviation. However, the population of the derived measurements and their large deviation in general, still prohibits any concrete conclusion other than assuming this offset is totally random.

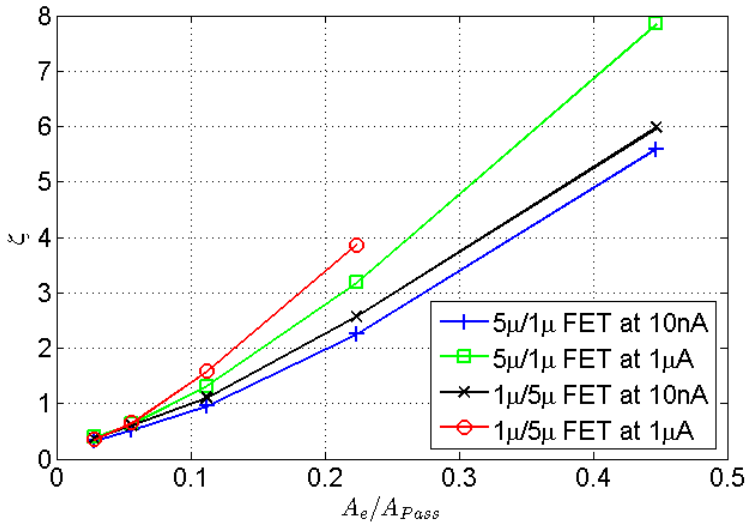

Figure 4.20.: ζ should have been proportional to the area ratio of the FET to sensing membrane according to simulation results, but it is not due to the parasitic decoupling capacitors.

4.7.4. Drift

Drift tests were run for three devices at a time, lasting for about one hour 20 minutes. Reference electrode potential was fixed at a point that would ensure all three devices were on and its current was monitored. Then, at the sweeping stage for extracting the characteristics of the devices, the three devices were tested together to make sure that they do not deviate differently with the drift. Since they were carrying different threshold and offset values, for comparison, their equivalent reference electrode potentials according to their currents over time were calculated.

The measurements show that unlike what had been reported in the literature [132], drift is not necessarily monotonic neither one-directional. However, it does show that it happens faster at the beginning and slows afterwards. Monitoring the reference electrode current allows the hypothesis that the initial monotonic behaviour occurs when the surface or solution is electrically charged and so the primary change is due to the discharge, which is relatively fast. At this phase, the current passing through the reference electrode also follows a similar pattern with large values at the beginning. One may see that the ISFETs with larger area are showing less change; Figure 4.21. Such a pattern may happen if the surface is changing too so that its influence shall be seen less for larger ISFETs as discussed in [171] and section 4.6.

On the other hand, when the current passing through the reference electrode is infinitesimal, here less than $0.5pA$, the direction of drift is not monotonic any more (Figure 4.22) and the smaller ISFETs may even face less drift (Figure 4.23). Figure 4.24 shows the drift for ISFETs with mesh sensing membrane suggesting the single-plate configuration showing less drift[14].

Nevertheless, the common pattern seen here is the direction of the reference electrode current change and the equivalent reference electrode voltage change/drift which are occurring opposite

[14]More measurements shall provide a better conclusion over mesh structure and drift comparison.

Table 4.8.: Reference electrode voltage and equivalent offset referring to the reference electrode at pH10.

	Average V_G or V_{Ref} (V)	**STD** V_G **or** V_{Ref} (V)	Average $V_{RefEqOffset}$ (V)	**STD** $V_{RefEqOffset}$ (V)
I_1_05	3.482	**0.230**	-1.038	**0.214**
I_1_10	1.115	**0.324**	0.094	**0.333**
I_1_20	-1.213	**4.347**	1.902	**4.348**
I_1_40	NA	**NA**	NA	**NA**
I_1_80	0.924	**1.453**	-0.445	**1.445**
I_5_05	4.110	**0.285**	-0.962	**0.255**
I_5_10	-0.189	**1.833**	1.817	**1.826**
I_5_20	-0.853	**4.708**	1.778	**4.720**
I_5_40	0.222	**0.302**	0.499	**0.337**
I_5_80	0.982	**1.429**	-0.368	**1.428**
I_M05	-3.229	**0.438**	3.903	**0.435**
I_M10	-3.319	**0.874**	4.000	**0.895**
I_Oct	0.406	**2.218**	0.776	**2.217**
M-1	0.360	**0.019**		
M-5	0.446	**0.020**		

each other at all the measurements.

4.8. Decoupling Parasitic Capacitors

In the primary simulations, a linear relation between ζ and the area ratio of the FET to sensing area was seen, whereas in the experimental results it appeared non-linear. The reason is believed to be the decoupling capacitors, which may also be a function of the sensing plate dimensions, particularly the ones between the extended floating gate and the substrate[15]. Therefore, equation (4.15b) which was derived based on Figure 4.5, needs to be reformulated for better estimation and judgement of the coupling factor.

$$\zeta = \frac{C_{Dec}}{C_{Pass}} \tag{4.26a}$$

$$\begin{aligned} C_{Dec} &= (C_{Ox}|C_D) + C_{GD} + C_{GS} + C_{GB} + C_P \\ &= C_{eOx} + C_P \end{aligned} \tag{4.26b}$$

$$C_P \approx C'_P.A_{Pass} + C''_P.P_{Pass} \tag{4.26c}$$

[15]Extracted parasitics using Cadence and the process library are provided in Appendix H. An alternative way would be using finite element analysis but here the conclusion is based on the experiment results.

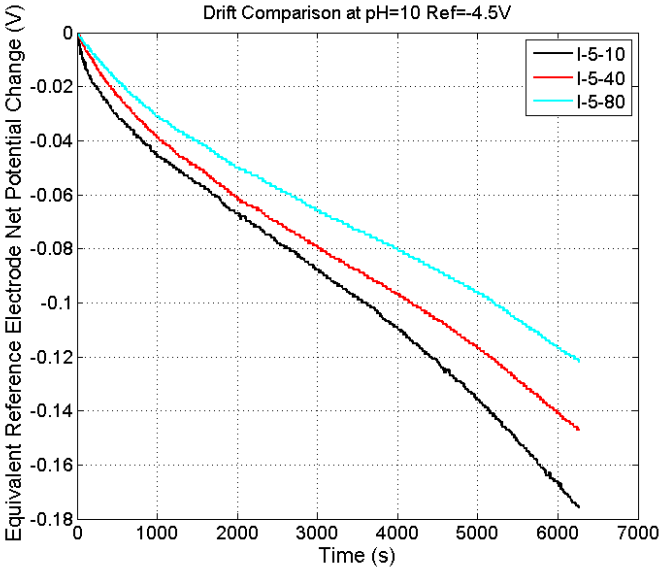

(a) Monotonic drift. Larger ISFET suffers less drift.

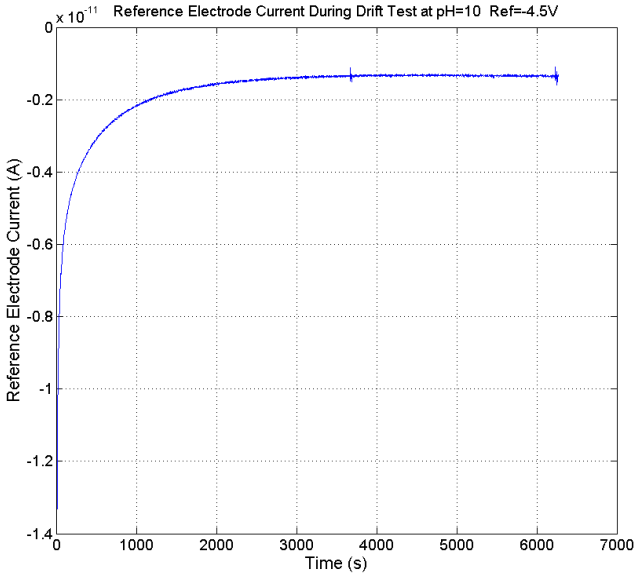

(b) Reference electrode current in a monotonic drift case.

Figure 4.21.: Monotonic drift with less drift for larger acrshortISFET.

C_{Dec} is the total decoupling capacitance made of the MOSFET capacitances, and the parasitic C_P mainly from the extension to the top-metal. Theoretically, C'_{Pass} and C'_P may set a minimum limit on ζ for very large sensing to FET area ratios; equation (4.27).

$$\zeta = \frac{C'_P.d^2 + C''_P.d + C_{eOx}}{C'_{Pass}d^2} \tag{4.27a}$$

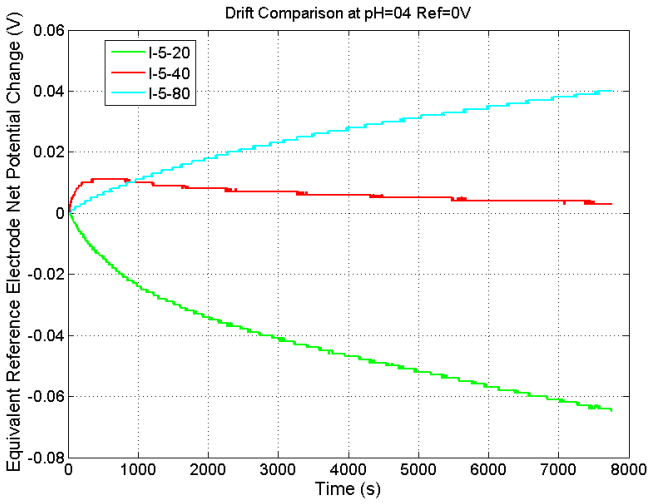

(a) Non-monotonic Drift.

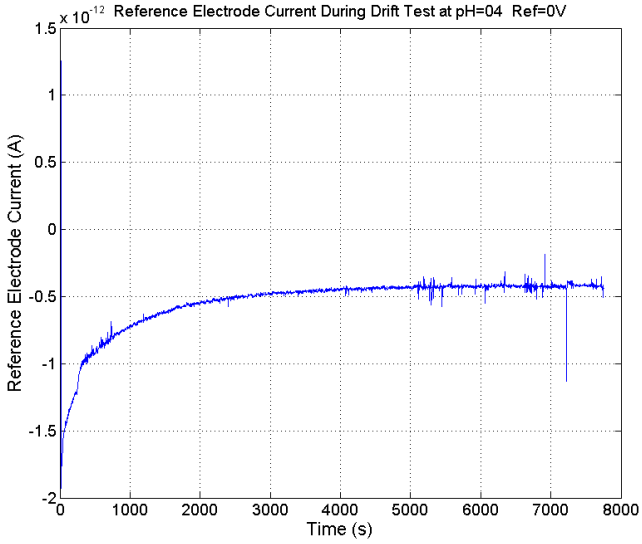

(b) Reference electrode current in a non-monotonic drift case.

Figure 4.22.: Non-monotonic drift.

$$\Rightarrow lim_{d\to\infty}\zeta = \frac{C'_P}{C'_{Pass}} \tag{4.27b}$$

Since the sensing plates were squares of side d and area d^2, for the test ISFETs, equation (4.27) can be written based on the square-root of the FET to sensing area ratio as

$$A_{Pass} = d^2 \tag{4.28a}$$

$$x^2 = A_e/A_{Pass} = 5/d^2 \Rightarrow d = \sqrt{5}/x \tag{4.28b}$$

$$\zeta = \frac{C'_P.d^2 + C''_P.d + C'_{eOx}.A_e}{C'_{Pass}d^2} \tag{4.28c}$$

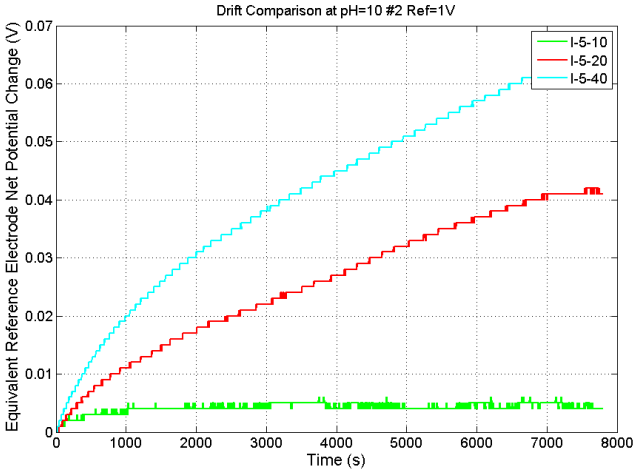

(a) Non-monotonic drift where ISFETs with smaller area may suffer less drift.

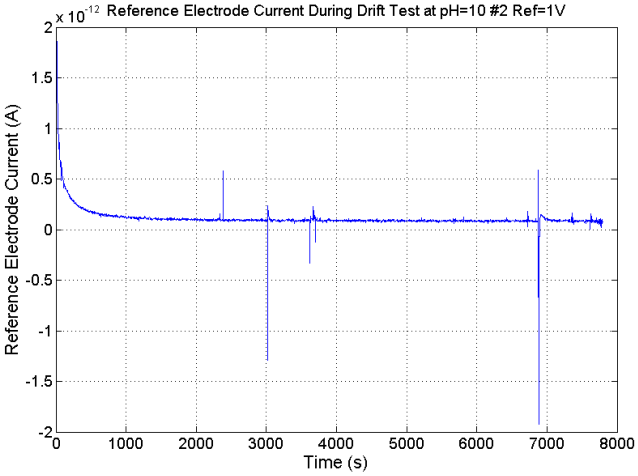

(b) Reference electrode current in a non-monotonic drift case where smaller ISFETs suffer less drift.

Figure 4.23.: Drift measurement with very low reference electrode leakage current.

$$= \frac{C'_{eOx}}{C'_{Pass}} x^2 + \frac{C''_P}{\sqrt{5} C'_{Pass}} x + \frac{C'_P}{C'_{Pass}} \tag{4.28d}$$

The derived ζ values are drawn and fitted quadratically in Figure 4.25. The curve-fit coefficients are provided in Table 4.9 and Table 4.10 which show that based on equation (4.28), the reason for deviation of the ζ from a linear relation in Figure 4.20 is mainly due to the perimeter-dependent capacitance[16] C''_P.

These results suggest that for a high coupling factor not only the sensing area to FET area should be large enough, but also the perimeter should be minimum. On the other hand, the

[16] A hypothesis may be that the trapped charges distribution in the metals. Electrical charges are keen on accumulating at the edges and outer surfaces of a metal. Hence, signifying the metal perimeter to substrate influence in the measurements. This hypothesis is drawn in Appendix F.

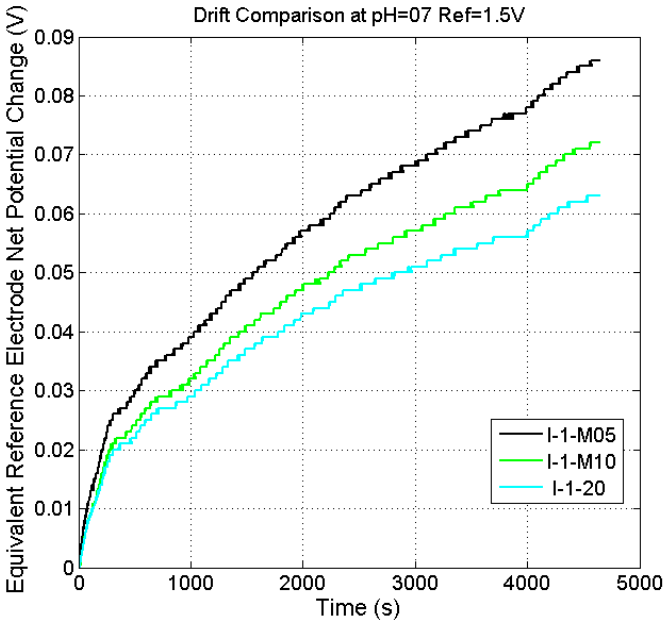

(a) A mesh sensing membrane giving the same area may not necessarily help with drift.

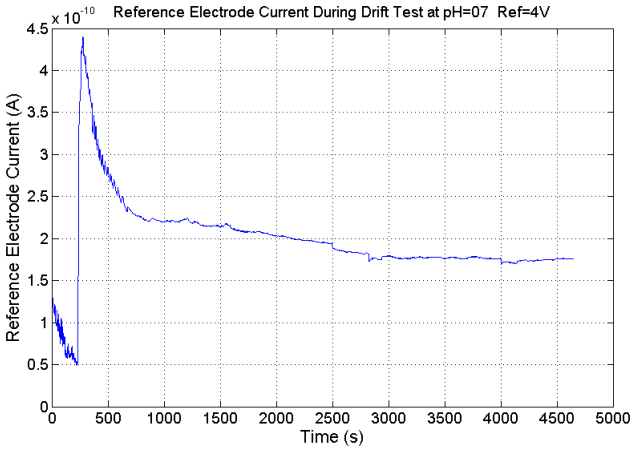

(b) Reference electrode current during drift comparison of a mesh sensing membrane.

Figure 4.24.: Drift measurement for ISFETs with mesh sensing membrane.

octagonal-shape ISFET I_Oct, with slightly higher area and lower perimeter in comparison with I_1_10, is not giving a better coupling (its ζ is larger); Table 4.5. It might be due to larger decoupling capacitors at the more corners (8 against 4) of the sensing membrane. In addition, the meshed-surface ISFETs of I_M05 and I_M10 give slightly better performance compared to similar ISFET of I_1_20 which may be due to their larger effective area.

In conclusion, the ζ-based (or area-ratio based) approach may emphasise the influence of decoupling capacitances and suggest that the ISFETs higher performance may be made of low FET area and relatively large sensing plates of square shape, which for certain transconductances requires a tread-off between power, area and coupling factor; and proper configurations or

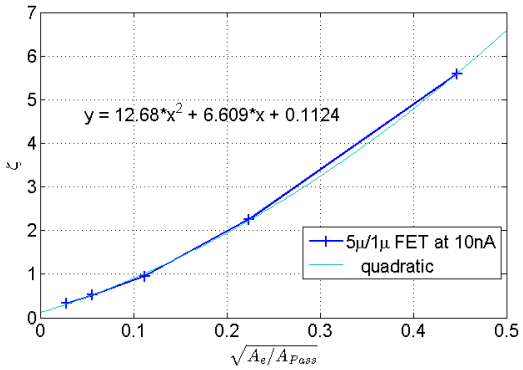

(a) ISFETs of $5\mu/1\mu$ FET at $10nA$.

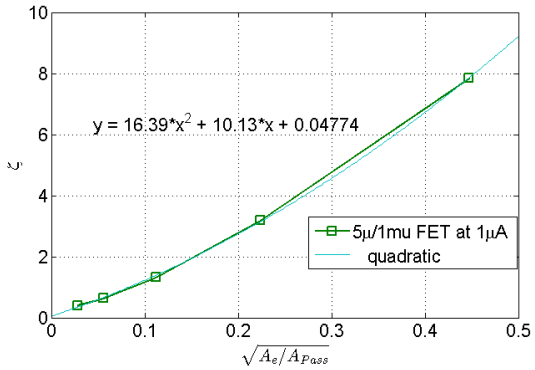

(b) ISFETs of $5\mu/1\mu$ FET at $1\mu A$.

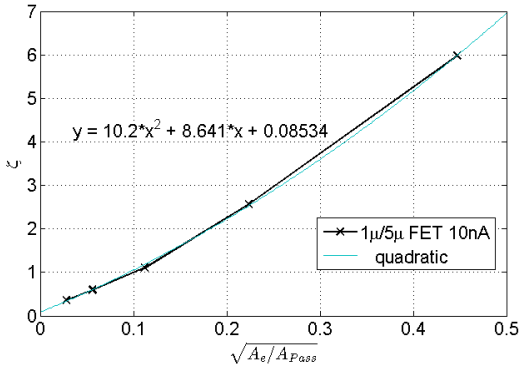

(c) ISFETs of $1\mu/5\mu$ FET at $10nA$.

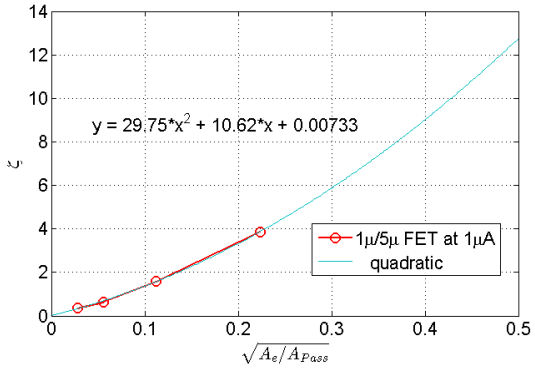

(d) ISFETs of $1\mu/5\mu$ FET at $1\mu A$.

Figure 4.25.: ζ versus the root of the FET to sensing area ratio $\sqrt{A_e/A_{Pass}}$, and the quadratic curve fit.

interface circuits that can suppress the decoupling effects.

4.9. Buffer Shield

Based on the experiment results showing a significant effect of decoupling parasitics from the sensing plate to the substrate, particularly the perimeter, the buffer shield is proposed for the future ISFET devices.

The idea is to have a metal plate beneath the top-metal sensing plate, shielding it from the substrate. But, in order to do so and to not add further decoupling, it should follow the same potential changes as on the top-metal. Consequently, the voltage on the floating-gate of the ISFET has to be buffered to the shield. The buffer shield may be used by any of the source-follower configurations in the readout circuits discussed in Chapter 5 section 5.1.1. Figure 4.26 suggests two configurations, one with directly connecting the shield to the source when the readout is a source-follower, and the other is to connect it to a buffering output of the readout.

Table 4.9.: Curve-fitting coefficients ($\zeta = P2.x^2 + P1.x + P0$) for ζ versus $x = \sqrt{A_e/A_{Pass}}$.

	$P2.x^2$	$P1.x$	$P0$	R
5u/1u at 10nA	12.682	6.609	0.1124	0.9998
5u/1u at 1uA	16.391	10.134	0.0477	0.9997
1u/5u at 10nA	10.196	8.6409	0.0853	0.9996
1u/5u at 1uA	29.754	10.616	0.0073	0.9996

Table 4.10.: Curve-fitting coefficients ($\zeta = p2/d^2 + p1/d + p0$) for ζ versus $1/d$.

	$p2/d^2$	$p1/d$	$p0$	R
5u/1u at 10nA	63.409	14.778	0.1124	0.9998
5u/1u at 1uA	81.954	22.661	0.0477	0.9997
1u/5u at 10nA	50.98	19.322	0.0853	0.9996
1u/5u at 1uA	148.77	23.738	0.0073	0.9996

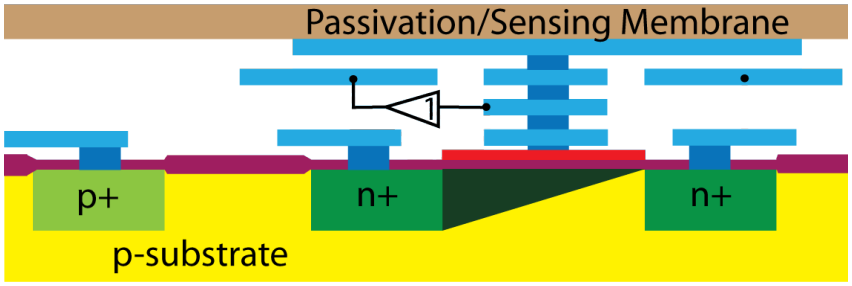

(a) A metal sheet below the top-metal sensing plate, surrounding the ISFET gate extension-vias connectors, and the edge of the top-metal plate, connected to a buffer of the floating-gate, may eliminate the top-metal to substrate decoupling parasitics effects.

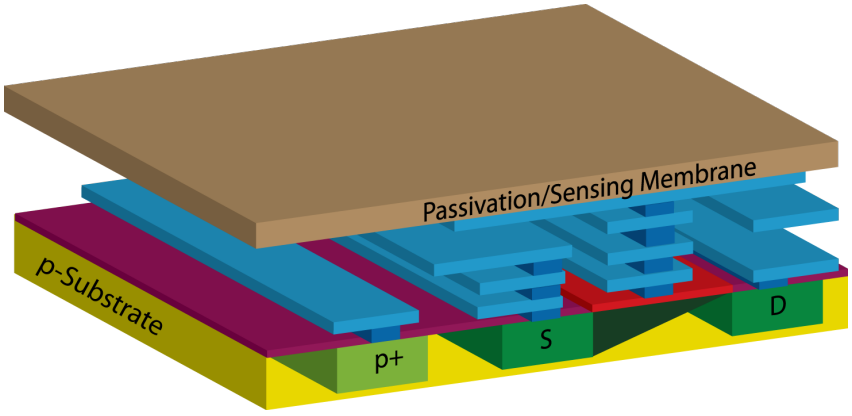

(b) A 3D overview of the Buffer Shield.

Figure 4.26.: Buffer shield overview for enhancing the ISFET coupling by shielding the top metal sensing plate from the substrate.

4.10. Design Trade-offs

Introducing ζ in section 4.3 into the ISFET voltage-current characteristics, and showing the dependency of ζ and the coupling on the dimensions, which influences the ISFET transconduc-

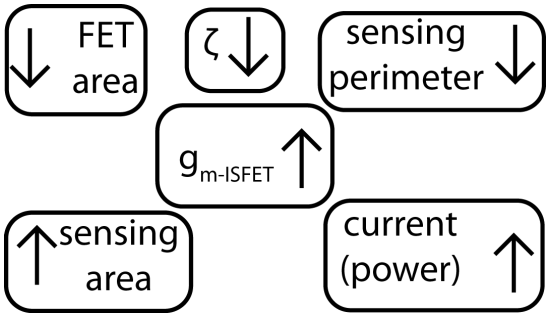

Figure 4.27.: ISFET design trade-offs.

tance and threshold voltage, reveals the trade-off in performance/limit of detection, area, and power; Figure 4.27.

On account of equation (4.24), for a certain transconductance, either the intrinsic FET transconductance needs to increase by current, or the area of the sensing membrane (to reduce ζ). For a higher precision (smaller limit of detection and higher resolution), to reduce the input-referred noise, based on equation (4.18), more area may be used for smaller ζ, or more power can be consumed to reduce the electrical noise. Similarly, to reduce the threshold, either have a higher supply compensating the smaller ISFET sensing to FET area-ratios (resulting in large ζ and threshold), or make the sensing plate big enough.

For example, comparing the smallest device (I_1_05) with highest ζ of 7.85 (a coupling factor of $1/(1+7.85) = 0.11$) with the largest device tested in this study (I_1_80) with ζ of 0.4 (a coupling factor of $1/(1+0.4) = 0.71$), considering a pH sensitivity of $50mV/pH$, converting 0.01 pH change with an ADC of $0.25mV$ least significant bit requires more than 4.5 times amplification for the smaller ISFET but no amplification for the larger one.

In addition, with the desire for deep sub-micron processes where better matching and smaller pitches allow high-density ISFET arrays, the trade-off may be more demanding as the thinner gate oxides (relatively higher gate oxide decoupling capacitance) and higher low-frequency noise, further influence the limit of detection and performance [104, 106, 108]. C'_{eOx} is inversely proportional to the gate oxide thickness ($C = \epsilon Area/Thickness$). The other alternative is etching away the passivation and replacing it with a thin insulator of higher permittivity like Ta_2O_5; Table 4.1.

Nevertheless, it should be noted that, besides the discussed geometrical effect on the decoupling parasitics, any readout circuit has to eliminate the Miller effect on the gate-drain capacitance which may magnify its decoupling effect. With the 180 deg phase difference between the gate and the drain, any potential amplification from gate to drain, as in common-source configurations, can enlarge the gate-drain decoupling capacitance. Therefore, the drain voltage should either be fixed or follow the floating-gate potential.

4.11. Summary

In this chapter the Ion-Sensitive Field Effect Transistor (ISFET) was described as a non-Faradaic sensor and a floating-gate device compatible with CMOS technology. Its operation was explained based on Gouy-Chapman and site-binding theories, showing its pH sensitivity dependency on the sensing membrane buffering capacity and temperature. ISFET non-idealities like DC offset and drift were also discussed.

The ISFET signal on the sensing membrane is capacitively coupled onto the floating gate of the intrinsic FET. Due to other capacitances at the gate, like the gate-body, gate-source, gate-drain, etc, only a fraction of the voltage signal may appear on the gate. The decoupling to coupling capacitance ratio was summarised in term ζ and more complete formula were provided for description of the ISFET voltage-current characteristic.

ζ-based design was introduced to take into account the decoupling effects and properly size the ISFETs. It was shown that the ratio of the sensing area to the FET area is a key factor particularly in unmodified CMOS ISFETs. The relatively thick Si_3N_4/SiO_2 passivation protection layer is used as the sensing membrane which is subject to consequential variations. A $0.35\mu m$ process was used to study the ζ and dimension behaviour.

Experiments of 8 dies at pH buffers of 4, 7 and 10, for 15 devices per die, in a Faraday cage, using $Ag/AgCl$ reference electrode and KEITHLEY 4200 device characterisation instrument, showed ζ (and so the coupling factor) dependency on the ratio of the sensing area to the FET area, as well as the perimeter of the sensing top-metal plate. The main decoupling capacitances were the gate oxide and the top-metal to well/substrate parasitics. ζ and area-ratio relations were derived and accordingly design trade-offs for optimum ISFET transconductance were discussed. A potential solution for the future ISFETs in reducing the decoupling effects of the top metal parasitics was described.

In addition, in drift studies an inverse relation of the drift direction and the reference electrode current was observed, which would suggest a potential means for controlling drift and predicting its direction. It is understood that the first phase of drift that shows faster change might be due to the pre-charge of the sensing membrane and its different potential than the reference electrode or the analyte. Whereas at very low sub-pico ampere currents of reference electrode, the drift in signal was not monotonic. Moreover, it was explained that one may suppress the drift influence in result of the sensing membrane degradation, by proper sizing for low ζ. Coupling factor is inversely related to ζ which itself is inversely proportional to the sensing membrane coupling capacitance. The coupling factor sensitivity is less for smaller ζ values and so is its sensitivity to the sensing membrane variation (either in result of process or chemical modification).

In the end, design trade-offs among area, coupling factor, transconductance, resolution, and power were discussed along with potential scaling effects. Following chapters will focus on the interface circuits trying to tackle some of the ISFET issues, particularly for genotyping and sequencing microchips.

5. Analogue Readout Circuits

While sensors create a bridge from the world of chemical and physical behaviour to the world of electronics, it is the art of engineering that with intelligence makes this translation meaningful. Chapter 2 described several aspects for an instrument monitoring (bio)chemical traits. Limit of detection, resolution and dynamic range of sensing arrays that enable running parallel tests were the specifications defining the merit of a system over another. Focusing on DNA sequencing and genotyping, Chapter 3 discussed the performance criteria for the ISFET-based systems where scaling, area utilisation for high yield and throughput, and low-level signal processing, highlighted the importance of developing intelligent design approaches.

Higher throughput is attractive for the larger coverage of a target DNA, but accuracy is the key to validate the usability of the produced data. Therefore, extensive effort is made on signal processing. In the discussed pH-based DNA detection systems, the processing performance is dependent on all stages of the operation including the ISFET sensors and the readouts.

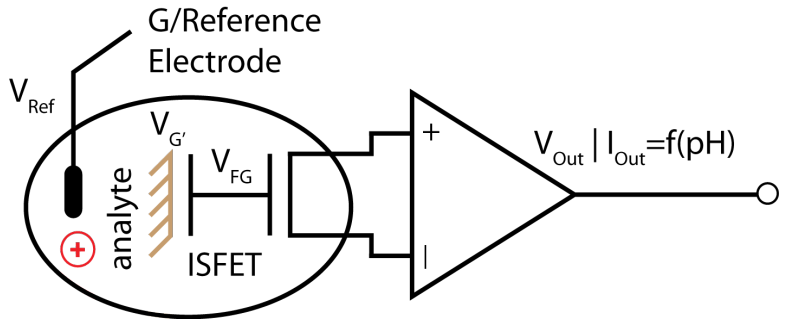

Figure 5.1.: ISFET readout provides an output current or voltage that is a function of the ions concentration.

In this chapter, readout circuits are reviewed and new ones are introduced. In a readout circuit, the ISFET is biased at a certain operating point and allows tracking of the changes on its floating-gate and so the induced chemical signal. A readout circuit is an interface/bridge between the ISFET and the signal processing units. The signal that a readout takes from the ISFET, is from the coupling of the potential on its sensing membrane insulator onto its intrinsic floating-gate. The sensing membrane potential ($V_{G'}$) is modulated by the ionic concentration ($pH = -log[H^+]$) and electrode-electrolyte-insulator junctions (γ). The analyte bulk is biased by a reference electrode (V_{Ref}). Chapter 4 explained the ISFET operation as well as its issues such as DC offset, signal drift and temperature dependency of the sensitivity. It provided further details on the signal coupling and the geometry of the ISFET. The coupling is dependent on the ratio of the total decoupling capacitance to the coupling capacitance (ζ). This relation is

summarised in equation (5.1)[1].

$$V_{FG} = \frac{V_{G'}}{1+\zeta} \tag{5.1a}$$

$$V_{G'} = V_{Ref} - V_{Chem} \tag{5.1b}$$

$$V_{Chem} = \gamma + S_{pH}.pH \tag{5.1c}$$

$$S_{pH} = \alpha \frac{kT}{q} ln(10) \tag{5.1d}$$

Having the pH-based sequencing and genotyping in mind from Chapter 3, the readouts will be compared based on scalability and possibility of in-pixel processing. Two new readout configurations are suggested by the author, one for the point-of-care genotyping with small-scale (dozens to thousands of ISFETs) arrays allowing on-chip and potentially in-pixel processing, and one for the large-scale (millions to billions of ISFETs) sequencing arrays background noise suppression.

For small-scale arrays of ISFETs like for genotyping, perhaps readouts with in-pixel signal processing would be preferable in low power hand-held devices. In an unmodified CMOS lab-on-chip, a manifold sitting on top of the micro-chip creating analysis chambers can limit the pitch of the sensors to a relatively large minimum. Therefore, the underneath FETs may be distant enough to have the gap filled by the readout circuit for each pixel/chamber. In genotyping, the temperature change for the thermal cycling amplification of DNA samples adds the influence of temperature on pH measurement too. A new readout eliminating such effects is proposed by the author.

In a very large-scale integrated array of sensors, for example sequencing, the ability to share the readout/interface among a fairly large sub-set of ISFETs is crucial. This forces recording and digital processing of the measurements including all the common-mode signals, whereas if an on-chip analogue scheme for removing the common-mode noise was possible, the processing load would have been relaxed. The on-chip processing area appeared to be another factor in defining what portion of the chip could be allocated to the sensors. For instance, about 2/3 of the first generation sequencing chip was the interface circuits and 1/3 the ISFETs (Chapter 3 Figure 3.10b). A new bulk-based common-mode rejection scheme as well as a physical implementation method is proposed by the author for suppressing the background and common-mode noise in the array readout.

5.1. Readout Circuits

The primary readout circuits introduced only buffer the potential changes on the floating-gate of the ISFET, leaving any processing or calibration separate from the interface. The succeeding

[1] In this equation k is the Boltzmann constant, T the absolute temperature, q the electron charge, and α the non-ideal sensitivity (sub-Nernstian sensitivity) factor.

works however tried to tackle part of the ISFET issues, such as random DC offset on the floating-gate, signal drift in a constant pH, and temperature dependency.

Limit of detection, linearity, and dynamic range can be critical depending on the design and application, where accurate measurement is necessary like in quantitative PCR for gene expression analysis. It might be less challenging where only a discrimination is required and the chemical signal is powerful enough to avoid any uncertainty or noise influence. Moreover, Chapter 4 explained that the geometry and operating region of the ISFET could influence the coupling and consequently the accuracy. For instance, when the coupling factor is small, operation in weak inversion may result in more variation than when biased at velocity saturation, despite benefiting less power consumption. This makes the readout non-linear.

Readouts with analogue outputs in the literature may be categorised into 5 general groups:

- **Basic Readouts** where the output voltage or current only conveys the coupled potential on the floating-gate, as does a buffer.
- **REFET-based Readouts** where unwanted common-mode signals are differentiated through comparison/differentiation from a reference ISFET/MOSFET.
- **PG-ISFET Readouts** where a programmable gate is added to the ISFET floating-gate via a control capacitor to tune and cancel the DC offset.
- **Translinear Readouts** where the ISFET is biased at weak inversion and normally an output current insensitive to the temperature is provided along with analogue computation.
- **Averaging Arrays** where an array of ISFETs, normally each paired with one of the above readout types, averages the signal from a set of ISFETs.

Another categorisation may divide them into linear (the basic readouts with follower configuration), linear differential (ISFET-REFET), linear with calibration (PG-ISFET-based), translinear and averaging readouts.

5.1.1. Basic Readouts

In the basic readouts, there is no processing of the measured signal and it is conveyed onto an output current or voltage. A basic configuration may be a source-follower, or a more complex configuration with feedback; Figure 5.2.

$$I_D = I_{D0} e^{V_{FG}/nU_T}[e^{V_S/U_T} - e^{-V_D/U_T}] \qquad \textit{Weak Inversion} \qquad (5.2a)$$

$$I_D = \mu_n C_{Ox} \frac{W}{L}[(V_{FG} - V_S - V_{th-ISFET})V_{DS} - \frac{V_{DS}^2}{2}]$$

$$\textit{Strong Inversion Triode} \qquad (5.2b)$$

$$I_D = \frac{\mu_n C_{Ox}}{2} \frac{W}{L}(V_{FG} - V_S - V_{th-ISFET})^2 \times$$

$$[1 + \lambda(V_{DS} - V_{DS-Sat})] \qquad \textit{Velocity Saturation} \qquad (5.2c)$$

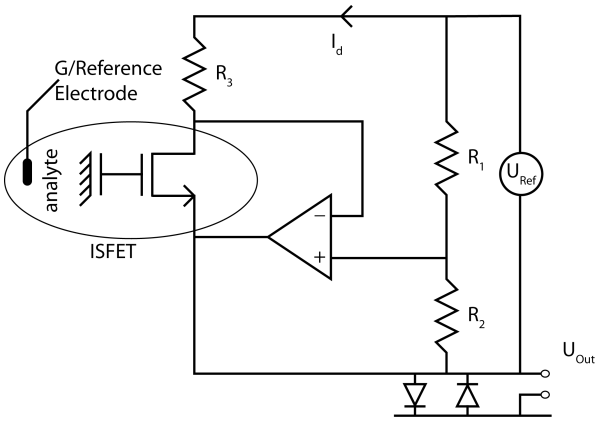

(a) Drain-source-follower redrawn from [114].

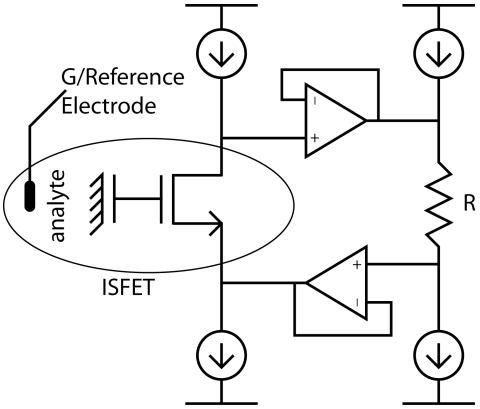

(b) A conventional drain-source-follower.

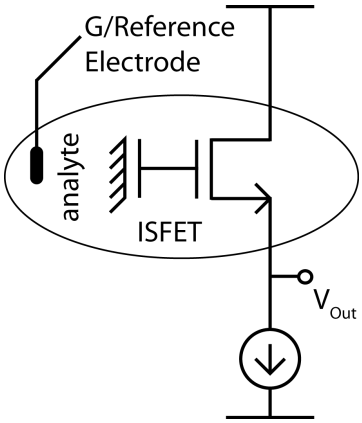

(c) Source-follower.

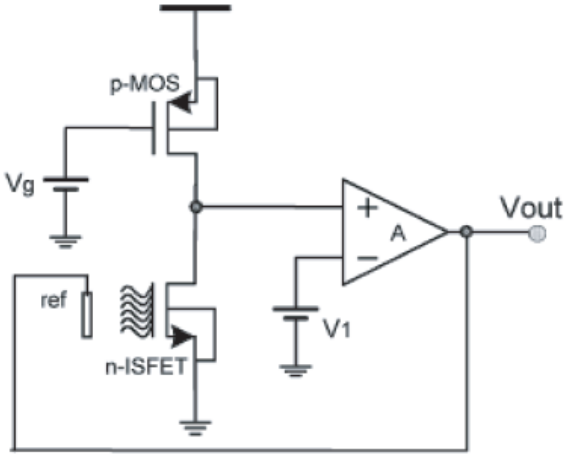

(d) Feedback-to-gate [172].

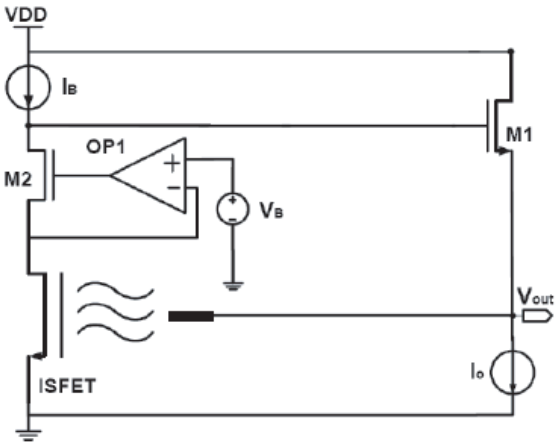

(e) Feedback-to-gate [173].

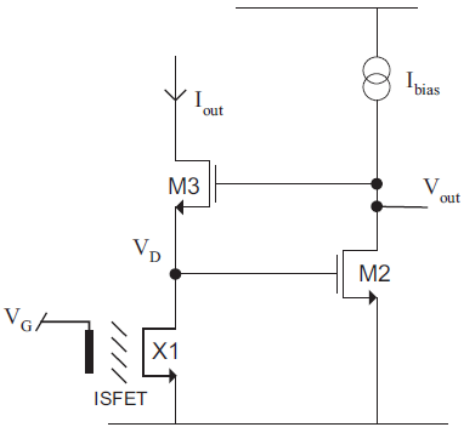

(f) Voltage-clamped [174].

Figure 5.2.: Basic readouts.

Drain-source Follower

Figure 5.2a and Figure 5.2b show the conventional drain-source-follower readouts. Through the feedback configuration and bias currents, the potential difference between the terminals and the drain current of the ISFET are kept constant. Therefore, any change coupled on the floating gate is tracked and buffered by the source and drain terminals. Figure 5.2c is a common-drain source-follower similarly buffering the input but with an attenuation for the limited transconductance of the common-drain configuration.

The advantage of the drain-source-follower is its linearity; but at a cost of area for the buffers, and sensitivity to the matching of the current sources. It does not do any processing and its operation range is limited by the supply rail. If a large offset is on the floating gate, it will be clipped.

Feedback to Gate

In the feedback-to-gate configuration, Figure 5.2d and Figure 5.2e, similar to the drain-source-follower, through feedback the drain current and the transistor terminal potentials are kept constant, but this time by readjusting the remote gate/reference electrode. The advantage of this configuration is the possible removal of DC offset effect if the reference electrode potential can cover a suitable range for cancelling out the offset effect. Also, with the feedback to gate, the decoupling capacitors effect[2] is removed, however scalability is an issue for large-scale integrated arrays.

Voltage Clamped

In a voltage-clamped configuration, Figure 5.2f, the potential at each of the terminals is fixed and the output current changes as a function of the pH. The linearity at this configuration is limited by the supply range and the cascode regulating transistor $M2$ operation in saturation. The ISFET may be biased at velocity saturation to give a linear voltage (pH) relation, or in weak inversion with an exponential characteristic.

5.1.2. REFET-ISFET Differential Pair

Reference FET (REFET) was introduced to reduce the noise and drift effects on the measurements. A REFET would experience a similar condition as an ISFET except the chance of responding to an occurring chemical reaction; Figure 5.3. This can be implemented in two ways. One way is to make REFET like an ISFET but with an insensitive membrane [114]. Another way is to make REFET completely the same as ISFET, but isolated and exposed to an analyte where no reaction may occur [74, 76].

Another configuration may be a conventional differential pair replacing one or both of the input transistors with ISFET or ISFET and REFET. An ISFET/MOSFET differential pair

[2]In Chapter 4 the ISFET coupling efficiency is explained and the parasitics degrading the coupling efficiency are explained.

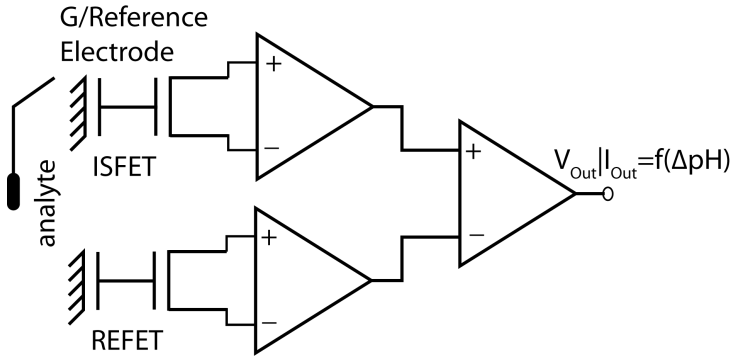

Figure 5.3.: ISFET-REFET differential measurement [114].

[175] may help in suppressing the electrical noise and an ISFET/REFET differential pair may help both electrical and chemical noise[3] reduction. However, besides the DC offset issue that may bias the ISFETs and REFETs out of the active region causing the circuit to stack to the power/ground rails, the gate-drain capacitance may degrade the signal (further discussed in Chapter 4 section 4.11). The drain node is not fixed and it is not following the gate. Therefore, with the Miller effect, the gain between the gate and the drain terminals of the ISFET/REFET, an equivalent larger decoupling capacitor appears on the floating-gate, degrading the signal coupling.

Nevertheless, while any ISFET may require a calibration of the reference electrode to overcome its random DC offset, differential measurements also require further calibration between the reference FET and the ISFET which makes it complicated for implementation in the ISFET arrays, particularly for large-scale arrays[4].

5.1.3. PG-ISFET

To overcome some of the ISFET issues, particularly the DC offset, based on multi-gate MOSFET structure Georgiou [177] introduced a programmable gate by adding a control capacitor (C_{CG}) to the ISFET floating gate; Figure 5.4. C_{Pass} is the sensing membrane or the passivation in unmodified CMOS. The trapped charge (V_{tc} offset) in the passivation can be cancelled out by properly tuning the control voltage V_{CG}; equation (5.3). If the drift trend was clear ($d(t)$: drift over time), then a similar change at the control gate could cancel that out too; equation (5.4). Drift has so far appeared random and not completely predictable[5].

$$C_{pass}V_{tc} = -C_{CG}V_{CG} \tag{5.3}$$

$$V_{CG}(t) = \frac{-C_{pass}.d(t)}{C_{CG}} \tag{5.4}$$

[3]Other configurations such as Wheatstone bridge were also investigated in [175].
[4]An example of such work developed by the author is [176].
[5]Perhaps potentially by the use of the reference electrode current as described in Chapter 4 section 4.7.4.

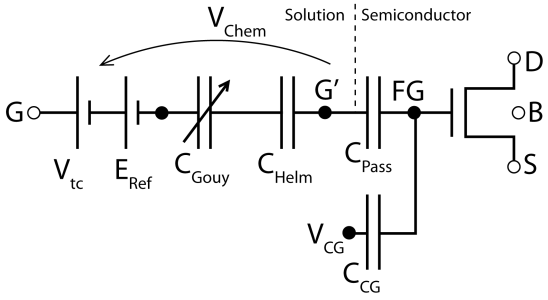

(a) PG-ISFET macro-model [177].

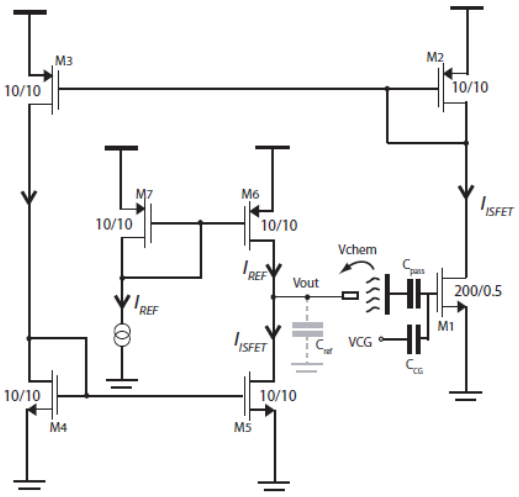

(b) A PG-ISFET adaptive readout [177].

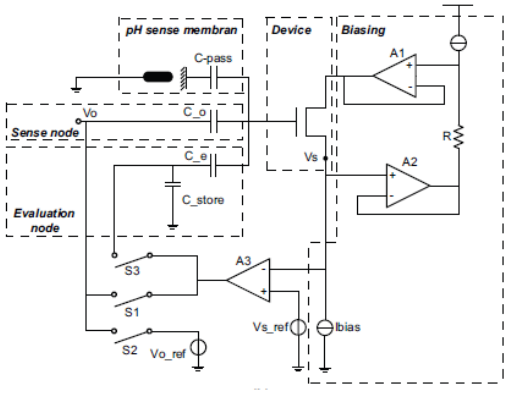

(c) Auto-offset removal readout [178].

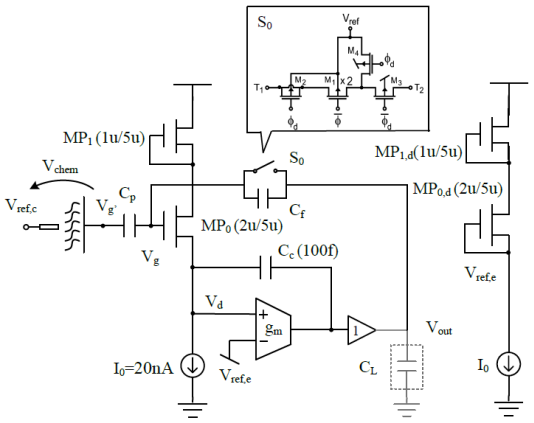

(d) Direct capacitive feedback readout [179].

Figure 5.4.: PG-ISFET readouts.

Using the programmable gate, several readouts/systems were developed to not only convey the pH changes, but also to tackle the DC offset. Some of these are depicted in Figure 5.4. Inherent in some of them is the aforementioned basic readouts.

Auto Offset Removal

In this configuration, Figure 5.4c, Liu [178, 180, 181] uses one programmable gate for evaluation of the offset and another for sensing, through the feedback amplifier and switching between sensing and evaluation modes. In the evaluation, the offset is cancelled out and the control voltage is stored on C_e. In the sensing mode, C_o tracks the changes. The advantage is that the readout signal is not affected by the dimensions, as it depends on the ratio of the sensing capacitor to the passivation coupling capacitance.

Direct Capacitive Feedback

Hu and Georgiou [179] directly reset the floating gate and tracked the changes through a feedback and a program gate in order to tackle the DC offset issue; Figure 5.4d. Similarly, this allows tracking the changes in between the resetting times, but not the total change.

While the programmable gate adds a degree of freedom in tuning the ISFET, it comes at a cost of the area and scalability. In particular, the decoupling capacitors increase and so the distance of the programmable gates and their accompanying decoupling parasitics needs to be precisely taken into account in the layout. In the reset-and-change-track configurations, certainly an integrator may help in keeping track of the total change over a longer period than the switching cycles.

5.1.4. Translinear Readouts

Based on the translinear circuits principle [182], Shepherd and Toumazou developed the biochemical translinear principle [183] which allowed current-mode processing on the chemical signal. The readouts based on this principle operate the ISFET in weak inversion. In these circuits the temperature effect on the pH sensitivity is eliminated by the intrinsic FET similar temperature dependency when operating in weak inversion[6].

H-Cell

pH is the logarithm of the inverse of H^+ concentration ($pH = -log[H^+]$). The voltage on the sensing membrane is linearly proportional to pH because of the exponential relation between the concentration and the potential in the analyte (Chapter 4, section 4.1). On the other hand, the MOSFET current in weak inversion has an exponential relation with its gate-source voltage.

$$[H^+]_i = [H^+]exp(\frac{-q\phi_i}{kT}) \tag{5.5}$$

$$I = I_{D0}exp(V_{GS}/nU_T)exp((n-1)V_{BS}/nU_T); U_T = kT/q \tag{5.6}$$

In equation (5.5) the relation between the concentration at the insulator surface $[H^+]_i$ and the concentration at the analyte bulk $[H^+]$ by the potential difference ϕ_i is shown (complete description in Chapter 4). Equation (5.6) is the weak inversion current-voltage of the MOSFET where I_{D0} is the reverse p-n junction current of the transistor, n the slope factor, k the Boltzmann constant, q the electron charge, T the temperature, V_{GS} the gate-source voltage, V_{BS} the bulk-source voltage, and U_T the thermal voltage. Based on these relations, Shepherd [183–185] developed the H-Cell interface depicted in Figure 5.5a.

The ISFET current, derived in equation (5.7) becomes an exponential function of the ion concentration, but with a power of α/n. In Figure 5.5a, V_{ref} biases the ISFET-MOSFET mirror pair ($M1$ and $X2$) at weak inversion, and the dynamic range of operation is limited to

[6]This does not include the reference electrode temperature sensitivity effect.

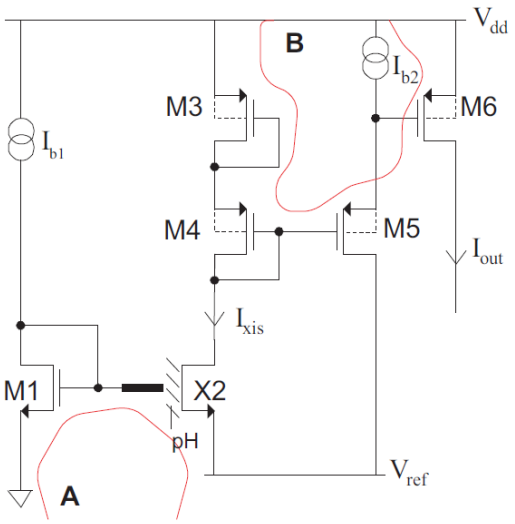

(a) H-Cell [183].

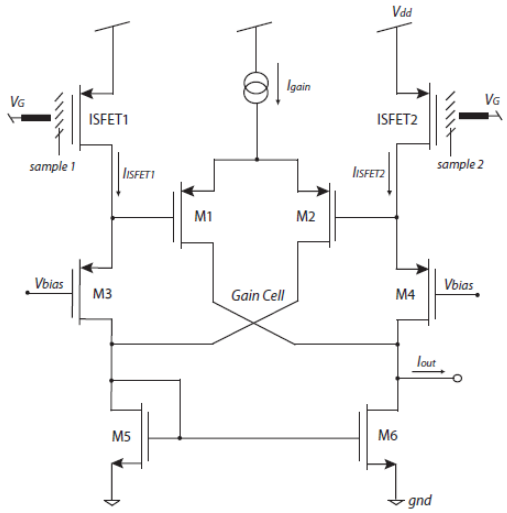

(b) Chemical Gilbert cell [186].

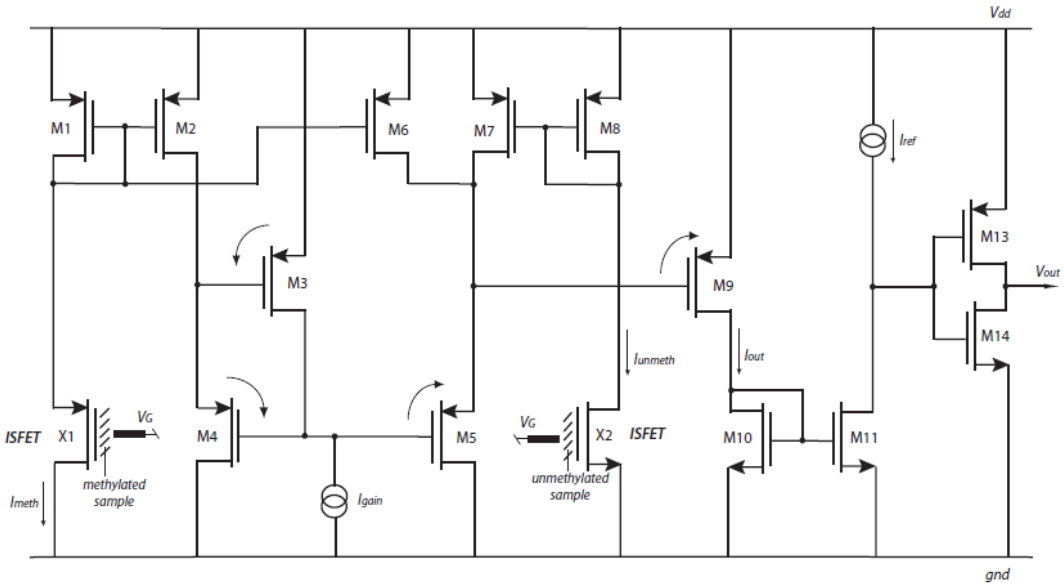

(c) DNA methylation cell [187].

Figure 5.5.: Translinear readouts.

the range they are kept in weak inversion. γ is the non-pH related parameters from the reference electrode to the surface of the ISFET.

$$I_{ISFET} = I_{b1} exp(-\gamma/nU_T) exp(-V_{ref}/U_T)[H^+]^{\alpha/n} \tag{5.7}$$

The PMOS transistors operating in weak inversion square the current in a translinear loop. In case α/n is 0.5, it may give a linear output function of the concentration. However, this is quite complex especially as the slope factor n changes by the voltage change on the gate.

Ideally when setting $I_{b2} = I_{b1}$,

$$I_{out} = I_{b1} exp(-2\gamma/nU_T) exp(-2V_{ref}/U_T)[H^+];\ If\ \alpha/n = 0.5 \tag{5.8}$$

Chemical Gilbert Cell

Kalofonou et al [186, 188, 189] developed a chemical Gilbert cell for the detection of DNA methylation. The chemical Gilbert cell allows differential measurement between the output currents of two ISFETs with a tunable gain input current. The output current is proportional to the difference in pH and controllable through the bias current I_{gain}; $I_{out} = A\Delta pH$, Figure 5.5b.

Kalofonou et al [187] also developed a current-mode divider which could calculate the ratio of currents from a pair of ISFET and REFET for the detection of DNA methylation; Figure 5.5c.

The advantage of weak inversion operation in terms of power is clear, while the similarity in the device characteristic and the analyte ionic interactions makes it even more attractive in order to eliminate the temperature influence on the readout (the thermal voltage kT/q in pH-sensitivity and weak inversion current-voltage characteristic). Moreover, Chapter 4 shows that decoupling (parameter ζ in equation 5.1) is less when operating in weak inversion. They may be therefore advantageous for small-scale arrays, but for scaling to large levels of integration, with the DC offset effect, biasing needs calibration and the operation becomes complex to tune each transistor for weak-inversion operation.

5.1.5. Averaging Arrays

Shepherd [125] and Chan et al [190, 191], proposed arrays of ISFETs with averaging instrumentation, by summing the current from different pixels, each with one of the basic readouts described (voltage-clamped and source-follower respectively). Shepherd's work (Figure 5.6a) simply averages out the current from the ISFETs using current-mirrors but Chan's work (Figure 5.6b), through a feedback configuration, outputs an average voltage from the source-follower readout.

In Figure 5.6b R_f and R_g make the feedback path from the output to the source of each ISFET. The ISFETs are biased by current sources of the same value I_0. Assuming they were biased in weak inversion, by ignoring the bulk effect and channel length modulation, the source voltage (v_xk) for each ISFET k with current (i_k) was derived to be

$$v_{xk} = V_G - V_{thk} - nU_T ln(\frac{i_k}{2n\beta_k U_T^2}) \tag{5.9}$$

where β is the gain factor of the transistor and n its weak inversion slope factor. The output voltage was calculated to be

$$v_{out} = (1 + \frac{R_f}{R_g})\frac{\Sigma(v_{xk})}{N} \tag{5.10}$$

However, besides area and matching, DC offset can still influence the output particularly in the former structure where the offset can keep an ISFET in a different region or completely off so that the signal rather than being improved, is further divided/attenuated.

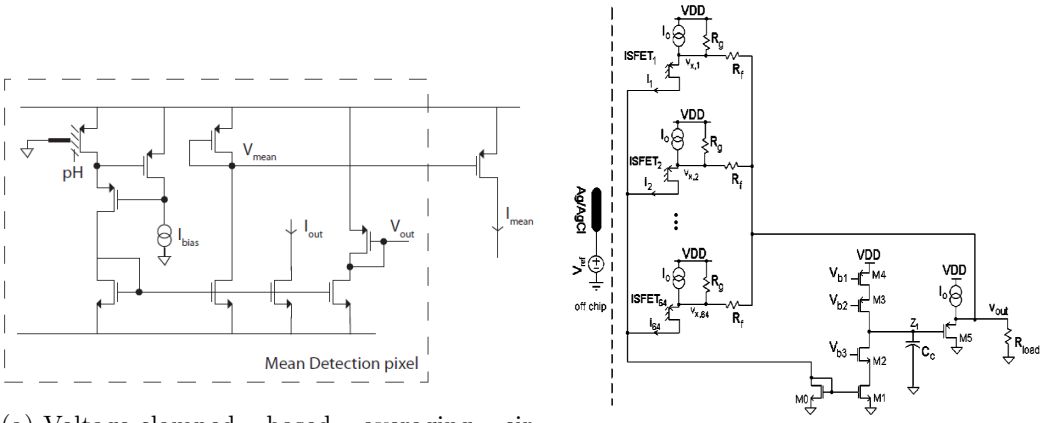

(a) Voltage-clamped based averaging circuit[125].

(b) Averaging circuit in [190, 191].

Figure 5.6.: Averaging array readouts.

5.2. Readout Design

In the previous section, some of the readout circuits in the literature transferring the sensed signals to the next processing electronic stages were reviewed. There is a dependency of readout design on the application and the overall set-up. Table 5.1 gives a summary of the advantages and disadvantages of the discussed readouts.

The design and configuration of a readout may be related to the dimensions for the feasibility of planting a microfluidic structure, the area of the microchip, the number/integrity of sensors, data, power, cost, etc. On the electronics design side, power dissipation might not seem as critical as for a prosthetic implant but still a substantial figure as temperature may influence the chemical reactions. Certainly for a hand-held set-up battery durance comes into play too[7] but may be ignored when on-chip heating drains the battery. Processing the signals locally and in analogue, or converting to digital and transmitting to a separate unit, is another point of trade-off in dealing with the information and resources.

For instance, in the sequencing work explained in Chapter 3, the high level of integration with small sensor pitch would not allow implementation of readouts in pixels, but the ISFETs were selected one at a time and connected to a drain-source follower readout. There was no explicit REFET pixel and the processing and detection of working ISFETs was dependent on an extensive analysis of the signal over tens of cycles of nucleotide incorporation reactions for the whole array. All this resulted in a huge computational burden. Another side of the story is the strength of chemical signals and ability to detect and discriminate the signal.

[7] In the discussed semiconductor-based genotyping technology in Chapter 3.

Table 5.1.: Analogue readouts advantages and disadvantages.

Readout	+	-
Source-follower	small area, scalable for both sequencing and genotyping	DC-offset limiting to supply rail, limited linearity
Drain-source follower	linear, used for both genotyping and sequencing	DC-offset limiting to supply rail
Feedback to gate	Control over reference electrode voltage, possible offset control, linear	not suitbale for large scale arrays
Indirect feedback to gate	Control over reference electrode voltage, possible offset control	not suitable for large scale arrays
Voltage Clamped	small area, scalable for sequencing and genotyping	limited linearity, DC-offset limiting the peration range
REFET-ISFET Differential Pair	linear, common-mode rejection	DC-offset limiting the operation range, not scalable
PG-ISFET adaptive	control over DC-offset, linear, not dependent on the ISFET geometry	large area, not scalable for large arrays
Auto-offset removal	Control over DC-offset, linear	large area, not suitable for large-scale arrays, clock dependency and switch leakage not suitable for slow tests
Direct capacitive feedback	eliminating DC-offset, linear, weak inversion operation	dependency on clock and switch leakage limiting the application, only tracking the change in short clock periods and not providing overall change, not suitable for large arrays
H-Cell	suppressing temperature effects, weak inversion operation	non-linear, sensitive to bias requiring calibration, not suitable for large scale arrays
Chemical Gilbert Cell	Weak inversion operation, comparative/differential measurement, current mode	requiring calibration for biasing, not scalble to large arrays
Methylation Cell	Comparative/ratio measurement, weak inversion operation	biasing and calibration dependent on the reference electrode, DC-offset limiting, not scalable for large arrays
Voltage-clamped averaging	Suppressing unwanted signals through current averaging,	biasing dependent on the reference electrode, not scalable, not linear
Averaging by feedback	supperssing unwanted signals through averaging, linear	DC-offset limiting, not scalable

Nevertheless, a main job on the circuit side that needs to be rectified is the operation of the ISFETs and the functionality of the readout. In the following sections, potential readout configurations that may help tackling DC offset on the chip are proposed by the author. Aside from a mixed-signal approach, a Piecewise Linear Approximating (PLA) readout and a bulk-based design are described. In the PLA readout large transistors are used and it is suggested for small-scale set-ups like genotyping. The bulk-based approach primarily looks at sequencing in large-scale integrated arrays.

5.3. Mixed Signal Calibration

In a mixed-signal calibration, the goal is to find and store the bias point for one or more of the ISFET terminals that results in a certain output level, before the start of the reaction. Then at

the time of reading the ISFET signal, use the stored bias information and compare the change in the output. The calibration may be through changing the reference electrode potential or the source, or using a control gate as in the PG-ISFET.

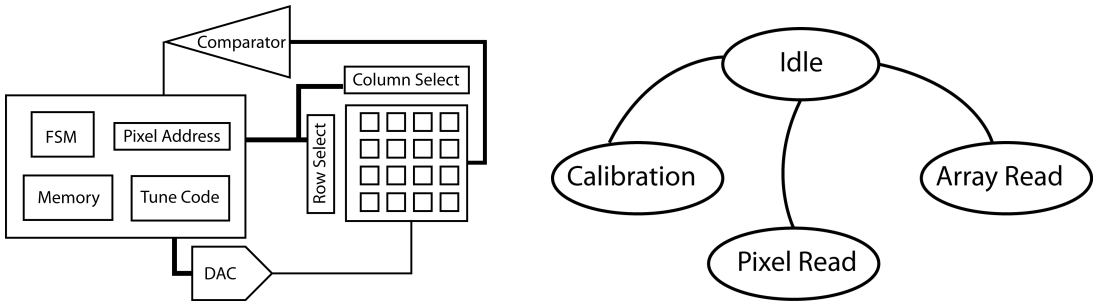

(a) Mixed-signal calibration system overview.

(b) Mixed-signal calibration Finite State Machine (FSM) overview.

Figure 5.7.: Mixed-signal calibration overview.

Another stage of calibration may be for equalising the readout outputs of ISFETs in an array or an ISFET-REFET pair for further analogue processing or comparison [176]. In this case, the reference electrode as the common terminal needs to be set at a level that operates the ISFETs in a region where their respective fine-tuning is feasible.

However, in such a method, the dynamic range of the tuning DAC (Digital to Analogue Converter) in overcoming the ISFET gate offset, and the ability to cover both negative and positive offsets, is a limit. Moreover, it adds to the complexity of the system by an increase in the size of the ISFET arrays, and requires a memory unit for the storage of tune codes. But in small scales, it may help reducing the data. For example, instead of storing all the bits from an ADC (Analogue to Digital Converter) digitising the ISFET readout voltage, we may work on the change.

5.4. Piecewise Linear Approximating

One of the key limiting issues of the ISFET, unresolved in almost all the readouts described, is the unknown offset of the ISFET floating gate. Among all, Hu and Georgiou [179], similarly considering the application of sequencing and genotyping, introduced frequent resetting of the floating-gate while having a direct capacitive feedback to it through a control capacitance as in the PG-ISFET; Figure 5.4d. Therefore, the readout would provide the change during the period between the resets. The timing of the reset signal is completely critical to the performance as CMOS switches have limited off resistances. Thus, it should be taken into account that the rate of voltage drop on the gate through the switch is less than the rate of pH change and the change in the period is tracked/recorded by the subsequent blocks. The clock cycle should be small enough to not miss any change either. Kim and Yoon [67] also used switches to connect sensing membranes to readouts.

Here a piecewise-linear approximating (PLA) readout is proposed by the author. In the PLA a similar gate-resetting approach but with no programmable gate or feedback is taken. Figure

5.8 displays an overview of the proposed system and Figure 5.9 the concept. In Figure 5.9 the first diagram on the left shows a linear input signal, pH change. The second is the ISFET non-linear current with no processing. However, the PLA resets the ISFET biasing to its start point. By periodically doing that, the current change seen is a slice of the current curve at its starting point where the slope is almost the same for the pieces (the red pieces) of the current. Integrating the piecewise approximate current changes gives the overall current change in a linear curve, consequently a linear relation with the pH change. An advantage of this configuration, besides a linear output while cancelling the temperature effect, is the integration of the changes to provide the total change of the signal over time.

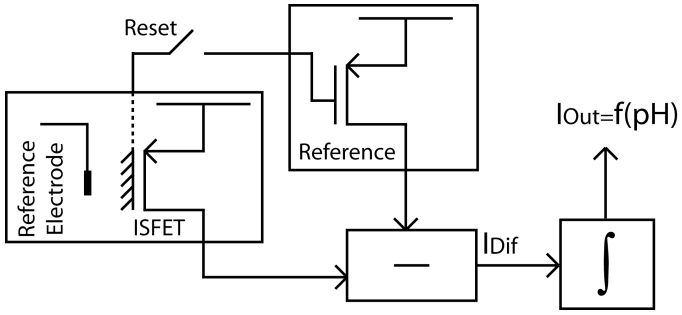

Figure 5.8.: Piecewise-linear approximating readout top-level diagram.

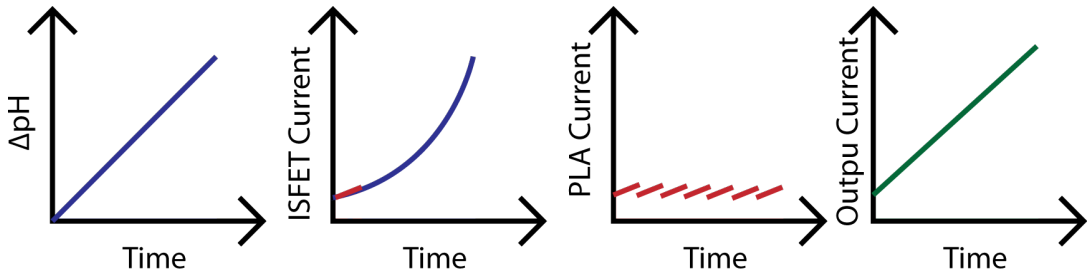

Figure 5.9.: Piecewise-linear approximating readout concept.

Therefore, the idea is to

- Bias the ISFET and a reference MOSFET at a certain operating point in weak inversion
- Compare the ISFET current change in result of the pH change with the reference MOSFET biased at the same operating point
- Take the difference, I_{Dif} of the currents as the pH variation changes the output current
- Re-bias the ISFET at the same operating point and repeat the comparison and differentiation
- Integrate the current changes to provide the total signal change in the output I_{Out}

This interface tries to

- Tackle the trapped charge DC offset effect on the ISFET floating gate
- Eliminate the slope factor n change effect
- Eliminate the exponential effect of the slope factor (n in equation 5.6) and the sub-Nernstian parameter α (equation 5.1) on the weak inversion operating ISFET
- Provide a linear current from an ISFET biased in weak inversion

5.4.1. Interface Circuit

The interface circuit depicted in Figure 5.10 biases the ISFET at weak inversion with a supply of $3.3V$. Weak-inversion region allows both the elimination of the temperature effects as in section 5.1.4, and a smaller decoupling factor ζ (discussed in detail in Chapter 4). A $20nA$ current source and a diode-connected MOSFET with the same aspect ratio of the ISFET floating-gate is used to provide the reference biasing point for resetting the ISFET gate. Cascode current-mirrors and regulated-cascode configurations have been used to ensure a precise differentiation of the ISFET current from the reference current. It makes a large enough output impedance and sets the output voltage at half the supply range ($Vdd/2$) for matching with the next stage, the integrator.

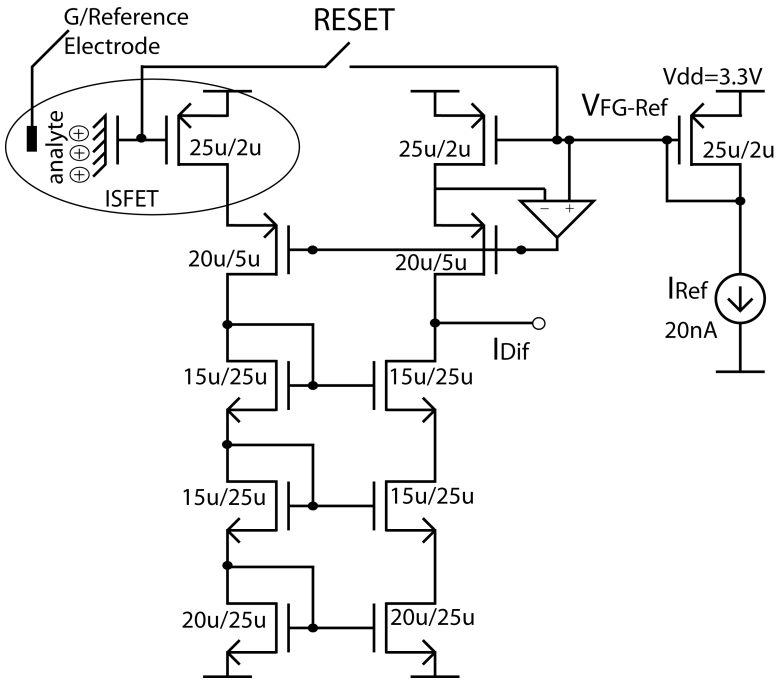

Figure 5.10.: Weak-inversion ISFET readout configuration. The ISFET floating-gate is reset to reference V_{Ref}, and its current, being a function of pH change after reset, is subtracted from the reference $20nA$ current as the readout output I_{Dif}.

In Figure 5.10, there is also a switch between the floating-gate of the ISFET and the reference voltage (the gate/drain of the diode-connected $20nA$-biased reference MOSFET). On a reset signal, this switch sets the floating gate of the ISFET at potential V_{FG-Ref}. As there is no

resistive path to the floating gate (ideally; the switch open resistance is limited), from the time the switch opens, the floating-gate voltage changes only if the voltage on the sensing membrane changes. But it should be noted that since the switch is not ideal, there exists a resistive path from the gate which does not let it appear as floating if the leakage rate and the switching frequency silence the main signal when the pH change rate is slower.

Therefore, for an application like pH-based genotyping that is after monitoring the transient change in the ionic concentration, rather than the absolute potential on the membrane [90], the switching helps reading the ISFET signal regardless of the trapped charge and offset on its gate. Figure 5.11 shows an example of how the reset and change-track works independent of the absolute potential on the sensing membrane.

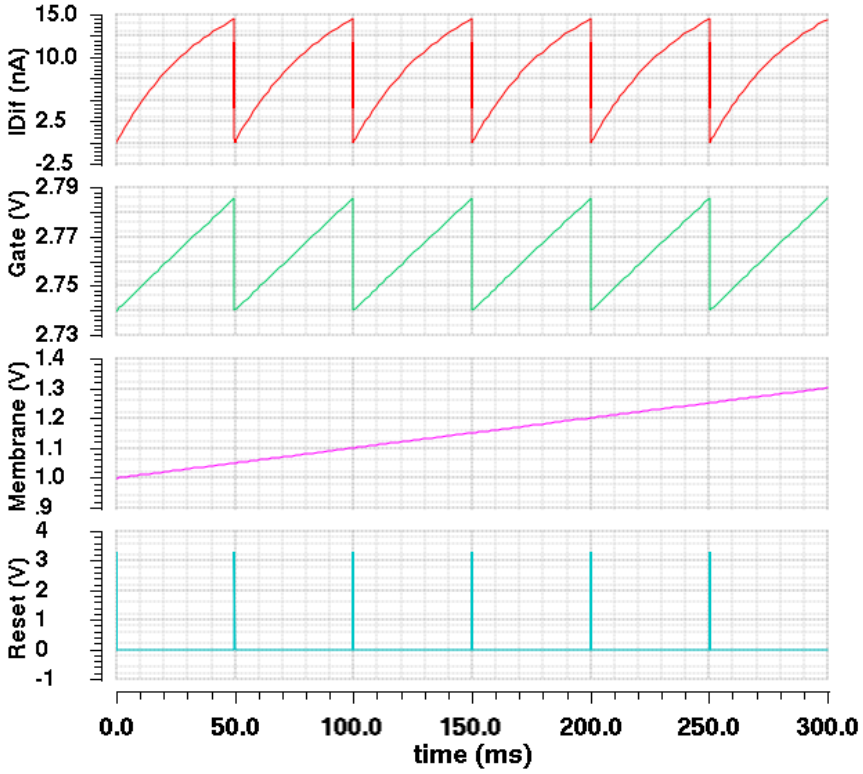

Figure 5.11.: An example of the readout transient operation for a ramp input while its floating gate is reset every 50ms, and so is the output current I_{Dif}.

To overcome the charge injection, dummy switches are used for a complementary transmission gate as in Figure 5.12 with its transient analysis on the leakage on the ISFET gate in Figure 5.13. The $38.5\mu V/s$ gives a proper change rate equivalent to less than 0.0008 pH change per second for a $50mV/pH$ sensitivity. Since the direction of the reaction in our targeted application (genotyping) is in the generation of H^+ ions (pH drop) and increase of the sensing membrane potential, PMOS[8]-based ISFET is used to be sure of the operation in weak inversion after resetting to the reference voltage.

[8]Positive charge carrier MOSFET

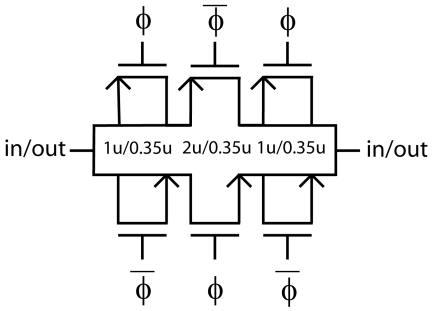

Figure 5.12.: Switch configuration using dummy pairs for the reduction of charge injection.

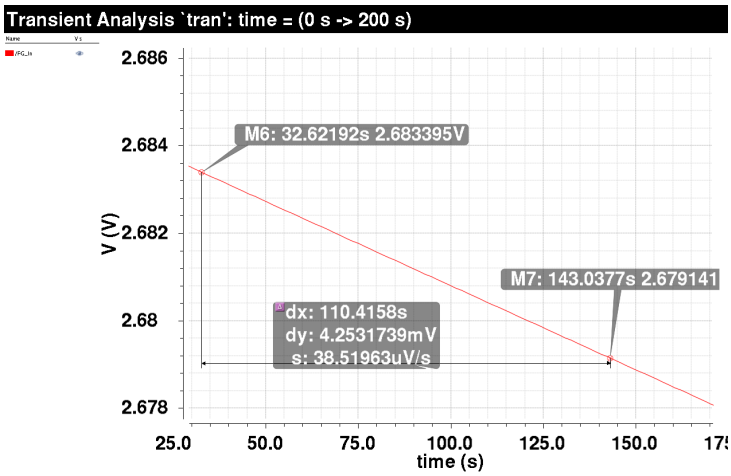

Figure 5.13.: Switch leakage test.

5.4.2. Class-A Switched Current Integrator

Figure 5.14 shows a class A switched-current integrator with cascode transistors [192]. Switched-current approach was introduced for digital processes. Among the other types of integration (like continuous-time transconductance-capacitance and switched capacitors), this type of integration was chosen for two reasons. One is the signal in current, and the other that integrating samples of the signal at certain times just before the next reset requires a discrete sampling and integration (in other words, a discrete-time sum of the samples for approximation).

In phase 2 ($\phi 2$) of the clock cycle $n-1$, transistor $M1$ is diode-connected and samples and records the input signal $i_{in}(n-1)$ by charging its gate capacitance. In phase 1 of the next cycle, transistor $M2$, which has stored the output from the previous cycle, is diode-connected and takes the excessive recorded current of $M1$. The cyclic switching, recording and summation develops an integrator with time and z domain responses as in equations (5.11).

$$i_{Out}(n) = i_{Out}(n-1) + 2i_{in}(n-1) \tag{5.11a}$$

$$I_{Out}(z) = \frac{2z^{-1}}{1-z^{-1}} I_{in}(z) \tag{5.11b}$$

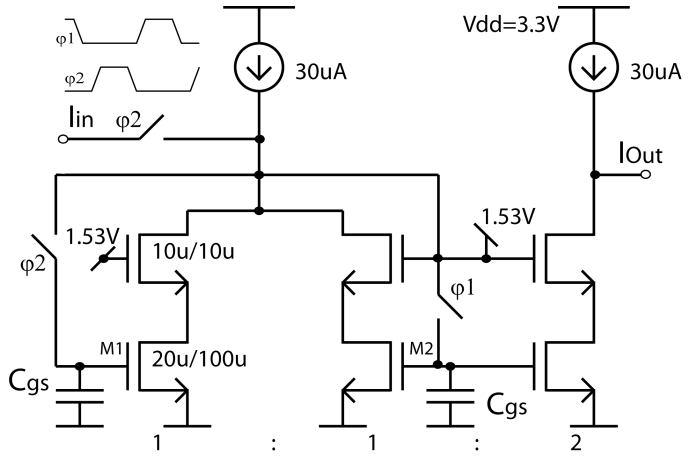

Figure 5.14.: Class-A switched-current integrator. The switching clocks should be non-overlapping.

The output current is:

$$i_{Out}(n) = 2\Sigma i_{in}(n-1) \tag{5.12a}$$

$$I_{Out}(t) = i_{Out}(n); \qquad nT \leq t < (n+1)T \tag{5.12b}$$

$$I_{Out}(t) = 2\int dI_{Dif} \tag{5.12c}$$

Same switch as for the readout was used and the circuit was optimised for overcoming the charge injection and overshoot on switching by increasing the transconductance of the memory transistors (which also reduces the input impedance) and switches, while biasing the input and output nodes at half the supply range ($Vdd/2$) similar to readout.

5.4.3. Piecewise Approximation

Setting up the readout and integrator as in Figure 5.8, the concentration change in between the resetting times may be preserved by the integration. Accordingly, the reset timing and the integrator clock cycles needs to be taken into consideration as the reset would act as a high-pass filter and the integrator as a low-pass.

In section 5.1 for translinear circuits it was shown that the weak-inversion output is exponentially dependent on the ratio of α/n. Here, by resetting the gate of the ISFET and differentiating its output current from the reference, the change of the signal in between the reset events is approximated with the same slope/transconductance. The integration then allows a linear sum of the piecewise sampled output signals forming a linearised function.

Having reset the ISFET floating-gate, its current may be written with Euler approximation

as in equation (5.13)

$$I_D = I_{Ref} + \frac{\delta I_D}{\delta V_{G'}} \mathrm{d}V_{G'} \tag{5.13a}$$

$$\mathrm{d}V_{G'} = S_{pH}.\mathrm{d}pH = \alpha \ln(10) U_T.\mathrm{d}pH \tag{5.13b}$$

$$\frac{\delta I_D}{\delta V_{G'}} = \frac{1}{nU_T} I_{Ref} \tag{5.13c}$$

Consequently, its subtraction from the reference current ($I_{Dif} = I_D - I_{Ref}$) will give a readout output current of

$$\mathrm{d}I_{dif} = I_{Ref} \frac{\alpha}{n} \ln(10) \mathrm{d}pH \tag{5.14}$$

In PLA the ISFET gate is reset at every clock cycle at the beginning of phase 1 (or after phase 2 goes down giving a non-overlapping gap between the phases) while its pulse width is short enough to not miss any reaction, and large enough to ensure the floating-gate voltage is adjusted. The integrator samples and sums up the change from the reset time to phase 2 of the clock cycle. The output current may be written as

$$I_{Out} = \int \mathrm{d}I_{dif} = \frac{\alpha}{n} \ln(10) I_{Ref} \Delta pH \tag{5.15}$$

As seen in equation (5.15), the ratio $\frac{\alpha}{n}$ is not anymore in the power but appears as a constant factor.

5.4.4. Simulation Results

The PLA circuits (Figure 5.8, Figure 5.10 and Figure 5.14) were designed and simulated in Cadence Spectre environment using a $0.35\mu m$ process library at $3.3V$ supply. For the tests with pH as the independent variable, a Verilog-A model (Appendix J) modulating a reference electrode voltage by pH was used. The readout and the integrator were also separately tested and optimised. A summary of their performance is provided in Table 5.2.

Table 5.2.: PLA readout and integrator characteristics.

	Readout	Integrator
Area est.	$(710\mu m)^2$	$(710\mu m)^2$
DC Power	$267.7\mu w$	$198\mu w$
Gain	$450nA/V$	$0dB$
3dB Bandwidth	$15kHz$	$77.4kHz@T = 0.1ms$
Total Input-Referred Noise ($1mHz to 100kHz$)	$4.48e^{-7}V^2$	$1.33e^{-19}A^2$

For comparison on the effect of piecewise integration on linearisation of the current-pH re-

lation, in Figure 5.15 the readout drain current over pH-change, considering three different α values, is drawn.

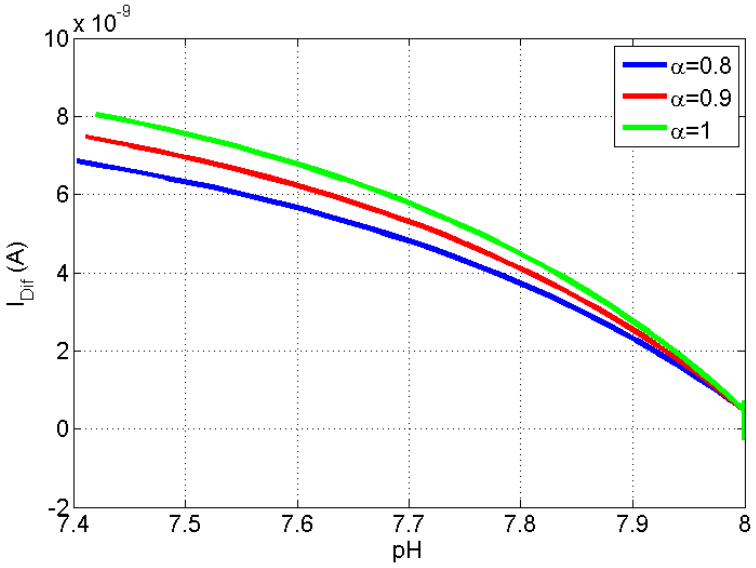

Figure 5.15.: Readout output current vs pH for different α values.

By piecewise approximation, the readout-integrator configuration outputs a current that is a linear function of the pH change. The simulation result for $\alpha = 1$ is provided in Figure 5.16. The simulation was run for several other α values. Table 5.3 provides linear curve-fitting parameters ($I_{Out} = P1.\Delta pH + P0$) derived for each α. The derived slopes, the $P1$s, are also fit linearly by $P1 \approx -20.57\alpha - 9.46$ which shows that α after piecewise approximation appears as a multiplying factor and not an exponential term.

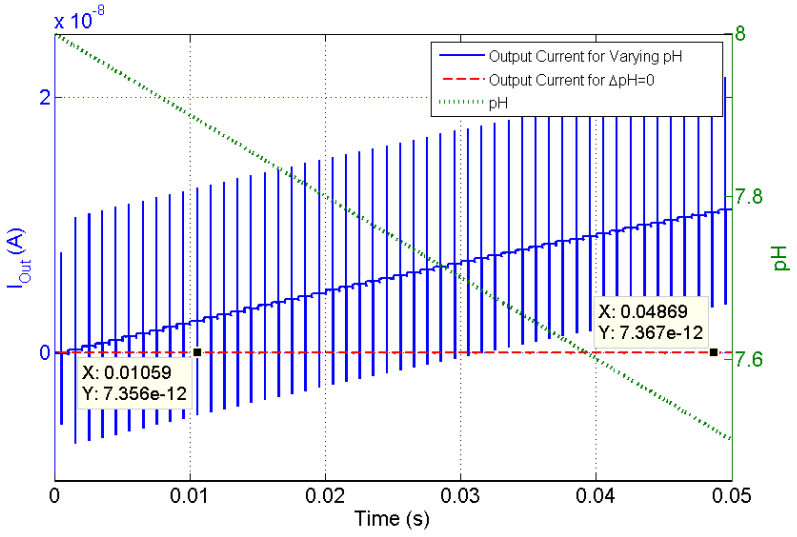

Figure 5.16.: Output current versus time while a ramp pH change was given to the input.

Table 5.3.: Linear curve-fitting parameters for $I_{Out}(nA) = P1\Delta pH + P0$.

α	0.8	0.85	0.9	0.95	1
$P1$	-25.91	-26.94	-27.97	-29	-30.03
$P0$	0.17	0.18	0.18	0.19	0.19

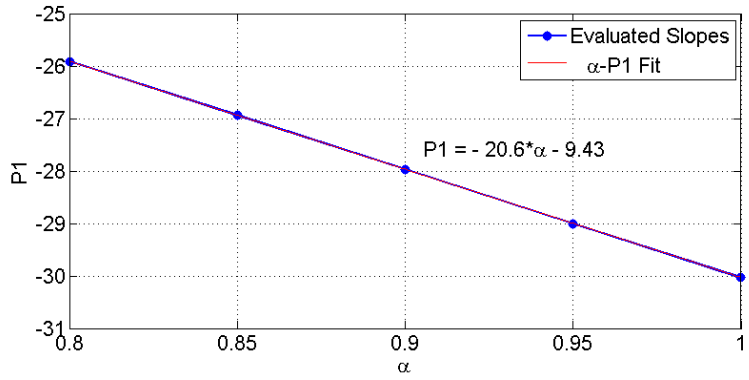

Figure 5.17.: Linear curve-fit of $P1$ and α which shows that the non-linearity from the sub-Nernstian term α in weak-inversion operation is eliminated.

5.4.5. PLA Pros and Cons

The proposed PLA configuration, in comparison with the works in literature (Table 5.1), provided a linear readout of pH change and eliminated the temperature dependency of the pH sensitivity with the inherent temperature dependency of FET by integrating the ISFET as part of the readout and biasing it in weak inversion. The resetting overcomes the DC offset and the integration provides a total of the signal changes, unlike the other methods relying on resetting and calibration.

However, its benefits come at a cost that limits its application. The resetting requires the signal to change faster than the switch leakage and demands proper clocking. Also it requires big enough ISFETs for providing capacitive storage of the voltage in parallel with the switch leakage effect. Therefore, it may be suitable for point-of-care microchips and not scalable for sequencing. The whole readout may be shared among an array of ISFETs via switching their drains to the readout. For each pixel/ISFET one reset switch is needed in addition to a pixel-select switch on the drain.

It is worth to mention that while the primary goal was to integrate the ISFET in the readout, for optimum design and advantage of its processing capability, it may be used as a following circuit to one of the linear readouts (e.g. the drain-source-follower in Figure 5.2b). In that case, the ISFET in the PLA may be replaced with a MOSFET with a large enough capacitor in series to its gate; Figure 5.18. Therefore, the output of the linear readout is switched and becomes the input of the new PLA independent of its biasing point. In this way, the ISFET floating gate remains floating and is saved from any leakage and the ISFET does not need to be big but the capacitor compensates for it.

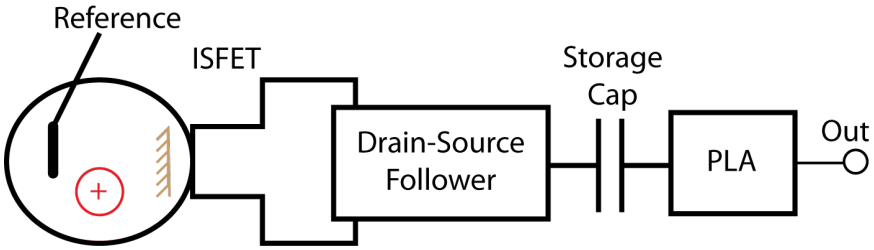

Figure 5.18.: Alternative approach for PLA.

5.5. REFET-based Calibration Using Bulk Terminal

REFET-based designs conventionally are in (differential) pair configurations. However, unknown DC offset on the ISFET and the REFET may bias the transistors in different operating regions that either unbalances the circuit making it non-operational, like in a differential pair, or requires calibration, on-chip or externally. Depending on the configuration, the dynamic range of operation may also be affected. In the ISFET arrays, the complexity of system increases significantly if an analogue REFET-based readout is used.

While this approach may be still practical in small-scale integrated systems, where the REFET and the ISFET can be physically paired, it is not feasible for large-scale arrays. For instance, in the sequencing system described in Chapter 3, millions of ISFETs are sitting in micro-meter pitches, randomly carrying reaction microbeads. The signal processing for the discrimination of pH-changes is done all digitally, bearing a common noise (the background signal as in Figure 3.12b in Chapter 3) in the measurements.

This section, explains how the common terminal of all ISFETs in an array, the bulk (back-gate), can be used to eliminate the common-mode noise in an analogue manner without any scaling issues.

5.5.1. Bulk Terminal Effect

The utilisation of bulk in analogue circuits provides higher dynamic range especially in the shrinking CMOS technology [193–200]; and in deep sub-micron devices, makes dynamic-threshold MOSFETs enhancing the speed of logic gates [201–207].

The effect of the bulk in the current-voltage characteristics of a FET is in the modulation of the threshold voltage, along with the body effect coefficient γ, surface potential Φ_F and the threshold voltage at zero source-bulk V_{TH0} [169].

$$V_{th} = V_{th0} + \gamma(\sqrt{\mid 2\Phi_F + V_{SB} \mid} - \sqrt{\mid 2\Phi_F \mid}) \tag{5.16}$$

Comparing the transconductance when the signal is applied through the bulk (g_{mb}) with the time it is applied through the gate (g_m), equations (5.17) and (5.18), we have $g_{mb} < g_m$. Thus, although increasing the bulk potential has the same effect as increasing the gate potential in terms of polarity, more voltage change is needed to have the same current change in the transistor than when the voltage is altered at the gate. This means a higher dynamic range

for the input signals applied from the bulk with a price of lower gain and higher input-referred noise.

$$g_m = \frac{\delta I_D}{\delta V_{GS}} \tag{5.17a}$$

$$I_D = f(V_{GS} - V_{th}, V_{DS}) \tag{5.17b}$$

$$g_{mb} = \frac{\delta I_D}{\delta V_{BS}} = g_m \frac{\gamma}{2\sqrt{2\Phi_F + V_{SB}}} = \eta g_m \tag{5.18}$$

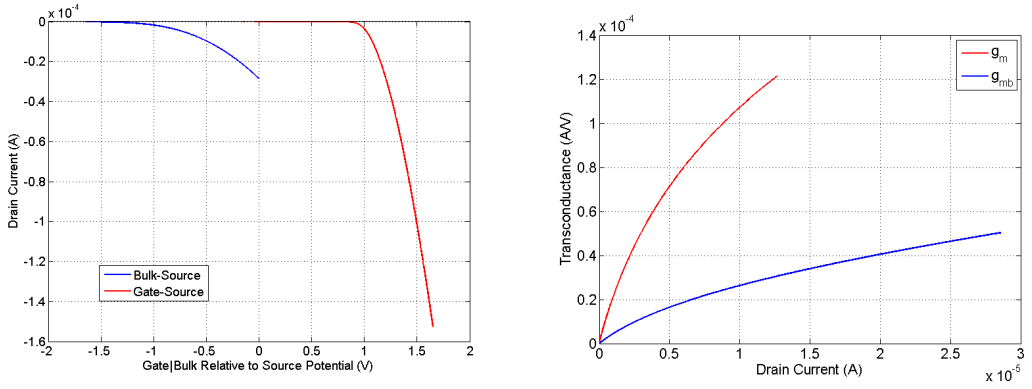

(a) Comparison of V_{GS} and V_{BS}.

(b) Comparison of g_m and g_{mb}.

Figure 5.19.: Comparison of applying voltage from the gate with the bulk for a $5\mu/1\mu$ MOSFET with $V_{DS} = Vdd/4 = 0.825$.

5.5.2. Bulk-based Common-mode Rejection

The idea proposed here by the author is fundamentally to suppress the background signal in large-scale sequencing microchips studied in Chapter 3 section 3.2. This background signal required off-chip processing to be eliminated from the signal sensed by the ISFETs in order to allow incorporation detection and base-calling. Since the back-gate can be shared by a number of the ISFETs, it can be used as the calibration point to cancel-out the common-mode signals, reducing the processing load.

Figure 5.20 gives an overview of the back-gate common-mode rejection. In order to use the bulk terminal for an array of ISFETs, in addition to a REFET, a MOSFET is also considered as a reference and it is connected to the same type of interface as for the ISFETs. The output of the reference MOSFET interface is compared with the output of the REFET or reference pixel. The bulk of the reference pixel is set up to cancel out any difference between the two reference outputs while the bulk of the reference MOSFET is fixed. Therefore, any change in the reference pixel is sensed by comparing it with the reference MOSFET. The bulk is tuned accordingly to cancel out that change. Since the bulk of the reference pixel is shared with

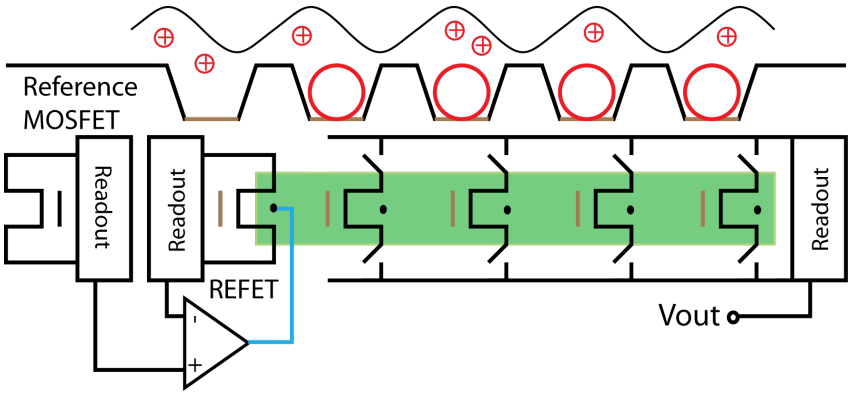

Figure 5.20.: Bulk-based common-mode rejection overview for large-scale sequencing arrays.

the other working ISFETs, those changes that are common are now cancelled out for them too. Thus, the common-mode noise, particularly the background noise in large-scale arrays in sequencing, may be suppressed.

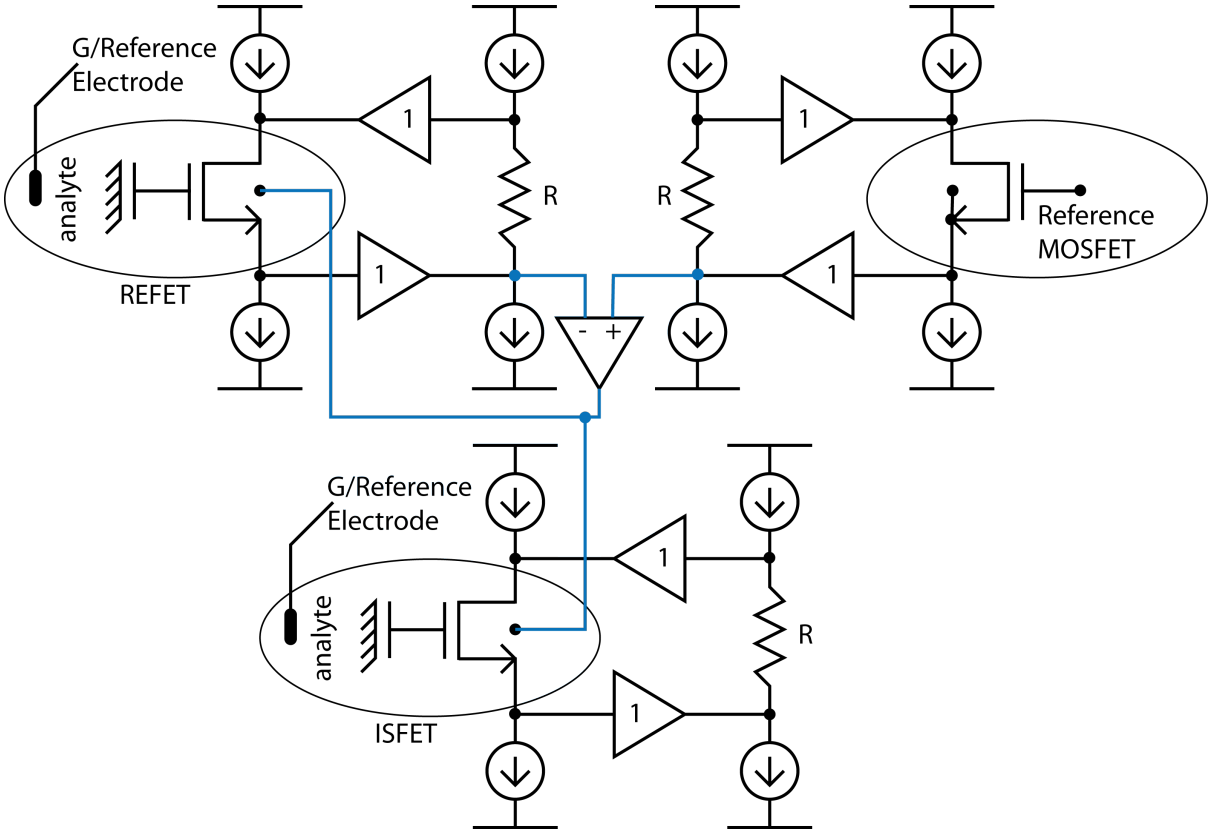

Figure 5.21.: Auto-calibration and single-FET differential measurement utilising bulk.

For example in Figure 5.21, in the conventional drain-source-follower, consider a common increase in the reference and working ISFETs due to a common noise. This causes the source of the reference pixel (and consequently the output of its interface) to increase. The reference pixel output is compared with the fixed output of the MOSFET interface (even this can be set as an external voltage, but making it this way makes it do auto-calibration). It is at the inverting

port of the differential amplifier, the output of which is connected to the bulk of the ISFETs and consequently reduces. Now the interface and the ISFETs seeing the bulk voltage decreased, force the source voltage to reduce in order to compensate for the change at the bulk. Therefore, the output is back to its previous value and the change caused by the noise is cancelled out; Figure 5.22.

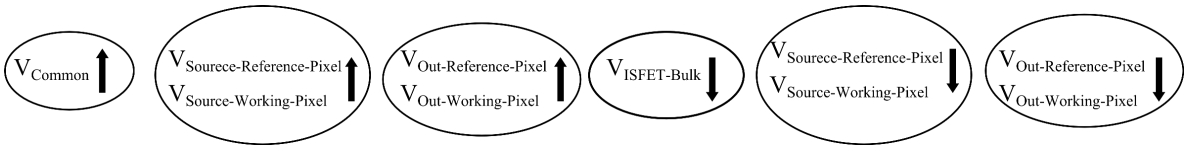

Figure 5.22.: Operation diagram for common-mode noise cancellation through bulk/back-gate.

With this method, in a simulation in a $0.35\mu m$ process, a common-mode gain of less than $-90dB$ (Figure 5.23) was achieved which is comparable to the common-mode rejection in differential pairs and Op-amps. Loads of $1pF$ were used at the outputs of the interfaces. However, it came at a cost of losing the buffer gain to about 0.775 ($-2.21dB$). The dynamic range on the floating-gate of the REFET to ensure that the bulk is below the source potential is about $230mV$.

5.5.3. Common-mode Range

To improve the range of compensation, both for the common-mode noise and the offset, rather than connecting the bulk of the reference MOSFET to the ground or its source, it can be connected to a point in the middle range so that a relatively symmetric wider operation range for the gates of the REFETs and the ISFETs is created. An example of this is depicted in Figure 5.24.

Considering the transistors in saturation with the drain currents fixed, for the reference MOSFET, the gate, source, and bulk potentials (noted by 0 subscript) can be derived as:

$$\begin{aligned} I_D &= 1/2\mu_n C_{Ox} W/L(V_{G0S0} - V_{th})^2(1 + \lambda V_{DS}) \\ &= \beta(V_{G0S0} - V_{th})^2(1 + \lambda V_{DS}) \qquad (5.19a) \\ I_D \text{ and } V_{DS} &\text{ are constant} \Rightarrow \\ V_{G0S0} - V_{th} &\equiv CTE \qquad (5.19b) \\ V_{G0} - V_{S0} - V_{th0} - \gamma(\sqrt{|2\Phi_F + V_{S0B0}|} - \sqrt{|2\Phi_F|}) &\equiv CTE \qquad (5.19c) \end{aligned}$$

Similarly for the REFET (noting with subscript i),

$$\begin{aligned} I_D &= \beta(V_{GiSi} - V_{th})^2(1 + \lambda V_{DS}) \qquad (5.20a) \\ I_D \text{ and } V_{DS} &\text{ are constant} \Rightarrow \end{aligned}$$

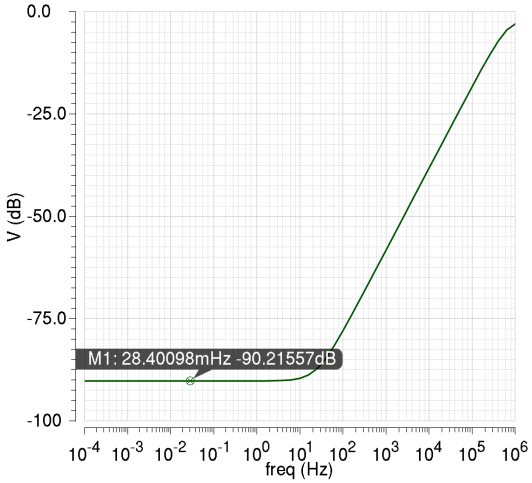

(a) Common-mode gain.

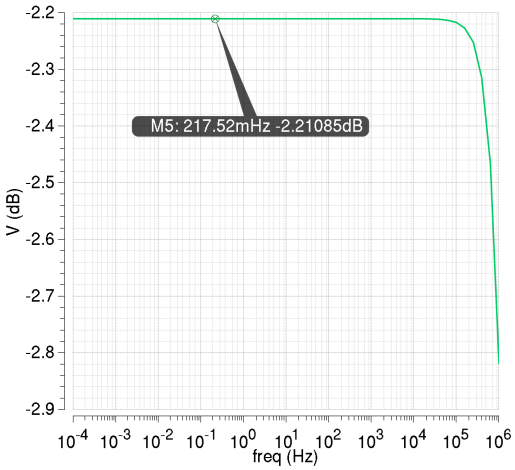

(b) Readout gain.

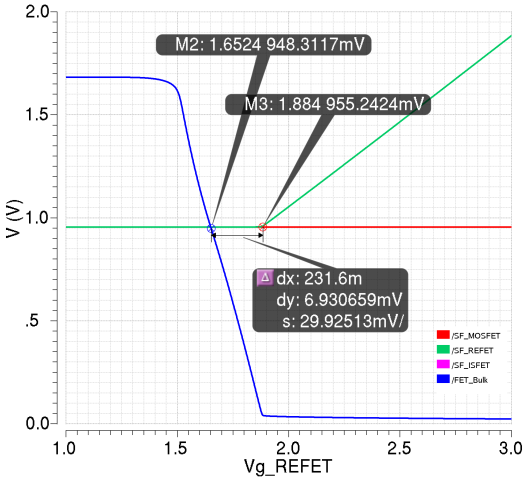

(c) REFET gate operation range.

Figure 5.23.: Bulk-based common-mode rejection with drain-source-follower readout.

$$V_{GiSi} - V_{th} \equiv CTE \tag{5.20b}$$

$$V_{Gi} - V_{Si} - V_{th0} - \gamma(\sqrt{|2\Phi_F + V_{SiBi}|} - \sqrt{|2\Phi_F|}) \equiv CTE \tag{5.20c}$$

The feedback through the differential amplifier, ensures the source of the REFET and the reference MOSFET are the same ($V_{Si} = V_{S0}$). Considering the bulk potential to be below the source potential, the equations can be rewritten based on the difference of the potential at the gate and the bulk of the REFET and the reference MOSFET.

$$(\Delta V_{Gi} + V_{G0}) - V_{S0} - V_{th0} - \gamma(\sqrt{2\Phi_F + V_{S0B0} - \Delta V_{Bi}} - \sqrt{2\Phi_F}) \equiv CTE \tag{5.21a}$$

Therefore, we can calculate how much the bulk changes (ΔV_{Bi}) to compensate for a change

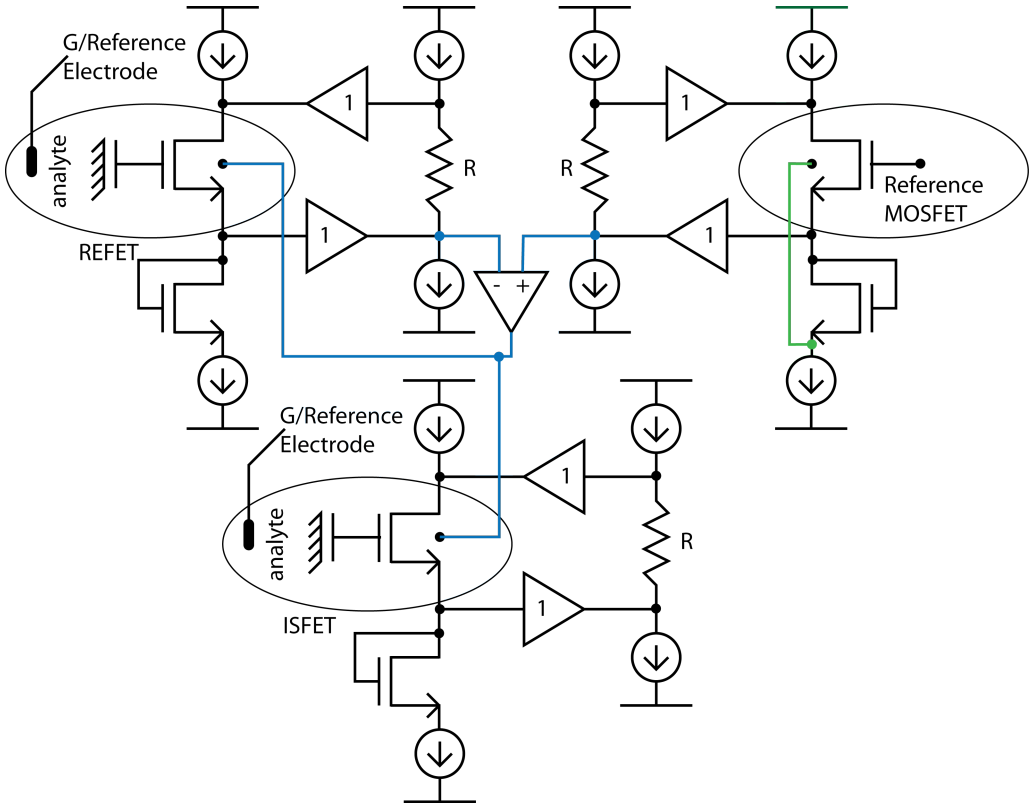

Figure 5.24.: Auto-calibration by bulk, using a diode-connected transistor in series to force $V_{BS} < 0$ avoiding a direct bias of the bulk p-n junctions.

at the gate of the REFET (ΔV_{Gi}) from the nominal reference bias of the MOSFET (V_{G0}), by taking the difference between (5.21) and (5.19).

$$\Delta V_{Gi} = \gamma(\sqrt{2\Phi_F + V_{S0B0} - \Delta V_{Bi}} - \sqrt{2\Phi_F + V_{S0B0}}) \tag{5.22}$$

According to the equation above, as the voltage on the gate of the REFET decreases ($\Delta V_{Gi} \downarrow$), the voltage on the bulk should increase ($\Delta V_{Bi} \uparrow$), but the maximum it can go is $2\Phi_F + V_{S0B0}$. Therefore, the minimum of the change range for the REFET gate is:

$$\Delta min(\Delta V_{Gi}) = -\gamma\sqrt{2\Phi_F + V_{S0B0}} \tag{5.23}$$

And if ΔV_{Gi} increases ($\Delta V_{Gi} \uparrow$), the bulk potential should drop ($\Delta V_{Bi} \downarrow$), which can at most change to the ground ($\Delta V_{Bi} = -V_{B0}$) and make the maximum change on the REFET gate to be compensated at

$$max(\Delta V_{Gi}) = \gamma(\sqrt{2\Phi_F + V_{S0}} - \sqrt{2\Phi_F + V_{S0B0}}) \tag{5.24}$$

$$-\gamma\sqrt{2\Phi_F + V_{S0B0}} < \Delta V_{Gi} < \gamma(\sqrt{2\Phi_F + V_{S0}} - \sqrt{2\Phi_F + V_{S0B0}}) \tag{5.25}$$

The source potential may be derived from equation (5.19) as (ignoring the channel length

modulation effect λV_{DS})

$$V_{S0} = V_{G0} - V_{th0} + \gamma\sqrt{2\Phi_F + V_{S0} + V_{B0}} - \gamma\sqrt{2\Phi_F} - \sqrt{I_D/\beta} \tag{5.26}$$

Increasing the reference gate potential and the aspect ratio or reducing the current may help with the range of operation. However, for a symmetric range:

$$\gamma\sqrt{2\Phi_F + V_{S0B0}} = \gamma(\sqrt{2\Phi_F + V_{S0}} - \sqrt{2\Phi_F + V_{S0B0}}) \Rightarrow \tag{5.27a}$$

$$2\sqrt{2\Phi_F + V_{S0B0}} = \sqrt{2\Phi_F + V_{S0}} \Rightarrow$$

$$V_{B0} = \frac{3}{4}(2\Phi_F + V_{S0}) \tag{5.27b}$$

5.5.4. Simplified Readout with wider Calibration Range

Similar to the configuration in Figure 5.24, but simplified by replacing the resistor and drain-source feedback buffers with a single PMOS, the readout is depicted in Figure 5.25. The common-mode gain rejection dropped slightly to $88.5dB$ with a readout gain of 0.817 ($-1.75dB$). The DC calibration range has increased to about $400mV$.

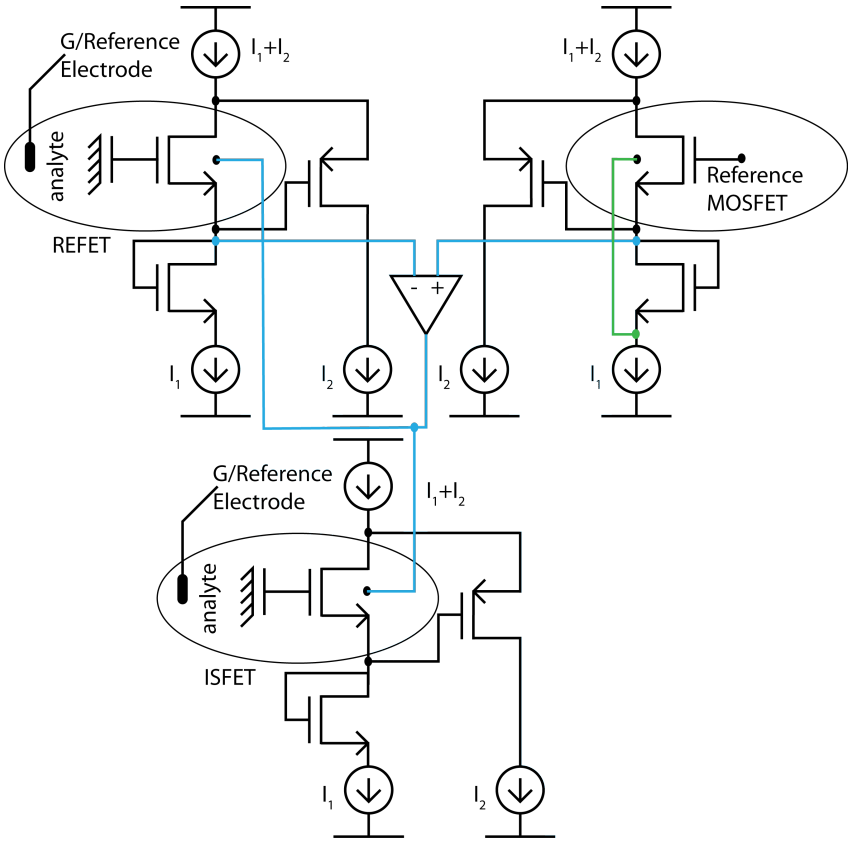

Figure 5.25.: Simplified drain-source-follower structure with wider bulk-based calibration range.

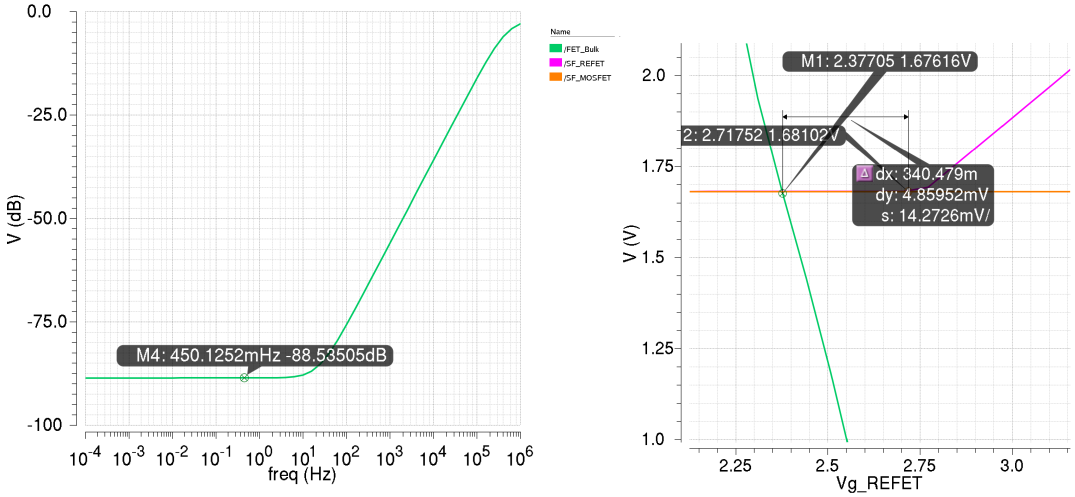

(a) Common-mode gain. (b) DC calibration range.

Figure 5.26.: Improvement in the DC calibration range by increasing the reference V_{SB} for the simplified drain-source-follower configuration.

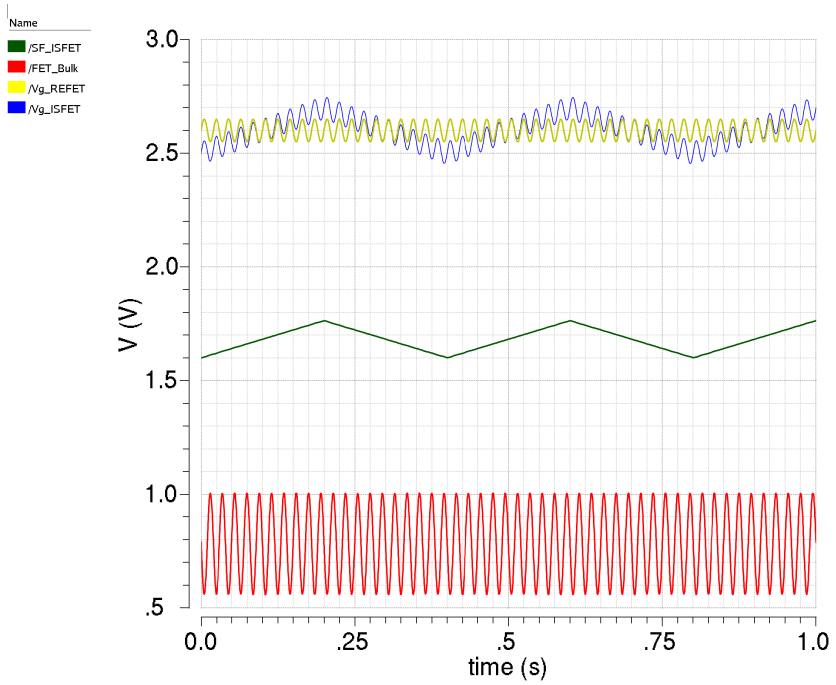

Figure 5.27.: A transient analysis showing the removal of a sine common-mode signal through the bulk-based calibration.

5.5.5. REFET Implementation for Large Scale Arrays

In the large-scale integrated ISFET arrays with micro-wells, as described in Chapter 3, the placement of microbeads into the wells is through centrifuge and random location of the beads. For distinguishing the bead-carrying wells from the empty ones several iterations of reactions was required along with computation and processing. Then the pixels with lower power change

would be considered as the REFETs.

REFET-based calibration, especially in analogue manner like the bulk-based calibration requires preferably knowing the REFETs in prior. Figure 5.28 shows a potential way on predetermining the REFETs for each row/column/subset of the array by dividing the well window so that the microbeads may not sit on those specific pixels. Those pixels may help monitoring the background signal level change on the array.

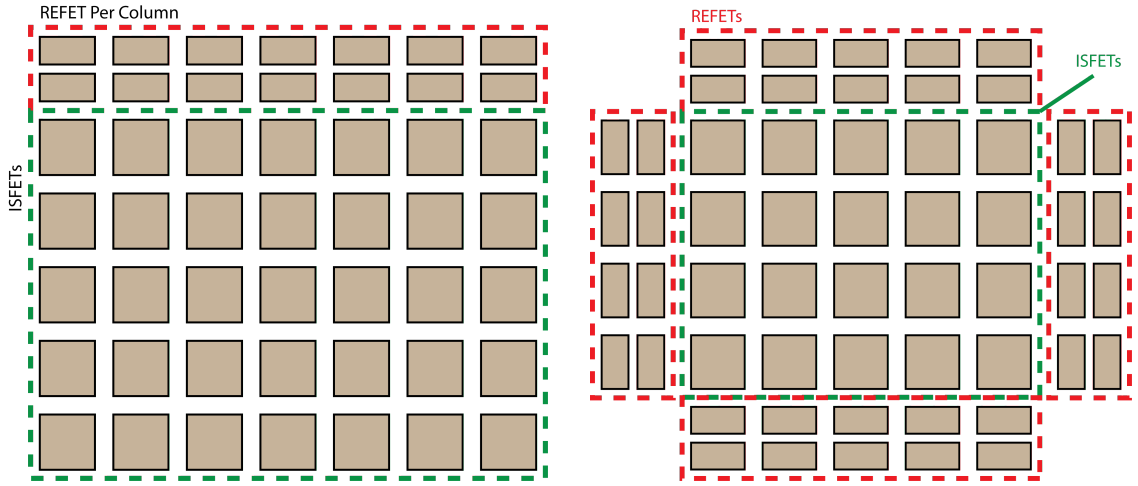

(a) REFETs at a side of the array or subsets of the whole array.

(b) REFETs around the array or subsets of the whole array.

Figure 5.28.: A potential way to make REFETs for large-scale integrated ISFET arrays with micro-wells in sequencing, is to divide the pixel window to not let any microbead in.

5.5.6. Pros and Cons

In this section the idea of utilising the back-gate terminal for eliminating the background noise signal in large-scale arrays was described. The advantage for such an on-chip processing would be saving on the cumbersome digital processing off the chip. However, for higher precision on reading the signal, it is necessary to have a proper readout configuration that would convey the signal from the ISFETs and REFETs with no loss. It is suggested to use the conventional drain-source follower configuration for optimum linear operation. The use of buffers and operational amplifiers as well as implementation REFETs with physical modification on top of the chip may reduce the yield from the chip. Moreover, it requires 3-well processes to accommodate variation of the body potential.

5.6. Summary

In this chapter, a review on the ISFET readouts with analogue outputs was provided, from the conventional readouts where the chemical signal is solely conveyed without using any amplification/transconduction of the ISFET (except the voltage clamped which would not be linear),

to the REFET-based circuits, ISFETs with programmable gates, translinear readouts, and averaging arrays. DC offset removal, area, linearity and scalability are essential for the ISFET arrays. Two new potential methods for addressing such requirements were introduced by the author.

In the piecewise linear approximation, by combining the two concepts of offset-resetting and weak-inversion operation, a novel readout was introduced to track and integrate potential changes in cyclic periods. Moving the processing to the pixels for genotyping assays, as described in Chapter 3, may help in optimising the utilisation of the area, and this readout may be a candidate.

In the bulk-based calibration, common-mode signals were shown to be significantly suppressed so that the measurements would not carry such unwanted signals to the succeeding processing stages, crucial for the large-scale arrays. The target application for it would be in sequencing microchips. For the future works, besides the mixed-signal calibration schemes, depending on the supply range of the instrumentation, bulk-based calibrations may help in improving the performance. Particularly for desktop devices that may not work on limited batteries, with triple-well processes and higher supply rails, DC offset shall not be a challenging issue. Depending on the process and supply, the bulk/back-gate terminal may be used in order to bias the ISFETs for measuring without any reference electrodes.

6. Digital Readout Circuits

Digital technology has spread significantly in our world. It allows robust computation. With scaling in silicon processes, it provides more digits at a smaller area. Interfacing the gadgets and peripherals is straightforward. Noise may not easily influence the signal, and the data is stored with no loss. However, it comes at a price of losing part of the information for quantization. It is an approximation of the actual values represented in binary codes of zeros and ones. The quantization plays a critical role in the accuracy of processing when applying it to an analogue world.

In sequencing and genotyping, or in a simpler expression DNA detection, we are in principle after two things. One is the logical approach of detection, on which ISFET-based DNA logic has been developed, and the other is quantification, in which we would like to count the happening of events. For example, as discussed in Chapter 2, in SNP detection we are after a Yes/No to tell if a specific mutation exists in the sample DNA or not. In gene expression analysis, we want to see how much the expression of a specific gene in the form of RNA is dominant to another one. In sequencing, we both need to detect an incorporation and to count the number of times it happens.

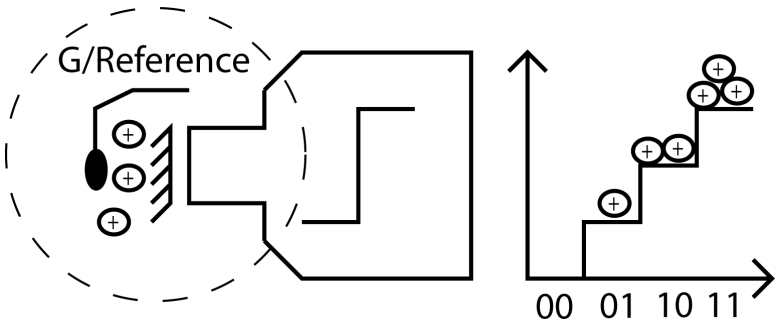

Figure 6.1.: ISFET digital readout overview. The idea is to make ISFET part of the digital conversion circuit for better accuracy over conversion and optimum use of area.

Previous chapters described the ISFET-based sequencing and genotyping industry. Issues like random DC offset, drift, and temperature sensitivity, along with challenges over scaling and robustness of readouts, were discussed. When it comes to sequencing, perhaps a higher level of integration of sensors/micro-wells is desirable to get a higher yield of the chip area where minimising the interface circuits size can be a great help. On the other hand, the signal is generated in a dynamic environment and demands a high level of accuracy in measurement. Besides the chemical signal strength (the pH change that is dependent on the chemistry of the reaction), the decoupling parasitic capacitances attenuate the signal reducing the signal-to-

noise ratio (SNR). Chapter 5 discussed the ISFET readouts with analogue output which may be followed by a conventional converter. In this chapter, the goal is to make ISFET part of a readout with digital output, in order to enhance the conversion precision, limit of detection, and utilisation of the area.

In digital conversion, at one stage we have a comparator(s) giving a zero or one if the input is below or above a quantization level. Yeow et al [208] in an array of ISFETs, took this approach and replaced one of the input transistors of a voltage comparator, Figure 6.2, with one ISFET from the array, comparing its gate potential (V_{ISFET}) with a user-defined threshold (V_{th}). Another digital approach to an ISFET readout is the chemical switch and ISFET-based logic gates.

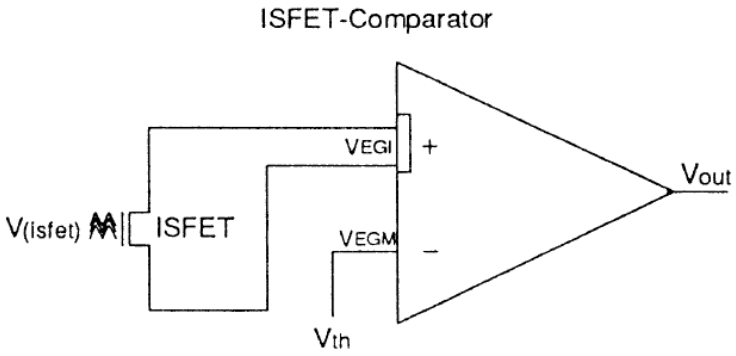

Figure 6.2.: ISFET comparator [208]. The ISFET replaces an input transistor of a comparator.

6.1. Chemical Switch and ISFET-based DNA Logic

An inverter with its input connected to a sensing membrane can be regarded as a chemical switch. Its output changes when the input passes a certain threshold of concentration. For DNA/SNP detection it was first introduced in [209] as a way toward ISFET-based DNA logic concept, building ISFET-based NAND and NOR gates comparing different SNPs. However, the ISFET was one type and the reference electrode potential was shared with the complementary transistor's gate. For example, in Figure 6.3 (a) the reference electrode for the NMOS ISFET is driving the gate of the complementary PMOS. Its reported switching operation showing the switching action in detection of a SNP is provided in Figure 6.4. Later, a chemical switch was proposed as an inverter of both PMOS and NMOS ISFETs [210, 211]; Figure 6.3 (b).

However, the operation of these approaches is limited by the attenuation in the coupling of the chemical signal to the floating gate of the ISFET, and the signal power to cover the switching transition range (the forbidden zone as in Figure 6.5). The signal needs to be strong enough to pass the transition between the maximum input low (V_{IL}) giving a high output (V_{OH}) and minimum high input (V_{IH}) giving a low output (V_{OL}). The reference electrode needs to be biased properly to not offset the input and let the transition be sensed. Chapter 4 explained the effect of the decoupling capacitors, making a fraction of the voltage change ($1/(1+\zeta)$)

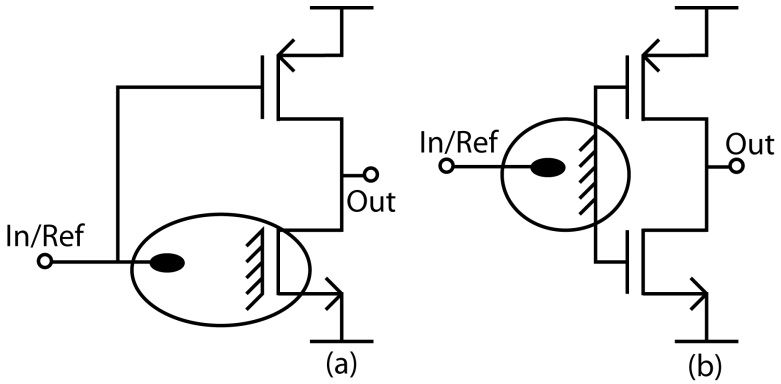

Figure 6.3.: Chemical switches; (a) used for SNP detection as in [209] and (b) chemical switch as in [210].

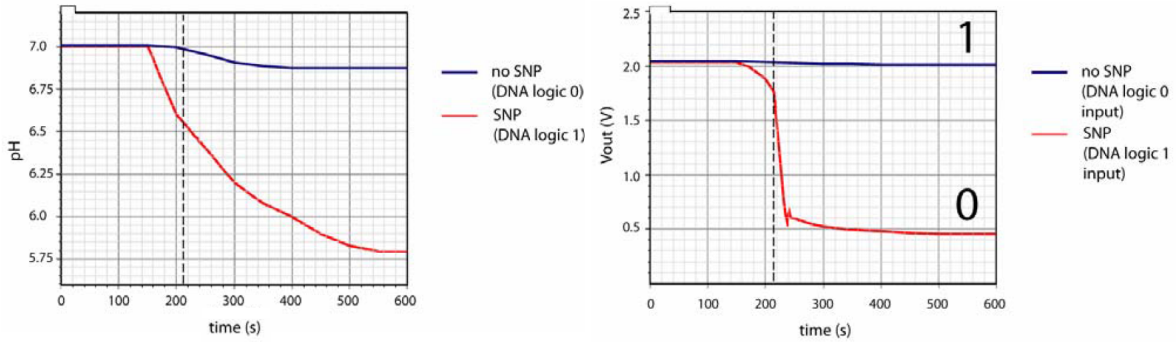

Figure 6.4.: Reported result in [209] for the two cases of no SNP present with blue curve and when SNP is detected in the red. The left figure is the pH change and the right is the output voltage.

on the sensing membrane appear on the gate. Accordingly, the inverter's switching transition range increases by the inverse of this factor, $(1 + \zeta)$. Besides the increase in the size of the ISFET for reducing this effect, the signal should change enough to make the intrinsic inverter switch. In addition, this is highly dependent on the reference electrode bias. The further away it is from the switching threshold, the higher the signal power (more pH change) needs to be. Consequently, the implementation for arrays, especially when sharing the reference electrode, gets complicated. Unless an indirect measurement is taken by sweeping the reference electrode, and recording the reference electrode potential change for each element as an equivalent to the pH change. However, in terms of resolution and limit of detection, the problem remains unresolved.

For the switching sensitivity issue, programmable-gate ISFET-based DNA logic was introduced [214] to improve the resolution of detection to 0.01 through a positive feedback; Figure 6.6. However, it requires implementation of capacitors, which take up area and are not welcomed for large-scale arrays. Also, the other issues like DC offset and drift still remain.

In this chapter the author proposes two new ISFET-based digital readout circuits. One uses a pseudo-inverter configuration to show how the resolution on a converter may be relaxed. The inverter is asymmetric and the signal dynamic range is limited as for the pH-change from nu-

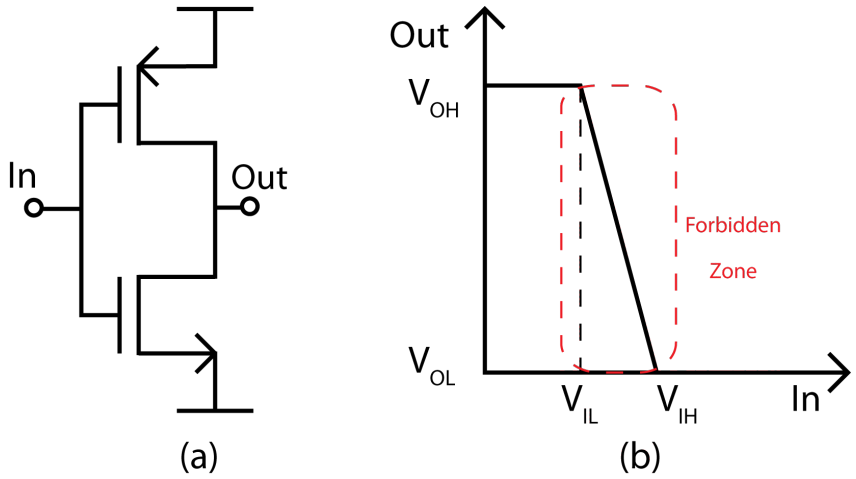

Figure 6.5.: CMOS inverter and its characteristic redrawn from [212, 213]. (a) CMOS inverter configuration. (b) There is a transition region that makes a gap between the maximum low input V_{IL} giving a high output V_{OH}, and minim high input V_{IH} giving a low output V_{OL}.

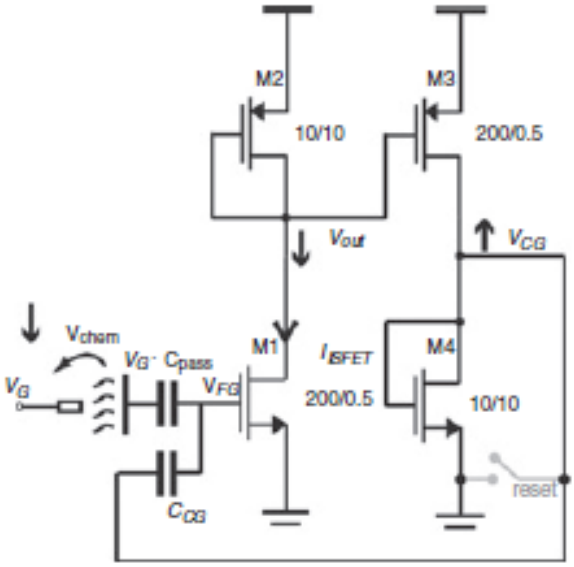

Figure 6.6.: PG-ISFET inverter having a positive feedback to switch for $0.01pH$ change [214].

cleotide incorporation. The other eliminates the temperature influence and tracks the changes. Its resolution may be set by sizing the transistors in its current-mirrors, with no limit on the dynamic range.

6.2. ISFET-based Pseudo Inverter

Figure 6.7a shows an ISFET-based pseudo-inverter configuration with a cascade of inverters, proposed by the author. To provide tune-ability and pixel selection, by turning on the pixel only when its output needs to be read, a pseudo-inverter configuration like Figure 6.3(a) is

made. However, instead of connecting its bias to the reference electrode, it is biased through a separate voltage that can tune the switching threshold of the inverter.

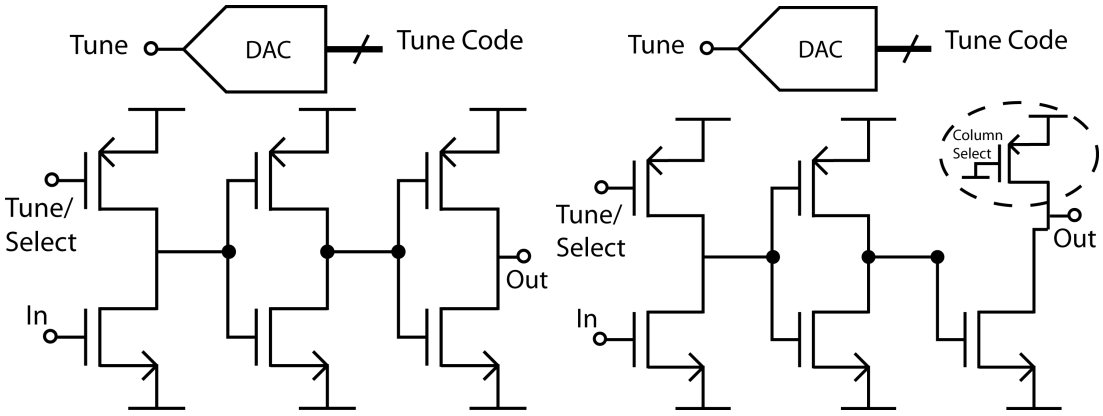

(a) ISFET-based pseudo-inverter with stack of inverters.

(b) The pseudo-inverter pixels may be read like ROM arrays.

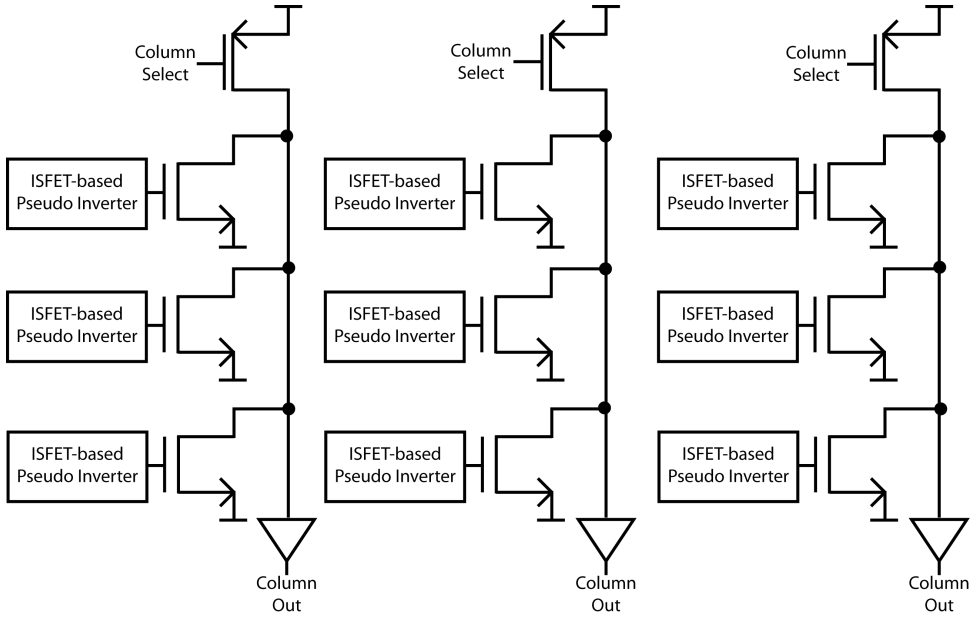

(c) The pseudo-inverter pixel array analogy to ROM arrays when the ISFET-based pseudo inverters are as in Figure 6.7b.

Figure 6.7.: ISFET-based pseudo-inverter.

In order to improve the sharpness of the output signal, a cascade of inverters is added, acting like a voltage comparator and buffer. From another point of view, this second stage can be considered as the switch and the first stage a pseudo push-pull amplifier. The third stage buffers the output. The last stage may be drawn as in Figure 6.7b to be a pull-down NMOS for array configuration. The drain of the NMOS, which is the pixel output, may share a line in a column with other pixels' outputs. When a pixel in that column is selected, a pull-up PMOS drives the line to VDD (or digitally 1). Only the pixel in the selected row can pull down the line, if its input voltage increases (the pH drops).

Following the ISFET-based DNA logic approach, at a calibration stage prior to running a test, the tune voltage biasing the ISFET-based inverter at the verge of switching can be recorded. At the time of reading the pixel for detection of a pH change, a pH drop causing the inverter to switch pulls down the line. In this manner, the dependency on the reference electrode is replaced by an internal tune voltage.

6.2.1. Resolution Enhancement

For every ΔV_{In} on the gate of the NMOS ISFET at the switching threshold of the inverter V_M [213], there is an equivalent ΔV_{Tune} that can switch back the output. In a symmetric inverter ($r = 1$ in equation (6.1)), the transistors are sized to make them equivalent. However, making them asymmetric can help reading the changes that are smaller than the resolution of the digital-to-analogue converter (DAC) that provides $Tune$ voltage. In other words, ΔV_{Tune} needs to change more to cancel out a change in ΔV_{In}. It comes at a cost of dynamic range, but considering the sequencing and genotyping application with limited equivalent range of few millivolts, this compromise may be a win.

$$V_M \approx \frac{rV_{dd}}{1+r} \tag{6.1a}$$

$$r = \frac{\mu_p C_{ox} \frac{W_p}{L_p}}{\mu_n C_{ox} \frac{W_n}{L_n}} \tag{6.1b}$$

$$\begin{aligned} \Delta V_{Tune} &= -\Delta V_{In} \times \frac{g_{m-NMOS}}{g_{m-PMOS}} = -\Delta V_{In} \frac{\sqrt{2 I_D \mu_n C_{ox} \frac{W_n}{L_n}}}{\sqrt{2 I_D \mu_p C_{ox} \frac{W_p}{L_p}}} \\ &= -\Delta V_{In} \sqrt{\frac{\mu_n \frac{W_n}{L_n}}{\mu_p \frac{W_p}{L_p}}} \end{aligned} \tag{6.2}$$

Figures 6.8a and 6.8b display the result of a sample simulation, which shows the equivalent change at $Tune$ voltage for a change in the input voltage In. The asymmetric design of the pseudo-inverter gives a 4.19 slope, as the relative change of $Tune$ to In.

6.2.2. Switching Threshold Change

When the supply voltage is high enough that at the switching threshold of the second stage, the NMOS and PMOS transistors of the first stage are in velocity saturation, the change in the switching threshold can be ignored if the gain of the first-stage transistors ($g_m/(g_{ds-NMOS} + g_{ds-PMOS})$) is sufficiently high. The range of this threshold is defined by the noise margins of the second stage inverters. The equivalent change in $Tune$ and In voltages will be:

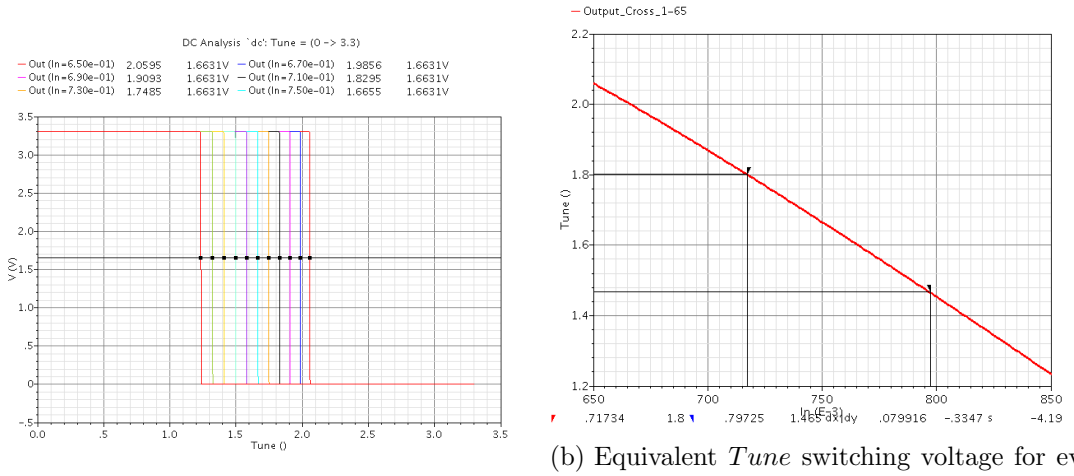

(a) Pseudo-inverter switching for different inputs at NMOS, sweeping $Tune$.

(b) Equivalent $Tune$ switching voltage for every input (In) in agreement with equation 6.2.

Figure 6.8.: Asymmetric switching may help indirect readout resolution.

$$\Delta V_{Tune} = \epsilon \times \frac{g_{ds-NMOS} + g_{ds-PMOS}}{g_{m-PMOS}} \tag{6.3}$$

$$\Delta V_{In} = \epsilon \times \frac{g_{ds-NMOS} + g_{ds-PMOS}}{g_{m-NMOS}} \tag{6.4}$$

If the tune voltage steps are bigger than this equivalent, the conversion of the signal changes are not affected. However, when the supply voltage is not high relative to the threshold voltages, especially in deep sub-micron processes, some error might happen. When the second stage inverter is designed to have a switching threshold of $VDD/2$ and it changes for ϵ, assuming the transistors are in strong inversion, equalising the currents in the transistors and representing their gain factors with K gives

$$\begin{aligned} &I_{D_N} = I_{D_P} \Rightarrow \\ &K_N(VDD/2+\epsilon)\{V_{In} + \Delta V - V_{tn} - 1/2(VDD/2+\epsilon)\} = \\ &K_P(VDD/2+\epsilon-VDD)\{V_{Tune} + \Delta V_{Tune} - VDD - V_{tp} - \\ &1/2(VDD/2+\epsilon-VDD)\} \end{aligned} \tag{6.5}$$

By expanding the brackets and cancelling the equivalent parameters as in Appendix K, the required $Tune$ voltage change is calculated with equation (6.6).

$$\Delta V_{Tune} = -\frac{K_N(VDD/2+\epsilon)}{K_P(VDD/2-\epsilon)}\Delta V_{In} \tag{6.6}$$

and the resulted error for the equivalent $Tune$ voltage change is

$$\Delta\Delta V_{Tune} = -\frac{K_N}{K_P}\frac{\epsilon}{VDD/2-\epsilon}\Delta V_{In} \tag{6.7}$$

By choosing a higher aspect ratio for the NMOS ISFET relative to the tuning PMOS, a higher resolution for following the changes on the ISFET NMOS is achieved, whereas the chance of error in $Tune$ voltage, in result of switching threshold change seems to increase too. However, the other parameter in defining this error, and indeed the lower limit for $Tune$ voltage is ϵ, which is set by the second stage inverter as the forbidden zone of the inverter [212]. It means that ϵ is considered as half of the difference between the maximum input voltage giving a high output and the minimum input voltage giving a low output for the second inverter. Putting it in another way, the higher the noise margin has the second stage inverter, the sharper the second stage inverter switches, the lower ϵ is, and the lower the error.

To overcome this deviation from the ideal relation between $Tune$ and In, the effect of the threshold voltage change error on the measurements, it is worth to consider the equivalent $Tune$ voltage change for ϵ change on the second stage input. Therefore, if the output of the first stage (the input of the second stage) is changing for ϵ, $Tune$ change is equal to:

$$\begin{aligned}
&\Delta V_{Tune-e} = \epsilon/A_{PMOS}\\
&A_{PMOS} = \frac{g_{m-PMOS}}{g_{ds-NMOS}+g_{ds-PMOS}}\\
&\Delta V_{Tune-e} = \frac{g_{ds-NMOS}+g_{ds-PMOS}}{g_{m-PMOS}}\epsilon
\end{aligned} \tag{6.8}$$

Equation (6.8) basically gives the minimum $Tune$ voltage change to not let the switching threshold of the second stage inverter affect the conversion. Therefore, the dominant noise from the tuning circuitry, becomes only the least significant bit (LSB) of the conversion for $Tune$ voltage. Consequently, as long as the gain of the PMOS is big enough to make equation (6.8) negligible, a relatively high gain for the NMOS transistor, equalises the LSB noise of the $Tune$ voltage to a negligible input-referred noise value. This is more illustrated in the next section.

6.2.3. Noise

The noise sources are $Tune$ voltage noise, PMOS noise, NMOS noise, second stage transistor equivalent noise, and chemical noise. Considering that the main input for the pixel is the chemical signal, the noise may be calculated as the power-sum of the input-referred noise (as their sources are independent) of the mentioned sources.

$$V^2_{n-Input} = V^2_{n-chem} + (1+\zeta)^2 V^2_{n-eq-In} \tag{6.9}$$

where

$$V_{n-eq-In} = (\frac{g_{m-PMOS}}{g_{m-NMOS}})^2 V^2_{n-Tune} + (\frac{g_{m-PMOS}}{g_{m-NMOS}})^2 (\Delta\Delta V_{Tune})^2 + V^2_{n-Inv} \tag{6.10}$$

while the third term by description in the previous section is negligible and $Tune$ voltage noise can be considered as

$$V_{n-Tune}^2 = V_{n-DAC}^2 + \frac{1}{4}V_{Tune-step}^2 \tag{6.11}$$

V_{n-DAC} is the DAC output noise, added by half the step size for $Tune$ voltage, considered as the quantization error.

Mostly, the dominant noise sources are from the $Tune$ step size and the chemical noise, when all the rest are negligible as long as the value of ζ (representing the decoupling effects on the signal) according to Chapter 4 is small enough. This noise from one point of view defines the resolution of the assay. From another point of view, it tells the minimum required pH-change to be able to interpret the occurrence of DNA elongation/hybridisation and detection of matching strands.

In SNP detection where the analyte is in chambers, it is more relaxed while it tells the minimum PCR cycles required to discriminate which primer has matched and which mutation in the target DNA exists. In genotyping and gene-expression, it tells to what accuracy the relative expression can be calculated. For sequencing, it tells the minimum sample required to have a correct record of the changes in the signals.

6.3. Jump and Track Conversion

In a sequencing array, we are interested in increasing the yield by allocating more space to the sensors and less to the interface. It is also important to read the array with a frame rate and accuracy that no H^+ (generated from the incorporation) is missed. The strength of the signal is defined by the number of samples, the volume of the micro-well and the diffusion and drift of ions. The dynamic range of the input signal is quite small, but the DC offset on the floating gates biases the transistors at different regions. Therefore, it is necessary to use a converter that can quickly converge to the signal, while at the same time can give a proper resolution.

The Pseudo-inverter configuration may allow relaxing the converter's LSB (or equivalently give a higher resolution) by its inherent mutual gain. Moreover, its fast conversion allows a high clock and frame rate operation. The Pseudo-inverter configuration is used in a *Jump and Track* configuration; proposed by the author.

In jump and track, the converter takes a successive approximation like in SAR ADCs[1] to convert the data. Then, by tracking the change on the signal, it over-samples the input. Over-sampling increases the resolution of an ADC, or the effective number of bits (ENOB) [215, 216]. Figure 6.9 gives an overview of the converter in an array.

6.3.1. Digital Conversion

A marching 1 (see Figure 6.10 and Figure 6.11a) is used for the control of conversion in the Jump phase. By reset signal going high, the marching 1 selects the most significant bit (MSB)

[1]Successive Approximation Register Analogue to Digital Converter

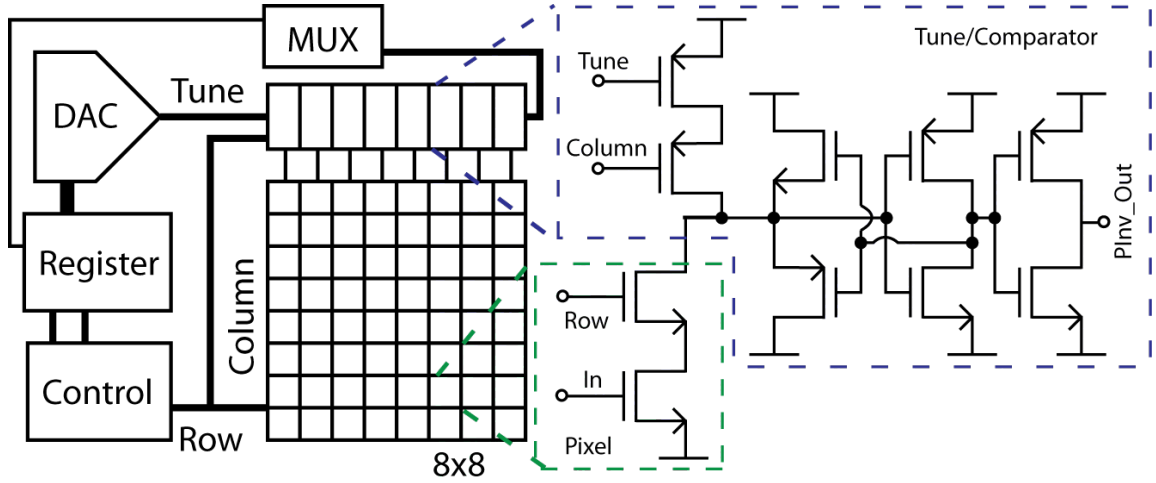

Figure 6.9.: An overview of an array of ISFETs with pseudo-inverter readout, and Jump and Track conversion.

register; Figure 6.11b. At every clock cycle it moves on to select the succeeding bit registers until the last one.

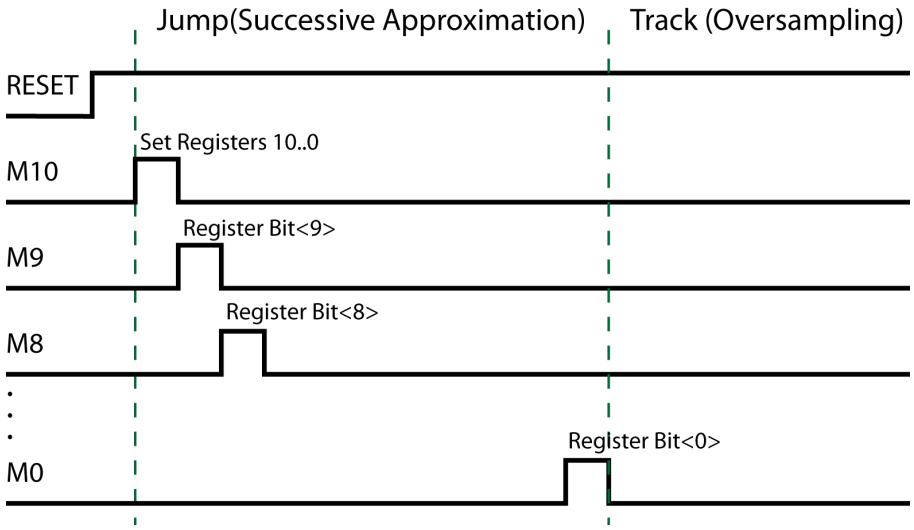

Figure 6.10.: A marching 1 control allows successive approximation and terminates after completion of the approximation to enable tracking/oversampling.

At the Jump phase, first all the bits at the *Tune* register are set to 0, except the MSB. The DAC output is in mid range $VDD/2$. The output of pseudo-inverter gives a comparison of the *Tune* PMOS and the ISFET NMOS currents. At the next clock cycle it replaces the MSB, while the immediate less significant bit is set to 1. In the following cycle also, the inverter output replaces the 1 while the next most significant bit (immediate less significant bit) is set to 1. Similarly the process continues to the LSB and the converter gives the *Tune* voltage closest to the equivalent voltage of the input. Then, the converter exits the jump mode to track the input.

In tracking, at every clock cycle, if the output of the pseudo-inverter is 1, it increases *Tune*

for 1 LSB by adding 1 with the $Tune$ code. If it is 0, it subtracts 1 from the $Tune$ code. To do so, the bit registers are made of a DFF to store the data, and combinational logic to do addition and subtraction; Figure 6.11c.

For a signal bandwidth of f_c, requiring a sampling of f_s ($f_s > 2f_c$ based on the Nyquist theorem to avoid aliasing), oversampling it with a frequency of $f_{OS} = 4^n f_s$ gives n extra bits to the N bit resolution of the converter when performing a moving average with an n-sample window on the N-bit data [217].

By the reset signal, the converter is controlled when to leave the tracking mode and again do a successive approximation as in the Jump state. Therefore, the oversampling rate is set by the frequency of the reset signal, which can be controlled externally.

6.3.2. Pseudo-inverter in Array

Figure 6.12 shows the pixel configuration for an array of 8×8. The second stage is a comparator with an inverter that gives it a positive feedback. The advantage of this configuration is in reducing the load impedance ($1/(g_{m-NMOS} + g_{m-NMOS})$) for the first stage inverter output, and helps the stack inverters switch faster for detecting a current difference between the first stage PMOS and NMOS transistors' currents. The $Tune$ PMOS part of the pseudo-inverter and the stacking inverters are shared for every column. The outputs of the 8 $Tune$ comparators are multiplexed to the bit register, as one pixel at a time is read.

6.3.3. Simulations

Design and simulations of the pseudo-inverter array were done in Cadence Spectre environment using a $0.35\mu m$ process library, considering a power supply of $3.3V$.

Figure 6.13 shows the DC analysis of the pseudo-inverter. Changing the In voltage, the inverter switches at a different $Tune$ voltage. The asymmetric design makes $Tune$ to change more than In. At the mid range bias of $Tune$ and its equivalent In, giving an output of $1.65V$ (the middle of switching transition), the DC gains from $Tune$ and In are respectively $95.8m$ and $450m$ which makes an equivalent mutual ratio of $g_{m-In}/g_{m-Tune} = 4.7$. The total input-referred noise at $1Hz$ is also respectively $8.805e-8V^2/Hz$ and $3.975e-9V^2/Hz$, which shows the input-referred noise for the ISFET by asymmetric transconductances is less for about 4.7^2 times. This gain is at the cost of losing dynamic range. Figure 6.13b shows that the input is limited to $1.05V$.

A parametric analysis for transient operation of the converter was run, giving an equivalent $Tune$ code to In relation as in Figure 6.13b. Figure 6.14a shows the transient response. When in saturation, there is no missing bit. However, in the corners, particularly the weak inversion region, several bits are missed. The reason is that the ratio of the transconductances of $Tune$ PMOS and In NMOS at this region is almost 1. More loss is when they are at different regions of operation with different rate of change in their transconductances. The LSB-equivalent of the 10-bit DAC is about $3.3mV$. Therefore, with $1mV$ steps of parametric analysis, there are periods of almost constant code. But when in transition at different regions of operation, the

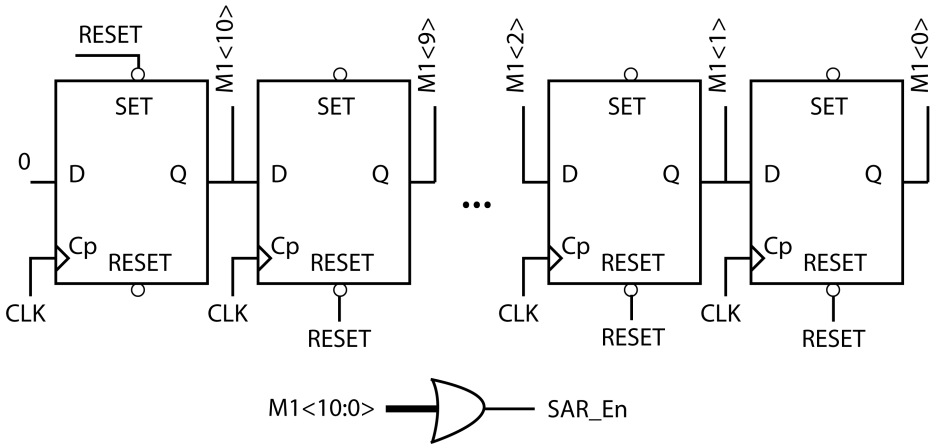

(a) After the active-low RESET goes high, marching 1 control circuit chooses successive bit registers for approximation at Jump phase. When the successive approximation ends, the 1 is terminated until the next time RESET goes low.

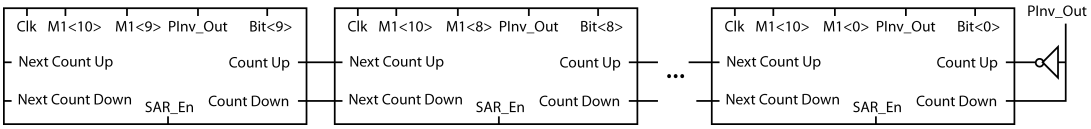

(b) 10-bit register containing the Tune code.

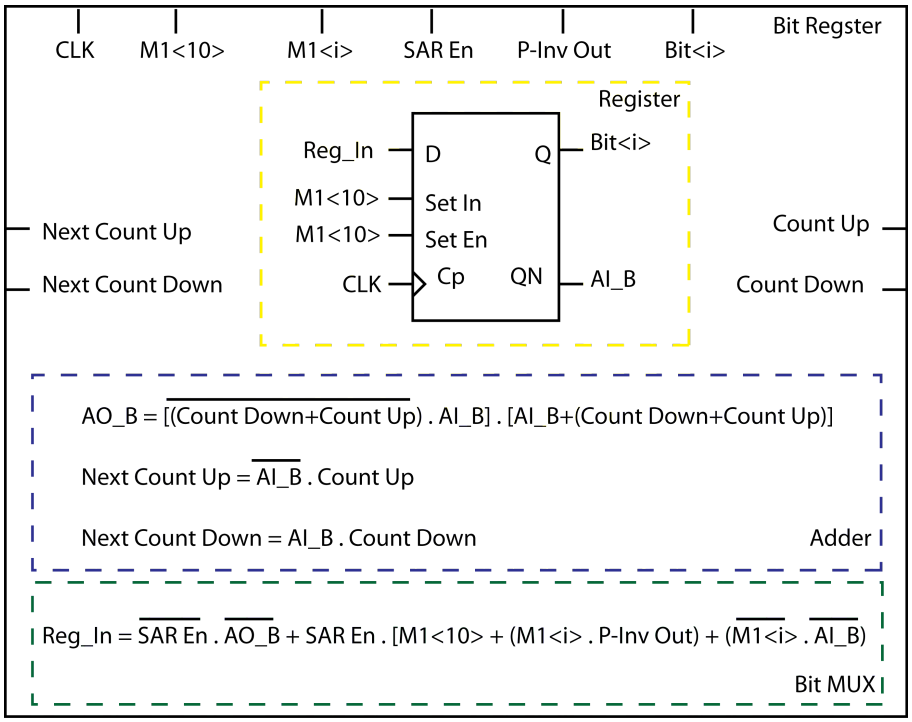

(c) The register consists of a DFF and combinational logic for each bit. The adder calculates the next bit value. The MUX selects the register's input; whether the adder output in tracking, or the pixel output in the successive approximation of the Jump phase.

Figure 6.11.: Logic blocks in Jump and Track converter.

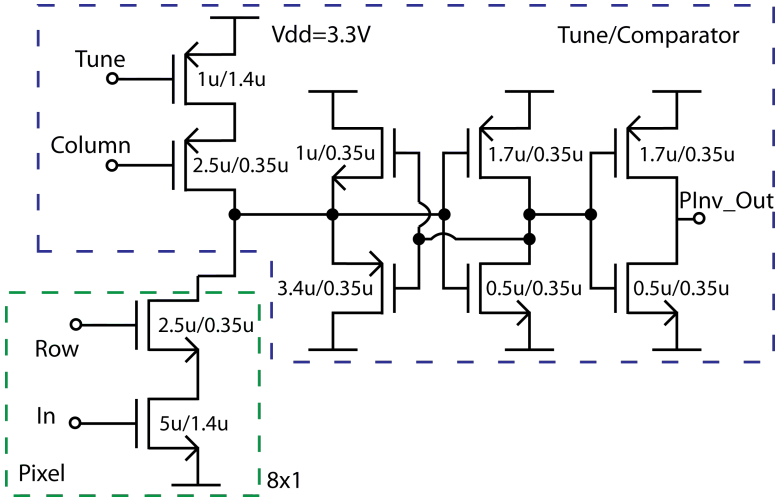

Figure 6.12.: Pseudo-inverter configuration in the array. The pixels are NMOS ISFETs with row-select NMOS. The *Tune* PMOS is shared for each column.

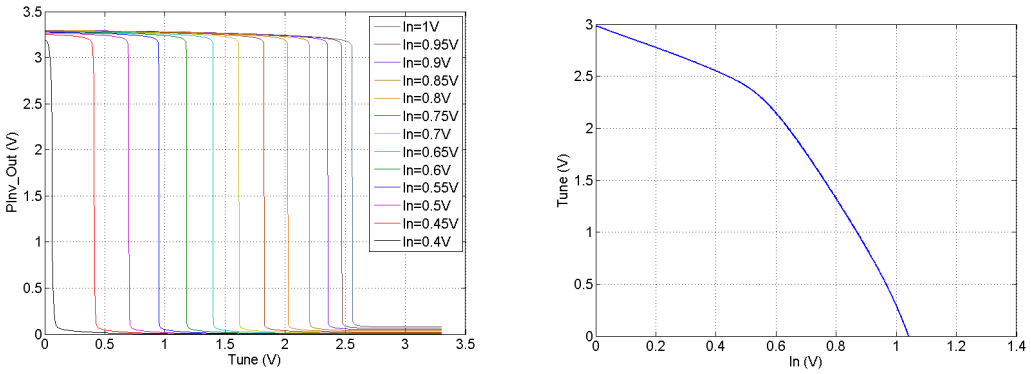

(a) DC sweep of *Tune* voltage showing the change in switching point by change of *In*.

(b) Switching point of *Tune* voltage for every *In*.

Figure 6.13.: DC analysis of the pseudo inverter switching.

relative transconductance for *Tune* PMOS appears smaller creating larger changes of the code.

Since the steps of sweeping *In* was limited[2] to $1mV$, the differential non-linearity[3] and integrated non-linearity[4], particularly with the non-linear DC relation, might not give a proper judgement. Nonetheless, the change in the *Tune* code against *In* can show that the reliable region may be where the code has not changed more than 1 unit. An equivalent mutual gain between the code and the input is shown in Figure 6.14b. The 1428 slope shows the almost equivalent relative transconductances for the *Tune* PMOS and *In* NMOS ($1428 * 3.3/1024 \approx 4.6$).

[2] A constraint over this was the simulation time and processing resource.
[3] The difference between the adjacent analogue inputs giving two adjacent digital outputs.
[4] Deviation in the LSB.

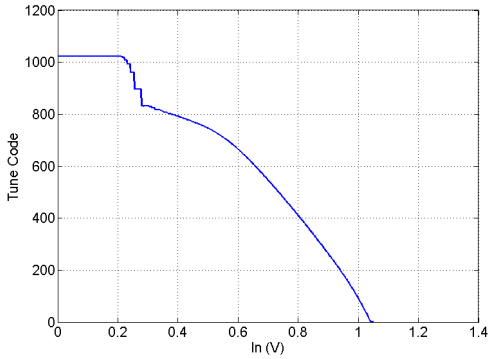

(a) Parametric analysis result on transient operation of the ADC.

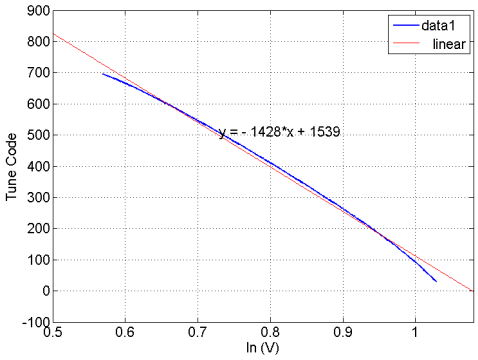

(b) A section of Figure 6.14a where the ISFET NMOS is in saturation.

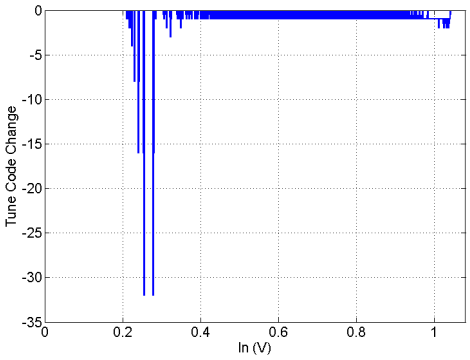

(c) Tune code-change showing the missing codes in 6.14a.

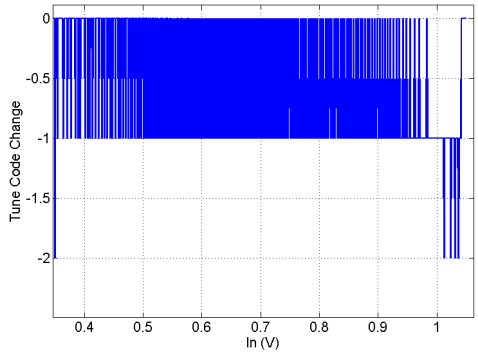

(d) A section of Tune code-change in Figure 6.14c where no code is missing.

Figure 6.14.: Parametric analysis result for $1mV$ steps of input voltage In and the converter output code from transient simulation.

6.3.4. Experiments

The fabricated array (Figure 6.15) was tested in a Faraday cage, using KEITHLEY 4200 and NXP mbed LPC 1768 micro-controller. The chip was glued on a PCB using epoxy. For the measurements, it was immersed into the pH buffer solution. An $Ag/AgCl$ reference electrode was swept by the KEITHLEY in $1mV$ steps every $2s$, after about 2 hours waiting for settling of the drift. The array was controlled by the micro-controller sending pixel address, clock, and reset signals, and recording the output of the converter register. The clock frequency was set to $1kHz$. In order to synchronise the KEITHLEY and the micro-controller, at every step of the sweeping, a trigger signal was sent from KEITHLEY to the micro-controller. After that, the micro-controller would start converting each pixel's input and send it to a PC. For every pixel, after completion of the conversion with successive approximation (the Jump mode), the input was tracked in 16 clock cycles for oversampling and averaging.

Figure 6.16 shows a pixel data conversion example from the experiments. Due to the effect of the clock signal coupled through the solution (as observed from the behaviour of the reference electrode current) in spite of the PCB insulator and epoxy, the measurements were not glitch-

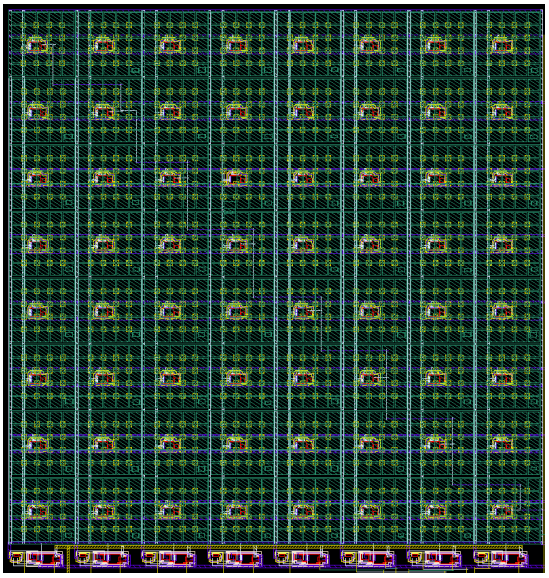

Figure 6.15.: ISFET-based pseudo-inverter array.

free. Nevertheless, the characteristic shows the inherent gain in the system. The smaller slope of the curve is a result of decoupling capacitances (ζ) described in Chapter 4.

6.3.5. Summary

The pseudo-inverter configuration can help in the improvement of the resolution of readout and conversion, as well as compensating for any attenuation of the signal from coupling. In fact, while it was a voltage approach, it is based on current comparison, indirectly translated into *Tune* voltage. It comes at a cost of dynamic range but when the input signal is small, it is not a high-price compromise. With oversampling, further improvement is achieved, and for the ease of operation, with the small changes at the input, part of the more significant bits may be ignored, and only the varying less significant bits may be taken into account[5]. On the other hand, if a current-mode conversion and analysis is developed, the dynamic range limit may be further relaxed and the readout may be simplified to for example voltage clamp (as in Chapter 5 part 5.1.1) and current comparators.

6.4. TICTC for pH Change

In Chapter 5, it was shown that by biasing the ISFET in weak inversion, it is possible to cancel out the temperature effect on the pH sensitivity with the thermal voltage parameter in the voltage-current characteristic of the transistor. Shepherd and Toumazou [183] developed the ISFET-based translinear principle and tried to suppress the temperature dependency of the ISFET interface output. Although the S_{pH} temperature sensitivity was cancelled out, the readout itself was still dependent on external calibration and biasing. The varying slope factor n, as well as the sub-Nernstian sensitivity parameter α, would make a non-linear relation between the

[5]This approach may save bandwidth in large-scale arrays, as in sequencing, discussed in Chapter 3.

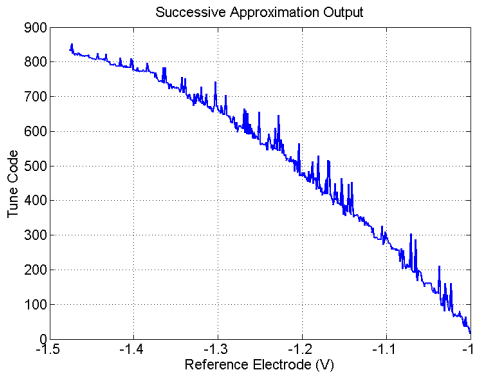

(a) *Tune* code at the successive approximation phase.

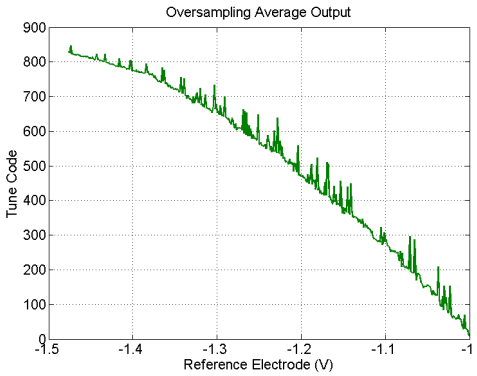

(b) *Tune* code average of the 16 times oversampling.

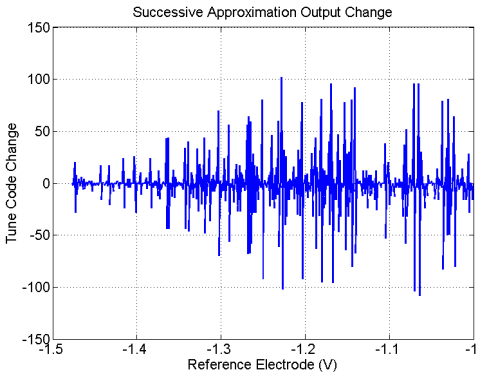

(c) *Tune* Code change with successive approximation.

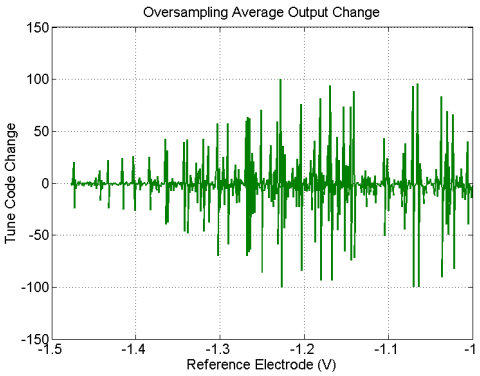

(d) *Tune* change from averaging the oversampled data.

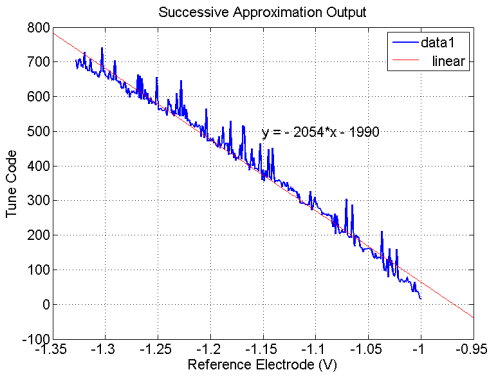

(e) Curve-fit of *Tune* code at successive approximation in the range the ISFET is in saturation.

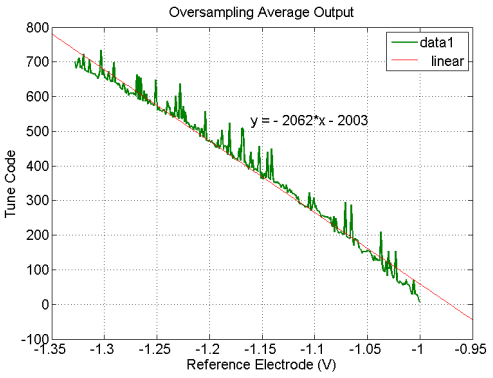

(f) Curve-fit of *Tune* code for the average of the oversampled data in the range the ISFET is in saturation.

Figure 6.16.: A sample data conversion in experiment from a pixel.

output current and the concentration. In section 5.4 Piecewise Linear Approximating readout was proposed which would help resolving the non-linearity issues.

With a similar outlook, here a temperature-insensitive continuous-time converter (TICTC) for pH-change measurement is proposed by the author. Figure 6.17 gives an overview of the ΔpH TICTC. In this readout/converter the ISFET gate is reset to a reference potential which biases the transistor in weak inversion. Then, its current is compared in two current mirrors. One current mirror compares it with a current that is more than the ISFET current at the reset for a difference equivalent to the LSB of the converter. The other current mirror compares it with a current that is one LSB less than the ISFET current at the reset. For better resolution and discrimination, the ISFET current is amplified *gain* times before comparison. Depending on which direction the pH has changed and accordingly which comparator switches, the bit-register taking a record of the changes may increment or decrement. Therefore, a 2's complement representation of the total change is provided. To make it continuous, a delay of the comparators output is used as the clock input of the register. A further delayed copy of it is also used to reset the Ion-Sensitive Field Effect Transistor (ISFET) gate. After the reset, the comparators output becomes 0 and the reset switch opens.

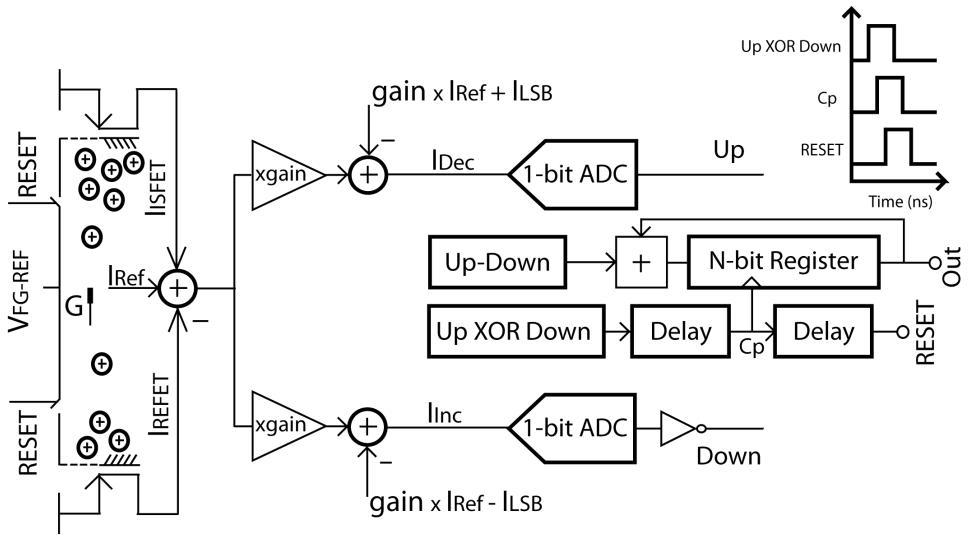

Figure 6.17.: ΔpH to digital converter top-level diagram.

By pH-change detection and re-biasing of the ISFET in weak inversion, the temperature effect is eliminated, and a linear converter with no dynamic range limit is developed. The 2's complement digital range is easily scalable by adding any number of registers for the required word. The equivalent LSB of the converter is set only by sizing the current-mirror transistors, giving a freedom in setting the resolution of the conversion to almost any desired value. The continuous-time approach removes any clock hassle from the converter and uses a delayed copy of the one-bit current comparators' output for loading the change at the register. There is no concern for offset and converter range saturation.

The REFET branch is added for the rejection of common-mode noise, prior to the amplification and comparison, but the system may work independent of the REFET with no change to

the rest of it. The next section briefly describes the readout operation with a quick review on weak inversion operation, discussed in detail in Chapter 5.

6.4.1. Weak Inversion Readout

Figure 6.18 shows the proposed readout with a supply of $3.3V$. The ISFET is biased at weak inversion with $20nA$ current, through the switch to the reference voltage V_{FG-Ref} and $V_{Cascode}$. The current-voltage characteristic of FET in weak inversion is

$$I_D = I_0 \frac{W}{L} e^{V_{GS}/n\frac{kT}{q}} e^{(n-1)V_{BS}/n\frac{kT}{q}} \tag{6.12}$$

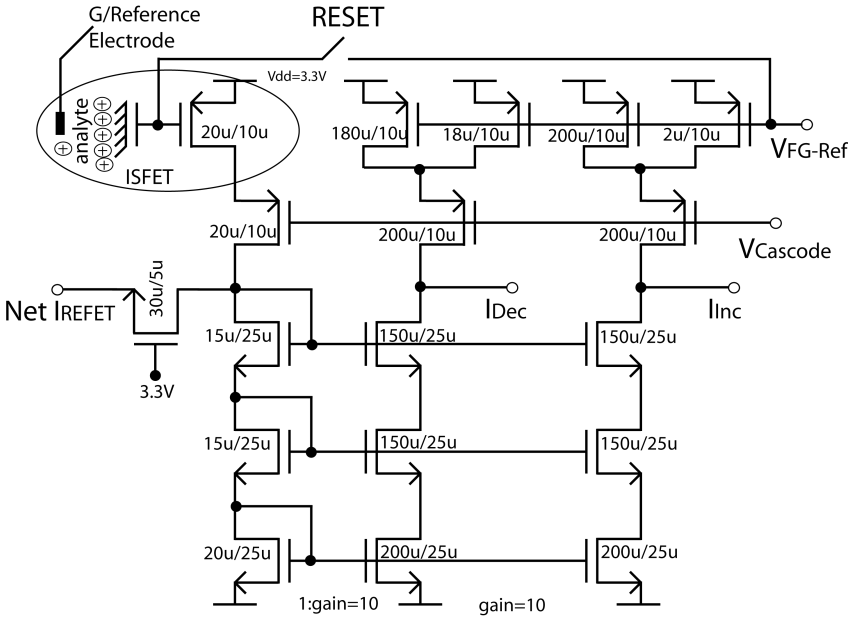

Figure 6.18.: ISFET readout operating in weak inversion. The current is mirrored and amplified to be compared with the threshold currents for any increase/decrease since the resetting of the ISFET floating gate.

n is the slope factor, mentioned to add non-linearity to the previous weak-inversion readouts. It is a function of the depletion layer and oxide capacitance ratio, varying normally between 1 and 1.5 as the terminal voltages change; $n = 1 + \frac{C_{ox}}{C_d}$ [123]. I_0 is a current constant, W/L the transistor channel aspect ratio, and the subscripts are the device terminals.

When the body effect is eliminated as for this design ($V_{BS} = 0$), the ISFET characteristic may be written as

$$I_D = I_0 \frac{W}{L} e^{|V_{FG}-V_{DD}|/n\frac{kT}{q}} \tag{6.13}$$

where V_{FG} is the floating gate voltage resulted from the capacitive coupling of the sensing membrane voltage. The transconductance may be derived as

$$g_m = \frac{\delta I_D}{\delta V_{FG}} = \frac{1}{nkT/q} I_D \tag{6.14}$$

Including the effect of capacitive division by term ζ (ratio of total decoupling capacitance to coupling capacitance) in the equations, with S_{pH} representing the sensitivity, and γ summarising the non-pH related potential changes from the reference electrode V_G to the sensing membrane,

$$V_{FG} = \frac{1}{1+\zeta}(V_G - V_{Chem}) \tag{6.15a}$$

$$V_{Chem} = \gamma + S_{pH}.pH \tag{6.15b}$$

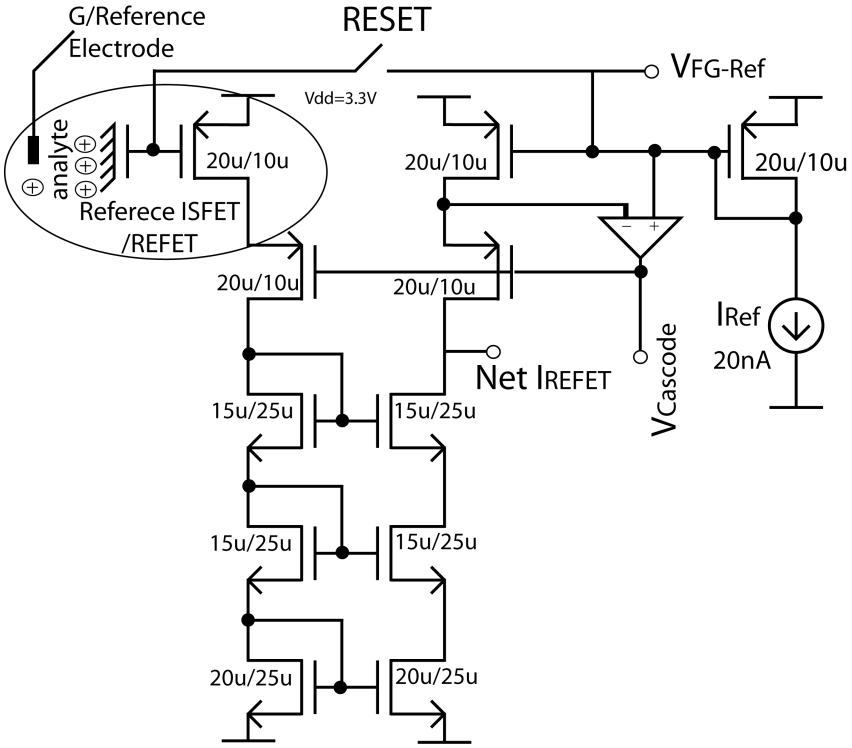

Figure 6.19.: REFET, or the reference pixel readout. The diode-connected and regulated cascode voltage provide the reference biasing for the readout.

6.4.2. Readout Operation

After the switch opens from resetting the floating gate voltage with the reference voltage, V_{FG-Ref} (made by biasing a diode-connected transistor with the same aspect ratio as the ISFET, Figure 6.19), if the pH changes for dpH, the ISFET current changes for dI_D as in equation (6.16), which is not dependent on the temperature anymore, as the thermal voltages in the equations cancel out each other.

$$dI_D = g_m dV_{FG} = \frac{1}{nkT/q} I_D dV_{FG} \tag{6.16a}$$

$$dV_{FG} = \frac{1}{1+\zeta} S_{pH} dpH = \frac{\alpha ln(10)}{1+\zeta} \frac{kT}{q} dpH \tag{6.16b}$$

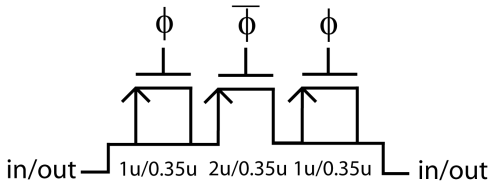

Figure 6.20.: Switch used for the ISFET gate reset.

$$dI_D = \frac{\alpha ln(10)}{n(1+\zeta)} I_D dpH \tag{6.16c}$$

The ISFET current is mirrored and amplified to be compared, to see if the current has increased or decreased. The change is compared with the LSB-equivalent current (I_{LSB}) that is needed for the conversion. According to equation (6.15b), when pH increases the floating gate voltage drops, and therefore the current in the PMOS ISFET increases, and vice versa. Thus, if $dI_D > +I_{LSB}$ the counter should count up one bit and if $dI_D < -I_{LSB}$ one down. These comparisons are done by amplifying the current for *gain* times and comparing it in the two branches of the circuit in Figure 6.18, with currents of $gain \times I_{Ref} - I_{LSB}$ and $gain \times I_{Ref} + I_{LSB}$. The comparison/differentiated currents of the two corresponding branches are shown as I_{Dec} and I_{Inc} respectively.

$$I_{Inc} = gain \times (I_D + dI_D) - (gain \times I_{Ref} + I_{LSB}) \tag{6.17a}$$
$$I_{Dec} = gain \times (I_D + dI_D) - (gain \times I_{Ref} - I_{LSB}) \tag{6.17b}$$
$$I_D = I_{Ref} \ \textit{by resetting} \tag{6.17c}$$
$$I_{Inc} = gain \times dI_D - I_{LSB} \tag{6.17d}$$
$$I_{Dec} = gain \times dI_D + I_{LSB} \tag{6.17e}$$

6.4.3. Digital Conversion

The two readout outputs of Figure 6.18 are fed to a pair of converters which drive the counter, as in Figure 6.21. In the counter, each bit is stored in a DFF, and its next value is calculated by combinational logic, depending on whether it should count up or down. The DFF stores the new value on the rising edge of the signal Cp. Cp is the delayed output of the XOR of the two comparators to ensure a proper gap for the calculation of the bits values. The ISFET gate reset is also a delay of Cp.

A main advantage of this structure is that the dynamic range of the signal is not limited by any process constraints like transistor thresholds or the supply voltage. It is easily expandable. Considering one sign bit and $N-1$ value bits, it can cover a range of $\pm(2^N - 1)dpH$, while dpH

may be set based on the LSB-equivalent, according to equations (6.16c) and (6.17c) to

$$I_{LSB} = \frac{\alpha ln(10)}{n(1+\zeta)} I_{Ref} dpH \times gain \tag{6.18a}$$

$$I_{LSB} = \frac{W_{LSB}}{W_{Ref}} I_{Ref} \tag{6.18b}$$

$$dpH \equiv \frac{1}{gain} . \frac{W_{LSB}}{W_{Ref}} . \frac{n(1+\zeta)}{\alpha ln(10)} \tag{6.18c}$$

This basically allows setting the precision of the conversion by the aspect ratio of the mirror transistors (both *gain* and $\frac{W_{LSB}}{W_{Ref}}$)[6] with no concern over the accuracy of the reference current, as long as the transistors are in weak inversion mode of operation. The resetting also keeps the operating point of the transistor fixed, and so the slope factor n. The sub-Nernstian coefficient α depends on the sensing membrane insulator [119], and for readouts in weak inversion with exponential current-pH relation, it can affect the linearity. Shepherd suggested its elimination through pre-setting n [183], but this might make the readout susceptible to its biasing. Nevertheless, here it is a multiplying factor and does not affect the linearity.

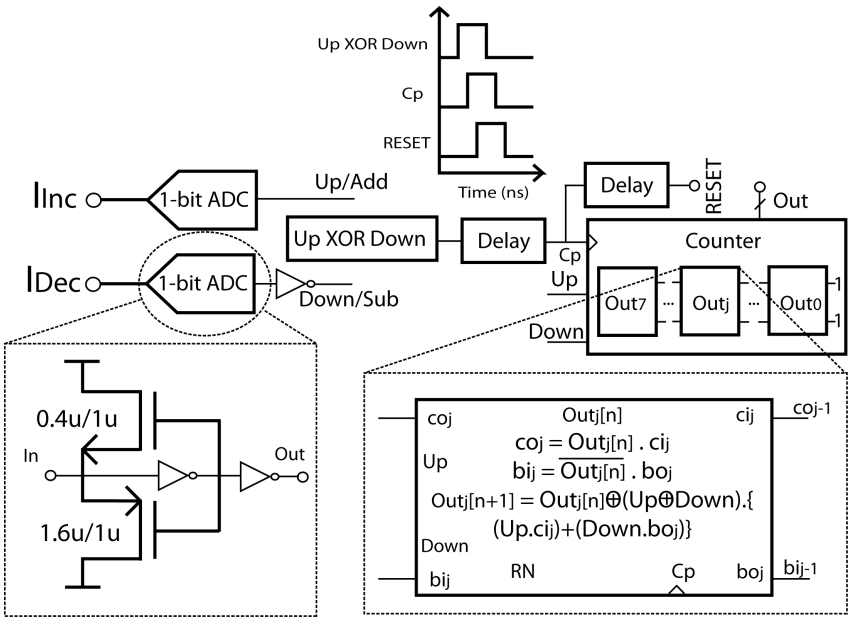

Figure 6.21.: Comparator and signed 2's complement counter. *RN* is a general reset signal used at the start of the test. It also drives *RESET* for resetting the ISFET/REFET at the start besides the comparators.

[6]Here the channel length in the mirror pairs was considered the same. Otherwise, it can come to the denominator of the widths in this equation and add one more degree of freedom in assigning the resolution of conversion.

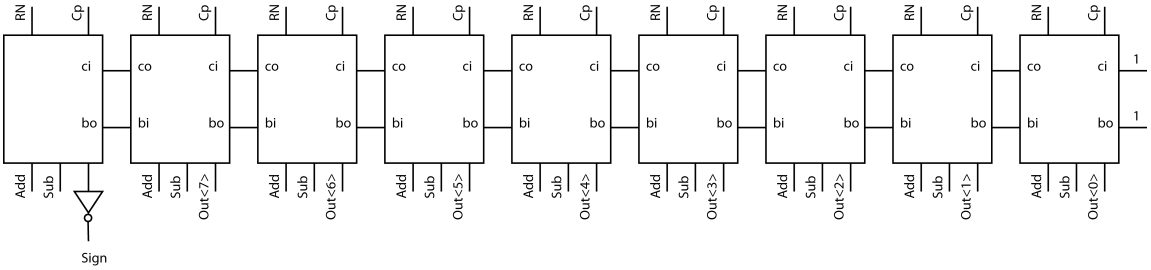

(a) Signed 2's complement register/counter.

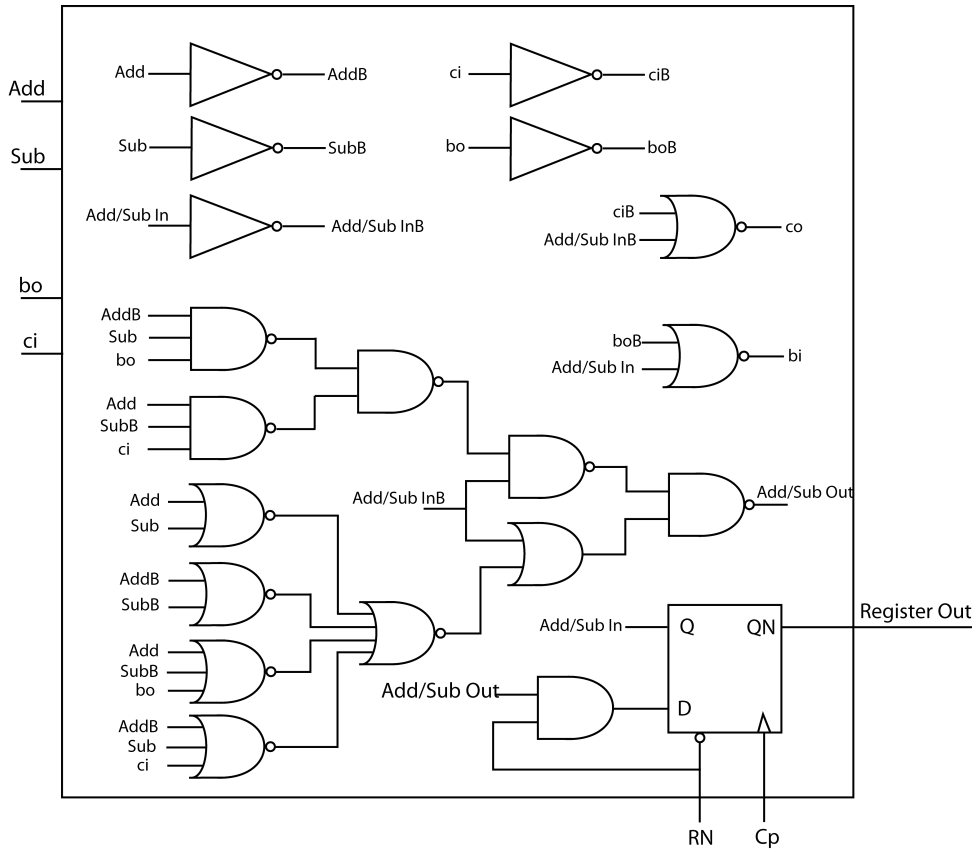

(b) The bit register is made of a DFF and combinational logic, which considering the immediate less significant bit's carry-out (c_o) and more significant bit's borrow-in (b_i), and the Add/Sub signals from the comparators, calculates its next value. RN is the active-low reset.

Figure 6.22.: The register and its bit configuration for the ΔpH TICTC.

6.4.4. Reference Pixel

Certainly the other factor playing an important role in the resolution is noise, to be less than the signal. This is simply satisfied from the readout side, especially as the signals are differentiated from the references, as seen in the simulation results.

While the introduced readout-converter may do single ISFET measurements, a reference pixel, similar to the REFET concept introduced in Chapter 5, may also be used for better conditioning of the signal before conversion. Therefore, a reference pixel is designed as in Figure 6.19, which

Table 6.1.: ΔpH Digital Converter Simulation Results Summary.

	27 $°C$	100 $°C$
S_{pH}	$56.5mV/pH$	$70mV/pH$
ISFET g_m	$491nA/V$	$420.3nA/V$
Readout G_m	$4.9657\mu A/V$	$4.2089\mu A/V$
Common Mode G_m	$324pA/V$	$281pA/V$
Common Mode Rejection Ratio	$83.71dB$	$83.51dB$
dpH	0.015	0.015
$dFG \equiv$ Differential Non-linearity	$503\mu V$	$660\mu V$
Effective Sensitivity dFG/dpH	$33.53mV/pH$	$44mV/pH$
Readout Output Noise	$3pA/\sqrt{Hz}V$	$3.1pA/\sqrt{Hz}$
Readout Output Noise Equivalent	$18\mu pH$	$17\mu pH$
Up/Down Pulse Width	$437ns$	$480ns$
RESET Pulse Width	$441ns$	$474ns$
Up/Down-RESET 50% Delay	$2.3ns$	$2.7ns$
Full Scale ΔpH	1.92	1.92

is reset along with the working ISFET. Its readout output current is subtracted from the ISFET current. This allows elimination of common-mode signals as well as any potential leakage from the resetting switch.

6.4.5. Simulation

Design and simulations of ΔpH-TICTC were done in Cadence Spectre environment using a $0.35\mu m$ technology library. An ISFET equivalent model in Verilog-A (with reference electrode voltage and pH as its inputs) was used to calculate an effective V_{Chem}. α in the model was set to 0.95 and C_{mem} was considered $0.5pF$. This would represent an ISFET sensing membrane of $150\mu m \times 150\mu m$, and a ζ of 2 [171][7]. W_{LSB}/W_{Ref} and $gain$ were set to 10. The whole system is estimated to occupy $(1020\mu m)^2$. A process library operational amplifier from the process was used which would consume about $267.5\mu w$ dominating the power consumption of the whole system ($269.086\mu w$).

DC, AC, noise, and transient analyses of the readout were done in corners of $27°C$ and $100°C$. While temperature could affect the floating gate voltage-change and sensitivity, in the converted results, it was ineffective as expected from equation (6.18). The simulated temperature-insensitive ΔpH-digital converter has a ΔpH resolution (dpH) of 0.015. The performance summary is provided in Table 6.1. The output current noises at $1Hz$ were estimated by equivalent pH changes, based on the effective sensitivity derived in the transient analysis and the transconductance of the readout. A sample of the transient analysis showing the operation of the converter is shown in Figure 6.23.

The switch was also tested for leakage over a period of $200s$; Figure 6.24. The $8.2\mu V/s$ drop

[7]This is a rough approximation based on the theoretical values in the library of the 0.35μ process. Otherwise, for a closer estimation to the practice, a value based on Chapter 4 results may be set. However, it does not influence the operation of the system described here.

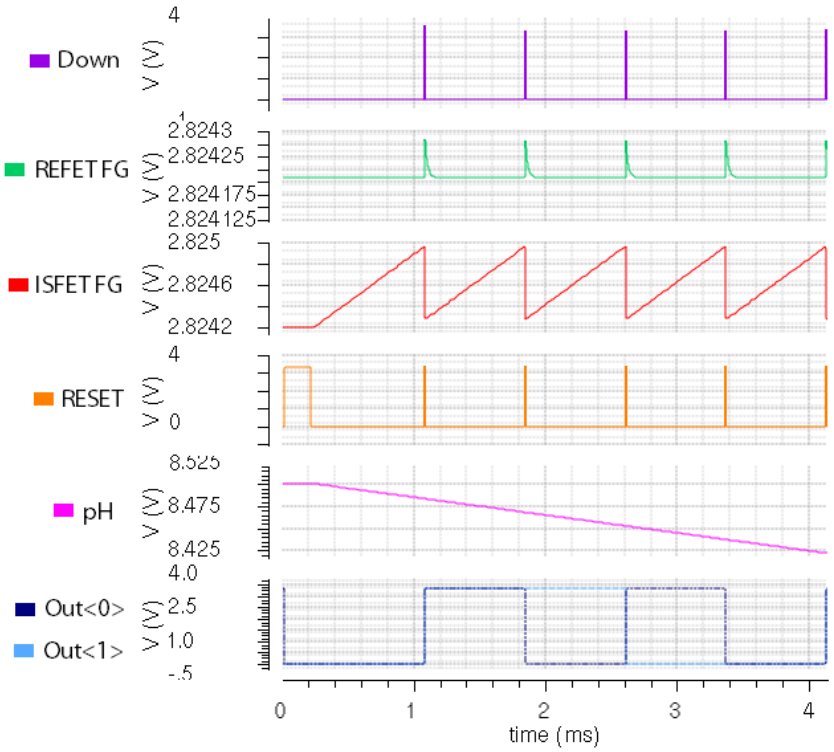

Figure 6.23.: Sample transient analysis result. As soon as the pH-change causes the current to pass the threshold, the comparators generate the signal in the direction of the change (here Down), modify the output and reset the floating gate again waiting for the next change.

rate, which can be approximated to $0.00015pH/s$ and $0.1dpH$ $(0.1LSB)$ for a sensitivity of $50mV/pH$, is small enough to not affect any of the reaction signals. The incorporation window to generate signal is less than a second happening at milliseconds for a single nucleotide[8].

6.4.6. Summary

The pH-change temperature-insensitive continuous-time converter provided a novel ISFET readout with digital conversion, operating in weak inversion. The signed digital output would represent the change in 2's complement. Resetting the floating gate of the ISFET eliminated the issue of random offset, and biased the transistor in weak inversion to allow making it temperature-insensitive. Corner analysis results proved the feasibility of its operation. The resetting and the registers operation were regulated by using delay elements and comparison of the change with the equivalent output LSB currents, which made the converter continuous-time. Another advantage of the readout would be its scalability both in resolution and dynamic range. There is no supply voltage limit on the range and its precision is only a matter of sizing, set mainly by the transistors' aspect ratios in the current-mirrors. The cancellation of the current in the resolution calculation equations also showed its robustness to the biasing circuit. However, the big sizes of transistors and the continuous-time operation would recommend this readout for

[8]Chapter 3 provides further details on the nucleotide incorporation.

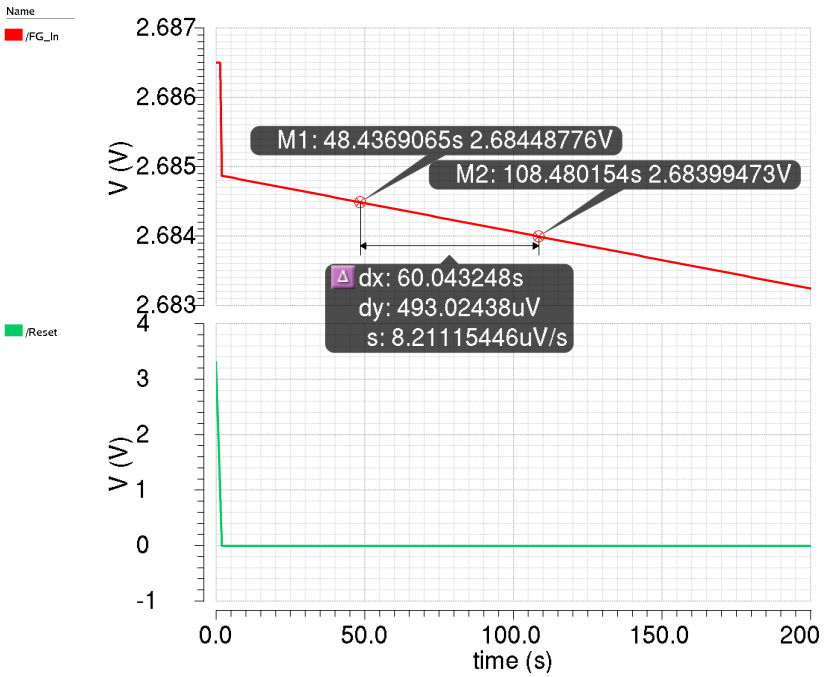

Figure 6.24.: Switch leakage transient analysis.

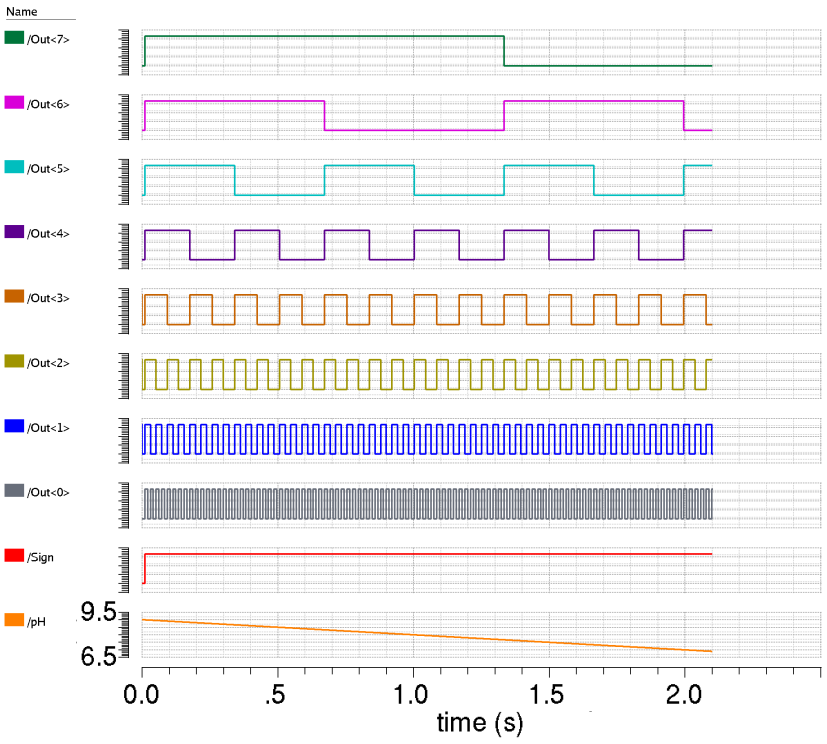

Figure 6.25.: Sample simulation of the ΔpH TICTC operation over time.

the small-scale genotyping microchips where the pixel area may be large for micro-chambers. Nevertheless, while this readout is primarily designed for including the ISFET in a transistor

role, it may be used as a following circuit to a voltage-buffer readout and have the ISFET replaced by a MOSFET and a series capacitor; Figure 6.26. Such a configuration may relax the switches leakage effect on the measurements by choosing a larger capacitor than the one on the ISFET gate. It also allows implementing smaller ISFETs and sharing the readout/converter.

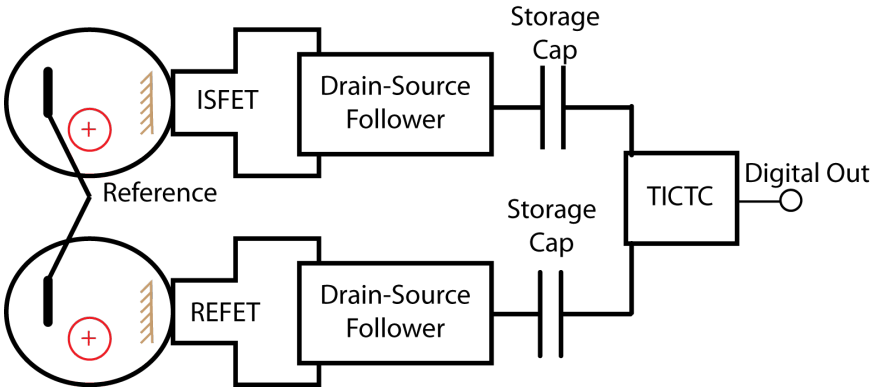

Figure 6.26.: Alternative approach for TICTC.

6.5. Summary

This chapter looked at the ISFET readouts with digital output and the ISFET-based DNA logic concept. It introduced new readouts that would help increasing the resolution of measurements. The advantage of the described digital readouts is the use of ISFET as a transistor with gain, rather than a sole sensor. Such an approach enhances the SNR. Accordingly, the ISFET current is compared for digitisation.

In the pseudo-inverter structure, asymmetrical design of the inverter gave an inherent relative gain, which could help the resolution of readout/conversion by indirect feedback to the gate of the pseudo transistor. On the other hand, for a higher dynamic range of operation, a general current-mode approach may give a better readout resolution. Another advantage would be using few components in the readout.

The temperature-insensitive pH-change converter, not only eliminated the temperature effect on the measurement, by the similarity in the characteristic of the device at weak inversion, but also gave a scalable linear output with no limit on its dynamic range. The resolution of the conversion, and so the limit of detection, was only dependent on the current-mirror transistors; their sizes and gains. However, for high performance and matching, large transistors are required, which is not appealing for large-scale integrated arrays and limit its application to genotyping microchips.

7. Conclusions and Future Work

The advent of semiconductors to many industries have made revolutionary changes, and so in sequencing and genotyping. The ISFET-based technology has the potential to drop the cost and increase the throughput bringing out the tests from centralised laboratories and machines with large footprint, to anywhere that is needed.

This thesis has been inspired by the sequencing and genotyping challenges and breakthroughs which can reshape and enhance the application of molecular biology achievements. While reviewing the alternative approaches, most effort has been dedicated to ISFET-based assays. Considering the performance criteria for both sequencing and point-of-care genotyping, ISFETs and interface circuits and systems were investigated. Taking into account the dependency of throughput on the number of sensors on a sequencing microchip, and knowing the high computation burden on the primary processing of signals, bulk-based auto-calibration and ISFET-based pseudo-inverter readouts were introduced. The former aiming for the background signal effect reduction and the latter to increase the quantization resolution, independent of conversion limit for a converter. For the point-of-care genotyping where unmodified CMOS process is advantageous, despite the non-ideal sensing membrane (the passivation insulating layer on the chip), temperature-insensitive readouts operating independent of the DC offset, with unlimited dynamic range to follow the ionic concentration changes, were proposed. Going deeper to the heart of such set-ups, ISFET as the building element of the pH-based DNA detection systems was investigated. Based on the geometrical effects, a more complete formula for the ISFET characteristic as well as a design methodology were proposed. Accordingly, scaling effects and trade-offs were highlighted and configurations to enhance the performance, within the standard CMOS fabrication process, were proposed.

7.1. Summary and Contributions

Throughout this thesis, two aspects of sequencing and genotyping were considered at each section with the focus on the ISFET-based systems. Here is a summary of each chapter.

7.1.1. Sequencing and Genotyping: Industry and Research

Chapter 2 discussed the works in sequencing and genotyping industry. In sequencing, since the introduction of Sanger's method, many inventions improved the cost and throughput. Until 2011 all the introduced instruments were based on imaging and optical detection requiring molecular modification for labelling. Although the recent news has been on reaching the $\$1,000$

milestone for the whole-genome sequencing by Illumina, the bulky machine would cost $\$1M$[1]. In genotyping maybe the changes were not as significant as for sequencing but likewise a technology shift enabling such tests at the point of care has been necessary. For such set-ups, DNA amplification, also used for sample preparation and/or genotyping and gene expression assays, requires temperature control on the system. Lab-on-chip instrumentations for sample-to-result Micro Total Analysis Set-up (μ-TAS)[2] did not succeed to replace the microarrays and PCR machines. Fully-electronic methods gained interest for eliminating the optical cameras and labelling by the use of biosensors. Among the reviewed methods of RedOx cycling, capacitive and impedance measurement, and charge coupling, detection of ionic concentration change using ion-sensitive transistors (ISFETs) appeared more advantageous. Electrode arrays of RedOx cycling were commercialised in products like e-SENSOR™and ElectraSense® but remained in bench-top configurations. Whereas detection based on the concentration change and implementation in CMOS technology have made the ISFET-based design promising for scaling, high level of integration, and cost. A potential competitor of this technology, current-measurement of nanopores with translocation of DNA strands, was also briefly described. Nonetheless, despite being almost the same age as the ISFET-based technology, it has left behind to introduce a reliable accurate set-up.

7.1.2. pH-based Genotyping and Sequencing

Chapter 3 described the two pioneering ISFET-based systems developed for genotyping and sequencing. Basing on the CMOS technology is the unique advantage that allows them to benefit from the cost-efficiency of the semiconductors mass production.

The genotyping microchip integrates resistive heaters, temperature sensors, and processing circuitry alongside an ISFET array. It is fabricated in an unmodified CMOS process where the sensing membrane of the ISFETs is the CMOS passivation layer. On top of the microchip a microfluidic manifold with dozens of reaction chambers sits. The miniaturised set-up in a few grams weight enables simultaneous DNA amplification and detection. Nevertheless, increasing the number of tests on the chip requires increasing the number of ISFETs and reconfiguring the processing circuitry. One way is multiplexing and another is implementing more intelligent readouts that condition the signal with less number of components. Other challenges are ISFET's coupling efficiency, DC offset, temperature dependency, process variation, and signal drift, which affect the accuracy of the system and complexity of processing.

The sequencing system pricing $\$80,000$[3] is less expensive and quicker than its optical rivals. At its heart is a microchip housing an array of ISFETs with micro-wells on top. Primed template DNA strands attached on microbeads are distributed onto the ISFET/micro-well array. Besides enzymes, nucleotides are flown onto the chip one at a time with interval washing steps. The ISFETs measure the ionic concentration change in the wells which signals the incorporation of

[1] The achieved $\$1,000$ in 2014 is under question whether it is the reagents and test cost excluding the device or it is inclusive. Nevertheless, the HiSeq X Ten machine aims for population-scale research.
[2] Micro Total Analysis Set-up.
[3] The first generation instrument price in 2011. It dropped to $\$50,000$ in 2014.

the nucleotides during the synthesis; in case of matching the template DNA and elongating the primer strand. The sequencing takes about 2 to 4 hours. However, its computational burden is mainly the low-level processing for base-calling. The background signal from the bulk analyte on top of the chip is a source of noise complicating the processing.

Improving the throughput, in addition to optimisation on the chemistry and array loading yield, requires an increase in the number of ISFETs. Although in principle scalable, higher levels of integration increases the signal loss for the faster diffusion of ions, reducing the detection window. Consequently, the chance of error rises resulting shorter accurate reads[4] while higher sampling rate and data adds to the computation burden. Moreover, the ISFET coupling efficiency may drop and the transistors flicker noise increase. Detection of homo-polymerisation (the incorporation of nucleotide for multiple bases), signal dephasing due to the leftover nucleotides from previous flows onto the array, and bead loading are the other challenges. Abstract modelling and simulations of the incorporation by the author highlighted the base-calling and scaling strains.

Optimisation solutions from the ISFET and readout design perspective for enhancing the signal measurement and overall system performance, for both of the set-ups made the focus of this research in the remaining chapters.

7.1.3. ISFET Geometry

Chapter 4 explained the operation of ISFET and its sensitivity dependency on temperature (proportional to absolute temperature) and the sensing membrane insulator-analyte buffering capacity. The buffering capacity is dependent on the number of binding sites the insulator provides where amorphous structures may be more favourable. Being a non-Faradaic sensor, the potential on the sensing membrane is coupled on the floating-gate of the ISFET. The capacitive coupling of the signal is degraded by decoupling parasitic capacitors which is a function of the ISFET geometry. In order to take into account the physical configuration of the ISFET into the current-voltage relations, a term ζ as the ratio of the decoupling to coupling capacitors was introduced by the author. The coupling capacitor is the capacitance made by the charges on the sensing membrane and the metal plate beneath the insulator defining the sensing area of the ISFET, and connected to the floating gate by metal vias. The decoupling capacitors are the intrinsic FET capacitors at the gate, particularly the gate oxide, and the parasitics from the extended metals and the sensing plate. In unmodified CMOS, the passivation layer is subject to considerable variations resulting in the variety of coupling among ISFETs. A ζ-based design methodology was proposed by the author to suppress some of the ISFET non-idealities (like threshold voltage and drift) and limit the variations under control by proper sizing. A concluding point for the readout circuit design would be to make sure drain potential is fixed or follows the gate to suppress the gate-drain capacitance (particularly increasing with the Miller effect).

[4]The read length for the highly integrated systems of Proton I ($165M$ sensors) and Proton II ($660M$ sensors) dropped to 200 and 100 bases respectively, from 400 bases in PGM 318 with $11M$ sensors.

Simulations and experiments supported the ζ-based design approach. Two sets of 5 ISFETs one with FETs of $5\mu m/1\mu m$ and one with $1\mu m/5\mu m$, with sensing membranes of $5\mu m \times 5\mu m$, $10\mu m \times 10\mu m$, $20\mu m \times 20\mu m$, $40\mu m \times 40\mu m$, and $80\mu m \times 80\mu m$ were designed. All the tests were repeated in $pH04$, $pH07$ and $pH10$ solutions for 8 dies. Considering the dominant decoupling source is the FET gate oxide, the ratio of the sensing membrane area to the FET area should be as high as possible for better coupling. ISFETs with higher sensing area have better coupling due to larger coupling capacitance. However, from the experiment results it appeared that the coupling and ζ were not changing as a sole function of the area, but a fairly linear of the square-root of the area, or the side of the square-shape sensing plates. It was derived that the parasitic decoupling capacitors increase as a function of the perimeter of the ISFETs. Therefore, for maximising the ISFET coupling factor, a shape with maximum area-to-perimeter ratio is preferred.

ISFETs with octagonal shape were designed and tested, but the experiment results showed that ISFETs with square sensing plates give better coupling of the signal according to their transconductances. One assumption is that the number of corners in a shape may also increase the decoupling parasitics. Layout-extract parasitics were also compared but their dependency on the area and so inconsistency with the experiment results further highlighted that the parasitics may be more dependent on the perimeter of the sensing membrane. ISFETs with meshed sensing membranes were also investigated especially for DC offset from the trapped charges on the ISFET, but they did not show considerable advantage over the single-plate configurations.

Therefore, it was concluded that for a certain area allocated to the ISFETs, for better coupling, the sensing plate should be of square shape with minimum inter-layer metals (via connections and metal layers beneath the top layer) used to extend the gate, and FET area should be limited to the minimum possible. Therefore, it highlights a trade-off over area, coupling efficiency, and power, for a certain transconductance.

In addition, monitoring the reference electrode current during the drift experiments showed that it changes in an opposite direction to the drift signal on the ISFET. Particularly at the beginning where the drift was fast as if there was a charge balancing between the microchip surface, the reference electrode, and the analyte bulk, causing the initial drift behaviour. Nevertheless, it gives the opportunity for future system designs to use the reference electrode current for the detection of rate and direction of drift.

To reduce the decoupling effects of the sensing plate parasitics, an ISFET with enhancing shield was proposed by the author. To improve the coupling, a metal plate at a layer below the sensing metal plate, surrounding its perimeter and shielding it from the substrate and other potential nodes, is considered. This shield is connected to a buffer of the floating-gate which may be through a buffer configuration of another FET, or a unity-gain amplifier sharing its input gate with the ISFET, or directly connected to the source of the ISFET when operating in a source-follower configuration.

7.1.4. Analogue Readout Circuits

Chapter 5 gave a summary of the ISFET readouts with analogue outputs. Majority of the primary readouts only convey the potential on the floating gate with no processing. Some of the recent published works tried to tackle the DC offset and drift issues by periodically resetting the readout, and measuring the change in between the reset events without integration. Weak inversion operating readouts with ratio calculation between an ISFET and a REFET (a reference ISFET intentionally measuring no pH change) provided continuous processed current-mode outputs. Use of REFET as a reference for eliminating the non-ideal behaviours and common noises is seen also in the ISFET-based sequencing and genotyping systems.

Mixed-signal approach for the calibration of ISFET readouts prior to a test was discussed. A piecewise linear approximating (PLA) readout which would reset and integrate the measurements periodically in current-mode was introduced by the author. It eliminates the temperature dependency, and its output current is not limited by the supply range. Considering the need for high area in the ISFETs with thick sensing membrane, as in the unmodified CMOS (for lower ζ and higher coupling), in the point-of-care microchips where reaction chambers may also limit the minimum area, the space underneath the large sensing areas can be used for such in-pixel conditioning readouts. However, it is only feasible when the signal change rate is higher than the resetting switches leakage and the resetting frequency. It is also suggested that this interface be used as a following system to a buffering readout (e.g. drain-source-follower) and have its ISFET replaced with a MOSFET and a capacitor. In that case the capacitor may improve the time constant and allow tracking signal changes in slower reactions while letting the ISFET gate floating for coupling.

A bulk-based design for auto-calibration and common-mode rejection was proposed by the author. The ISFET back-gate may be used for cancelling out the DC offset, or in an array of ISFETs it may be used for auto-calibration in a certain range of offsets, and common-mode rejection. For the sequencing arrays with the background signal increasing the processing load, common-mode elimination through the back-gate was proposed by physically defining the reference pixels that would not accommodate microbeads. It was shown how to maximise the symmetric dynamic range by the placement of diode-connected voltage-control transistors. However, this configuration prefers fabrication in 3-well processes where the back-gate may be available as a controllable terminal.

7.1.5. Digital Readout Circuits

Chapter 6 reviewed the ISFET-based DNA logic concept and chemical switch. In some genotyping tests like SNP detection, it is a single bit of information that is acquired from the reaction/ISFET, whether the biomarker matched and the pH dropped or not. Therefore, switches may replace the analogue readouts by biasing the reference electrode in a way that a certain pH-change switches the ISFET-based inverter.

One of the key challenges described in Chapter 3 for sequencing arrays is the signal amplitude being a percentage of the pH, demanding high-resolution converters. On the other hand, the

dynamic range of the signal is small. Trying to maximise the number of sensors on the chip and reducing the area of the interface circuits, ISFET-based pseudo-inverter readouts were proposed by the author with asymmetric sizing of the FETs. The unequal transconductance of the ISFET and its complementary MOSFET gives an inherent gain. This amplification helps reading the potential changes in a limited range, but linearly with a reduced number of transistors, and equivalently increases the resolution of conversion and minimises the input-referred noise. This configuration may be used for a mixed-signal calibration scheme, using the complementary MOSFET as a tuning element for the ISFET-based switch.

Since the ISFETs of an array may experience a random DC offset, for the pseudo-inverter-based readout, Jump and Track converter was designed by the author. At the jump state, the converter with successive approximation finds the gate potential for the complementary MOSFET making the pseudo-inverter at the verge of switching. Then it enters the track mode which can oversample and switch according to the output of the pseudo-inverter. To increase the switching fan-out and reducing the transition gap, a stack of inverters buffer the pseudo-inverter output.

For the point-of-care microchip, similar to the linear approximating readout, a continuous-time converter measuring the pH-change with the elimination of DC offset and temperature effect, was developed by the author. This ΔpH-to-digital converter operates in weak inversion and is not limited by the supply range. The similarity of the temperature dependency in the weak inversion FET operation and the sensitivity of the sensing membrane allows elimination of this factor from the measurements. Re-biasing the transistor ensures linear operation. Its measurement dynamic range is easily extended by adding digital register blocks. However, similar to PLA readout it needs the resetting switch leakage to be under control. Hence it may be used as a processing unit following a linear buffering readout and have its ISFET replaced with a MOSFET and a series capacitor for slower reactions.

7.2. Future Work

Better performance in sequencing and genotyping requires improvements at all stages of preparation, detection and analysis. Some of the potential works for future investigation and implementation are as follows.

7.2.1. Applying the Trends in Optical Methods

Besides the technological innovations in the signal detection in the reviewed optical methods, different approaches in running the sequencing were taken for enhancing the accuracy. Use of reversible chain termination in sequencing by synthesis that limits the error from homopolymerisation, and utilising the enzyme ligase for the incorporation of oligonucleotides rather than polymerase and nucleotides (potentially increasing the read length and adding redundancy) are examples of possible next trends in the ISFET-based sequencing.

7.2.2. Processing and Base-calling

Chapter 3 described that the current method of processing and base-calling in the ISFET-based sequencing relies on the modelling of the signal and fitting the measured signal to the model, which puts a high burden on the computation. A more complete model requires further consideration of the physical and chemical effects on the signal, particularly the ionic flux exchange process on top of the sequencing microchips. An optimum simulation of the situation requires development of a CAD[5] tool combining the chemical reactions procedure, fluidic motion and diffusions, and electrical field change to make the calculations closer to the reality. On the other hand, machine learning algorithms may help in optimising the data processing and controlling the data generation rate by flexible sampling and clock frequency.

7.2.3. ISFET with Buffer Shield

Chapter 4 emphasised the effects of the ISFET geometry on its signal coupling efficiency, highlighting the negative effect of the parasitics. At the end of the chapter, based on the experiment results analysis, a new ISFET configuration has been proposed. Further research and measurements needs to be undertaken for the new structure to justify its usability.

7.2.4. Drift Control

One of the key challenges in the use of ISFETs has been the signal drift. In the measurements in Chapter 4 it was highlighted that the reference electrode current change direction is opposite the ISFET drift. This may be a method for controlling and predicting drift in the systems. Further research is required to enable designing optimum systems.

7.2.5. Back-gate Calibration for large-scale ISFET arrays

Chapter 5 proposed using the back-gate terminal for the elimination of the common mode and background noise in large-scale ISFET arrays of the sequencing microchips. While the simulation results showed potential suppression of the common-mode signals, fabrication in triple-well processes and experiments are needed to support the analysis.

7.2.6. Local Processing

For the ISFET-based genotyping lab-on-chip, based on the results of Chapter 4, and considering the fact that the use of unmodified CMOS process with microfluidic manifold on top of the chip makes the sensing area large, while recommending a relatively smaller FET, the interface and processing circuits may be implemented within the reaction chamber footprint inside the microchip for each pixel/chamber/ISFET, or locally shared among neighbouring sensors. This way may increase the yield and ease the scaling. In addition to the circuits reviewed specifically

[5]Computer Aided Design

for the ISFET readouts, new approaches of piecewise linear approximation and continuous-time temperature-insensitive data conversion techniques were introduced. A next step toward optimisation of the ISFET-based SoCs is fabrication and test of such circuits.

7.2.7. Medium Scale Integration

While the ISFET-based technology introduced two categories of products (a portable lab-on-chip genotyping and a desktop sequencing), a future system enabling both on a single microchip considering the preparation and computation integration may be a next step in this technology.

7.2.8. Geotagging and Cloud Control with Local Intelligence

One of the key interests in molecular studies for epigenetics, pathogens and infectious diseases, particularly at the point of care, is the geographical location of the gene (species) under test. Future systems shall include geotagging to their generated data and be connected via cloud for robust live control of the genetic changes and traces.

7.2.9. Integration of Sample Preparation

One of the time and labour consuming parts of the experiments is the preparation of sample from extraction to loading of the assay. Several microfluidic and enzymatic methods have been developed but complete integration of the sample preparation has only been reported for bench-top genotyping instruments. One of the potential methods developed for lab-on-chip μ-TAS is the use of magnetic beads and directing them by magnetic fields. Semiconductor microchips are able to host micro-coils and magnetic field sensor-readouts like Hall sensor and MagFETs. A next step in the point-of-care sample-to-result approach may be the investigation and implementation of such systems on the microchip.

References

[1] F. Sanger, S. Nicklen, and A. R. Coulson, "Dna sequencing with chain-terminating inhibitors," *Proceedings of the National Academy of Sciences of the United States of America*, vol. 74, no. 12, pp. 5463–5467, 1977.

[2] L. Liu, Y. Li, S. Li, *et al.*, "Comparison of next-generation sequencing systems.," *Journal of biomedicine & biotechnology*, vol. 2012, p. 251 364, 2012. [Online]. Available: `http://www.pubmedcentral.nih.gov/articlerender.fcgi?artid=3398667\&tool=pmcentrez\&rendertype=abstract`.

[3] M. L. Metzker, "Sequencing technologiesithe next generation," *Nature reviews.Genetics*, vol. 11, no. 1, p. 31, 2009.

[4] J. M. Rizzo and M. J. Buck, "Key principles and clinical applications of "next-generation" dna sequencing," *Cancer prevention research (Philadelphia, Pa.)*, vol. 5, no. 7, pp. 887–900, 2012.

[5] D. C. Koboldt, K. M. Steinberg, D. E. Larson, *et al.*, "The next-generation sequencing revolution and its impact on genomics," *Cell*, vol. 155, no. 1, pp. 27–38, 2013.

[6] C. A. H. 3rd, "Dna sequencing: bench to bedside and beyond," eng, *Nucleic acids research*, vol. 35, no. 18, pp. 6227–6237, 2007, LR: 20130904; JID: 0411011; OID: NLM: PMC2094077; 2007/09/12 [aheadofprint]; ppublish.

[7] D. G. MacArthur and M. Lek, "The uncertain road towards genomic medicine," *Trends in Genetics*, vol. 28, no. 7, pp. 303–305, Jul. 2012.

[8] M. A. Quail, M. Smith, P. Coupland, *et al.*, "A tale of three next generation sequencing platforms: comparison of ion torrent, pacific biosciences and illumina miseq sequencers," *BMC genomics*, vol. 13, pp. 341–216413–341–, 2012.

[9] B. Merriman, I.-T. R. Team, and J. M. Rothberg, "Progress in ion torrent semiconductor chip based sequencing," *Electrophoresis*, vol. 33, no. 23, pp. 3397–3417, 2012.

[10] F. B. Myers, R. H. Henrikson, J. Bone, and L. P. Lee, "A handheld point-of-care genomic diagnostic system," *PloS one*, vol. 8, no. 8, e70266, 2013.

[11] A. Niemz, T. M. Ferguson, and D. S. Boyle, "Point-of-care nucleic acid testing for infectious diseases," *Trends in biotechnology*, vol. 29, no. 5, pp. 240–250, May 2011.

[12] A. C. Palmer and R. Kishony, "Understanding, predicting and manipulating the genotypic evolution of antibiotic resistance," *Nature Reviews Genetics*, vol. 14, no. 4, pp. 243–248, 2013.

[13] M. Mir, A. Homs, and J. Samitier, "Integrated electrochemical dna biosensors for labonachip devices," *Electrophoresis*, vol. 30, no. 19, pp. 3386–3397, 2009.

[14] A. S. Nezhad, "Future of portable devices for plant pathogen diagnosis," *Lab on a Chip*, vol. 14, pp. 2887–2904, 16 2014. DOI: 10.1039/C4LC00487F. [Online]. Available: http://dx.doi.org/10.1039/C4LC00487F.

[15] H. Fletcher, I. Hickey, and P. Winter, *BIOS Instant Notes in Genetics*, Third. Taylor & Francis, 2007, ISBN: 0-4153-7619-X.

[16] Robinson and T. R. Robinson, *Genetics For Dummies*, 2nd ed. Hoboken: John Wiley Sons, Inc., 2010, ISBN: 0-470-55174-7.

[17] T. Brown, *Introduction to genetics: a molecular approach*. Garland Science, 2012.

[18] F. W. Huang, E. Hodis, M. J. Xu, *et al.*, "Highly recurrent tert promoter mutations in human melanoma," *Science*, vol. 339, no. 6122, pp. 957–959, 2013.

[19] J. R. DePhillipo and R. P. Ricciardi, *Kits and methods for assessing skin health*, 2007.

[20] R. P. Ricciardi, *Methods for assessing the susceptibility of a human to diminished health and wellness*, US Patent App. 12/541,486, 2010. [Online]. Available: http://www.google.com/patents/US20100304373.

[21] Weissensteiner, T. Weissensteiner, H. G. Griffin, and A. M. Griffin, *PCR Technology: Current Innovations, Second Edition*. Hoboken: CRC Press, 2004, ISBN: 0-8493-1184-5.

[22] K. J. Shaw, "Rapid pcr amplification using a microfluidic device with integrated microwave heating and air impingement cooling," *Lab on a chip*, vol. 10, no. 13, p. 1725, 2010.

[23] C. Toumazou and S. Purushothaman, *Qpcr using solid-state sensing*, US Patent 7,888,015, 2011. [Online]. Available: https://www.google.com/patents/US7888015.

[24] A. ElHatem and S. Buhler, *On chip heater element and temperature sensor*, US Patent 4,899,180, 1990. [Online]. Available: https://www.google.com/patents/US4899180.

[25] M. Vincent, Y. Xu, and H. Kong, "Helicase-dependent isothermal dna amplification," *EMBO reports*, vol. 5, no. 8, pp. 795–800, 2004.

[26] P. J. Asiello, "Miniaturized isothermal nucleic acid amplification, a review," *Lab on a chip*, vol. 11, no. 8, p. 1420, 2011.

[27] W. Wong, "Dna logic : a novel approach to semiconductor based genetics," PhD thesis, Imperial College London, 2011.

[28] T. P. Niedringhaus, D. Milanova, M. B. Kerby, *et al.*, "Landscape of next-generation sequencing technologies," *Analytical Chemistry*, vol. 83, no. 12, pp. 4327–4341, 2011.

[29] E. R. Mardis, "Next-generation sequencing platforms," *Annual review of analytical chemistry*, vol. 6, pp. 287–303, 2013.

[30] J. Llandro, J. Palfreyman, A. Ionescu, and C. Barnes, "Magnetic biosensor technologies for medical applications: a review," *Medical and biological engineering and computing*, vol. 48, no. 10, pp. 977–998, 2010.

[31] C. J. Smith and A. M. Osborn, "Advantages and limitations of quantitative pcr (qpcr)based approaches in microbial ecology," *FEMS microbiology ecology*, vol. 67, no. 1, pp. 6–20, 2009.

[32] G. J. McLachlan, K.-A. Do, and C. Ambroise, *Analyzing microarray gene expression data : Wiley series in probability and statistics*. Hoboken: John Wiley Sons, Inc., 2004, ISBN: 0-471-22616-5.

[33] H. Vikalo, B. Hassibi, and A. Hassibi, "A statistical model for microarrays, optimal estimation algorithms, and limits of performance," *Signal Processing, IEEE Transactions on*, vol. 54, no. 6, pp. 2444–2455, 2006, ID: 1.

[34] Affymetrix. [Online]. Available: `http://www.affymetrix.com/estore/about_affymetrix/outreach/educator/microarray_curricula.affx#1_2`.

[35] M. Ronaghi, "Pyrosequencing sheds light on dna sequencing," *Genome research*, vol. 11, no. 1, pp. 3–11, 2001.

[36] M. Margulies, "Genome sequencing in microfabricated high-density picolitre reactors," *Nature*, vol. 437, no. 7057, p. 376, 2005.

[37] A. Masoudi-Nejad, Z. Narimani, and N. Hosseinkhan, "Next generation sequencing and sequence assembly," vol. 4, pp. 11–39, 2013. [Online]. Available: `http://link.springer.com/10.1007/978-1-4614-7726-6`.

[38] D. R. Bentley, S. Balasubramanian, H. P. Swerdlow, *et al.*, "Accurate whole human genome sequencing using reversible terminator chemistry.," *Nature*, vol. 456, no. 7218, pp. 53–59, 2008. [Online]. Available: `http://www.pubmedcentral.nih.gov/articlerender.fcgi?artid=2581791\&tool=pmcentrez\&rendertype=abstract`.

[39] W. J. Ansorge, "Next-generation dna sequencing techniques.," *New biotechnology*, vol. 25, no. 4, pp. 195–203, 2009. [Online]. Available: `http://www.ncbi.nlm.nih.gov/pubmed/19429539`.

[40] [Online]. Available: `www.illumina.com`.

[41] M. Foquet, K. T. Samiee, X. Kong, *et al.*, "Improved fabrication of zero-mode waveguides for single-molecule detection," *Journal of Applied Physics*, vol. 103, no. 3, p. 034 301, 2008.

[42] P. M. Lundquist, C. F. Zhong, P. Zhao, *et al.*, "Parallel confocal detection of single molecules in real time," *Optics Letters*, vol. 33, no. 9, pp. 1026–1028, 2008.

[43] J. Eid, A. Fehr, J. Gray, *et al.*, "Real-time dna sequencing from single polymerase molecules," *Science (New York, N.Y.)*, vol. 323, no. 5910, pp. 133–138, 2009.

[44] J. S. Daniels, "Labelfree impedance biosensors: opportunities and challenges," *Electroanalysis*, vol. 19, no. 12, p. 1239, 2007.

[45] J. S. Daniels, "An integrated impedance biosensor array," PhD thesis, Stanford University, 2010.

[46] R. Thewes, F. Hofmann, A. Frey, *et al.*, "Sensor arrays for fully-electronic dna detection on cmos," in *Solid-State Circuits Conference, 2002. Digest of Technical Papers. ISSCC. 2002 IEEE International*, ID: 1, vol. 1, 2002, 350–473 vol.1.

[47] F. Hofmann, A. Frey, B. Holzapfl, *et al.*, "Fully electronic dna detection on a cmos chip: device and process issues," in *Electron Devices Meeting, 2002. IEDM '02. Digest. International*, ID: 1, 2002, pp. 488–491.

[48] M. Schienle, A. Frey, F. Hofmann, *et al.*, "A fully electronic dna sensor with 128 positions and in-pixel a/d conversion," in *Solid-State Circuits Conference, 2004. Digest of Technical Papers. ISSCC. 2004 IEEE International*, ID: 1, 2004, 220–524 Vol.1, ISBN: 0193-6530.

[49] A. Frey, M. Schienle, C. Paulus, *et al.*, "A digital cmos dna chip," in *Circuits and Systems, 2005. ISCAS 2005. IEEE International Symposium on*, ID: 1, 2005, 2915–2918 Vol. 3.

[50] C. Yang, Y. Huang, B. L. Hassler, *et al.*, "Amperometric electrochemical microsystem for a miniaturized protein biosensor array," *Biomedical Circuits and Systems, IEEE Transactions on*, vol. 3, no. 3, pp. 160–168, 2009, ID: 1.

[51] A. L. Ghindilis, M. W. Smith, K. R. Schwarzkopf, *et al.*, "Combimatrix oligonucleotide arrays: genotyping and gene expression assays employing electrochemical detection," *Biosensors and Bioelectronics*, vol. 22, no. 910, pp. 1853–1860, 2007.

[52] C. Guiducci, C. Stagni, G. Zuccheri, *et al.*, "Dna detection by integrable electronics," *Biosensors and Bioelectronics*, vol. 19, no. 8, pp. 781–787, 2004.

[53] C. Stagni, C. Guiducci, L. Benini, *et al.*, "A fully electronic label-free dna sensor chip," *Sensors Journal, IEEE*, vol. 7, no. 4, pp. 577–585, 2007, ID: 1.

[54] C. Guiducci, C. Stagni, G. Zuccheri, *et al.*, "A biosensor for direct detection of dna sequences based on capacitance measurements," in *Solid-State Device Research Conference, 2002. Proceeding of the 32nd European*, ID: 1, 2002, pp. 479–482.

[55] D. D. Venuto, S. Carrara, and B. Ricc, "High resolution electronics for label free capacitive dna detection," in, G. Fung, Ed., ser. Sequence and Genome Analysis: Methods and Applications. iConcept Publisher, 2010. [Online]. Available: `ISBN:978-0-9807330-6-8`.

[56] B. Lee, K.-H. Lee, J.-O. Lee, *et al.*, "An electronic dna sensor chip using integrated capacitive read-out circuit," in *Engineering in Medicine and Biology Society (EMBC), 2010 Annual International Conference of the IEEE*, ID: 1, 2010, pp. 6547–6550, ISBN: 1557-170X.

[57] D. D. Venuto and B. Ricco, "High resolution read-out circuit for dna label-free detection system," in *Quality Electronic Design, 2008. ISQED 2008. 9th International Symposium on*, ID: 1, 2008, pp. 708–711.

[58] D. D. Venuto, S. Carrara, and B. Ricc, "Design of an integrated low-noise read-out system for dna capacitive sensors," *Microelectronics Journal*, vol. 40, no. 9, pp. 1358–1365, Sep. 2009.

[59] E. Katz, "Probing biomolecular interactions at conductive and semiconductive surfaces by impedance spectroscopy: routes to impedimetric immunosensors, dnasensors, and enzyme biosensors," *Electroanalysis*, vol. 15, no. 11, p. 913, 2003.

[60] S. Ingebrandt, Y. Han, F. Nakamura, *et al.*, "Label-free detection of single nucleotide polymorphisms utilizing the differential transfer function of field-effect transistors," *Biosensors and Bioelectronics*, vol. 22, no. 12, pp. 2834–2840, 2007.

[61] A. Poghossian, "Label-free detection of charged macromolecules by using a field-effect-based sensor platform: experiments and possible mechanisms of signal generation," *Applied physics.A, Materials science processing*, vol. 87, no. 3, pp. 517–524, 2007.

[62] A. Hassibi and T. H. Lee, "A programmable 0.18- cmos electrochemical sensor microarray for biomolecular detection," *Sensors Journal, IEEE*, vol. 6, no. 6, pp. 1380–1388, 2006, ID: 1.

[63] A. Manickam, A. Chevalier, M. McDermott, *et al.*, "A cmos electrochemical impedance spectroscopy (eis) biosensor array," *Biomedical Circuits and Systems, IEEE Transactions on*, vol. 4, no. 6, pp. 379–390, 2010, ID: 1.

[64] T. Sakata and Y. Miyahara, "Dna sequencing based on intrinsic molecular charges," *Angewandte Chemie*, vol. 118, no. 14, pp. 2283–2286, 2006.

[65] M. Barbaro, A. Bonfiglio, L. Raffo, *et al.*, "Fully electronic dna hybridization detection by a standard cmos biochip," *Sensors and Actuators B: Chemical*, vol. 118, no. 1-2, pp. 41–46, 2006.

[66] S.-J. Kim, M. Shenoi, K. Yoo, *et al.*, "Label-free cmos dna quantification with on-chip noise reduction schemes," in *Solid-State Sensors, Actuators and Microsystems Conference, 2007. TRANSDUCERS 2007. International*, ID: 1, 2007, pp. 947–950.

[67] S.-J. Kim and E. Yoon, "Label-free cmos bio sensor with on-chip noise reduction scheme for real-time quantitative monitoring of biomolecules," *Biomedical Circuits and Systems, IEEE Transactions on*, vol. 6, no. 3, pp. 189–196, 2012, ID: 1.

[68] A. Manickam, R. Singh, N. Wood, *et al.*, "A fully-electronic charge-based dna sequencing cmos biochip," in *VLSI Circuits (VLSIC), 2012 Symposium on*, ID: 1, 2012, pp. 126–127.

[69] Y. Maruyama, S. Terao, and K. Sawada, "Label free cmos dna image sensor based on the charge transfer technique," *Biosensors and Bioelectronics*, vol. 24, no. 10, pp. 3108–3112, 2009.

[70] E. Souteyrand, "Direct detection of the hybridization of synthetic homo-oligomer dna sequences by field effect," *The journal of physical chemistry.A*, vol. 101, no. 15, p. 2980, 1997.

[71] T. Sakurai, "Real-time monitoring of dna polymerase reactions by a micro isfet ph sensor," *Analytical Chemistry*, vol. 64, no. 17, p. 1996, 1992.

[72] C. Toumazou and S. Purushothaman, *Apparatus and method for the detection of localised fluctuactions of ionic charge by ion sensitive field effect transistors during a chemical reaction*, WO Patent App. PCT/GB2002/000,965, 2003. [Online]. Available: `http://www.google.com.na/patents/WO2003073088A2?cl=un`.

[73] S. Purushothaman, C. Toumazou, and J. Georgiou, "Towards fast solid state dna sequencing," in *Circuits and Systems, 2002. ISCAS 2002. IEEE International Symposium on*, ID: 1, vol. 4, 2002, IV–169IV–172 vol.4–.

[74] S. Purushothaman, "The effect of ion sensitive field effect transistor technology to dna sequencing," PhD thesis, Imperial College London, 2006.

[75] S. Purushothaman, C. Toumazou, and C.-P. Ou, "Protons and single nucleotide polymorphism detection: a simple use for the ion sensitive field effect transistor," *Sensors and Actuators B: Chemical*, vol. 114, no. 2, pp. 964–968, 2006.

[76] D. M. Garner, H. Bai, P. Georgiou, *et al.*, "A multichannel dna soc for rapid point-of-care gene detection," in *Solid-State Circuits Conference Digest of Technical Papers (ISSCC), 2010 IEEE International*, ID: 1, 2010, pp. 492–493, ISBN: 0193-6530.

[77] G. M. Credo, X. Su, K. Wu, *et al.*, *Label-free electrical detection of pyrophosphate generated from dna polymerase reactions on field-effect devices.*

[78] [Online]. Available: `https://nanoporetech.com/technology/introduction-to-nanopore-sensing/introduction-to-nanopore-sensing`.

[79] D. H. Stoloff and M. Wanunu, "Recent trends in nanopores for biotechnology," *Current opinion in biotechnology*, vol. 24, no. 4, pp. 699–704, 2013.

[80] W. J. Greenleaf and A. Sidow, "The future of sequencing: convergence of intelligent design and market darwinism," *Genome biology*, vol. 15, no. 3, p. 303, 2014.

[81] B. Razavi, *Design of Analog CMOS Integrated Circuits*. McGraw-Hill, 2001.

[82] A. Hassibi, R. Navid, R. W. Dutton, and T. H. Lee, "Comprehensive study of noise processes in electrode electrolyte interfaces," *Journal of Applied Physics*, vol. 96, no. 2, pp. 1074–1082, 2004. [Online]. Available: `http://link.aip.org/link/?JAP/96/1074/1`.

[83] A. Hassibi, S. Zahedi, R. Navid, *et al.*, "Biological shot-noise and quantum-limited signal-to-noise ratio in affinity-based biosensors," *Journal of Applied Physics*, vol. 97, no. 8, pp. 084 701–084 70110–, 2005, ID: 1.

[84] H. Vikalo, A. Hassibi, and B. Hassibi, "Optimal estimation of gene expression levels in microarrays," *GENSIPS 2005*, 2005. [Online]. Available: `http://www-smirc.stanford.edu/papers/GENSIPS_05_Estimation.pdf`.

[85] N. Couniot, A. Afzalian, and D. Flandre, "Scaling laws and performance improvements of integrated biosensor microarrays with multi-pixel per spot," *Sensors and Actuators B: Chemical*, vol. 166167, no. 0, pp. 184–192, 2012.

[86] S. Das, "On scaling laws of biosensors: a stochastic approach," *Journal of Applied Physics*, vol. 105, no. 10, p. 102 021, 2009.

[87] M. J. Madou, "Scaling issues in chemical and biological sensors," *Proceedings of the IEEE*, vol. 91, no. 6, p. 830, 2003.

[88] B. Jang, "Biosensor systems in standard cmos processes: fact or fiction?" *IEEE Transactions on Industrial Electronics*, vol. 56, no. 4, p. 979, 2009.

[89] C. Yang, "Amperometric electrochemical microsystem for a miniaturized protein biosensor array," *IEEE Transactions on Biomedical Circuits and Systems*, vol. 3, no. 3, p. 160, 2009.

[90] C. Toumazou, L. M. Shepherd, S. C. Reed, *et al.*, "Simultaneous dna amplification and detection using a ph-sensing semiconductor system," *Nature Publishing Group*, 2013/06/09. [Online]. Available: `http://www.nature.com/nmeth/journal/vaop/ncurrent/abs/nmeth.2520.html#supplementary-information`.

[91] J. M. Rothberg, W. Hinz, T. M. Rearick, *et al.*, "An integrated semiconductor device enabling non-optical genome sequencing," *Nature*, vol. 475, no. 7356, pp. 348–352, 2011.

[92] C. Toumazou and S. Purushothaman, *Sensing apparatus and method*, US Patent App. 12/711,249, 2010. [Online]. Available: `http://www.google.com/patents/US20100151479`.

[93] C. Toumazou, T. S. L. K. Thay, and P. Georgiou, "A new era of semiconductor genetics using ion-sensitive field-effect transistors: the gene-sensitive integrated cell," *Philosophical Transactions of the Royal Society A: Mathematical, Physical and Engineering Sciences*, vol. 372, no. 2012, p. 20 130 112, 2014.

[94] J. Bustillo, K. Fife, B. Merriman, and J. Rothberg, "Development of the ion torrent cmos chip for dna sequencing," in *Electron Devices Meeting (IEDM), 2013 IEEE International*, ID: 1, 2013, pp. 8.1.1–8.1.4.

[95] J. M. Rothberg, J. Bustillo, M. Milgrew, *et al.*, *Integrated sensor arrays for biological and chemical analysis*, 2011.

[96] J. M. Rothberg, W. Hinz, K. Johnson, *et al.*, *Methods and apparatus for measuring analytes using large scale fet arrays*, US Patent 7,948,015, 2011. [Online]. Available: `https://www.google.com/patents/US7948015`.

[97] T. Rearick and J. Schultz, *Model for analyzing data from sequencing-by-synthesis operations*, US Patent App. 13/339,846, 2012. [Online]. Available: `https://www.google.com/patents/US20120172241`.

[98] N. Pourmand, M. Karhanek, H. H. Persson, *et al.*, "Direct electrical detection of dna synthesis," *Proceedings of the National Academy of Sciences of the United States of America*, vol. 103, no. 17, pp. 6466–6470, 2006.

[99] J. Ahn, "Comparative analysis of electrical detection methods of dna synthesis," *Journal of nanoscience and nanotechnology*, vol. 12, no. 7, p. 5125, 2012.

[100] K. Fife, *One-transistor pixel array*, US Patent 8,217,433, 2012. [Online]. Available: `https://www.google.com/patents/US8217433`.

[101] T. Rearick, "Models for analyzing data from sequencing-by-synthesis operations," no. US20130303384 A1, 2013, US Patent App. 13/892,116. [Online]. Available: `https://www.google.com/patents/US20130303384`.

[102] A. Agah, M. Aghajan, F. Mashayekhi, *et al.*, "A multi-enzyme model for pyrosequencing," *Nucleic acids research*, vol. 32, no. 21, e166, 2004.

[103] S. Franssila, *Front Matter*. Wiley Online Library, 2004.

[104] J. Go and M. A. Alam, "Physics and scaling prospects of ph-based genome sequencers," in *Device Research Conference (DRC), 2012 70th Annual*, ID: 1, 2012, pp. 273–274, ISBN: 1548-3770.

[105] J. Go and M. A. Alam, "The future scalability of ph-based genome sequencers: a theoretical perspective," *Journal of Applied Physics*, vol. 114, no. 16, p. 164 311, 2013.

[106] K. W. Chew, K. S. Yeo, and S. F Chu, "Impact of technology scaling on the 1/f noise of thin and thick gate oxide deep submicron nmos transistors," *Circuits, Devices and Systems, IEE Proceedings* -, vol. 151, no. 5, pp. 415–421, 2004, ID: 1.

[107] H. Wong, "Low-frequency noise study in electron devices: review and update," *Microelectronics Reliability*, vol. 43, no. 4, pp. 585–599, Apr. 2003.

[108] E. Simoen, "On the flicker noise in submicron silicon mosfets," *Solid-state electronics*, vol. 43, no. 5, p. 865, 1999.

[109] K. J. Shaw, P. T. Docker, J. V. Yelland, *et al.*, "Rapid pcr amplification using a microfluidic device with integrated microwave heating and air impingement cooling," *Lab on a Chip*, vol. 10, no. 13, pp. 1725–1728, 2010.

[110] Y. Yanagawa, N. Itabashi, S. Migitaka, *et al.*, "On-chip base sequencing using a two-stage reaction-control scheme: 3.6-times-faster and 1/100-reduced-data-volume isfet-based dna sequencer," in *Biomedical Circuits and Systems Conference (BioCAS), 2013 IEEE*, ID: 1, 2013, pp. 178–181.

[111] H. Esfandyarpour, K. B. Parazi, M. F. Oldham, *et al.*, "Systems and methods for genetic and biological analysis," no. WO2012166742 A3, 2013.

[112] P. Bergveld, "Development of an ion-sensitive solid-state device for neurophysiological measurements," *Biomedical Engineering, IEEE Transactions on*, vol. BME-17, no. 1, pp. 70–71, 1970, ID: 1.

[113] J. Bausells, J. Carrabina, A. Errachid, and A. Merlos, "Ion-sensitive field-effect transistors fabricated in a commercial cmos technology," *Sensors and Actuators B: Chemical*, vol. 57, no. 1-3, pp. 56–62, 1999.

[114] P. Bergveld, "Thirty years of isfetology: what happened in the past 30 years and what may happen in the next 30 years," *Sensors and Actuators B: Chemical*, vol. 88, no. 1, pp. 1–20, 2003.

[115] S. Martinoia and G. Massobrio, "A behavioral macromodel of the isfet in spice," *Sensors and Actuators B: Chemical*, vol. 62, no. 3, pp. 182–189, 2000.

[116] S. Martinoia, G. Massobrio, and L. Lorenzelli, "Modeling isfet microsensor and isfet-based microsystems: a review," *Sensors and Actuators B: Chemical*, vol. 105, no. 1, pp. 14–27, 2005.

[117] L. Bousse, N. F. D. Rooij, and P. Bergveld, "Operation of chemically sensitive field-effect sensors as a function of the insulator-electrolyte interface," *Electron Devices, IEEE Transactions on*, vol. 30, no. 10, pp. 1263–1270, 1983, ID: 1.

[118] D. E. Yates, S. Levine, and T. W. Healy, "Site-binding model of the electrical double layer at the oxide/water interface," *J.Chem.Soc.*, vol. 70, no. 0, pp. 1807–1818, 1974. [Online]. Available: `http://dx.doi.org/10.1039/F19747001807`.

[119] R. E. G. van Hal, J. C. T. Eijkel, and P. Bergveld, "A novel description of isfet sensitivity with the buffer capacity and double-layer capacitance as key parameters," *Sensors and Actuators B: Chemical*, vol. 24, no. 1-3, pp. 201–205, Mar. 1995.

[120] R. van Hal, J. Eijkel, and P. Bergveld, "A general model to describe the electrostatic potential at electrolyte oxide interfaces," *Advances in Colloid and Interface Science*, vol. 69, no. 1-3, pp. 31–62, 1996.

[121] M. W. Shinwari, M. J. Deen, and D. Landheer, "Study of the electrolyte-insulator-semiconductor field-effect transistor (eisfet) with applications in biosensor design," *Microelectronics Reliability*, vol. 47, no. 12, pp. 2025–2057, Dec. 2007.

[122] P. Woias, L. Meixner, D. Amandi, and M. Schonberger, "Modelling the short-time response of isfet sensors," *Sensors and Actuators B: Chemical*, vol. 24, no. 1, pp. 211–217, 1995, journal: Sensors and Actuators B: Chemical". [Online]. Available: `http://www.ingentaconnect.com/content/els/09254005/1995/00000024/00000001/art85045`.

[123] P. Georgiou and C. Toumazou, "Isfet characteristics in cmos and their application to weak inversion operation," *Sensors and Actuators B: Chemical*, vol. 143, no. 1, pp. 211–217, 2009.

[124] S. E. Naimi, B. Hajji, I. Humenyuk, *et al.*, "Temperature influence on ph-isfet sensor operating in weak and moderate inversion regime: model and circuitry," *Sensors and Actuators B: Chemical*, vol. 202, no. 0, pp. 1019–1027, 2014.

[125] L. M. Shepherd, "Low-power computational interfacing with cmos isfets," PhD thesis, Imperial College London, 2008.

[126] P. R. Barabash, R. S. C. Cobbold, and W. B. Wlodarski, "Analysis of the threshold voltage and its temperature dependence in electrolyte-insulator-semiconductor field-effect transistors (eisfet's)," *Electron Devices, IEEE Transactions on*, vol. 34, no. 6, pp. 1271–1282, 1987, ID: 1.

[127] J. C. Chou and Y. F. Wang, "Temperature characteristics of a-si: h gate isfet," *Materials Chemistry and Physics*, vol. 70, no. 1, pp. 107–111, 2001.

[128] B. Hajji, S. E. Naimi, I. Humenyuk, *et al.*, "Behavioral modeling of the ph-isfet temperature influence," in *Electronics, Circuits and Systems, 2007. ICECS 2007. 14th IEEE International Conference on*, ID: 1, 2007, pp. 419–422.

[129] M. J. Milgrew, "Matching the transconductance characteristics of cmos isfet arrays by removing trapped charge," *IEEE Transactions on Electron Devices*, vol. 55, no. 4, p. 1074, 2008.

[130] P. Georgiou, "Isfet threshold voltage programming in cmos using hot-electron injection," *Electronics Letters*, vol. 45, no. 22, p. 1112, 2009.

[131] S. Jamasb, "A physically-based model for drift in al2o3-gate ph isfet's," *Solid State Sensors and Actuators, 1997.TRANSDUCERS '97 Chicago., 1997 International Conference on*, vol. 2, p. 1379, 1997.

[132] S. Jamasb, S. D. Collins, and R. L. Smith, "A physical model for threshold voltage instability in si3n4-gate h+-sensitive fet's (ph isfet's)," *Electron Devices, IEEE Transactions on*, vol. 45, no. 6, pp. 1239–1245, 1998, ID: 1.

[133] P. A. Hammond and D. R. S. Cumming, "Performance and system-on-chip integration of an unmodified cmos isfet," *Sensors and Actuators B: Chemical*, vol. 111-112, pp. 254–258, 2005.

[134] L. Bousse, "Comparison of the hysteresis of ta2o5 and si3n4 ph-sensing insulators," *Sensors and actuators.B, Chemical*, vol. 17, no. 2, p. 157, 1994.

[135] L. Bousse, H. D. Vlekkert, and N. Rooij, "Hysteresis in al2o3-gate isfets," *Sensors and actuators.B, Chemical*, vol. 2, no. 2, pp. 103–110, 1990.

[136] M. Niu, X.-F. Ding, and Q.-Y. Tong, "Effect of two types of surface sites on the characteristics of si3n4-gate ph-isfets," *Sensors and Actuators B: Chemical*, vol. 37, no. 1, pp. 13–17, 1996.

[137] Y. G. Vlasov, "Analytical characteristics and sensitivity mechanisms of electrolyte-insulator-semiconductor system-based chemical sensors:a critical review," *Analytical and bioanalytical chemistry*, vol. 376, no. 6, p. 788, 2003.

[138] T. Mikolajick, R. Khnhold, and H. Ryssel, "The ph-sensing properties of tantalum pentoxide films fabricated by metal organic low pressure chemical vapor deposition," *Sensors and Actuators B: Chemical*, vol. 44, no. 13, pp. 262–267, Oct. 1997.

[139] A. S. Poghossian, "The super-nernstian ph sensitivity of ta2o5-gate isfets," *Sensors and Actuators B: Chemical*, vol. 7, no. 13, pp. 367–370, Mar. 1992.

[140] J. Go, P. R. Nair, and M. A. Alam, "Theory of signal and noise in double-gated nanoscale electronic ph sensors," *Journal of Applied Physics*, vol. 112, no. 3, p. 034 516, 2012.

[141] J. Matsuo, T. Hizawa, K. Sawada, *et al.*, "Charge transfer type ph sensor with super high sensitivity," in *Solid-State Sensors, Actuators and Microsystems Conference, 2007. TRANSDUCERS 2007. International*, ID: 1, 2007, pp. 1881–1884.

[142] K. B. Parizi, A. J. Yeh, A. S. Poon, and H. Wong, "Exceeding nernst limit (59mv/ph): cmos-based ph sensor for autonomous applications," in *Electron Devices Meeting (IEDM), 2012 IEEE International*, IEEE, 2012, pp. 24.7. 1–24.7. 4.

[143] J. Go, P. R. Nair, B. Reddy, *et al.*, "Beating the nernst limit of 59mv/ph with double-gated nano-scale field-effect transistors and its applications to ultra-sensitive dna biosensors," in *Electron Devices Meeting (IEDM), 2010 IEEE International*, IEEE, 2010, pp. 8.7. 1–8.7. 4.

[144] Y. Rayanasukha, S. Porntheerapat, W. Bunjongpru, *et al.*, "High sensitive nanocrystal titanium nitride eg-fet ph sensor," *Advanced Materials Research*, vol. 802, pp. 232–236, 2013.

[145] B. D. LIU, Y. K. SU, and S. C. CHEN, "Ion-sensitive field-effect transistor with silicon nitride gate for ph sensing," *International Journal of Electronics*, vol. 67, no. 1, pp. 59–63, 1989, doi: 10.1080/00207218908921055; M3: doi: 10.1080/00207218908921055; 16. [Online]. Available: `http://dx.doi.org/10.1080/00207218908921055`.

[146] C. Can, A. Gtz, A. Merlos, *et al.*, "Multilayer isfet membranes for microsystems applications," *Sensors and Actuators B: Chemical*, vol. 35, no. 1-3, pp. 136–140, Sep. 1996.

[147] B. Paln, F. V. Santos, J. M. Karam, *et al.*, "New isfet sensor interface circuit for biomedical applications," *Sensors and Actuators B: Chemical*, vol. 57, no. 13, pp. 63–68, 1999.

[148] E. Lauwers, J. Suls, W. Gumbrecht, *et al.*, "A cmos multiparameter biochemical microsensor with temperature control and signal interfacing," *Solid-State Circuits, IEEE Journal of*, vol. 36, no. 12, pp. 2030–2038, 2001, ID: 1.

[149] P. A. Hammond, D. Ali, and D. R. S. Cumming, "Design of a single-chip ph sensor using a conventional 0.6um cmos process," *Sensors Journal, IEEE*, vol. 4, no. 6, pp. 706–712, 2004, ID: 1.

[150] V. P. Chodavarapu, A. H. Titus, and A. N. Cartwright, "Cmos isfet microsystem for biomedical applications," in *Sensors, 2005 IEEE*, 2005, 4 pp. DOI: `10.1109/ICSENS.2005.1597648`.

[151] H.-S. Wong and M. H. White, "A cmos-integrated 'isfet-operational amplifier' chemical sensor employing differential sensing," *Electron Devices, IEEE Transactions on*, vol. 36, no. 3, pp. 479–487, 1989, ID: 1.

[152] C. G. Jakobson, U. Dinnar, M. Feinsod, and Y. Nemirovsky, "Ion-sensitive field-effect transistors in standard cmos fabricated by post processing," *Sensors Journal, IEEE*, vol. 2, no. 4, pp. 279–287, 2002, ID: 1.

[153] J.-C. Chou and C.-Y. Weng, "Sensitivity and hysteresis effect in al2o3 gate ph-isfet," *Materials Chemistry and Physics*, vol. 71, no. 2, pp. 120–124, 2001.

[154] S. Shim, J. Han, and S. Hong, "A cmos rf polar transmitter of a uhf mobile rfid reader for high power efficiency," *Microwave and Wireless Components Letters, IEEE*, vol. 18, no. 9, pp. 635–637, 2008, ID: 1.

[155] Y. L. Chin, "A novel sno2/al discrete gate isfet ph sensor with cmos standard process," *Sensors and actuators.B, Chemical*, vol. 75, no. 1-2, p. 36, 2001.

[156] Y.-L. Chin, J.-C. Chou, T.-P. Sun, *et al.*, "A novel ph sensitive isfet with on chip temperature sensing using cmos standard process," *Sensors and Actuators B: Chemical*, vol. 76, no. 13, pp. 582–593, 2001.

[157] P.-K. Shin, "The ph-sensing and light-induced drift properties of titanium dioxide thin films deposited by mocvd," *Applied Surface Science*, vol. 214, no. 14, pp. 214–221, 2003.

[158] T.-M. Pan and K.-M. Liao, "Structural properties and sensing characteristics of y2o3 sensing membrane for ph-isfet," *Sensors and Actuators B: Chemical*, vol. 127, no. 2, pp. 480–485, 2007.

[159] Y. L. Chin, "Titanium nitride membrane application to extended gate field effect transistor ph sensor using vlsi technology," *Japanese journal of applied physics*, vol. 40, p. 6311, 2001.

[160] S. Wakida, *Ph-sensitive isfets based on titanium nitride and their application to battery monitor*, 1991.

[161] C. G. Jakobson, M. Feinsod, and Y. Nemirovsky, "Low frequency noise and drift in ion sensitive field effect transistors," *Sensors and Actuators B: Chemical*, vol. 68, no. 1-3, pp. 134–139, 2000.

[162] C. G. Jakobson and Y. Nemirovsky, "1/f noise in ion sensitive field effect transistors from subthreshold to saturation," *Electron Devices, IEEE Transactions on*, vol. 46, no. 1, pp. 259–261, 1999, ID: 1.

[163] U. Guth, "Solid-state reference electrodes for potentiometric sensors," *Journal of solid state electrochemistry*, vol. 13, no. 1, p. 27, 2009.

[164] A. van den Berg, A. Grisel, H. H. van den Vlekkert, and N. F. de Rooij, "A microvolume open liquid-junction reference electrode for ph-isfets," *Sensors and Actuators B: Chemical*, vol. 1, no. 16, pp. 425–432, Jan. 1990.

[165] Y. A. Tarantov, A. S. Kartashev, A. A. Kruchinin, *et al.*, "Optical and thermal sensitivity of ph-isfet with ta2o5 membrane," *Sensors and Actuators A: Physical*, vol. 28, no. 3, pp. 197–202, Aug. 1991.

[166] T. Datta-Chaudhuri, P. Abshire, and E. Smela, "Packaging commercial cmos chips for lab on a chip integration," *Lab on a Chip*, vol. 14, no. 10, pp. 1753–1766, 2014.

[167] L. Li, X. Liu, and A. J. Mason, "Die-level photolithography and etchless parylene packaging processes for on-cmos electrochemical biosensors," in *Circuits and Systems (ISCAS), 2012 IEEE International Symposium on*, ID: 1, 2012, pp. 2401–2404, ISBN: 0271-4302.

[168] P. A. Hammond and D. R. S. Cumming, "Encapsulation of a liquid-sensing microchip using su-8 photoresist," *Microelectronic Engineering*, vol. 73-74, pp. 893–897, Jun. 2004.

[169] Y. Tsividis, *Operation and Modeling of The MOS Transistor*, Second. Oxford University Press, 1999.

[170] Y. Liu, P. Georgiou, T. Prodromakis, *et al.*, "An extended cmos isfet model incorporating the physical design geometry and the effects on performance and offset variation," *Electron Devices, IEEE Transactions on*, vol. 58, no. 12, pp. 4414–4422, 2011, ID: 1.

[171] M. Sohbati, Y. Liu, P. Georgiou, and C. Toumazou, "An isfet design methodology incorporating cmos passivation," in *Biomedical Circuits and Systems Conference (BioCAS), 2012 IEEE*, ID: 1, 2012, pp. 65–68.

[172] A. Morgenshtein, L. Sudakov-Boreysha, U. Dinnar, *et al.*, "Cmos readout circuitry for isfet microsystems," *Sensors and Actuators B: Chemical*, vol. 97, no. 1, pp. 122–131, 2004.

[173] D. Y. Chen, P. K. Chan, and M. S. Tse, "A cmos isfet interface circuit for water quality monitoring," in *Sensors, 2005 IEEE*, ID: 1, 2005, 4 pp.

[174] L. Shepherd, P. Georgiou, and C. Toumazou, "A novel voltage-clamped cmos isfet sensor interface," in *Circuits and Systems, 2007. ISCAS 2007. IEEE International Symposium on*, ID: 1, 2007, pp. 3331–3334.

[175] P. Bergveld, "The operation of an isfet as an electronic device," *Sensors and Actuators*, vol. 1, no. 0, pp. 17–29, 1981.

[176] M. Sohbati, P. Georgiou, and C. Toumazou, "Refet replication for isfet-based snp detection arrays," in *Circuits and Systems (ISCAS), 2013 IEEE International Symposium on*, ID: 1, 2013, pp. 185–188, ISBN: 0271-4302.

[177] P. Georgiou and C. Toumazou, "An adaptive cmos-based pg-isfet for ph sensing," in *Circuits and Systems, 2009. ISCAS 2009. IEEE International Symposium on*, ID: 1, 2009, pp. 557–560.

[178] Y. Liu and C. Toumazou, "An isfet based sensing array with sensor offset compensation and ph sensitivity enhancement," in *Circuits and Systems (ISCAS), Proceedings of 2010 IEEE International Symposium on*, ID: 1, 2010, pp. 2283–2286.

[179] Y. Hu and P. Georgiou, "A direct-capacitive feedback isfet interface for ph reaction monitoring," in *Circuits and Systems (ISCAS), 2013 IEEE International Symposium on*, ID: 1, 2013, pp. 189–192, ISBN: 0271-4302.

[180] L. Yan, P. Georgiou, T. G. Constandinou, *et al.*, "An auto-offset-removal circuit for chemical sensing based on the pg-isfet," in *Circuits and Systems, 2009. ISCAS 2009. IEEE International Symposium on*, ID: 1, 2009, pp. 1165–1168.

[181] Y. Liu, "Engineering robust cmos isfet smart sensor systems," PhD thesis, Imperial College London.

[182] C. Toumazou, F. J. Lidgey, and D. G. Haigh, "Current-mode circuits from a translinear viewpoint: a tutorial," in, ser. Analogue IC Design: The Current-Mode Approach. London, U.K.: Peter Peregrinus, 1990, p. 11.

[183] L. M. Shepherd and C. Toumazou, "A biochemical translinear principle with weak inversion isfets," *Circuits and Systems I: Regular Papers, IEEE Transactions on*, vol. 52, no. 12, pp. 2614–2619, 2005, ID: 1.

[184] L. Shepherd and C. Toumazou, "Weak inversion isfets for ultra-low power biochemical sensing and real-time analysis," *Sensors and Actuators B: Chemical*, vol. 107, no. 1, pp. 468–473, 2005.

[185] C. Toumazou and L. Shepherd, "Using transistors to linearise biochemistry," *Electronics Letters*, vol. 43, no. 2, pp. 65–67, 2007, ID: 1.

[186] M. Kalofonou and C. Toumazou, "Isfet based chemical gilbert cell," *Electronics Letters*, vol. 47, no. 16, pp. 903–904, 2011, ID: 1.

[187] M. Kalofonou, P. Georgiou, C.-P. Ou, and C. Toumazou, "An isfet based translinear sensor for dna methylation detection," *Sensors and Actuators B: Chemical*, vol. 161, no. 1, pp. 156–162, 2012.

[188] M. Kalofonou, P. Georgiou, and C. Toumazou, "An isfet based chemical gilbert cell," in *Biomedical Circuits and Systems Conference (BioCAS), 2011 IEEE*, ID: 1, 2011, pp. 365–368.

[189] M. Kalofonou and C. Toumazou, "Isfet based chemical gilbert cell," *Electronics Letters*, vol. 47, no. 16, pp. 903–904, 2011, ID: 1.

[190] W. P. Chan, B. Premanode, and C. Toumazou, "64 ph-isfet averaging array employing global negative current feedback," *Electronics Letters*, vol. 45, no. 11, pp. 536–537, 2009, ID: 1.

[191] W. P. Chan, "An integrated isfets instrumentation system in standard cmos technology," *IEEE Journal of Solid-State Circuits*, vol. 45, no. 9, p. 1923, 2010.

[192] C. Toumazou, J. B. Hughes, and N. C. Battersby, *Switched-currents: an analogue technique for digital technology*, 5. IET, 1993, ISBN: 0-86341-294-7.

[193] Y. Haga and I. Kale, "Bulk-driven dc level shifter," in *Circuits and Systems (ISCAS), 2011 IEEE International Symposium on*, ID: 1, 2011, pp. 2039–2042, ISBN: 0271-4302.

[194] L. Yani, Y. Yintang, and Z. Zhangming, "A novel low-voltage low-power bulk-driven cascade current mirror," in *Advanced Computer Theory and Engineering (ICACTE), 2010 3rd International Conference on*, ID: 1, vol. 3, 2010, pp. V3–78V3–83–, ISBN: 2154-7491.

[195] R. He and L. Zhang, "Evaluation of modern mosfet models for bulk-driven applications," in *Circuits and Systems, 2008. MWSCAS 2008. 51st Midwest Symposium on*, ID: 1, 2008, pp. 105–108, ISBN: 1548-3746.

[196] T. Serrano-Gotarredona, B. Linares-Barranco, and A. G. Andreou, "A general translinear principle for subthreshold mos transistors," *Circuits and Systems I: Fundamental Theory and Applications, IEEE Transactions on*, vol. 46, no. 5, pp. 607–616, 1999, ID: 1.

[197] Y. Haga, H. Zare-Hoseini, L. Berkovi, and I. Kale, "Design of a 0.8 volt fully differential cmos ota using the bulk-driven technique," in *Circuits and Systems, 2005. ISCAS 2005. IEEE International Symposium on*, ID: 1, 2005, 220–223 Vol. 1.

[198] S. S. Rajput and S. S. Jamuar, "Low voltage analog circuit design techniques," *Circuits and Systems Magazine, IEEE*, vol. 2, no. 1, pp. 24–42, 2002, ID: 1.

[199] T. Smedes, J. Knol, and A. J. Annema, "A simple model for analogue applications of dynamic threshold mosts," in *Solid-State Device Research Conference, 1999. Proceeding of the 29th European*, ID: 1, vol. 1, 1999, pp. 484–487.

[200] V. Niranjan and M. Gupta, "An analytical model of the bulk-dtmos transistor," vol. 8, p. 329, 2012.

[201] F. Assaderaghi, D. Sinitsky, S. Parke, *et al.*, "A dynamic threshold voltage mosfet (dtmos) for ultra-low voltage operation," in *Electron Devices Meeting, 1994. IEDM '94. Technical Digest., International*, ID: 1, 1994, pp. 809–812, ISBN: 0163-1918.

[202] A. Jimenez-P, F. J. D. la Hidalga-W, and M. J. Deen, "Modelling of the dynamic threshold mosfet," *Circuits, Devices and Systems, IEE Proceedings* -, vol. 152, no. 5, pp. 502–508, 2005, ID: 1.

[203] S. Kakimoto, T. Okuno, Y. Iwase, *et al.*, "Self-corrective device and architecture to ensure lsi operation at 0.5 v using bulk dynamic threshold mosfet with a self-adaptive power supply," in *Solid-State Circuits Conference, 2003. Digest of Technical Papers. ISSCC. 2003 IEEE International*, ID: 1, 2003, 402–502 vol.1, ISBN: 0193-6530.

[204] T.-L. Hsu, D. D.-L. Tang, and J. Gong, "Low-frequency noise properties of dynamic-threshold (dt) mosfet's," *Electron Device Letters, IEEE*, vol. 20, no. 10, pp. 532–534, 1999, ID: 1.

[205] K. Ragini, M. Satyam, and B. Jinaga, "Variable threshold mosfet approach (through dynamic threshold mosfet) for universal logic gates," *arXiv preprint arXiv:1003.6030*, 2010.

[206] S.-C. Wong and M.-S. Liang, *Dynamic threshold mosfet using accumulated base bjt level shifter for low voltage sub-quarter micron transistor*, 1999.

[207] C. Hu, P. K. Ko, F. Assaderaghi, and S. Parke, *Dynamic threshold voltage mosfet having gate to body connection for ultra-low voltage operation*, 1996.

[208] T. C. W. Yeow, M. R. Haskard, D. E. Mulcahy, *et al.*, "A very large integrated ph-isfet sensor array chip compatible with standard cmos processes," *Sensors and Actuators B: Chemical*, vol. 44, no. 13, pp. 434–440, Oct. 1997.

[209] W. Wong, L. Shepherd, P. Georgiou, and C. Toumazou, "Towards isfet based dna logic for rapid nucleic acid detection," in *Sensors, 2009 IEEE*, ID: 1, 2009, pp. 1451–1454, ISBN: 1930-0395.

[210] A. Al-Ahdal and C. Toumazou, "High gain isfet based cmos chemical inverter," *Sensors and Actuators B: Chemical*, vol. 171, pp. 110–117, 2012.

[211] A. Al-Ahdal and C. Toumazou, "Isfet based chemical switch," *Sensors Journal, IEEE*, vol. PP, no. 99, pp. 1–1, 2011, ID: 1.

[212] D. H. Neil H. E. Weste, *CMOS VLSI Design*, 3rd ed. Pearson Education, 2005, pp. 94–100, ISBN: 0-321-26977-2.

[213] J. M. Rabaey, A. Chandrakasan, and N. Borivoje, *Digital Integrated CircuitsA Design Perspective*. Publishing House of Electronic Industry, 2004, pp. 185–188.

[214] W. Wong, P. Georgiou, C. P Ou, and C. Toumazou, "Pg-isfet based dna-logic for reaction monitoring," *Electronics Letters*, vol. 46, no. 5, pp. 330–332, 2010, ID: 1.

[215] R. J. Baker, *CMOS Circuit Design, Layout, and Simulation*, 3rd. Wiley-IEEE Press, 2010, ISBN: 0470881321, 9780470881323.

[216] R. J. Van de Plassche, *CMOS integrated analog-to-digital and digital-to-analog converters*. Kluwer Academic Publishers Dordrecht, 2003, vol. 2.

[217] T. Instruments, "Oversampling techniques using the tms320c24x family," *Europe Texas Instruments*, 1998.

[218] B. Palan, K. Roubik, M. Husak, and B. Courtois, "Cmos isfet-based structures for biomedical applications," in *Microtechnologies in Medicine and Biology, 1st Annual International, Conference On. 2000*, ID: 1, 2000, pp. 502–506.

[219] L. A. Lee, S. R. Marx, R. Yotter, *et al.*, "Performance comparison of ph sensors fabricated in a cmos process," in *Sensors, 2004. Proceedings of IEEE*, 2004, 772–775 vol.2.

[220] J.-L. Chiang, S.-S. Jan, J.-C. Chou, and Y.-C. Chen, "Study on the temperature effect, hysteresis and drift of ph-isfet devices based on amorphous tungsten oxide," *Sensors and Actuators B: Chemical*, vol. 76, no. 13, pp. 624–628, 2001.

[221] H.-K. Liao, J.-C. Chou, W.-Y. Chung, *et al.*, "Study of amorphous tin oxide thin films for isfet applications," *Sensors and Actuators B: Chemical*, vol. 50, no. 2, pp. 104–109, 1998.

[222] T.-M. Pan and K.-M. Liao, "Comparison of structural and sensing characteristics of pr2o3 and prtio3 sensing membrane for ph-isfet application," *Sensors and Actuators B: Chemical*, vol. 133, no. 1, pp. 97–104, 2008.

[223] H. Voigt, F. Schitthelm, T. Lange, *et al.*, "Diamond-like carbon-gate ph-isfet," *Sensors and Actuators B: Chemical*, vol. 44, no. 13, pp. 441–445, Oct. 1997.

[224] L.-T. Yin, J.-C. Chou, W.-Y. Chung, *et al.*, "Study of indium tin oxide thin film for separative extended gate isfet," *Materials Chemistry and Physics*, vol. 70, no. 1, pp. 12–16, 2001.

[225] S.-S. Jan, Y.-C. Chen, and J.-C. Chou, "Effect of mg2+-dopant on the characteristics of lead titanate sensing membrane for ion-sensitive field-effect transistors," *Sensors and Actuators B: Chemical*, vol. 108, no. 12, pp. 883–887, 2005.

[226] Y.-H. Liao and J.-C. Chou, "Fabrication and characterization of a ruthenium nitride membrane for electrochemical ph sensors," *Sensors*, vol. 9, no. 4, pp. 2478–2490, 2009.

[227] Y.-H. Chang, Y.-S. Lu, Y.-L. Hong, *et al.*, "Highly sensitive ph sensing using an indium nitride ion-sensitive field-effect transistor," *Sensors Journal, IEEE*, vol. 11, no. 5, pp. 1157–1161, 2011.

A. Publications

Conference Papers

M. Sohbati, Y. Liu, P. Georgiou, and C. Toumazou, "An ISFET Design Methodology Incorporating CMOS Passivation," *Biomedical Circuits and Systems Conference (BioCAS), 2012 IEEE*

M. Sohbati, P. Georgiou, and C. Toumazou, "REFET Replication for ISFET-based SNP Detection Arrays," *International Symposium on Circuits and Systems Conference (ISCAS), 2013 IEEE*

M. Sohbati, P. Georgiou, and C. Toumazou, "A Piecewise Linear Approximating ISFET Readout," *Biomedical Circuits and Systems Conference (BioCAS), 2013 IEEE*

M. Sohbati, and C. Toumazou, "A Temperature Insensitive Continuous Time ΔpH to Digital Converter," *International Symposium on Circuits and Systems Conference (ISCAS), 2014 IEEE*

Journal Papers

M. Sohbati, and C. Toumazou, "Trade-offs in Unmodified CMOS ISFETs", *IEEE Sensors, 2014*

Articles

M. Sohbati, and C. Toumazou, "Personalised Microchips for Healthcare", *IEEE Potentials*– Accepted for March 2015 Issue

B. Nucleotide Incorporation Simulation MATLAB Codes

Step Concentraion Change Function

- Delta_Enz=0;
- Delta_dNTP=0;
- Delta_Mg=0;

```
function Delta_Reagents=ChangesByIncorporation(dt, Reagents)

DNAn=Reagents(1);
Enz=Reagents(2);
dNTP=Reagents(3);
Mg=Reagents(4);
EnzDNAn=Reagents(5);
EnzDNAndNTP=Reagents(6);
EnzaDNAndNTP=Reagents(7);
EnzaDNAndNTPMg=Reagents(8);
EnzaDNAn1_PPiMg=Reagents(9);
EnzaDNAn1_PPi=Reagents(10);
EnzDNAn1_PPi=Reagents(11);
PPi=Reagents(12);
EnzDNAn1=Reagents(13);
DNAn1=Reagents(14);

kon=1.2*10^7;
koff=0.06;
kf1=1.25*10^7;
kr1=250;
kf2=50;
kr2=3;
kf3=9.5*10^5;
kr3=100;
kf4=150;
kr4=40;
```

```
kf5=100;
kr5=9.5*10^5;
kf6=4;
kr6=4;
kf7=60;
kr7=1.45*10^4;

    %Eq0: Enz + DNAn <=> EnzDNAn        kon, koff
    Delta_EnzDNAn=dt*(kon*Enz*DNAn-koff*EnzDNAn);
    Delta_Enz=dt*(koff*EnzDNAn-kon*Enz*DNAn+kr1*EnzDNAndNTP-
    kf1*EnzDNAn*dNTP+koff*EnzDNAn1-kon*Enz*DNAn1);
```

Delta_Enz=0;

```
    Delta_DNAn=dt*(koff*EnzDNAn-kon*Enz*DNAn);

    %Eq1: EnzDNAn + dNTP <=> EnzDNAndNTP        kf1, kr1
    Delta_EnzDNAndNTP=dt*(kf1*EnzDNAn*dNTP-kr1*EnzDNAndNTP+
    kr2*EnzaDNAndNTP-kf2*EnzDNAndNTP);
    %EnzDNAn-->added inprevious set
    Delta_dNTP=dt*(kr1*EnzDNAndNTP-kf1*EnzDNAn*dNTP);
```

Delta_dNTP=0;

```
    %Eq2: EnzDNAndNTP <=> EnzaDNAndNTP      kf2, kr2
    Delta_EnzaDNAndNTP=dt*(kf2*EnzDNAndNTP-kr2*EnzaDNAndNTP+
    kr3*EnzaDNAndNTPMg-kf3*EnzaDNAndNTP*Mg);

    %Eq3: EnzaDNAndNTP +Mg  <=>EnzaDNAndNTPMg
    Delta_Mg=dt*(kr3*EnzaDNAndNTPMg-kf3*EnzaDNAndNTP*Mg+
    kf5*EnzaDNAn1_PPiMg-kr5*Mg*EnzaDNAn1_PPi);
```

Delta_Mg=0;

```
    Delta_EnzaDNAndNTPMg=dt*(kf3*EnzaDNAndNTP*Mg-kr3*EnzaDNAndNTPMg+
    kr4*EnzaDNAn1_PPiMg-kf4*EnzaDNAndNTPMg);

    %Eq4: EnzaDNAndNTPMg <=> EnzaDNAn1_PPiMg
    Delta_EnzaDNAn1_PPiMg=dt*(kf4*EnzaDNAndNTPMg-kr4*EnzaDNAn1_PPiMg+
    kr5*EnzaDNAn1_PPi*Mg-kf5*EnzaDNAn1_PPiMg);

    %Eq5: EnzaNDAn1_PPiMg <=>EnzaDNAn1_PPi + Mg
    Delta_EnzaDNAn1_PPi=dt*(kf5*EnzaDNAn1_PPiMg-kr5*Mg*EnzaDNAn1_PPi+
```

```
    kr6*EnzDNAn1_PPi-kf6*EnzaDNAn1_PPi);

    %Eq6: EnzaDNAn1_PPi + MG <=> EnzDNAn1_PPi
    Delta_EnzDNAn1_PPi=dt*(kf6*EnzaDNAn1_PPi-kr6*EnzDNAn1_PPi+
    kr7*EnzDNAn1*PPi-kf7*EnzDNAn1_PPi);

    %Eq7: EnzDNAn1_PPi <=> EnzDNAn1 + PPi
    Delta_PPi=dt*(kf7*EnzDNAn1_PPi-kr7*EnzDNAn1*PPi);
    Delta_EnzDNAn1=dt*(kf7*EnzDNAn1_PPi-kr7*EnzDNAn1*PPi+
    kon*Enz*DNAn1-koff*EnzDNAn1);

    Delta_DNAn1=dt*(koff*EnzDNAn1-kon*Enz*DNAn1);



    Delta_Reagents=[Delta_DNAn, Delta_Enz, Delta_dNTP, Delta_Mg, Delta_EnzDNAn,
     Delta_EnzDNAndNTP, Delta_EnzaDNAndNTP, Delta_EnzaDNAndNTPMg,
     Delta_EnzaDNAn1_PPiMg, Delta_EnzaDNAn1_PPi, Delta_EnzDNAn1_PPi,
     Delta_PPi, Delta_EnzDNAn1, Delta_DNAn1];

end
```

Homopolymerization Simulation Function

```
function [HPlus_series, PPi_series, dNTP_series, pH_series, DNAn_series,
  DNAn1_series]=HP_Incorporation(hp_length, DNAn, Enz, dNTP, Mg,
  diffusion_factor, beta_factor, pH0, time_tot, dt,flow_time)

%DNAn_series, DNAn2_series, DNAn3_series, DNAn4_series, DNAn5_series
%time_tot=10;
%dt=0.0001; %100us
%time=[0:dt:time_tot-dt];
% % hp_length=1;
% %
% % pH0=8;
% % diffusion_factor=0.5;
% % beta_factor=1;
% %
% % DNAn=10^(-6);
% % Enz=10^(-6);
% % dNTP=10^(-6);
% % Mg=1*10^(-6);
```

```
%diffusion_delay=0;%/dt;

EnzDNAn=0;
EnzDNAndNTP=0;
EnzaDNAndNTP=0;
EnzaDNAndNTPMg=0;
EnzaDNAn1_PPiMg=0;
EnzaDNAn1_PPi=0;
EnzDNAn1_PPi=0;
PPi=0;
EnzDNAn1=0;
DNAn1=0;

Reagents=zeros(hp_length,14);

Reagents(1,:)=[DNAn, Enz, dNTP, Mg, EnzDNAn, EnzDNAndNTP, EnzaDNAndNTP,
   EnzaDNAndNTPMg, EnzaDNAn1_PPiMg, EnzaDNAn1_PPi, EnzDNAn1_PPi,
   PPi, EnzDNAn1, DNAn1];
Reagents(:,2)=Enz;
Reagents(:,3)=dNTP;
Reagents(:,4)=Mg;

Delta_Reagents=zeros(hp_length,14);

%%Delta_Reagents=[Delta_DNAn, Delta_Enz, Delta_dNTP, Delta_Mg, Delta_EnzDNAn,
  Delta_EnzDNAndNTP, Delta_EnzaDNAndNTP, Delta_EnzaDNAndNTPMg,
  Delta_EnzaDNAn1_PPiMg, Delta_EnzaDNAn1_PPi, Delta_EnzDNAn1_PPi,
  Delta_PPi, Delta_EnzDNAn1, Delta_DNAn1];

Enz_series=zeros(1, time_tot/dt);
Enz_series(1)=Enz;

DNA_series=zeros(hp_length+1, time_tot/dt);
DNA_series(1,1)=DNAn;
dNTP_series=zeros(1, time_tot/dt);
dNTP_series(1)=dNTP;
Mg_series=zeros(1, time_tot/dt);
Mg_series(1)=Mg;

PPi_series=zeros(1, time_tot/dt);
```

```
%DNAn1_series=zeros(1, time_tot/dt);



Delta_HPlus_series=zeros(1, time_tot/dt);
Delta_HPlus=zeros(1, time_tot/dt);
pH_series=zeros(1, time_tot/dt);
pH_series(1)=pH0;
HPlus_series=zeros(1, time_tot/dt);
HPlus_series(1)=10^(-pH_series(1));
HPlus_background=10^(-pH0)*ones(1, time_tot/dt);

flow_time_ctrl=0;

for i=1:time_tot/dt-1

    for j=1:hp_length
        Delta_Reagents(j,:)=ChangesByIncorporation(dt,Reagents(j,:));
    end;

    %DNA Concentration Change
    Reagents(1,1)=Reagents(1,1)+Delta_Reagents(1,1);
    if hp_length>1
        for j=2:hp_length
            Reagents(j,1)=Reagents(j,1)+Delta_Reagents(j,1)+Delta_Reagents(j-1,14);
            Reagents(j-1,14)=Reagents(j,1);
        end;
    end;



    Reagents(hp_length,14)=Reagents(hp_length,14)+Delta_Reagents(hp_length,14);

    flow_time_ctrl=flow_time_ctrl+dt;



    if (flow_time_ctrl<flow_time)
        Delta_Reagents(:,2:4)=0;
    end;

    %Enzyme Concentration Change
    Reagents(:,2)=Reagents(1,2)+sum(Delta_Reagents(:,2));
    %dNTP Concentration Change
```

```
    Reagents(:,3)=Reagents(1,3)+sum(Delta_Reagents(:,3));
    %Mg Concentration Change
    Reagents(:,4)=Reagents(1,4)+sum(Delta_Reagents(:,4));
    %PPi Concentration Change
    Reagents(:,12)=Reagents(1,12)+sum(Delta_Reagents(:,12));
    %Remaining
    Reagents(:,6:11)=Reagents(:,6:11)+Delta_Reagents(:,6:11);

    %Enz.Dna Change
    Reagents(1,5)=Reagents(1,5)+Delta_Reagents(1,5);
    if hp_length>1
        for j=2:hp_length
            Reagents(j,5)=Reagents(j,5)+Delta_Reagents(j,5)+Delta_Reagents(j-1,13);
            Reagents(j-1,13)=Reagents(j,5);
        end;
    end;

    Reagents(hp_length,13)=Reagents(hp_length,13)+Delta_Reagents(hp_length,13);
    %

    DNA_series(1:hp_length,i+1)=Reagents(:,1);
    DNA_series(1+hp_length,i+1)=Reagents(hp_length,14);
    Enz_series=Reagents(1,2);
    dNTP_series(i+1)=Reagents(1,3);
    Mg_series(i+1)=Reagents(1,4);
    PPi_series(i+1)=Reagents(1,12);
    %DNAn1_series(i+1)=Reagents(14);

    Delta_HPlus(i)=sum(Delta_Reagents(:,12));
    Delta_HPlus_series(i+1)=Delta_HPlus_series(i)+Delta_HPlus(i);

  %  if i>diffusion_delay
     %   HPlus_series(i+1)=HPlus_series(i)+Delta_HPlus(i-diffusion_delay)/beta_factor+
   %  (diffusion_factor/beta_factor)*(HPlus_background(i)-HPlus_series(i));
   % else
   %     HPlus_series(i+1)=HPlus_series(i)+(diffusion_factor/beta_factor)*
   % (HPlus_background(i)-HPlus_series(i));
    %end;
    HPlus_series(i+1)=HPlus_series(i)+Delta_HPlus(i)/beta_factor+
    (diffusion_factor/beta_factor)*(HPlus_background(i)-HPlus_series(i));
    pH_series(i+1)=-log(HPlus_series(i+1))/log(10);
```

```
end;

DNAn_series=DNA_series(1,:);
DNAn1_series=DNA_series(2,:);
%DNAn_hplength_series=DNA_series(hp_length+1,:);
% DNAn2_series=DNA_series(3,:);
% DNAn3_series=DNA_series(4,:);
% DNAn4_series=DNA_series(5,:);
% DNAn5_series=DNA_series(6,:);

end
```

Incorporation Simulation Code

```
hp_length_max=2;
color_code=['b','k','g','r','y'];

flow_time=1;
time_tot=10;
dt=0.0001; %100us
time=[0:dt:time_tot-dt];

pH0=8;
diffusion_factor=0.8;
beta_factor=1;

DNAn=1*10^(-6);
Enz=3*10^(-6);
dNTP=3*10^(-6);
Mg=3*10^(-6);

hp_length=hp_length_max;


%for hp_length=1:hp_length_max
    [HPlus_series, PPi_series, dNTP_series, pH_series, DNAn_series, DNAn1_series]=
    HP_Incorporation(hp_length, DNAn, Enz, dNTP,Mg, diffusion_factor, beta_factor,
                    pH0, time_tot,dt,flow_time);
%     pH_change_series=pH_series;
%     integrated_pH_change=pH_series;
```

```
%
%     for i=1:length(pH_series)
%         pH_change_series(i)=pH_series(i)-pH_series(1);
%     end;
%
%     for i=1:length(pH_series)
%         integrated_pH_change(i)=dt*sum(pH_change_series(1:i));
%     end;

% end;
```

C. pH Sensitive Materials in CMOS

Table C.1.: pH sensitive materials.

Sensing Membrane	S_{pH} (mV/pH)	pH Range	Drift (mV/h)	Hysteresis (mV)	Technology Process	Reference Number
Si_3N_4	46	4-9	1	2-5		[145]
Ta_2O_5/SiO_2	58-59	4-9	-	-	-	[151]
Si_3N_4	54.5	1.7-11	-	-	2.5μ 2P1M	[146]
Si_3N_4	52-58	-	-	-	2.5μ 2P1M	[147]
Si_3N_4/SiO_2	53	6-8	-	-	1.2μ 2P1M	[148]
$SiO_xN_y/Si_3N_4/SiO_2$	17-20	4-9	-	-	-	[151]
SiO_2	25-35	1.7-11	-	-	2.5μ 2P1M	[146]
SiO_2	24-36	-	-	-	2.5μ 2P1M	[147]
SiO_xN_y	47	3-11	-	-	Atmel ES2 1.0μ 1P2M	[113]
SiO_xN_y	41	1.7-11	-	-	Atmel ES2 1.0μ 1P2M	[146]
SiO_xN_y	25	3-11	-	-	AMS 0.6μ 2P3M	[218]
Al_2O_3	0.22	5-8	-	-	AMI 1.6μ	[219]
Si_3N_4/SiO_xN_y	43	-	3.5	-	AMS 0.6μ 3M	[149]
Si_3N_4/SiO_xN_y	48	3-7	<5	-	AMS 0.6μ 3M	[133]
Si_3N_4	40-45	1-7	-	-	AMI 1.5μ 2M	[150]
Ta_2O_5/SiO_2	58	3-11	0.5	-		[138]
$a-WO_3/SiO_2$	44.85	1-7	<3.35	<15.7		[220]
TiO_2/Al	58	2-10	3.96	-	UMC 0.5μ 2P2M	[156]
Ta_2O_5/Al	56.6	4-9	1-5	-	AMI 1.2μ and 1.6μ	[152]
Al_2O_3/Al	48.8	4-9	1-5	-	AMI 1.2μ and 1.6μ	[152]
$Ta_2O_5/Pt/Al$	50.2	4-9	0.3	-	AMI 1.2μ and 1.6μ	[152]
$a-SnO_2/SiO_2$	58	2-10	0.23	2.5		[221]
TiO_2/SiO_2	58	3-11	1.6-2.9	3.4-16.9		[157]
Y_2O_3	56.09	2-12	1.24	13.6		[158]
$PrTiO_3$	56.8	2-12	1.77	2.84		[222]
Diamond Carbon	54-59	1-12	0.0078	-		[223]
ITO	58	2-12	-	9.8	EGFET	[224]
Al_2O_3	53.23	1-13	-	2-4	Sentron 1090	[153]
PMT	57-59	2-12	0.2-0.4	1-3		[225]
RuN	58.03	1-13	2.15	2.7-9.1	SEGFET	[226]
TiN	59	1.68-10.1	-	-		[160]
TiN	57	2-10	-	0.5/cycle		[159]
Ta_2O_5	59.7	-	1.7	0.9		[134]
Al_2O_3	50	4-10	-	3-6		[135]
SnO_2/Al	58	2-10				[155]
InO/InN	58.3	2-12				[227]

D. Optimum ISFET Shape

In section 4.5 and 4.8 the shape of ISFET was noted that may impact the decoupling capacitances. Ideally, the maximum area to perimeter ratio is intended to maximise the coupling and minimise the decoupling. For a sensing membrane of n equal sides

$$\begin{aligned}
&\textit{Area:}\\
&\quad a = n \times \frac{d}{2} \times \cot\frac{\pi}{n} \times \frac{d}{2} = \frac{n}{4} d^2 \cot\frac{\pi}{n}\\
&\textit{Perimeter:}\\
&\quad p = nd\\
&\quad \frac{a}{p} = \frac{d}{4}\cot\frac{\pi}{n}\\
&\quad \sqrt{\frac{\cot\frac{\pi}{n}}{n}} \times \sqrt{a}/2
\end{aligned} \tag{D.1}$$

$$\begin{aligned}
\textit{Maximum } \frac{a}{p} &\rightarrow \frac{\delta\frac{a}{p}}{\delta n} == 0\\
&\rightarrow \frac{-\frac{\pi}{n}\tan\frac{\pi}{n} - \cot\frac{\pi}{n}}{n^2} == 0
\end{aligned}$$

The factor $\sqrt{\frac{\cot\frac{\pi}{n}}{n}}$ and the derivative plots are depicted in Figures D.1a and D.1b. Theoretically, the optimum case is for the infinity, or indeed pixels of circle shape as the function is a monotonic. However, practically, it might not worth due to the complexity and cost of fabrication.

For a square shape sensing membrane,

$$\begin{aligned}
a &= d_1 \times d_2\\
p &= 2 \times (d_1 + d_2) = 2 \times (d_1 + a/d_1)\\
min(p) =? &=> \frac{\delta p}{\delta d_1} = 0 =>\\
d_1 &= \sqrt{a} = d_2 =>\\
\frac{a}{p} &= d/4 = \sqrt{a}/4
\end{aligned} \tag{D.2}$$

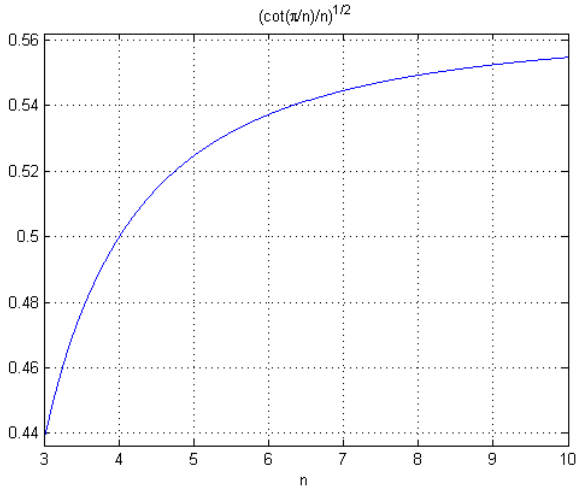

(a) $\sqrt{\frac{\cot\frac{\pi}{n}}{n}}$ vs n.

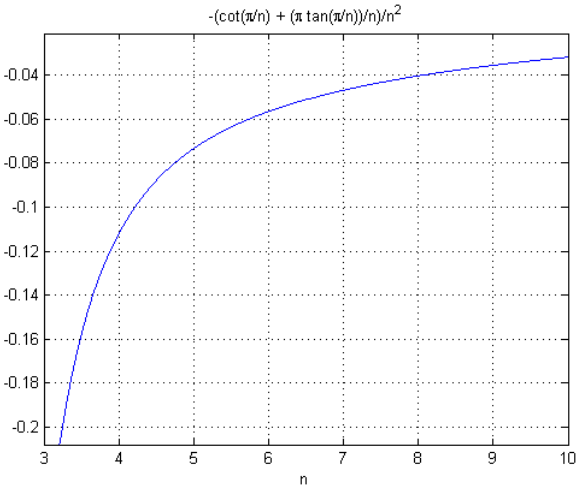

(b) Derivative of $\sqrt{\frac{\cot\frac{\pi}{n}}{n}}$ vs n.

Figure D.1.: Area to Perimeter and shape.

and for an octagonal shape sensing membrane giving about 10% higher area to perimeter

$$\begin{aligned} a &= 2(1+\sqrt{2})d^2 \\ p &= 8 \times d \\ \frac{a}{p} &= \frac{a}{8\sqrt{\frac{a}{2(1+\sqrt{2})}}} = \sqrt{\frac{1+\sqrt{2}}{2}}\frac{\sqrt{a}}{4} \\ &\approx 1.1\frac{\sqrt{a}}{4} \end{aligned} \tag{D.3}$$

E. Primary Experiment Results

A primary analysis on the dimension effect and encouraged further experiments was done with two sample dies. The results support the experiments on the new chip designed and provided in the main body.

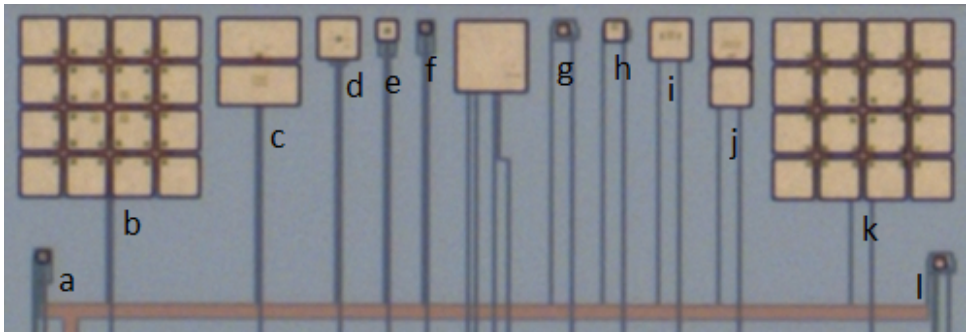

Figure E.1.: Primary test ISFET devices layout.

E.1. Experimental Result Summary

The drift analysis also showed that the signal of ISFETs with smaller sensing area to FET area ratio (larger ζ) may deviate more than larger ones (smaller ζ).

Table E.1.: Primary test devices.

Device Name	Sensing Membrane Dimension	Intrinsic MOSFET W/L	Item in Figure E.1
I-M-1	Reference MOSFET	$5\mu m/1\mu m$	a
I-1-80	$80\mu m \times 80\mu m$	$5\mu m/1\mu m$	b
I-1-40	$20\mu m \times 40\mu m$	$5\mu m/1\mu m$	c
I-1-20	$20\mu m \times 20\mu m$	$5\mu m/1\mu m$	d
I-1-10	$10\mu m \times 10\mu m$	$5\mu m/1\mu m$	e
I-1-05	$5\mu m \times 5\mu m$	$5\mu m/1\mu m$	f
I-5-05	$5\mu m \times 5\mu m$	$1\mu m/5\mu m$	g
I-5-10	$10\mu m \times 10\mu m$	$1\mu m/5\mu m$	h
I-5-20	$20\mu m \times 20\mu m$	$1\mu m/5\mu m$	i
I-5-40	$40\mu m \times 40\mu m$	$1\mu m/5\mu m$	j
I-5-80	$80\mu m \times 80\mu m$	$1\mu m/5\mu m$	k
I-M-5	Reference MOSFET	$1\mu m/5\mu m$	l

Table E.2.: Calculation of ζ.

	10nA	100nA	1uA	10uA	avg	std
I_1_05	5.442039	5.202993	NA	NA	5.322516	0.169031∗
I_1_10	2.535358	2.70188	3.214108	3.943581	3.098732	0.632973
I_1_20	0.961036	1.15479	1.320357	1.530217	1.2416	0.242043
I_1_40	0.458478	0.497325	0.549224	0.603553	0.527145	0.063061
I_1_80	0.26849	0.320656	0.346356	0.340153	0.318914	0.035354
I_5_05	NA	NA	NA	NA	NA	NA
I_5_10	2.892835	3.672092	3.885983	NA	3.483637	0.522707
I_5_20	1.418094	1.530267	1.572086	1.652688	1.543284	0.097709
I_5_40	0.770767	0.874327	0.898446	0.915706	0.864812	0.064952
I_5_80	0.298441	0.332726	0.320205	0.300988	0.31309	0.016302

∗ The values for strong inversion and velocity saturation regions are not counted as it wasn't possible to measure due to high offset.

Table E.3.: Simulation and experimental calculated ζ value comparison.

	Simulation @$10nA$	Experimental @$10nA$	Simulation @$1\mu A$	Experimental @$1\mu A$
I-1-05	12.384	5.442	NA	NA
I-1-10	3.107	2.535	6.011	3.214
I-1-20	0.773	0.961	1.505	1.320
I-1-40	0.232	0.458	0.368	0.549
I-1-80	0.055	0.268	0.099	0.346
I-5-05	12.694	NA	NA	NA
I-5-10	3.179	2.893	51.86	3.886
I-5-20	0.779	1.418	2.847	1.572
I-5-40	0.190	0.771	0.7117	0.898
I-5-80	0.051	0.298	0.1435	0.320

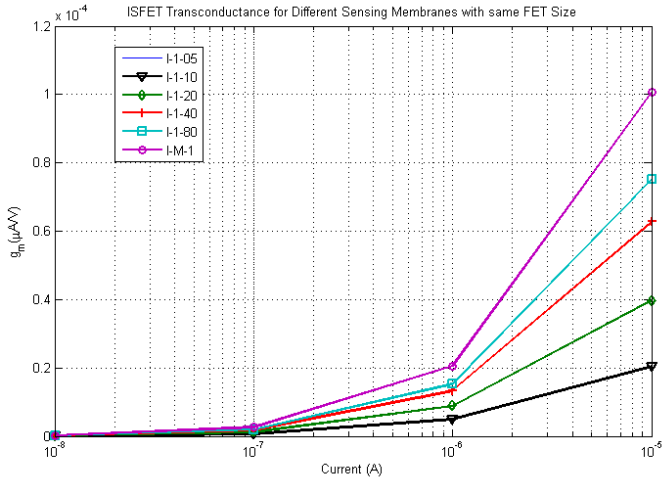

Figure E.2.: ISFETs and their counter-part MOSFET transconductance at different currents for FET of $5\mu m/1\mu m$.

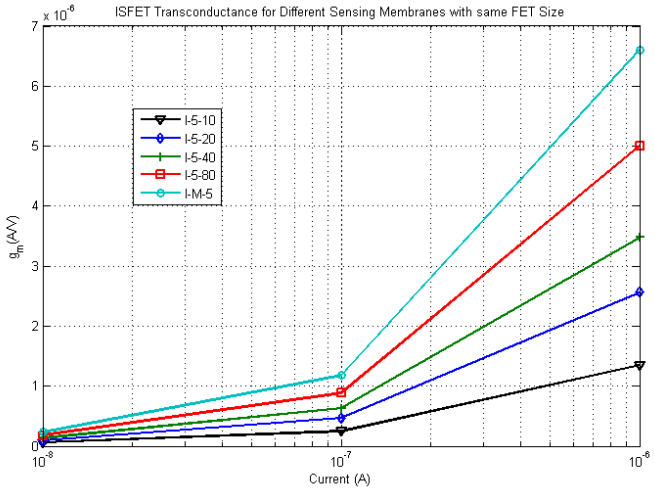

Figure E.3.: ISFETs and their counter-part MOSFET transconductance at different currents for FET of $1\mu m/5\mu m$.

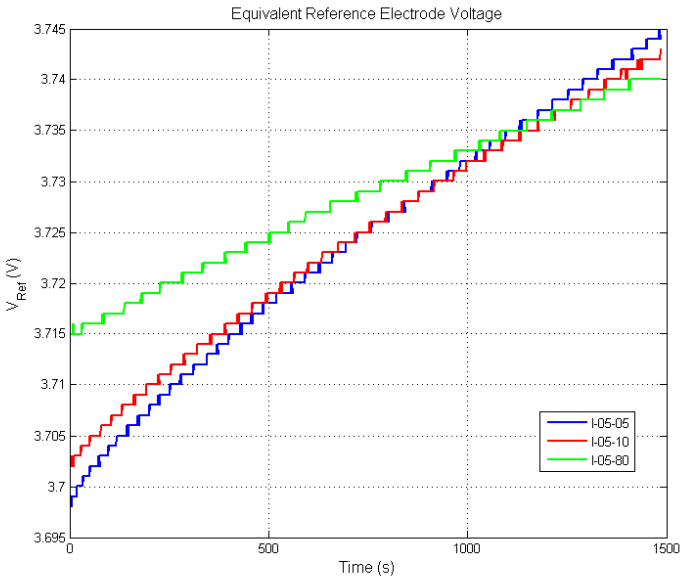

Figure E.4.: Equivalent reference electrode voltage over time.

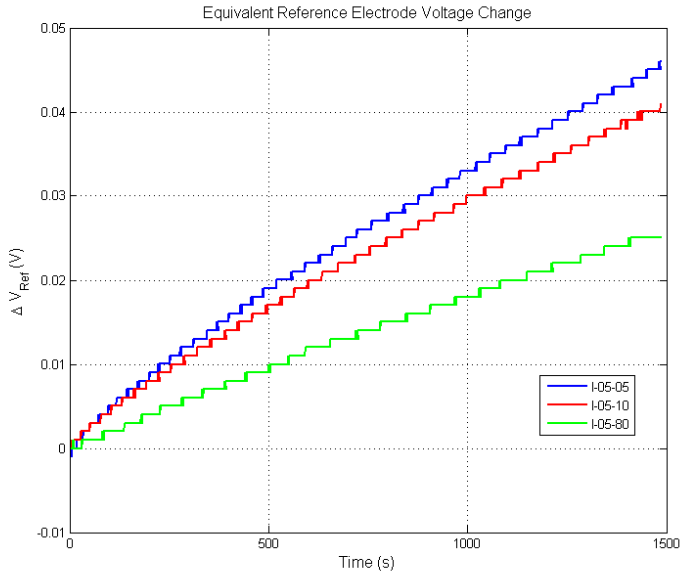

Figure E.5.: Equivalent reference electrode voltage change over time.

F. A Hypothesis for Dominance of Side-Wall Parasitics

In literature, the random offset in threshold of ISFETs, and generally floating gate FETs, has been reported to be resulted from trapped charge. It has always been treated as a memorised charge in the floating gate and metals. Considering the Gauss's law, net charge projects an electric field and in conductors, the excess charge resides on the surfaces and the field inside is zero. Therefore, the trapped charge may be a reason to create electric field and charge parasitic capacitances made by the metal layer.

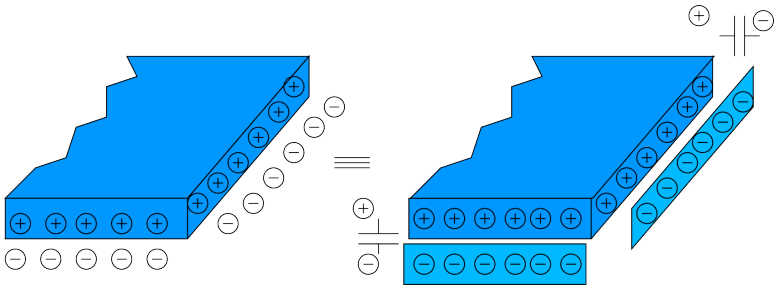

(a) Electrostatic induced charge in a metal assuming in potential V_M equivalent circuit model.

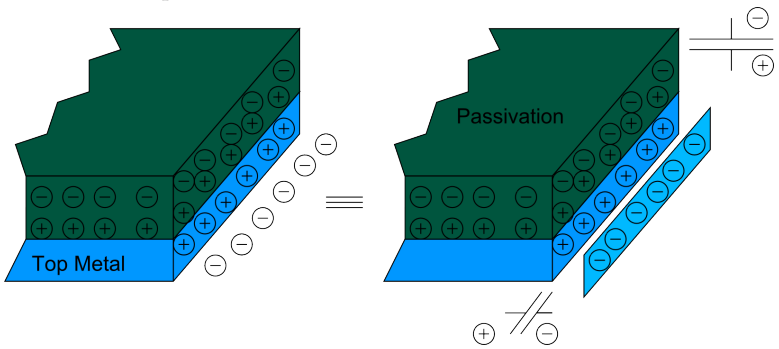

(b) Top metal induced trapped charge including passivation trapped charge equivalent.

Figure F.1.: Trapped charge and side-wall parasitics.

G. Experiment Set-up

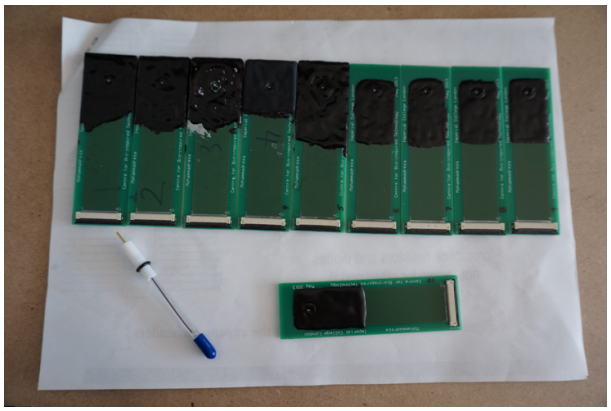

(a) 9 test dies/chips and the Ag/AgCl reference electrode. Number one was eliminated due to the insulation problem.

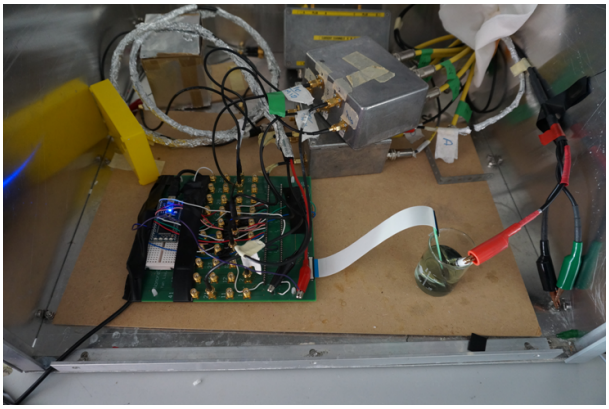

(b) Set-up inside the Faraday cage.

(c) Keithly 4200 device characterizing instrument.

Figure G.1.: Test devices and set-up in the lab.

H. Post-layout Calibre Extract Simulations

Table H.1 summarises the simulation results based on the Calibre extract of the test ISFETs layouts which similarly shows how the decoupling parasitic capacitances may increase by the increase in extended metal gate size. This may only support the experimental result mismatch to the primary simulation results where an inversely linear relation between the sensing area and ζ would be seen.

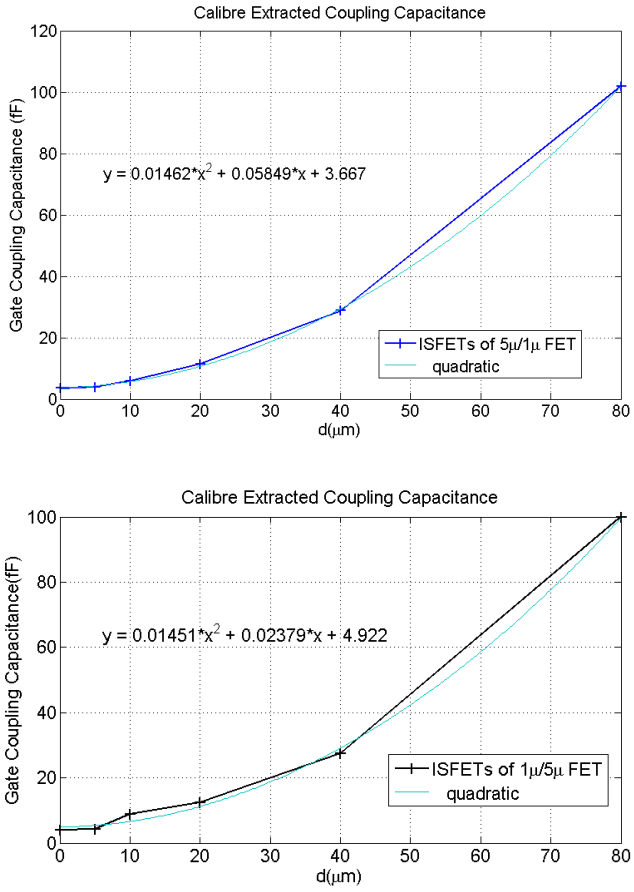

Figure H.1.: Calibre extracted coupling capacitance at the gate vs sensing membrane side size d.

Table H.1.: Calibre extracted simulation results.

	C_{pass} fF	C Total	V_{Pass} $10nA$	g_m $10nA$	g_m/g_{m0} $10nA$	ζ $10nA$	V_{Pass} $1\mu A$	g_m $1\mu A$	g_m/g_{m0} $1\mu A$	ζ $1\mu A$
I_1_05	0.566	3.93E-15	NaN	NaN	NaN	NaN	NaN	NaN	NA	NA
I_1_10	2.265	5.89E-15	2.1640	5.77E-08	0.2005	3.9887	3.1010	3.32E-06	0.1577	5.3420
I_1_20	9.060	1.15E-14	1.1190	9.60E-08	0.3334	1.9996	1.6920	5.70E-06	0.2709	2.6908
I_1_40	36.240	2.88E-14	0.7868	1.25E-07	0.4324	1.3124	1.2330	7.66E-06	0.3644	1.7440
I_1_80	144.960	1.02E-13	0.6181	1.77E-07	0.6144	0.6275	0.9093	1.31E-05	0.6205	0.6115
I_5_05	0.566	4.25E-15	6.2360	2.04E-08	0.0842	10.8698	NaN	NaN	NA	NA
I_5_10	2.265	8.82E-15	3.4210	2.33E-08	0.0959	9.4256	NaN	NaN	NaN	NaN
I_5_20	9.060	1.24E-14	1.4340	6.96E-08	0.2868	2.4862	2.9090	1.33E-06	0.2055	3.8669
I_5_40	36.240	2.75E-14	0.8824	1.22E-07	0.5010	0.9959	1.6070	2.86E-06	0.4414	1.2657
I_5_80	144.960	1.00E-13	0.7130	1.70E-07	0.7027	0.4231	1.1640	4.98E-06	0.7687	0.3008
I_M05	9.06	1.35E-14	1.0900	1.08E-07	0.3762	1.6584	1.5750	7.06E-06	0.3358	1.9779
I_M10	9.06	1.13E-14	1.1240	9.67E-08	0.3357	1.9785	1.7080	5.56E-06	0.2645	2.7803
I_Oct	2.314	5.56E-15	2.0830	5.99E-08	0.2081	3.8055	2.9880	3.42E-06	0.1627	5.1473
M_1		3.57E-15	0.3654	2.88E-07			0.5464	2.10E-05		
M_5		3.97E-15	0.4565	2.43E-07			0.7849	6.47E-06		

I. Coupling to Decoupling Ratio $1/\zeta$

While in Chapter 4 the experiment results on the relation of ζ as the decoupling to coupling capacitance ratio was provided, its inverse may give a complementary view on the influence of decoupling capacitors. $1/\zeta$ should be proportional to the area of the sensing membrane as the sole parameter changing among the ISFET devices under test. However, it shows a linear relation with its square root, which is equivalent to the side of the square-shape sensing membrane. This relation is the main sparkle on identifying the strong effect of the perimeter on decoupling, and a hypothesis on generation of side-wall capacitances by the residual trapped charges concentrating at the outer surface and edges of the gate-extending metals and sensing metal plate.

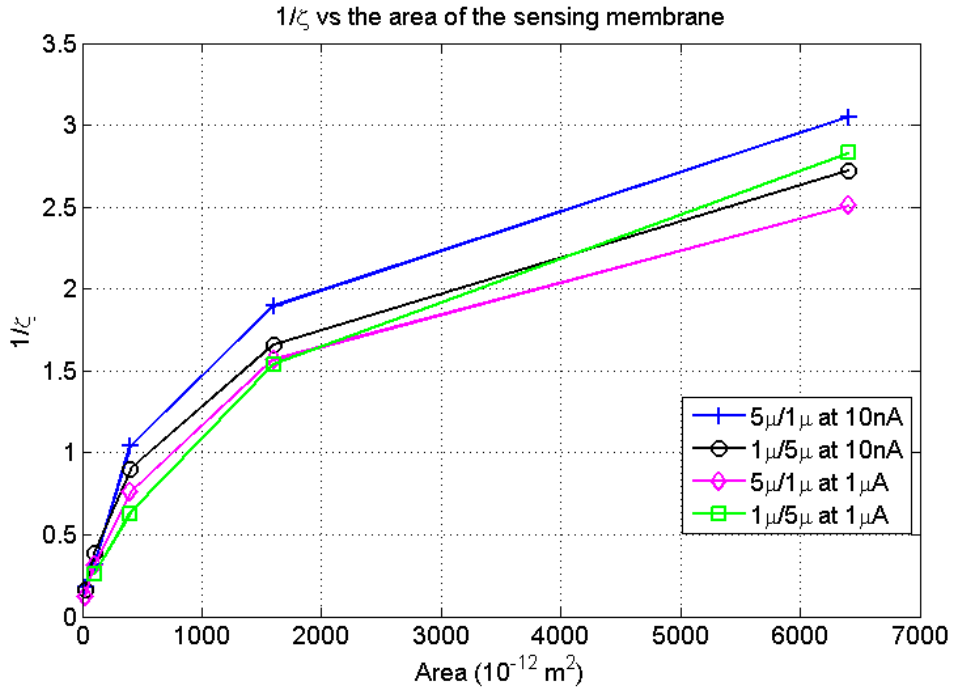

Figure I.1.: $1/\zeta$ vs the sensing area. It should have been linear but due to the decoupling capacitors it is not.

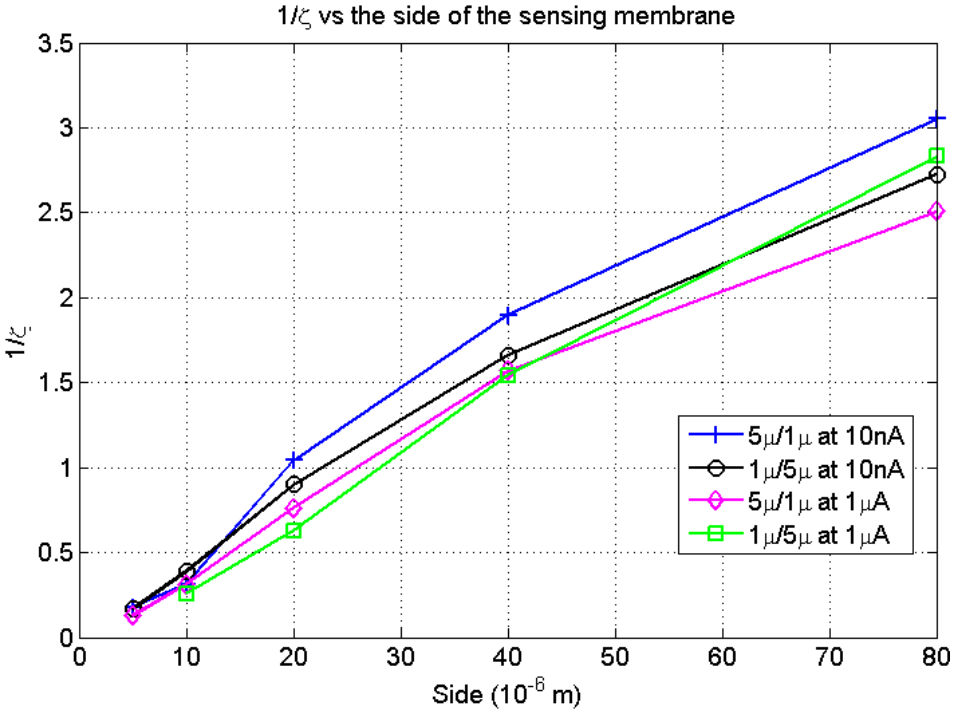

Figure I.2.: $1/\zeta$ vs the sensing plate side.

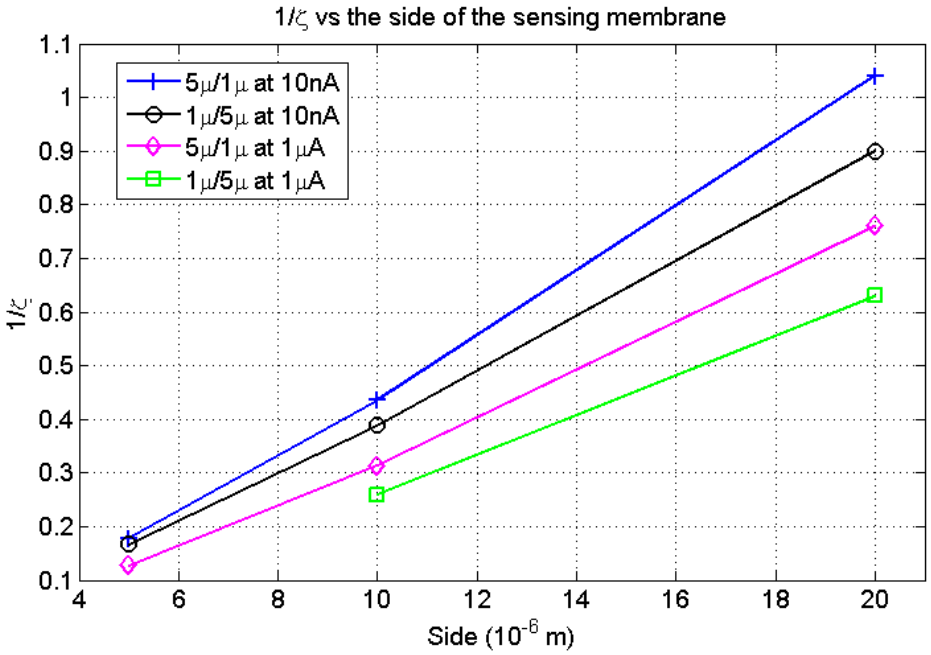

Figure I.3.: $1/\zeta$ vs the sensing plate side for the single-plate devices highlighting the linear relation with the side size.

J. Veriloga Model for ISFET

\\VerilogA for ISFET, *chembasic*, veriloga
'include "constants.vams"
'include "disciplines.vams"
module $chembasic(ref, pH, gate)$;
input ref, pH;
inout $gate$;
electrical $n10, ref, pH, gate$;
parameter real $alpha = 0.95$;
real $Eabs$;
real $Phim$;
real $Erel$;
real $Chieo$;
real $Philj$;
analog begin
$Ebs = 4.7$;
$Phim = 4.7$;
$Erel = 0.2$;
$Chieo = 3e - 3$;
$Philj = 1e - 3$;
$V(ref, n10) <+ Eabs - Phim - Erel + Chieo + Philj$;
$V(gate, n10) <+ -1 * 2.3 * alpha * \$vt * (V(pH) - 3)$;
end
endmodule

K. Error in Pseudo Inverter Pixel

The currents for the two transistor is the same and their drain voltages are connected to each other. There fore we have

$$\begin{aligned} &I_{D_N} = I_{D_P} \Rightarrow \\ &K_N(V_D)\{V_{In} + -V_{tn} - 1/2V_D\} = \\ &K_P(V_D - VDD)\{V_{Tune} + -VDD - V_{tp} - 1/2(V_D - VDD)\} \end{aligned} \tag{K.1}$$

Considering a change of ϵ in drain voltage as a change in the switching threshold of the second stage inverter, and changes in input voltage and tune voltage of respectively ΔV_{In} and ΔV_{Tune}.

$$\begin{aligned} &I_{D_N} = I_{D_P} \Rightarrow \\ &K_N(V_D + \epsilon)\{V_{In} + \Delta V_{In} - V_{tn} - 1/2(V_D + \epsilon)\} = \\ &K_P(V_D + \epsilon - VDD)\{V_{Tune} + \Delta V_{Tune} - VDD - V_{tp} - 1/2(V_D + \epsilon - VDD)\} \\ &\Rightarrow \\ &K_N(V_D + \epsilon)\{V_{In} - V_{tn} - 1/2(V_D + \epsilon)\} + K_N(V_D + \epsilon)\Delta V_{In} = \\ &K_P(V_D + \epsilon - VDD)\{V_{Tune} - VDD - V_{tp} - 1/2(V_D + \epsilon - VDD)\} + K_P(V_D + \epsilon - VDD)\Delta V_{Tune} \end{aligned} \tag{K.2}$$

The first term on each side of the last equal sign is the same and follow each other. The second terms has to be equal too so that the currents become equal.

$$\begin{aligned} &K_N(V_D + \epsilon)\Delta V_{In} = K_P(V_D + \epsilon - VDD)\Delta V_{Tune} \\ &\Delta V_{Tune} = \frac{K_N(V_D + \epsilon)}{K_P(V_D + \epsilon - VDD)}\Delta V_{In} \\ &V_D = VDD/2 \\ &\Delta V_{Tune} = -\frac{K_N(VDD/2 + \epsilon)}{K_P(VDD/2 - \epsilon)}\Delta V_{In} \end{aligned} \tag{K.3}$$

While ideally $\epsilon = 0$, the error in the change of the tune voltage becomes

$$\Delta\Delta V_{Tune} = -\frac{K_N}{K_P}\frac{\epsilon}{VDD/2 - \epsilon} \tag{K.4}$$

The value of ϵ is defined by the lower and higher threshold range for the inverter switching threshold.